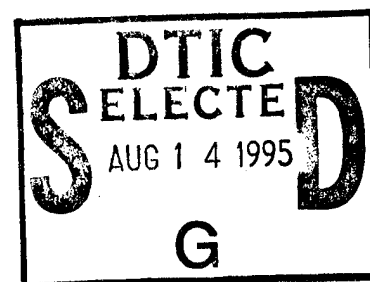


AFIT/DS/ENY/95-4



THE DEPENDENCE OF THE TIME-ASYMPTOTIC  
STRUCTURE OF 3-D VORTEX BREAKDOWN  
ON BOUNDARY AND INITIAL CONDITIONS

DISSERTATION  
Jeffrey Curtis Tromp  
Wright Laboratory, Wright-Patterson Air Force Base, OH

AFIT/DS/ENY/95-4

19950811 055

Approved for public release; distribution unlimited

THE DEPENDENCE OF THE TIME-ASYMPTOTIC  
STRUCTURE OF 3-D VORTEX BREAKDOWN  
ON BOUNDARY AND INITIAL CONDITIONS

DISSERTATION

Presented to the Faculty of the School of Engineering  
of the Air Force Institute of Technology  
Air University  
In Partial Fulfillment of the  
Requirements for the Degree of  
Doctor of Philosophy

Jeffrey Curtis Tromp, B.S., M.S.  
Wright Laboratory, Wright-Patterson Air Force Base, OH

Accession For	
NTIS	CRA&I <input checked="" type="checkbox"/>
DTIC	TAB <input type="checkbox"/>
Unannounced <input type="checkbox"/>	
Justification _____	
By _____	
Distribution /	
Availability Codes	
Dist	Avail and/or Special
A-1	

July, 1995

Approved for public release; distribution unlimited

THE DEPENDENCE OF THE TIME-ASYMPTOTIC  
STRUCTURE OF 3-D VORTEX BREAKDOWN  
ON BOUNDARY AND INITIAL CONDITIONS

Jeffrey Curtis Tromp, B.S., M.S.

Wright Laboratory, Wright-Patterson Air Force Base, OH

Approved:

<u>R. S. Phan</u>	<u>27 JUL 95</u>
<u>Michael J. Stoecken</u>	<u>27 Jul 95</u>
<u>[Signature]</u>	<u>27 JUL 95</u>
<u>Pao S. Ly</u>	<u>28 July 95</u>

[Signature]

R.A. Calico, Jr.

Dean, School of Engineering

### *Acknowledgements*

The successful completion of this work required support from many different people and organizations. At this time, I would like to thank those who were instrumental in helping me perform this research.

First of all, there is the financial support. This work was sponsored by the Air Force Office of Scientific Research (AFOSR). I also gratefully acknowledge my employers, Wright Laboratory, for funding my residence at AFIT under the AFMC/AFIT work-study program. Computer support was obtained through AFOSR funding, and through the Department of Defense (DoD) High Performance Computing (HPC) Modernization Program. In particular, this work was supported in part by a grant of HPC time from the DoD HPC center, Bay St. Louis, MS., on a Cray C-90 supercomputer.

Second, I received a great deal of support and encouragement from my coworkers at Wright Laboratory. My supervisor, Mr Dieter Multhopp, allowed me time away from my normal responsibilities so that I could complete this work. This separation of duties is the key to the success of the work-study program. Thanks to Mr Jerry Jenkins, for his constant support of this work and for our many insightful discussions.

Third, I would like to thank my research advisor, Dr Philip Beran, for our many talks on vortex breakdown, and for always keeping a positive outlook on this research.

Finally, I would like to thank my wife Lisa, who was most instrumental in the completion of this research. Her patience and understanding is greatly appreciated.

Jeffrey Curtis Tromp



## *Table of Contents*

	Page
Acknowledgements . . . . .	iii
Table of Contents . . . . .	iv
List of Figures . . . . .	x
List of Tables . . . . .	xiv
List of Symbols . . . . .	xvi
Abstract . . . . .	xx
 I. Introduction . . . . .	 1
1.1 Objectives . . . . .	9
1.2 Approach . . . . .	10
1.3 Outline of Study . . . . .	11
 II. Background . . . . .	 14
2.1 Synopsis of Previous Work on Vortex Breakdown . . . . .	14
2.1.1 Theoretical Work . . . . .	14
2.1.2 Experimental Work . . . . .	20
2.1.3 Numerical Work . . . . .	24
2.2 Previous Applications of the Compact Scheme . . . . .	30
 III. The Time-Accurate Navier-Stokes (TANS) Model . . . . .	 31
3.1 Geometry and Grid . . . . .	31
3.2 Governing Equations . . . . .	35
3.3 Transformation to Computational Coordinates . . . . .	39
3.4 Boundary Condition Formulation . . . . .	40

	Page
3.4.1 Specification of Boundary Locations . . . . .	40
3.4.2 Inflow-1 . . . . .	43
3.4.3 Inflow-2 . . . . .	45
3.4.4 Outflow . . . . .	48
3.4.5 Wall-1 . . . . .	48
3.4.6 Wall-2 . . . . .	49
3.5 Discrete Boundary Conditions . . . . .	53
3.5.1 Inflow-1: Discrete Form . . . . .	54
3.5.2 Inflow-2: Discrete Form . . . . .	55
3.5.3 Outflow: Discrete Form . . . . .	56
3.5.4 Wall-1: Discrete Form . . . . .	57
3.5.5 Wall-2: Discrete Form . . . . .	57
3.6 Solution Procedure . . . . .	60
3.6.1 Spatial and Temporal Discretization . . . . .	60
3.6.2 Artificial Dissipation . . . . .	62
3.6.3 Sweeping Strategy . . . . .	63
3.6.4 Evaluation of Explicit Right-Hand Side Terms . . . . .	64
3.6.5 Modification of Sweeping Strategy . . . . .	66
3.6.6 Freestream Conservation . . . . .	67
3.7 Computational Resources and TANS Performance . . . . .	67
3.7.1 Computational Resources . . . . .	67
3.7.2 TANS Performance . . . . .	68
3.8 Visualization . . . . .	69
3.9 Recorded Data . . . . .	71
3.9.1 Calculation of $Q$ . . . . .	71
3.9.2 Calculation of $\Delta^n U_{\max}$ . . . . .	71
3.9.3 Calculation of $u_s$ , $v_s$ and $w_s$ . . . . .	71

	Page
3.9.4 Calculation of $u_c(x)$ . . . . .	72
3.10 Definition of the $L_2$ Norm . . . . .	72
IV. Grid Requirements & Validation . . . . .	73
4.1 Grid Requirements . . . . .	73
4.1.1 Effects of Axial Node Spacing . . . . .	74
4.1.2 Effects of Tube Length . . . . .	76
4.1.3 Effects of Radial Node Spacing: Second-Order Accuracy . . . . .	77
4.1.4 Effects of Radial Node Spacing: Fourth-Order Accuracy . . . . .	79
4.1.5 Effects of Tube Radius . . . . .	79
4.1.6 Grid Requirements for PAC Model . . . . .	81
4.1.7 Summary of Grid Requirements . . . . .	83
4.2 Validation . . . . .	83
V. Results . . . . .	87
5.1 Results for $Re = 100$ . . . . .	87
5.2 Results for $Re = 250$ . . . . .	91
5.2.1 Evidence of a Hopf Bifurcation . . . . .	92
5.2.2 The Effect of Three-Dimensionality on $Q$ . . . . .	104
5.2.3 Flow Visualization . . . . .	108
5.3 Results for $Re = 500$ . . . . .	115
5.3.1 Solution Behavior Near the Primary Limit Point . . . . .	115
5.3.2 The Growth and Decay of Asymmetric Flow Near the Inflow Boundary . . . . .	121
5.4 Results for $Re = 1000$ . . . . .	123
5.4.1 Axisymmetric Solutions for $Re = 1000$ . . . . .	124
5.4.2 Solutions for Vortex Strengths Less Than $\mathcal{V}_p$ . . . . .	126
5.4.3 Solutions for Vortex Strengths Greater than $\mathcal{V}_p$ . . . . .	130

	Page
5.4.4 Evidence of a Hopf Bifurcation Near the Primary Limit Point . . . . .	131
5.4.5 Results for Further Increases in $\mathcal{V}$ . . . . .	134
5.4.6 Solution Sensitivity to Tube Length . . . . .	140
5.4.7 Flow Visualization for $Re = 1000$ . . . . .	140
VI. Summary . . . . .	145
6.1 The TANS Model . . . . .	145
6.1.1 The Compact Scheme . . . . .	145
6.1.2 The Multiblock Grid . . . . .	148
6.2 Summary of Results for $Re = 250$ : The Hopf Bifurcation in the Presence of Unique Axisymmetric Solutions . . . . .	149
6.2.1 Evidence of a Hopf Bifurcation . . . . .	149
6.2.2 The Relationship Between the Emergence of Three-Dimensional Flow and $Q$ . . . . .	150
6.2.3 Assessment of Grid and Geometry Effects: $Re = 250$ . .	150
6.3 Summary of Results for $Re = 500$ and $Re = 1000$ : Hopf Bifurcation in the Presence of Nonunique Axisymmetric Solutions . . .	151
6.3.1 The Role of the Primary Limit Point . . . . .	152
6.3.2 Assessment of Grid and Geometry Effects: $Re = 1000$ .	154
6.4 Relationship Between Observed Types of Flow Structures with Experiments . . . . .	155
6.5 A Summary Assessment of Numerical Accuracy . . . . .	159
VII. Conclusions and Recommendations . . . . .	161
7.1 Conclusions . . . . .	161
7.2 Recommendations . . . . .	164
7.2.1 Improvements to TANS Model . . . . .	164
7.2.2 Further Validation . . . . .	165

	Page
7.2.3 Additional Studies with the Tube Geometry . . . . .	166
7.2.4 Time-Varying Circulation . . . . .	167
Appendix A. The Navier-Stokes Equations . . . . .	169
A.1 Dimensional Equations of Motion . . . . .	169
A.2 Dimensional Equations of Motion in Vector Form . . . . .	171
A.3 Nondimensionalization of Equations of Motion . . . . .	171
A.4 Final Form of Equation of Motion . . . . .	173
Appendix B. The Pseudo-Arclength Continuation (PAC) Model . . . . .	175
B.1 Definitions . . . . .	175
B.2 The Pseudo-Arclength Continuation Model . . . . .	178
B.2.1 The PAC Method . . . . .	178
B.2.2 Governing Equations . . . . .	179
B.2.3 Boundary Conditions . . . . .	182
B.3 Solution Interpolation Between 2-D and 3-D Grids . . . . .	183
B.3.1 Cubic Spline Interpolation . . . . .	183
B.3.2 Validation . . . . .	185
B.3.3 Restart File Generation . . . . .	186
Appendix C. Grid Generation . . . . .	188
C.1 Grid Construction . . . . .	188
C.2 Assessment of Grid Quality . . . . .	189
Appendix D. TANS Validation . . . . .	192
D.1 Incompressible Flow over a Flat Plate . . . . .	192
D.2 Compressible Flow over a Flat Plate . . . . .	194
D.3 Unsteady Couette Flow . . . . .	197
D.4 Unsteady Heat Conduction . . . . .	199

	Page
Appendix E.      Simplified Euler Equations for Steady, Axisymmetric Flow . . .	203
E.1    Development of the Bragg-Hawthorne Equation . . . . .	203
E.2    Extension to Compressible Flows . . . . .	206
Appendix F.      Derivation and Application of the Beam-Warming Scheme . . .	211
F.1    The Fourth-Order Compact Scheme Approximation . . . . .	211
F.2    A General 3 Time-Level Marching Scheme . . . . .	213
F.3    The Beam-Warming Scheme Applied to Equations in Nonconser- vative Form . . . . .	216
Appendix G.      TANS Run Matrix and Grid Specification . . . . .	219
G.1    Estimate of Computer Usage . . . . .	223
Bibliography . . . . .	224

# *List of Figures*

Figure	Page
1. Vortex breakdown in leading-edge vortices over a delta wing . . . . .	2
2. The Type 0 (bubble) breakdown . . . . .	4
3. The Type 2 (spiral) breakdown . . . . .	4
4. A representative solution branch of axisymmetric solutions . . . . .	6
5. The Type 6 flow disturbance . . . . .	22
6. The Type 5 (double-helix) flow disturbance . . . . .	23
7. The Type 4 flow disturbance . . . . .	23
8. The Type 3 flow disturbance . . . . .	24
9. Characteristic solution diagram for the Bragg-Hawthorne equation . . . .	28
10. Coordinate systems: (a) Cartesian, (b) cylindrical . . . . .	32
11. Tube geometry . . . . .	33
12. Schematics of a single-block computational domain . . . . .	34
13. Crossplane grid for G1: (a) physical, (b) computational . . . . .	35
14. Axial slice of grids through $z = 0$ : (a) G1, (b) G2 . . . . .	36
15. Schematic of crossplane grid in the computational domain . . . . .	41
16. Inflow-2 density profiles . . . . .	46
17. Illustration of sweeping strategy: (a) $\eta$ sweep (b) $\zeta$ sweep . . . . .	64
18. Schematic of computational domain showing treatment of cut boundaries .	66
19. Effect of axial node spacing on centerline axial velocity . . . . .	75
20. Effect of domain length on centerline axial velocity . . . . .	76
21. Effect of crossplane node spacing on centerline axial velocity . . . . .	78
22. Effect of crossplane node spacing on centerline axial velocity using the fourth-order compact scheme . . . . .	80
23. Comparison of 2-D solution paths between the PAC model and the model used by Beran and Culick (1992) for $Re = 250$ . . . . .	82
24. Comparison between TANS and PAC solutions for $\mathcal{V}=1.0$ . . . . .	85

Figure	Page
25. Comparison between TANS and PAC solutions for $\mathcal{V}=1.7$ . . . . .	86
26. $Q$ versus time for $\mathcal{V}=1.8$ . . . . .	88
27. Evidence of periodic flow for $\mathcal{V} = 1.8$ and $Re = 100$ . . . . .	89
28. Minimum axial velocity, $Q$ , versus vortex strength, $\mathcal{V}$ , for $Re=100$ . . . . .	90
29. $Q$ versus time for $M = 0.3$ and $Re = 250$ . . . . .	93
30. Effect of time step and tube length on $Q$ for $M = 0.3$ and $Re = 250$ . . . . .	94
31. Comparison between TANS and PAC solutions for Run 17, $\mathcal{V}=1.5$ . . . . .	96
32. Crossplane velocity components $v_s$ and $w_s$ versus time . . . . .	97
33. Axial velocity component $u_s$ versus time . . . . .	98
34. Phase plot for $\mathcal{V} = 1.53$ . . . . .	99
35. Phase plot for $\mathcal{V} = 1.55$ . . . . .	99
36. Phase plot for $\mathcal{V} = 1.65$ . . . . .	100
37. Phase plot for $\mathcal{V} = 2.3$ . . . . .	100
38. Evidence of a Hopf bifurcation for $M = 0.3$ and $Re = 250$ . . . . .	101
39. Velocity vectors for $\mathcal{V} = 1.5$ and $1.53$ . . . . .	104
40. Velocity vectors for $\mathcal{V} = 1.65$ and $1.8$ . . . . .	105
41. Velocity vectors for $\mathcal{V} = 2.1$ and $2.3$ . . . . .	106
42. Contours of radial vorticity, $\hat{\xi}$ , for $\mathcal{V} = 1.53$ . . . . .	112
43. Particle traces showing development of three-dimensionality . . . . .	113
44. Particle traces showing periodic rotation of flow structure . . . . .	114
45. Axisymmetric solution path for $Re = 500$ and $M = 0.3$ . . . . .	116
46. $Q$ versus time for $Re = 500$ . . . . .	118
47. Periodic behavior of flow computed at $\mathcal{V} = 1.5$ and $Re = 500$ . . . . .	119
48. $\Omega_1$ versus time for $Re = 500$ . . . . .	120
49. Growth and decay of asymmetric disturbance $\Omega_2(x, t)$ versus $x$ for various times . . . . .	122
50. 2-D solution paths $Re = 1000$ and $M = 0.3$ : (a) global view, (b) magnified view . . . . .	125



Figure	Page
51. $Q$ versus time for Runs 36-38 (grid G1) . . . . .	127
52. Schematic representation of grid convergence for second and fourth-order schemes. . . . .	129
53. $Q$ versus time for Runs 39-41 (grid G2) . . . . .	130
54. $Q$ versus time for Runs 42-44 (grid G3) . . . . .	131
55. $Q$ versus time for $M = 0.3$ and $Re = 1000$ . . . . .	132
56. Crossplane velocity components $v_s$ and $w_s$ versus time for $Re = 1000$ . . .	133
57. Axial velocity component $u_s$ versus time for $Re = 1000$ . . . . .	134
58. Phase plots for $\mathcal{V} = 1.5$ and $1.6$ . . . . .	134
59. Evidence of a Hopf bifurcation near the primary limit point for $Re = 1000$	135
60. $Q$ versus time for $Re = 1000$ and $M = 0.3$ . . . . .	137
61. Crossplane velocity components $v_s$ and $w_s$ versus time for $Re = 1000$ . . .	138
62. Axial velocity component $u_s$ versus time for $Re = 1000$ . . . . .	138
63. Phase plots showing loss of periodic behavior . . . . .	139
64. Sensitivity of $Q(t)$ to tube length . . . . .	142
65. Particle traces showing development of three-dimensionality with increasing vortex strength . . . . .	143
66. Particle traces showing evolution of the spiral mode of vortex breakdown as vortex strength is increased . . . . .	144
67. Plot of the axial position (abscissa) of flow disturbances 0-6 as a function of $Re_{FL}$ and the swirl parameter $\Omega_{FL}$ . . . . .	156
68. A representative solution branch depicting limit points . . . . .	176
69. Graphical representation of Hopf bifurcations: (a) supercritical, (b) subcritical . . . . .	178
70. Graphical representation of the pseudo-arclength continuation solution procedure . . . . .	180
71. Typical crossplane grids (top and bottom blocks omitted for clarity): (a) initial grid, (b) final grid . . . . .	189
72. Results of grid-rotation study . . . . .	191

Figure		Page
73.	Comparison of streamwise velocity profiles for steady, flat-plate flow . . .	194
74.	Temperature profiles for compressible, flat-plate flow . . . . .	197
75.	Formation of Couette flow . . . . .	199
76.	Unsteady heat conduction . . . . .	202

# *List of Tables*

Table	Page
1. 3-D grid parameters . . . . .	36
2. Comparison of centerline values of $\rho_c$ between PAC model and results of Morton (1989) . . . . .	47
3. Performance of the TANS code . . . . .	69
4. Run matrix for grid resolution study . . . . .	74
5. 2-D grid parameters . . . . .	83
6. Summary of TANS run parameters for validation . . . . .	84
7. Summary of TANS run parameters for $Re = 100$ . . . . .	87
8. Comparison of 2-D (PAC) and 3-D (TANS) minimum axial velocities for $Re = 100$ . . . . .	90
9. Summary of TANS run parameters for $Re = 250$ . . . . .	91
10. Quantification of the agreement between PAC solutions and axisymmetric TANS solutions . . . . .	95
11. Summary of computed flow parameters for $Re = 250$ . . . . .	102
12. Comparison of minimum azimuthal vorticities for 2-D and 3-D flows . . . . .	107
13. Summary of TANS model parameters for $Re = 500$ . . . . .	116
14. Summary of results for $Re = 500$ . . . . .	117
15. Summary of TANS run parameters for $Re = 1000$ . . . . .	124
16. Summary of computed flow parameters for $Re = 1000$ . . . . .	136
17. Summary of quantified results . . . . .	159
18. Cubic spline results . . . . .	186
19. Effect of boundary conditions . . . . .	186
20. Pressure values at two points in the crossplane for various grid rotation angles . . . . .	191
21. Time marching schemes . . . . .	216
22. TANS run matrix . . . . .	220
22. TANS run matrix (con't) . . . . .	221

Table		Page
23.	3-D grid parameters . . . . .	221
24.	2-D grid parameters . . . . .	222

### *List of Symbols*

$c_p$	: Specific heat at constant pressure.
$c_v$	: Specific heat at constant volume.
$e$	: Symmetric strain tensor for axisymmetric flow in cylindrical coordinates.
$i$	: Node index in the $\xi$ direction.
$j$	: Node index in the $\eta$ direction.
$j1$	: Node index of $\eta$ at a grid cut.
$j2$	: Node index of $\eta$ at a grid cut.
$k$	: Node index in the $\zeta$ direction.
$k1$	: Node index of $\zeta$ at a grid cut.
$k2$	: Node index of $\zeta$ at a grid cut.
$mflops$	: Number of floating point operations (in millions) per second of CPU time.
$n$	: Time level or azimuthal wave number.
$nx$	: Number of nodes in the $\xi$ direction.
$ny$	: Number of nodes in the $\eta$ direction.
$nz$	: Number of nodes in the $\zeta$ direction.
$p$	: Pressure, nondimensional.
$\vec{q}$	: Heat flux vector for 3-D flow in Cartesian coordinates.
$\hat{\vec{q}}$	: Heat flux vector for axisymmetric flow in cylindrical coordinates.
$r$	: Radial coordinate in cylindrical system, nondimensional.
$t$	: Time, nondimensional.
$u$	: Velocity component in the $x$ direction, nondimensional.
$u_c$	: $u$ evaluated along each centerline node.
$u_s$	: $u$ evaluated along the centerline at $x = 7$ .
$\hat{u}$	: Velocity component in the $r$ direction, nondimensional.
$v$	: Velocity component in the $y$ direction, nondimensional.
$v_s$	: $v$ evaluated along the centerline at $x = 7$ .
$\hat{v}$	: Velocity component in the $\theta$ direction, nondimensional.
$w$	: Velocity component in the $z$ direction, nondimensional.

$w_s$	: $w$ evaluated along the centerline at $x = 7$ .
$\hat{w}$	: Velocity component in the $\hat{z}$ direction, nondimensional.
$x$	: Streamwise coordinate in Cartesian system, nondimensional.
$x_1$	: Tube geometry parameter denoting length of the constricted region.
$x_2$	: Grid parameter denoting length of the clustered region.
$y$	: Crossplane coordinate in Cartesian system, nondimensional.
$z$	: Crossplane coordinate in Cartesian system, nondimensional.
$\hat{z}$	: Streamwise coordinate in cylindrical system, nondimensional.
$A$	: Nonconservative equivalent of the $x$ -flux Jacobian matrix.
$B$	: Nonconservative equivalent of the $y$ -flux Jacobian matrix.
$C$	: Nonconservative equivalent of the $z$ -flux Jacobian matrix.
$D$	: Vector of viscous and heat transfer terms.
$DPI$	: CPU time per iteration per node.
$H$	: Global maximum of $d\hat{v}/d\theta$ .
$J$	: Transformation Jacobian.
$L$	: Tube length, nondimensional.
$L_2$	: The $L_2$ norm of a vector $\underline{x}$ consisting of $n$ elements is $L_2 \equiv [\frac{1}{n} \sum_{i=1}^n x_i^2]^{1/2}$ .
$M$	: Reference Mach number.
$Pr$	: Prandtl number.
$Q$	: Global minimum of axial velocity.
$Re$	: Reynolds number based on vortex core radius, $r_0$ , and reference velocity.
$Re_{FL}$	: Reynolds number based on tube diameter and average inlet axial velocity.
$R_0$	: Tube radius, nondimensional.
$T$	: Temperature, nondimensional.
$\mathcal{A}$	: Nonconservative equivalent of the $\xi$ -flux Jacobian matrix.
$\mathcal{B}$	: Nonconservative equivalent of the $\eta$ -flux Jacobian matrix.
$\mathcal{C}$	: Nonconservative equivalent of the $\zeta$ -flux Jacobian matrix.
$\mathcal{I}^1$	: Set of inlet node indices = $\{(i, j, k) : i = 1; (j, k) = \mathcal{R}^c\}$ .
$\mathcal{I}^2$	: Set of wall node indices = $\{(i, j, k) : i = 2, \dots, nx - 1; (j, k) = \mathcal{R}^w\}$ .
$\mathcal{I}^3$	: Set of outlet node indices = $\{(i, j, k) : i = nx; (j, k) = \mathcal{R}^c\}$ .

$\mathcal{I}^{\text{ref}}$	: Reference node indices = $\{(i, j, k) : i = 1; (j, k) = \mathcal{R}^w\}$ .
$\mathcal{R}^1$	: $\{(j, k) : j = 1, \dots, ny; k = k1, \dots, k2\}$ .
$\mathcal{R}^2$	: $\{(j, k) : j = j1, \dots, j2; k = 1, \dots, k1 - 1\}$ .
$\mathcal{R}^3$	: $\{(j, k) : j = j1, \dots, j2; k = k2 + 1, \dots, nz\}$ .
$\mathcal{R}^4$	: $\{(j, k) : j = 1; k = k1, \dots, k2\}$ .
$\mathcal{R}^5$	: $\{(j, k) : j = ny; k = k1, \dots, k2\}$ .
$\mathcal{R}^6$	: $\{(j, k) : j = j1, \dots, j2; k = 1\}$ .
$\mathcal{R}^7$	: $\{(j, k) : j = j1, \dots, j2; k = nz\}$ .
$\mathcal{R}^c$	: Crossplane node indices = $\mathcal{R}^1 \cup \mathcal{R}^2 \cup \mathcal{R}^3$ .
$\mathcal{R}^w$	: Crossplane node indices at the wall = $\mathcal{R}^4 \cup \mathcal{R}^5 \cup \mathcal{R}^6 \cup \mathcal{R}^7$ .
$S$	: A compact operator defined by $1 + \delta^2/6$ .
$\mathcal{V}$	: Vortex strength.
$\alpha$	: Tube contraction parameter.
$\beta$	: Grid clustering parameter.
$\gamma$	: Ratio of specific heats, $c_p/c_v$ , or eigenvalues.
$\delta$	: Central-difference operator ( $\delta u_i = u_{i+1} - u_{i-1}$ ) or Kronecker delta.
$\delta^2$	: Finite-difference operator ( $\delta^2 u_i = u_{i+1} - 2u_i + u_{i-1}$ )
$\delta t$	: Time lag used for generating phase plots.
$\zeta$	: Computational coordinate, nondimensional.
$\hat{\zeta}$	: Axial component of vorticity, nondimensional.
$\eta$	: Computational coordinate, nondimensional.
$\hat{\eta}$	: Azimuthal component of vorticity, nondimensional.
$\hat{\eta}_m$	: Global minimum of $\hat{\eta}$ .
$\theta$	: Azimuthal coordinate in cylindrical system, nondimensional.
$\theta_1$	: Time-integration parameter.
$\theta_2$	: Time-integration parameter.
$\theta_3$	: Time-integration parameter.
$\theta_4$	: Time-integration parameter.
$\mu$	: Fluid viscosity, nondimensional.
$\xi$	: Computational coordinate, nondimensional.

$\hat{\xi}$	: Radial component of vorticity, nondimensional.
$\rho$	: Density, nondimensional.
$\rho_c$	: Inflow density assuming axisymmetric and columnar flow.
$\tau$	: Symmetric stress tensor for 3-D flow in Cartesian coordinates.
$\hat{\tau}$	: Symmetric stress tensor for axisymmetric flow in cylindrical coordinates.
$\omega_e$	: Explicit damping coefficient.
$\Gamma$	: Vortex circulation.
$\Delta r$	: Average radial node spacing, nondimensional.
$\Delta t$	: Time step, nondimensional.
$\Delta x$	: Axial node spacing in $x$ direction, nondimensional.
$\Delta x_0$	: Axial node spacing at $x = 0$ and $x > x_2$ .
$\Delta^n U$	: Solution increment defined by $U^{n+1} - U^n$ .
$\Delta^n U_1$	: Solution increment following the $\xi$ sweep.
$\Delta^n U_2$	: Solution increment following the $\eta$ sweep.
$\Phi$	: Viscous dissipation function for 3-D flow in Cartesian coordinates.
$\hat{\Phi}$	: Viscous dissipation function for axisymmetric flow in cylindrical coordinates.
$\Omega$	: Minimum/maximum values of $v + w$ considering all centerline nodes.
$\Omega_1$	: Sum of $v_s$ and $w_s$ .
$\Omega_2$	: Absolute value of $v(x, t) + w(x, t)$ along the tube centerline.
$\Omega_{FL}$	: Vortex strength based on average inlet axial velocity.



*Abstract*

The three-dimensional, compressible Navier-Stokes equations in primitive variables are solved numerically to simulate vortex breakdown in tubes. Time integration is performed with an implicit Beam-Warming algorithm, which uses fourth-order compact operators to discretize spatial derivatives. Initial conditions are obtained by solving the steady, compressible, and axisymmetric form of the Navier-Stokes equations using Newton's method. The effects of three-dimensionality on tube flows that are initially axisymmetric and stable to 2-D disturbances are examined. Stability of the axisymmetric "base" flow is assessed through 3-D time integration.

Calculations performed at a Mach number of 0.3 and Reynolds number of 250 for increasing vortex strengths yield two significant results. First, there exists a critical vortex strength, beyond which stable axisymmetric (2-D) solutions become unstable and temporally evolve into asymmetric (3-D), unsteady flows. The character of the stability change indicates a supercritical Hopf bifurcation. Second, axisymmetric solutions that are stable in 2-D and contain reversed flow are unstable in 3-D. Furthermore, such solutions time-asymptote to 3-D unsteady solutions, which may or may not have reversed flow, depending on the vortex strength. This behavior is correlated in terms of the vorticity dynamics.

Axisymmetric solutions at a Mach number of 0.3 and Reynolds number of 1000 contain regions of nonuniqueness. Within this region, 3-D time integration reveals only unique solutions, with nonunique, axisymmetric initial conditions converging to a unique solution that is steady and axisymmetric. Past the primary limit point, which approximately identifies the appearance of critical flow, the solutions bifurcate into 3-D periodic flows. Thus, the author postulates that the development of critical flow is approximately coincident with the loss of stability associated with a Hopf bifurcation.

Flow visualization of the resulting time-asymptotic flow structures, as vortex strength is increased, reveal the growth of flow asymmetries. These asymmetric flows ultimately result in the spiral mode of breakdown.

# THE DEPENDENCE OF THE TIME-ASYMPTOTIC STRUCTURE OF 3-D VORTEX BREAKDOWN ON BOUNDARY AND INITIAL CONDITIONS

## *I. Introduction*

Vortex breakdown is an aerodynamic phenomenon of swirling flows. It was first observed over the suction side of a delta wing in an experiment by Peckham and Atkinson (1957). Almost two centuries before this discovery, in 1780, the same phenomenon was observed in waterspouts, as reported by Lugt (1989). Vortex breakdown, or simply breakdown, is a feature of rotational flows involving a concentrated core of vorticity imbedded in a nearly irrotational flow that moves approximately parallel to the vortex. The term breakdown is used specifically in this work to identify the development of a stagnation point, followed by a limited region of reversed flow where the core size increases dramatically. Another term used in the literature is vortex bursting, which refers to the abrupt increase in core size without the appearance of a stagnation point.

The study of vortex breakdown is important in both external and internal aerodynamics. For example, the bursting of a vortex over a delta wing severely alters airplane dynamics by producing significant changes in the slopes of lift, drag, and moment coefficients (Sarpkaya (1971B)). In addition, the turbulent wake of vortex breakdown can promote fluid/structure interactions such as tail buffeting (Shah et al. (1990)). In internal combustion, Faler and Leibovich (1978) noted that promoting breakdown leads to a recirculating fluid that can be used as a "fluid-dynamic flameholder." In all of these examples, the ability to control the breakdown process could result in improved performance and/or safety of airplanes.

The pronounced effect of vortex breakdown on a delta wing is well illustrated in a photograph (Figure 1) taken from the experiments of Lambourne and Bryer (1961). Dye injection reveals two distinct types of breakdown, the nearly-axisymmetric bubble type

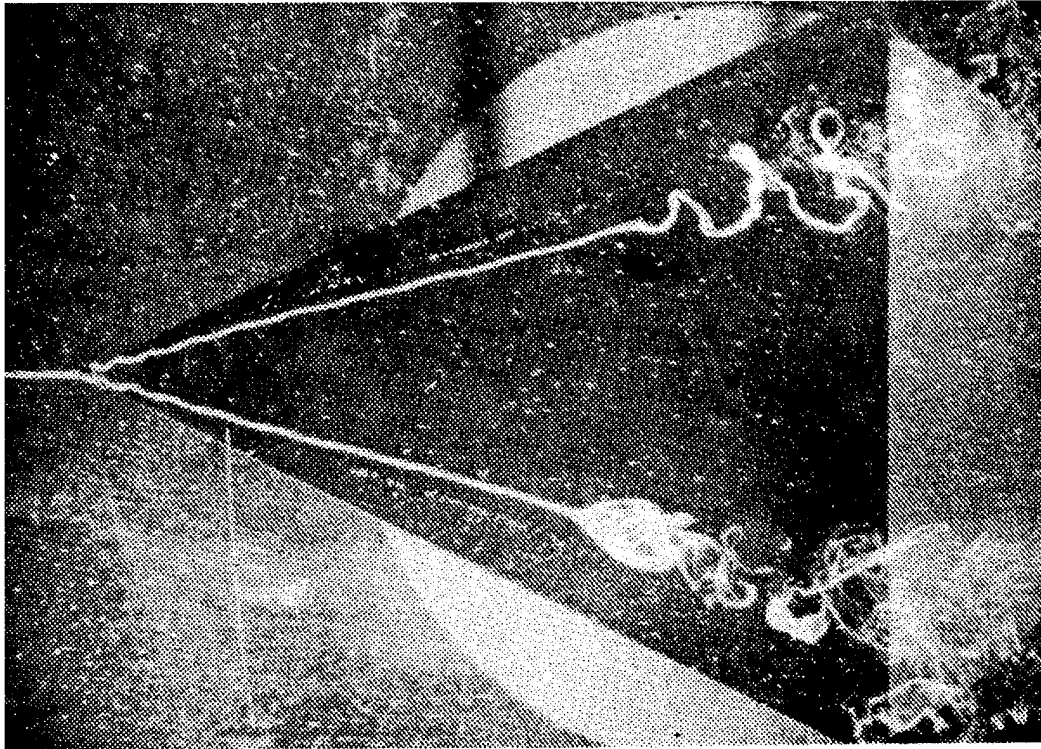


Figure 1. Vortex breakdown in leading-edge vortices over a delta wing. The breakdown in the lower portion of the figure is the bubble type, while the spiral type is in the upper portion (Lambourne and Bryer (1961)).

(later designated as Type 0 by Faler and Leibovich (1977)) and the highly three-dimensional spiral type (Type 2). The bubble type (lower portion of the figure) is characterized as a nearly axisymmetric swelling of the upstream vortex core in the shape of a bubble; a stagnation point exists on the vortex axis and is surrounded by a limited region of reversed flow. The spiral type has a three-dimensional character, which appears as a kink of the vortical core into a helical pattern.

Vortex breakdown can also occur inside a simple tube geometry. Breakdown in tubes has been reported in numerous experiments (Faler and Leibovich (1977), Garg and Leibovich (1979), Sarpkaya (1971B), Brücker (1993)) and computations (Beran and Culick (1992), Beran (1994), Darmofal (1993), Darmofal and Mufman (1994), Lopez (1994)). The motivation for studying tube flows is the simplifying geometry.

The relevancy of the study of breakdown in tubes to breakdown over a delta wing depends on the specific aspect of the study. Practical aspects of breakdown such as the breakdown position and parametric criteria for breakdown are highly dependent on the flow geometry, boundary conditions, and the method of vortex generation, all of which differ between tube flows and flows over wings. However, studies using tubes, such as this study, which focus on the breakdown structure and its qualitative behavior are believed by the author to be quite relevant to breakdown over wings, since experimental and computational evidence suggests that the resulting breakdown structures look similar and behave similarly. For example, compare the bubble and spiral breakdown in Figure 1 with the tube-generated bubble and spiral breakdown in Figures 2-3. The breakdown structures are found to be quite similar in form. Furthermore, Visbal (1993B) computed a bubble type breakdown over a delta wing, and commented that the resulting isosurface of total pressure provides a visualization of the bubble structure that is quite similar to the bubble structure in the tube experiments of Faler and Leibovich (1977). Finally, Leibovich (1984) claims that the main characteristics of vortex breakdowns above delta wings at high incidences appear to agree with experimental findings of flows in tubes. The behavior of the breakdown structures with changes in flow circulation are also similar. In both tube flows and flows over delta wings, an increase in flow circulation results in a forward movement of the breakdown position.

Tube geometries have been used in the past to study the nearly axisymmetric bubble breakdown, employing a simplified set of governing equations valid only for axisymmetric flow. The numerical (tube) calculations of Beran and Culick (1992), Beran (1994), Darmofal (1993), Darmofal and Murman (1994) and Lopez (1994) have all exploited this simplifying assumption, although it is known from flow experiments that the bubble form is only approximately axisymmetric.

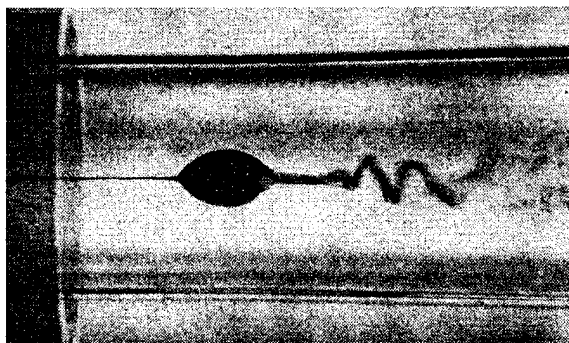


Figure 2. The Type 0 (bubble) breakdown (Faler and Leibovich (1977)).

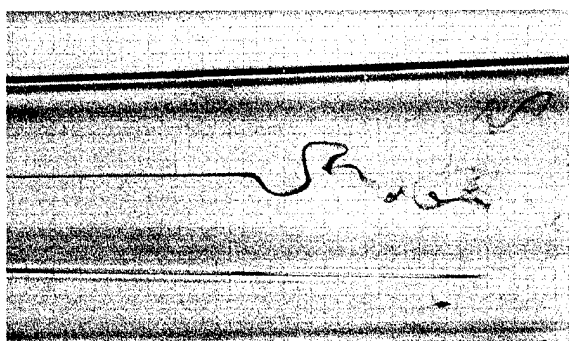


Figure 3. The Type 2 (spiral) breakdown (Faler and Leibovich (1977)).

A tube geometry would be particularly useful for numerically examining the stability of flows to 3-D disturbances. The tube geometry naturally gives rise to axisymmetric flows, assuming the vortex strength is sufficiently low that naturally occurring asymmetries do not develop. These axisymmetric flows provide a model of the vortex core, without the complication of the three-dimensional leading-edge geometry and flow structure. The ability to isolate an axisymmetric vortex core from the leading-edge geometry allows for a cleaner identification of the emerging vortex core asymmetries and their role in the development of breakdown. However, it is unclear how this isolation of the core from the surrounding 3-D delta-wing flow impacts the emergence of core asymmetries. Therefore, the growth of asymmetries in tubes may serve only as a guide in helping future studies content with the more complex issue of wing flow instability.

Another aspect of the study of flows in tubes is that it allows for the computation of both axisymmetric and asymmetric flows under identical conditions. This would help examine a scenario of the emergence of the spiral (asymmetric) mode of breakdown put forth by Leibovich (1984). In this scenario, the growth of axisymmetric disturbances in the vicinity of breakdown eventually lead to the instability of these disturbances to asymmetric waves. The gain in energy of the spiral mode is postulated to come at the expense of energy in the axisymmetric mode. A study which considers both the axisymmetric and asymmetric solutions for identical conditions could numerically assess the scenario put forth by Leibovich (1984).

An interesting feature of axisymmetric tube solutions is the appearance of nonunique solutions (Beran and Culick (1992), Lopez (1994)). A characterization of the nonunique solutions is shown in Figure 4, plotted in terms of the minimum axial velocity,  $Q$ , and the vortex strength. The solid lines represent solutions that are stable to axisymmetric disturbances, while the dashed line represents unstable solutions. As the vortex strength is increased, a fold in the solution space occurs, resulting in a primary limit point at  $V_2$ . The limit point is found to occur before the development of bubble breakdown ( $Q < 0$ ). As the vortex strength is slightly increased from  $V_2$ ,  $Q$  abruptly changes from positive to negative, indicating the formation of bubble breakdown. For flows with breakdown, decreasing the vortex strength results in generally larger (less negative) values of  $Q$ , until the secondary

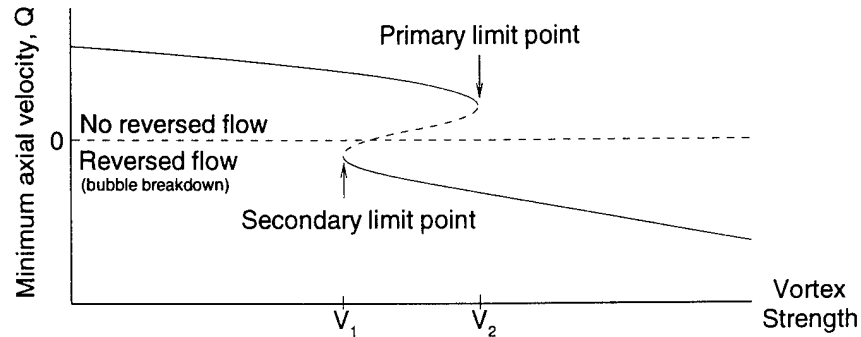


Figure 4. A representative solution branch of axisymmetric solutions: stable branch (solid lines); unstable branch (dashed line).

limit point is encountered. The nonuniqueness of solution paths as the vortex strength is increased and then decreased results in what is known as a hysteresis loop. Between  $V_1$  and  $V_2$ , nonunique axisymmetric solutions exist. Appendix B.1 provides additional descriptions of the terminology associated with the axisymmetric solution paths.

The location of the primary limit point in an axisymmetric solution space has been associated with changes in the flows ability to support upstream propagation of axisymmetric waves. Beran and Culick (1992) found that for sufficiently high Reynolds numbers, a parabolized version of the axisymmetric governing equations, known as the quasi-cylindrical (QC) equations, agree well with solutions of the Navier-Stokes equations when the vortex strength is below the primary limit point, but fail to converge to a solution as the vortex strength is increased towards the primary limit point. The failure point of the parabolic QC equations is believed by Hall (1972) to be the approximate point at which the flow can support upstream propagating, axisymmetric waves. A flow which can support both upstream and downstream propagation of axisymmetric waves at some axial location is referred to as a subcritical flow (Section 2.1.1.1). In contrast, a flow which can only support the downstream propagation of axisymmetric waves is referred to as a supercritical flow. Thus, the work of Beran and Culick (1992) and Hall (1972) suggest that the flow transitions from supercritical flow to subcritical flow at a vortex strength which is approximately equal to the primary limit point.

The stability of unique and nonunique axisymmetric solutions to three-dimensional disturbances has not been investigated. For example, assuming axisymmetry, the time integration of two different initial conditions may lead (depending on parameter values) to two distinct, stable time-independent solutions. However, it is uncertain if one of these solutions prevails when the vortex is generated by 3-D time integration, or if a third, distinct 3-D solution develops. Similarly, it is also unclear how asymmetric flows modify the underlying hysteresis loop present for an axisymmetric flow.

Therefore, the three-dimensional and temporal nature of vortex breakdown in a tube is considered in this study. Solution paths consisting of time-asymptotic 3-D solutions are compared, under identical parameter settings, to solution paths formed by solving the axisymmetric governing equations. In this way, the relevancy of 2-D solutions is revealed. Furthermore, this study investigates the transition between 2-D and 3-D flows in the presence of 2-D solution paths, which may or may not contain nonunique solutions. Thus, the following questions can be answered in this study:

1. Under what conditions is the axisymmetric assumption valid?
2. Under what conditions is the assumption of steady flow valid?
3. How does a solution branch consisting of steady, axisymmetric flows bifurcate onto another branch containing 3-D flows?
4. Does nonuniqueness in 2-D solution paths play a role in the structure of 3-D solution paths?
5. Does the criticality of 2-D flows have any bearing on the nature of the 3-D solution space?

An analysis of the emergent 3-D characteristics of swirling flows and the associated consequences for vortex breakdown has not been investigated in previous studies. In fact, a unique feature of this study is that solutions to the steady, axisymmetric governing equations are used as initial conditions for time-integration of the 3-D equations of motion. Thus, transient solutions which deviate away from the initial condition do so as a direct consequence of three-dimensional disturbances.



Previous computations with the 3-D equations of motion (Section 2.1.3) have instead provided valuable information on the structure of the 3-D breakdowns. Most notably, calculations have been performed for flows in unconfined domains (Breuer and Hänel (1989), Spall et al. (1990), Spall and Gatski (1991)) and over delta wings (Visbal (1993A, 1993B, 1995)). These works provide descriptions of the various time-asymptotic breakdown structures encountered, including the spiral and bubble forms. Spall and Gatski (1991) also compute breakdown structures other than the spiral or bubble type, which are documented in the tube experiments of Faler and Leibovich (1977) (Section 2.1.2.1). These works do not, however, consider the deviations of the emerging 3-D vortex core from the underlying axisymmetric flow.

The principle issues of a 3-D study include flow unsteadiness, compressibility, three-dimensionality and solution nonuniqueness. The importance of these factors is illustrated by the following points:

- Experimental evidence shows that all forms of breakdown are unsteady. Flow unsteadiness is allowed in this study. However, the vortex strength is held constant during time integration, equivalent in concept to holding the angle-of-attack constant during the computation of the flow over a delta-wing. Thus, dynamic effects due to breakdown (Beran (1994)), such as the dynamic lag in breakdown position with angle-of-attack, can not be considered in this study.
- The assumption of incompressibility has been invaluable to the study of vortex breakdown. However, for flows of aerodynamic interest such as flow over delta wings, future work must consider the effect of compressibility on the structure of breakdown, the criteria for breakdown, and the existence of nonunique solutions. There is already evidence that for flows in tubes, increasing Mach number can cause the disappearance of nonunique flow states (Morton (1989)). In addition, Visbal (1995) concludes that for a  $75^\circ$  delta wing, the large axial jet associated with leading-edge vortices result in supersonic core velocities if the freestream Mach number is greater than 0.3. While compressible flow is modeled in this study, the effect of compressibility is not considered. A fixed reference Mach number of  $M = 0.3$  is prescribed.

- Experimental evidence shows that even the bubble breakdown contains regions of three-dimensional flow. A 3-D time-integration study can determine how the presence of three dimensionality affects the time-asymptotic breakdown structure of initially axisymmetric flows, yielding new information on the relevancy of axisymmetric solutions.
- The stability of nonunique axisymmetric flows to 3-D disturbances has not been established.

In addition to the contributions towards the understanding of vortex breakdown, this study documents the development of a highly accurate, time-integration algorithm. The most notable feature of this algorithm is the implementation of fourth-order, spatially-accurate (compact) operators to discretize derivatives, replacing the traditional method of approximating derivatives using second-order differences. Furthermore, a unique, multi-block grid structure is incorporated into the time-integration algorithm. This grid structure allows the vortex core to be computed without an approximate treatment of the algorithm, which is necessary with a conventional single-block grid. This work appears to be the first to use the compact scheme in solving the unsteady, compressible, three-dimensional Navier-Stokes equations with a multiblock grid structure.

### *1.1 Objectives.*

The primary goal of this investigation is to determine the time-asymptotic behavior and three-dimensional stability of compressible vortices as initial and boundary conditions are varied. Axisymmetric “base” flows and time-asymptotic 3-D flows, given identical parameter values, are compared. The specific objectives are as follows:

1. For fixed Mach and Reynolds numbers and varying vortex strength,  $\mathcal{V}$ , determine the critical vortex strength at which 3-D solutions first become distinct from the associated 2-D base flows.
2. Characterize the change in solution behavior at the critical vortex strength by identifying the type of bifurcation.

3. For fixed Mach and Reynolds numbers and varying  $\mathcal{V}$ , characterize the nature of 3-D solutions in the vicinity of nonunique axisymmetric solutions.
4. Classify the computed 3-D structures in accordance with the forms of disturbances documented by the experiments of Faler and Leibovich (1977).

### 1.2 Approach.

The computational approach to this study is given in this section, along with the selected ranges of parameter values.

The computational approach is as follows. First, a numerical algorithm provides the axisymmetric initial condition for a specified vortex strength,  $\mathcal{V}$ , given fixed values of the freestream Mach number,  $M$ , and the Reynolds number,  $Re$ . This axisymmetric solution is then interpolated onto a 3-D mesh using a fourth-order-accurate cubic-spline scheme, described in Appendix B.3. Then, time-integration is carried out by a 3-D, time-integration algorithm.

Steady, axisymmetric initial conditions are computed using a pseudo-arclength continuation (PAC) technique. The PAC method allows for the calculation of solution paths with folds, which occur at the higher  $Re$  considered here. The PAC algorithm provides a one-parameter family of axisymmetric solutions, where the parameter is the vortex strength. The nominal Mach number,  $M = 0.3$ , was chosen to provide “near incompressibility” while avoiding convergence problems associated with computing at low Mach numbers. The Reynolds numbers considered are 100, 250, 500, and 1000. Axisymmetric solution spaces for  $Re$  of 100 and 250 were found not to contain folds, whereas folds in the solution space exist at  $Re$  of 500 and 1000.

The 3-D time-integration model, referred to as the Time-Accurate Navier-Stokes (TANS) model, is developed specifically for this work. The TANS model incorporates two unique features. First, the TANS model uses a multiblock grid structure in the crossflow plane. The grid structure allows for a nearly Cartesian arrangement of nodes in the vicinity of the centerline, while maintaining near orthogonality at the circular tube wall. Second, the TANS model incorporates fourth-order compact operators into an approximate fac-

torization, Beam-Warming solution procedure. The compact scheme discretizes explicit spatial derivatives to fourth-order accuracy. Traditional central-difference discretizations are typically only second-order accurate. Results in Section 3.7 will show that the net reduction in CPU time using the compact scheme over central differencing (and assuming fewer required nodes) is about 42%. Furthermore, the compact scheme yields higher solution accuracy.

### *1.3 Outline of Study.*

A summary of previous work in vortex breakdown is given in Chapter II, along with a summary of previous computations using the compact scheme.

The TANS model is described in Chapter III. The geometry and grid are described in Section 3.1. The governing equations in physical and computational space are developed in Sections 3.2 and 3.3. Boundary conditions are formulated in Section 3.4 for flow in a tube with slip. The solution procedure is developed in Section 3.6. The solution procedure is a Beam-Warming approximate factorization scheme, incorporating fourth-order compact operators. A description of the method used to visualize the evolving 3-D flows is given in Section 3.8, along with definitions of the recorded data.

Baseline grid requirements and code validation are presented in Chapter IV. Baseline grid requirements are found in Section 4.1 by using a second-order, central-difference form of the TANS model. The utility of the fourth-order compact operators is demonstrated in Section 4.1.4 by showing that the number of nodes in the crossplane grid can be reduced from that required with the second-order scheme, while maintaining similar levels of spatial accuracy. Code validation is performed by solving several model problems (Appendix D) and by cross-validating the TANS and PAC models (Section 4.2) under conditions which lead to steady, axisymmetric flow.

Chapter V presents the results of this study. Section 5.1 presents results for flows at  $Re = 100$ . Flows at this  $Re$  were used primarily for validation purposes and to provide preliminary results for flows at higher  $Re$ . The vortex strength at which 3-D solutions first become distinct from the associated axisymmetric base flow is identified.

Section 5.2 presents results for flows at  $Re = 250$ , where the axisymmetric solutions are unique. This section provides validation of the preliminary results of Section 5.1. A sequence of runs are presented which indicate that as  $\mathcal{V}$  is steadily increased, a critical value is reached where solutions change from 2-D and steady to 3-D and periodic. The effects of further grid refinement, tube length, and time step are also included. Several recorded parameters are plotted to illustrate the onset of asymmetry and periodicity. Flow visualizations are presented to illustrate the various flow structures encountered at this  $Re$ .

Section 5.3 presents results for flows at  $Re = 500$ . The 2-D solutions at this  $Re$  contain a region of nonuniqueness. However, the span of vortex strength over which the nonuniqueness occurs is determined to be too narrow to allow for a detailed examination. Time integration is performed on nonunique, axisymmetric initial conditions. The nature of the resulting time-asymptotic solutions in this region of nonunique axisymmetric solutions is documented.

Section 5.4 presents results for flows at  $Re = 1000$ . The 2-D solution space at this  $Re$  contains a broader range of nonunique solutions than at  $Re = 500$ . The axisymmetric solution paths are shown in Section 5.4.1, using three different axisymmetric grids to assess solution sensitivity to node spacing and tube length. Flows with vortex strengths prescribed to be less than the primary limit point are discussed in Section 5.4.2. Results for three different 3-D grids are shown to illustrate solution sensitivity to node spacing and tube length. Flows with vortex strengths prescribed to be greater than (but close to) the primary limit point are presented in Section 5.4.3. Solution sensitivity to tube length for vortex strengths beyond the primary limit point is discussed in Section 5.4.6. Flow visualization is presented in Section 5.4.7.

A summary of the results of this work are presented in Chapter VI, while conclusions and recommendations are given in Chapter VII.

Appendix A contains the dimensional and nondimensional form of the governing equations used by the TANS model, as well as a description of the nondimensionalization process.

The PAC model is described in Appendix B, starting with the definitions of frequently used terms pertaining to nonlinear systems in Section B.1. The PAC model is described in Section B.2. A similar description of a PAC model for a streamfunction / vorticity formulation (as applied to breakdown) can be found in the work of Beran and Culick (1992). The PAC algorithm is implemented using the same boundary conditions and tube geometry as in the TANS model, using a simple algebraic grid. The cubic spline method, used to interpolate PAC solutions onto the 3-D grid, is described in Section B.3.

Appendix C contains details on the grid generation process, and presents the results of a grid rotation study.

Solutions to model problems solved with the TANS model are contained in Appendix D. Solutions for steady, incompressible and compressible flat plate flow, unsteady Couette flow, and unsteady heat conduction are contained in Sections D.1-D.4 respectively.

Appendix E contains the development of simplified equations for steady, axisymmetric and inviscid flow. The Bragg-Hawthorne equation, valid for incompressible flow, is developed in Section E.1. The author extends the Bragg-Hawthorne analysis to treat compressible flows in Section E.2.

Modifications to the traditional Beam-Warming solution procedure are discussed in Appendix F. The fourth-order compact scheme operator is derived in Section F.1, while the general form of the time-marching schemes is derived in Section F.2. The compact and time-marching schemes are incorporated into the Beam-Warming scheme in Section F.3.

## *II. Background*

This chapter provides a summary of the existing vortex breakdown work, as well as a summary of previous applications of the compact scheme.

This background information was obtained from references found during an extensive literature search of over 250 relevant technical papers. While all of the work cited in Section 2.1 pertains to breakdown research, particular attention is given to discussions on flow criticality, 3-D calculations, the experiment of Faler and Leibovich (1977), and work which considers the implications of solution nonuniqueness.

Section 2.2 contains a summary of previous work using the compact-scheme approximation. It is found in this review that this work appears to be the first to use the compact scheme in solving the unsteady, compressible, three-dimensional Navier-Stokes equations with a multiblock grid structure.

### *2.1 Synopsis of Previous Work on Vortex Breakdown.*

The existing work in vortex breakdown will be categorized into theoretical, experimental and numerical work, as covered in Sections 2.1.1–2.1.3 respectively.

There have been several review papers on vortex breakdown. The works of Hall (1972) and Leibovich (1978) are reviews that primarily consider the axisymmetric form of breakdown. Leibovich (1984) considers theories based on criticality and relevant work on the asymmetric forms of breakdown. Reports which serve to document (in-part) AFOSR-sponsored research in vortex breakdown is given by Leibovich (1991) and Berger (1989).

The remaining portions of this report often refer to terms that pertain to the study of nonlinear systems. Brief definitions of some of these terms are found in Appendix B, including definitions of bifurcation, limit point, Hopf bifurcation, nonunique solutions, hysteresis, stable branch, and unstable branch.

*2.1.1 Theoretical Work.* Theoretical work in vortex breakdown has focused primarily on theories based on axisymmetric flows. These flows are also assumed to be steady, inviscid and incompressible. Since this study focuses on the unsteady, three-dimensional

aspects of vortex breakdown, direct comparison of the numerical results with the axisymmetric theories will not be possible. Nevertheless, an overview of two theories is presented. The first is given in Section 2.1.1.1, and is known as the conjugate-flow theory, (Benjamin (1962, 1967)). This theory is relevant to this work because it introduces an important concept—flow criticality. The second theory is due to Brown and Lopez (1990), who establish a relationship between the production of negative azimuthal vorticity and reversed flow. This theory is utilized in Chapter V to help correlate the observed flow behavior with the emergence of flow asymmetries.

*2.1.1.1 The Conjugate Flow Theory and Critical Flow.* As pointed out by Leibovich (1984), the main unifying element, whether originally recognized or not, in all formulations of criteria for onset of purely axisymmetric breakdown is the concept of critical flow. The most studied of the axisymmetric theories is due to Benjamin (1962, 1967) and is known as the conjugate-flow theory. The conjugate-flow theory applies to axisymmetric flows with (primarily) no axial gradients. In addition, the flow is assumed to be steady and incompressible. Viscous losses are incorporated in the theory by a dissipation parameter,  $q$ , which represents the loss in total head across the tube. The theory provides a condition for which breakdown can be expected, but does not offer a prediction of where the breakdown occurs. In addition, the theory does not offer any information on the structure of the breakdown.

Before discussing the conjugate-flow theory, a review of a few fundamental concepts on the behavior of waves is in order (Whitham (1974)). Waves can usually be classified into two types: hyperbolic and dispersive. Hyperbolic waves are named after the hyperbolic partial differential equations from which they are formulated, such as the classic wave equation. Hyperbolic waves are characterized as having frequencies,  $\omega$ , which are directly proportional to the wavenumber,  $\kappa$ , where  $\kappa$  is inversely proportional to the wavelength:

$$\omega = W(\kappa) = c_0 \kappa$$



The phase velocity,  $c$ , defined in general by

$$c(\kappa) = \frac{W(\kappa)}{\kappa}$$

is therefore a constant,  $c_0$ , for hyperbolic waves over all wavenumbers  $\kappa$ .

Dispersive waves, which are found in vortical flows, get their name from the nonlinear dependence of frequency on wavenumber, implying that waves can disperse due to different phase speeds. A particular 1-D wave solution,  $\varphi$ , can be written in the form

$$\varphi = \epsilon e^{i(\kappa x - \omega t)}$$

where  $\epsilon$  is the wave amplitude, which generally depends on the spatial coordinate  $x$  and time,  $t$ . In general, flow disturbances consist of a spectrum of such waves, producing a complicated wave train that contains a range of wavenumbers. The different values of wavenumber propagate through the wave train with a speed known as the group velocity, defined as

$$C(\kappa) = \frac{dW(\kappa)}{d\kappa}$$

In dispersive mediums, the ability of disturbances to propagate upstream is determined by the group velocity, not the phase velocity (Leibovich (1984)). A negative group velocity is required for upstream propagation of a disturbance, while a positive group velocity indicates downstream propagation.

The conjugate-flow theory states that vortex breakdown is a finite transition between two dynamically conjugate-flow states (Benjamin (1962)). The upstream flow (Flow A) must necessarily <sup>1</sup> be supercritical, i.e., a flow which cannot support standing axisymmetric waves. The group velocity of supercritical flows is positive, i.e., in the downstream direction. The conjugate flow (Flow B) downstream of the breakdown region is always subcritical, meaning it can support axisymmetric waves traveling either upstream or downstream. The critical flow condition is obtained when a standing wave is possible, corresponding to a wave of zero phase velocity. Squire (1960) suggested that breakdown first becomes possible

---

<sup>1</sup>For no external agencies acting on the flow.

when the flow becomes critical. In his work, however, Squire only considered infinitesimal, infinitely long waves. In 1962, Benjamin showed that the group velocity of standing waves of this type is positive. Thus, Benjamin argued that if the flow was critical, then waves of this type can only form in the rear of a disturbing agency and cannot propagate upstream.

In mathematical terms, Benjamin's (1962) theory relies on the solution of a Sturm-Liouville system with appropriate boundary conditions. This system is derived by starting with the Bragg-Hawthorne equation (developed in Appendix E.1). The streamfunction is allowed to take the form of the sum of a base-flow streamfunction,  $\Psi(y)$ , plus a perturbation:

$$\psi(y, z) = \Psi(y) + \epsilon \phi(y) e^{\gamma z}$$

where  $y \equiv \frac{1}{2}r^2$ ,  $r$  is the radial coordinate, and  $z$  is the axial coordinate. The small perturbation assumption limits the applicability of the theory to "small" deviations between Flows A and B. The Sturm-Liouville system can then be written in terms of the perturbation streamfunction in a limiting process as  $\epsilon \rightarrow 0$ , resulting in

$$\ddot{\phi} + \left( \frac{\gamma^2}{2y} + P(\Psi, y) \right) \phi = 0$$

where  $P(\Psi, y)$  depends on the total head and vortex circulation. Solving for  $\phi$  consists of solving an eigenproblem for which an infinite spectrum of real <sup>2</sup> eigenvalues  $\gamma_0^2, \gamma_1^2, \gamma_2^2 \dots$  and corresponding eigenfunctions exist. A supercritical flow occurs when all of the eigenvalues are positive, i.e., no wave solution exists. A subcritical flow exists if at least one eigenvalue is negative. The critical condition therefore occurs when the smallest eigenvalue is identically zero.

Benjamin (1962) then proceeded to obtain solutions to the perturbation streamfunction by defining a flow force  $S$ , as

$$S \equiv 2\pi \int_0^a (p + \rho w^2) dy$$

---

<sup>2</sup>This is a consequence of  $\frac{1}{2y} > 0$ . See Boyce and DiPrima (1969), Theorem 11.1.

where  $a = \frac{1}{2}R^2$  and  $R$  is the local tube radius. The flow force represents the sum of axial momentum flux and axial pressure force. Benjamin assumed that the difference between the flow force of Flow A and the flow force at the breakdown point were balanced by the presence of a viscous force term, which was assumed to be  $\mathcal{O}(\epsilon^3)$ . The introduction of the flow force,  $S$  resulted in three basic types of solutions. As  $q$  approaches zero (the inviscid limit) the conjugate flow is a solitary wave. For small (but finite) values of  $q$ , the conjugate flow is a cnoidal <sup>3</sup> wave. As  $q$  is increased further, a limiting value is reached where the solution becomes columnar, i.e., free of axial gradients. Then breakdown is not possible.

It should be noted that Benjamin's definition of critical flow is based on the phase velocity going to zero, not the group velocity. Tsai and Widnall (1980) define criticality based on the group velocity, where a positive group velocity indicates supercritical flow and negative group velocity indicates subcritical flow. Leibovich (1984) apparently clears up this inconsistency in definitions by showing that Benjamin's criterion for supercriticality is always consistent with a definition based on group velocity when the flow is axisymmetric. Furthermore, he argues that flows that are subcritical based on a phase velocity criterion are also subcritical based on the more fundamental group velocity criterion.

Computations of group velocities from experimental data for both axisymmetric ( $n = 0$ ) and asymmetric ( $n = \pm 1$ ) disturbances were performed by Tsai and Widnall (1980). They conclude that flows with the axisymmetric (bubble) form of breakdown are supercritical upstream and subcritical downstream to both  $n = 0$  and  $n = 1$  modes. Flows with the spiral form of breakdown are found to be supercritical upstream for  $n = 0$  and  $n = \pm 1$ , while the downstream flow is subcritical only for  $n = 0$ . These results assume that the definitions for supercritical flow and subcritical flow are applied independently to both axisymmetric and asymmetric waves. In this study, however, the terms subcritical / supercritical refer to the flows ability / inability to produce upstream propagating axisymmetric waves.

---

<sup>3</sup>An obscure term used to describe a periodic wave defined with the  $cn$  function, which is employed in the solution of elliptic integrals.

2.1.1.2 *The Theory of Brown and Lopez.* Brown and Lopez (1990) have proposed that the production of negative azimuthal vorticity,  $\hat{\eta}$ , is necessary to retard the axial velocity component of an axisymmetric swirling flow. Thus, according to the theory, the appearance of negative azimuthal vorticity is necessary for breakdown to occur. However, negative azimuthal vorticity may exist in a flow without breakdown.

The components of the Brown and Lopez theory relevant to this work are summarized by Darmofal (1993) and reproduced below utilizing a cylindrical coordinate system. The axial and radial coordinates are given by  $\hat{z}$  and  $r$  respectively. The radial, azimuthal and axial components of velocity are denoted by  $\hat{u}$ ,  $\hat{v}$  and  $\hat{w}$  respectively. The radial, azimuthal and axial components of vorticity are denoted  $\hat{\xi}$ ,  $\hat{\eta}$  and  $\hat{\zeta}$ , and are defined as

$$\hat{\zeta} = \frac{1}{r} \left[ \frac{\partial(r\hat{v})}{\partial r} - \frac{\partial\hat{u}}{\partial\theta} \right] \quad (1)$$

$$\hat{\xi} = \frac{1}{r} \frac{\partial\hat{w}}{\partial\theta} - \frac{\partial\hat{v}}{\partial\hat{z}} \quad (2)$$

$$\hat{\eta} = \frac{\partial\hat{u}}{\partial\hat{z}} - \frac{\partial\hat{w}}{\partial r} \quad (3)$$

The velocity field,  $\vec{u}(\vec{x}) = (\hat{u}, \hat{v}, \hat{w})^T$ , is decomposed into an irrotational and a rotational part

$$\vec{u}(\vec{x}) = \vec{u}_i(\vec{x}) + \vec{u}_r(\vec{x}) \quad (4)$$

where the irrotational portion produces no vorticity:

$$\nabla \times \vec{u}_i = 0 \quad (5)$$

The velocity  $\vec{u}_r(\vec{x})$  due to the vorticity  $\vec{w}(\vec{x}')$  is given by

$$\vec{u}_r(\vec{x}) = -\frac{1}{4\pi} \int \frac{\vec{s} \times \vec{w}(\vec{x}')}{s^3} dV \quad (6)$$

where  $\vec{s} \equiv \vec{x} - \vec{x}'$ .

Brown and Lopez (1990) assume that axial deceleration of the flow, a prominent feature of breakdown flowfields, is due primarily to the rotational portion of the velocity field. Furthermore, for axisymmetric flow, the stagnation point is assumed to lie along the vortex core,  $r = 0$ . Then, Eq. 6 can be written for the axial velocity component along  $r = 0$  as

$$\hat{w}_r(0, \hat{z}) = \frac{1}{2} \int_{-\infty}^{\infty} \int_0^{\infty} \frac{r'^2 \hat{\eta}(r', z')}{[r'^2 + (\hat{z} - z')^2]^{\frac{3}{2}}} dr' dz' \quad (7)$$

The integrand of Eq. 7 consists of positive quantities, with the possible exception of the azimuthal vorticity,  $\hat{\eta}$ . Therefore, given that the rotational portion of the axial velocity,  $w_r$ , far upstream of breakdown is positive, breakdown along the axis can only occur if the flow contains negative azimuthal vorticity.

*2.1.2 Experimental Work.* The earliest advancements in the study of vortex breakdown were made by experimentalists who studied the phenomenon over wings. After the work of Peckham and Atkinson (1957) came the experiments of Lambourne and Bryer (1961). They studied factors that affected the position of the breakdown point, and concluded that the essential condition for the breakdown to occur is a low total pressure within the vortex core coupled with an adverse pressure gradient along the axis.

Lambourne and Bryer (1961) also conducted a vortex-tube experiment, an idea further promoted by Harvey (1962). Harvey utilized a swirl-vane apparatus as part of a wind-tunnel experiment, essentially separating the vortex breakdown problem from the more complicated flowfield resulting from a swept wing. This was the beginning of a trend towards "cleaner" studies of vortex breakdown involving tubes. Quantitative measurements were still very difficult, however, as noted by Harvey (1962), because of a hypersensitivity of the breakdown structure to probe disturbances. This limitation existed for subsequent experiments in the sixties and early seventies by Elle (1960), Kirkpatrick (1964) and Sarpkaya (1971A, 1971B, and 1974). In the late seventies, advancing technology spawned the use of Laser-Doppler Anemometry (LDA) in the experimental work of Faler and Leibovich (1977, 1978). LDA provided data on flowfield velocities without the disturbances induced by probes. Faler and Leibovich (1978) used LDA to map the internal flowfield of the bubble breakdown. Mean streamlines were constructed and revealed a

two-celled bubble structure. More recently, Uchida et al. (1985) used LDA to obtain data for both the bubble and spiral forms, while Suematsu et al. (1986) performed experiments in converging and diverging pipes to study the effects of pressure gradients on breakdown position. Suematsu et al. (1989) also performed an experiment to study the temporal behavior of the axisymmetric bubble.

*2.1.2.1 Experimentally Observed Flow Disturbances in Tubes.* Various types of large-amplitude flow disturbances, in addition to the bubble and spiral types (Figures 2-3) are reported in the tube experiment of Faler and Leibovich (1977).

As Reynolds number and circulation are varied, six distinct flow disturbances are observed using dye injection. Two are classified as Type 0 and Type 1 bubbles, which are distinguished by the means in which the dye injection fills and empties the bubble area. The spiral form is designated as Type 2. Both the bubble and spiral types are found to contain regions of reversed flow. In addition, the bubble and spiral types of breakdown occur at relatively large values of vortex strength and Reynolds number.

Flow disturbances denoted as Types 3-6 are found to occur at generally lower values of vortex strength and Reynolds number. Furthermore, for fixed Reynolds number and increasing vortex strength, Types 3-6 generally occur in reverse order, starting with Type 6 and progressing to Type 3. Further increases in swirl generally lead to the Type 2 spiral, followed by the bubbles forms, Types 0-1.

The detailed descriptions of Types 0-6, given by Faler and Leibovich (1977), are summarized below. Types 0-2 represent bubble and spiral forms of breakdown, and are also described briefly at the beginning of this Chapter. The disturbances are described in their general order of appearance as vortex strength is increased. Types 5 and 6 do not contain reversed flow, whereas reversed flow is evident in the physical descriptions of Types 4, 3, 2, 1 and 0.

The Type 6 disturbance occurs at low Reynolds numbers and low vortex strengths, and is characterized as a gentle, off-axis deflection of the central dye filament (Figure 5). The initial disturbance moves off-axis at a nearly constant azimuthal direction. The dye filament begins to rotate (with the same direction of the base flow) only after the dye



Figure 5. The Type 6 flow disturbance (Faler and Leibovich (1977)).

reaches a significant off-axis distance of about one-half of the tube radius. The filament continues to expand in radial extent until it nearly reaches the tube wall. Noticeable oscillations then become evident, breaking up the filament. Figure 5 represents a Type 6 disturbance in which the dye filament simultaneously moves off axis and shears into a tape. Both a sheared and unsheared form of the Type 6 disturbance are reported in the experiment.

The Type 5 disturbance is more commonly known as the double-helix disturbance. It was first observed in the experiments of Sarpkaya (1971A), and later confirmed by Faler and Leibovich (1977). The Type 5 disturbance usually evolves directly from the Type 6 disturbance. The sheared filament of the Type 6 disturbance can, under fixed flow conditions, produce a second branch of the original filament (Figure 6). The central dye filament shears into triangular shape sheet, with the two branches of the filament separating near the aft portion of this region. The two branches rotate around each other with the same sense as the base flow.

The Type 4 disturbance is also capable of forming directly from the Type 6 disturbance, or it can be produced by slightly increasing the swirl parameter. The Type 4 disturbance evolves from the Type 6 disturbance when the deflected dye filament begins to roll up, back towards the initial deflection point. A tight spiral form develops, ultimately resulting in a region of recirculating flow. In Figure 7, the Type 4 flow is found to exit from the recirculation zone in one of two emptying tails.



Figure 6. The Type 5 (double helix) flow disturbance (Faler and Leibovich (1977)).

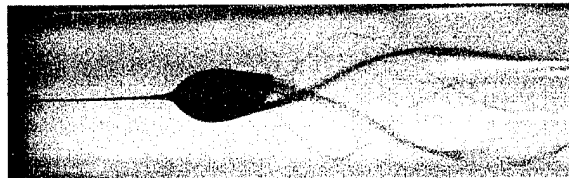


Figure 7. The Type 4 flow disturbance (Faler and Leibovich (1977)).

The Type 3 disturbance, according to Faler and Leibovich (1977), has characteristics of both the Type 4 and the Type 2 breakdowns. In the Type 3 disturbance, the central dye filament decelerates rapidly to form a sharp kink, similar to a spiral breakdown. Some of the dye deflects off-axis, shearing slightly and spreading laterally to mark the remnants of the Type 4 disturbance (Figure 8). The kinked filament oscillates from side to side in a preferential plane and does not rotate as it does during spiral breakdown.

The spiral mode of breakdown is designated as a Type 2 disturbance. In this form, the central dye filament decelerates rapidly and forms an abrupt kink (Figure 2, Chapter I). The dye deflects off-axis and forms a corkscrew shape, which rotates as a coherent structure in the same direction as the base flow. The sense of winding of the filament is in the same direction of the base flow as well (Faler and Leibovich (1977)). However, the winding of the corkscrew shape observed in the experiments of Brücker (1993) is opposite that of the base flow.

Two types of bubble breakdown are observed by Faler and Leibovich (1977). In both Types 0 and 1, the central filament expands radially in a nearly axisymmetric fashion as



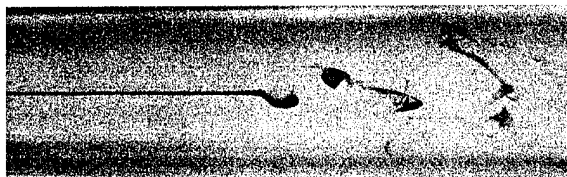


Figure 8. The Type 3 flow disturbance (Faler and Leibovich (1977)).

a stagnation point forms on the tube centerline. The Type 0 form (Figure 2, Chapter I) is the most axisymmetric of the six types of disturbances, however, even this form has asymmetric features. In particular, the rear of the recirculation bubble, where fluid enters and exits the bubble region, is observed by Faler and Leibovich to be asymmetric. The Type 1 bubble is even more asymmetric. The smooth outer appearance of the Type 0 bubble is replaced with a more ragged appearance. The nose of the Type 1 bubble is found to be asymmetric as well.

*2.1.3 Numerical Work.* The first numerical study of vortex breakdown was by Hall (1967). Hall suggested an analogy between the known failure of the laminar boundary-layer equations at the separation point and the failure of the parabolic quasi-cylindrical (QC) equations <sup>4</sup> at the breakdown point. His results showed that the solution to the QC equations failed at a distance of about 1-1.5 times the inlet vortex radius downstream of the experimentally observed breakdown point of Kirkpatrick (1964).

Kopecky and Torrance (1973) were the first to model vortex breakdown using the Navier-Stokes equations. They assumed steady, axisymmetric and incompressible flow. These assumptions were also made in the studies of Grabowski and Berger (1976), Hafez et al. (1986), Hafez et al. (1987), Beran (1987, 1989), Beran and Culick (1992), and Salas and Kuruvila (1989). Grabowski and Berger calculated bubble-type breakdowns for Reynolds numbers,  $Re$  <sup>5</sup> up to 200 using the artificial compressibility method of Chorin (1967). Hafez et al. (1986) studied the differences between computed solutions of the Euler and Navier-Stokes equations. They observed different structures between the bubbles calcu-

<sup>4</sup>The parabolized set of equations for swirling flows at high  $Re$  is commonly referred to as the quasi-cylindrical (QC) Equations.

<sup>5</sup>Reynolds number cited herein is based on inflow vortex radius and freestream axial velocity.

lated from the Euler equations versus those calculated from the Navier-Stokes equations at low Reynolds numbers. Hafez et al. (1987) and Beran (1987) used a direct Newton solver, and extended the range of  $Re$  in which axisymmetric bubbles could be calculated. Beran (1987) also combined the Newton solver with a pseudo-arclength continuation method. This allows for the efficient computation of neighboring steady-state solutions as a parameter such as  $Re$  or circulation is varied.

Four works were found that dealt with steady, axisymmetric, and compressible vortex breakdown. Liu et al. (1986) studied vortices which were assumed to be small in radius as compared to a suitable breakdown length scale. This is referred to as the slender-vortex approximation and is valid for high  $Re$ . They found certain "compatibility conditions" which must be satisfied for the vortex to remain slender. They also studied the dependence of the breakdown on upstream conditions for various Mach and Reynolds numbers. Morton (1989) determined that increasing Mach number inhibits the breakdown process. Results from this study also showed that for fixed  $Re$  and circulation, increasing Mach number could cause the disappearance of non-unique solutions. Kandil and Kandil (1991) performed work similar in scope to that of Liu et al. (1986). A review of work based on the slender-vortex approximation was done by Krause (1986).

Several studies have been reported that include the temporal behavior of axisymmetric vortex breakdown. Salas and Kuruvila (1989) provided a stability analysis for breakdown flows at Reynolds numbers of 200 and 400. This analysis consisted of performing unsteady calculations with the steady-state solution plus a 5% random perturbation as the initial condition. The behavior of the  $L_2$  norm <sup>6</sup> of the streamfunction was then plotted versus time to determine stability. The results showed that the  $Re = 200$  flow was stable to axisymmetric disturbances. The  $Re = 400$  flow showed the  $L_2$  norm oscillating about the steady-state value. This behavior was attributed to a Hopf bifurcation, although only one complete cycle of the  $L_2$  norm was presented. Krause et al. (1983) reported that flows where no breakdown occurred were steady, while those flows calculated past the point where the quasi-cylindrical equations failed were unsteady. The unsteady

---

<sup>6</sup>The  $L_2$  norm of a vector  $\underline{x}$  consisting of  $n$  elements is given by:  $L_2 \equiv [\frac{1}{n} \sum_{i=1}^n x_i^2]^{1/2}$

calculations revealed a two-celled bubble structure which were similar in shape to the bubble shown in the experiments of Faler and Leibovich (1978). Similar results were given by Shi (1985). Wu and Hwang (1991) studied the effects of the wall boundary condition on flow inside tubes. A periodic solution was found for  $Re = 200$  when the wall boundary was considered as a "viscous" wall as opposed to an "inviscid" wall. Menne (1988) studied the unsteady behavior of both the isolated and tube vortex. This study indicated that for isolated (unbounded) vortices, the specification of an inflow condition of zero axial gradient of the radial velocity may be ill-posed after some finite time. However, the same boundary condition applied to vortices in tubes were found to be well posed. Other unsteady, axisymmetric numerical studies were performed by Lugt and Abboud (1987), Pagan and Benay (1988), and Neitzel (1988). Compressibility was added by Kandil, Kandil and Liu (1991A, 1991B), and by Kandil and Kandil (1992). These works concentrated on the supersonic flow regime.

Recent numerical studies have been reported in which the breakdown was not assumed to be axisymmetric. Kuruvila and Salas (1990) developed an unsteady Beam-Warming algorithm with the inviscid fluxes discretized using Roe's scheme. Multigrid was used to accelerate three computed solutions for  $Re = 100, 375$  and  $400$  and Mach number,  $M = 0.1$ , to a steady-state. They found two types of nearly axisymmetric breakdown: the nearly closed bubble breakdown (Type 0), and a mushroom type whose structure has a flattened rear end. Liu and Menne (1989) investigated breakdown using a quasi-3D Navier-Stokes algorithm based on incompressible flow. The quasi-3D nature of the algorithm is due to the use of a Fourier decomposition in the circumferential direction to describe the asymmetric influences. The effect of enforcing asymmetric inflow conditions was investigated in their study. Spall and Ash (1987) solved the unsteady, 3-D Navier-Stokes equations and, consistent with Kuruvila and Salas as well as Liu and Menne, observed the formation of the bubble breakdown in an unbounded flow. Spall et al. (1990) performed a study considering the unsteady, 3-D, and incompressible nature of breakdown. Their results revealed that the bubble form ( $Re = 200$ ) of breakdown showed little temporal change in outer appearance; however, large structural changes occurred in the interior of the bubble. Later work by Spall and Gatski (1990, 1991) revealed for the first time a

numerical solution of the spiral form of breakdown. The spiral form was found through a process where the swirl ratio and  $Re$  were held fixed while adjustments were made in the freestream axial velocity distribution. The rotation of the helical structure was the same as the direction of the base vortical flow, which is consistent with experiments in tube flows with a swirl-vane generator. The direction is opposite to that found for breakdown over delta wings.

Few researchers have actively considered the nonuniqueness of solutions. Berger (1989) stated that bifurcation processes of a mathematical nature are fundamental in understanding the two kinds of vortex breakdown.

Leibovich and Kribus (1990) considered large-amplitude wave deviations from columnar vortices as static bifurcations of the Bragg-Hawthorne equation (BHE). The BHE is a steady, axisymmetric form of Euler's equations, and is derived in Appendix E.1. Figure 9 shows a characteristic solution diagram for the BHE. Táasan (1986) identified a branch of soliton solutions, which is shown as branch III in Figure 9. This branch bifurcates at point A from the so-called trivial branch, which represents a family of specifying flows that must be invoked when constructing the BHE. The specifying flow is typically chosen to be columnar. Leibovich and Kribus identified branches II and IV. Branch II represents columnar solutions that correspond to the conjugate flows proposed by Benjamin (1962, 1967). The point A in Figure 9 corresponds to the critical state. Points on branch II below this critical value of vortex strength,  $\mathcal{V}$ , correspond to the supercritical flows, while points above correspond to subcritical flows. Branch IV identifies solutions that exhibit wavetrain-type behavior. This branch extends from a second bifurcation point B.

Beran and Culick (1992), using a tube geometry, compared the solution paths resulting from the BHE to corresponding solution paths of the Navier-Stokes (NS) equations for  $Re$  up to 6000. The assumptions of steady, axisymmetric flow were retained. Furthermore, a constriction of the tube wall was used, inhibited breakdown from occurring near the inflow boundary and conflicting with the prescribed inflow conditions. Allowance for slip was also made at the wall, neglecting the influences of a wall boundary layer.

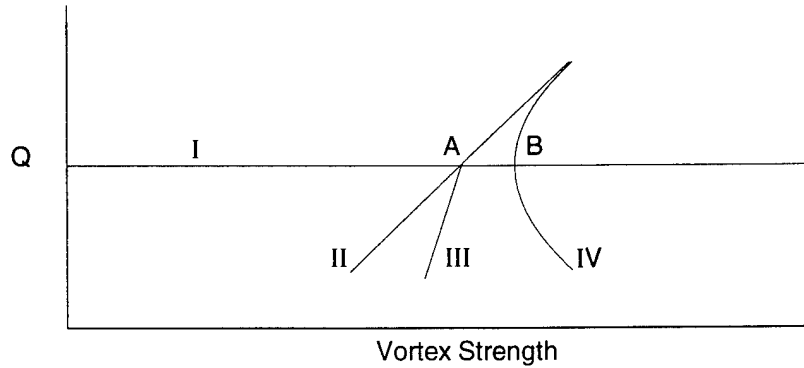


Figure 9. Characteristic solution diagram for the Bragg-Hawthorne equation: (I) trivial branch; (II) principal conjugate branch; (III) soliton wave branch; (IV) wavetrain branch, and two bifurcation points: (A) primary; (B) secondary.  $Q$  represents the minimum axial velocity along the centerline. (Beran and Culick (1992)).

Beran and Culick (1992) found that the paths of the NS equations were distinctly different from the BHE paths. However, they provided a scenario under which a slight movement of the bifurcation points A and B of Figure 9 could help explain the qualitative nature of their solutions at various points along the NS solution paths. In particular, if the bifurcation point B was allowed to move to the left of the bifurcation point A such that  $V_B < V_A$ , then the qualitative behavior of the solutions at certain points along the NS paths agreed in character with the character of the nearest BHE path.

Thus, the inviscid solution space yielded valuable information that served two purposes. First, the inviscid (BHE) solutions provided a reference set of paths that can be assumed to be in proximity to the NS paths for sufficiently high  $Re$ . This provides, to some degree, a check on the validity of computed NS paths. Second, the inviscid paths allowed for an analysis of the effects of viscosity on the change in structure of the NS solution paths.

Beran (1994) also examined the 2-D stability of the axisymmetric solution paths reported by Beran and Culick (1992). Time-integration was used to determine the stability of solutions obtained under the assumption of steady flow. The branch of solutions found between the two computed limit points was found to be unstable, while the other two

branches before the first limit point and after the second limit point were stable to 2-D disturbances.

Lopez (1994), also confirmed the stability of solutions computed by Beran and Culick (1992). In addition, Lopez found a branch of unsteady, axisymmetric solutions that appear to be disconnected from the previously known steady branches. The vortex strengths associated with the unsteady branch are relatively large at low Reynolds numbers, but decrease steadily as Reynolds number is increased.

The consideration of solution nonuniqueness has also lead to a link between the formation of a limit point and flow criticality. Beran and Culick (1992) provided numerical evidence establishing a link between the appearance of reversed flow and the movement across a limit point as vortex strength is increased. Solutions to both the QC equations and the NS equations were obtained and compared. The QC equations were found to fail at a vortex strength which was close to the limit point computed from the NS equations. The failure of the parabolic QC equations was linked to the presence of critical flow. Thus, this work provides numerical evidence that establishes a relationship between the appearance of a limit point in the axisymmetric solution space and the first appearance of critical flow. For vortex strengths past the limit point, stable breakdown solutions were computed.

Darmofal (1994) computed the criticality of axisymmetric flows in a tube by solving the stationary perturbation equations of Hall (1972). He concluded that breakdown (in 2-D flows) coincides with the occurrence of flow criticality. This result agrees with Squire's (1960) suggestion that breakdown is associated with the appearance of flow criticality, despite the issue of Squire considering only infinitely long, standing waves in his analysis.

However, a definite relationship between flow criticality and the location of a limit point cannot be obtained from the results of Darmofal (1994), since limit points can not be precisely identified from the numerical procedure. Nevertheless, visual inspection of solution paths show that the slope of the paths at flow criticality are nearly infinite, which implies that the critical point and the limit point are at least approximately coincident.

## *2.2 Previous Applications of the Compact Scheme.*

The use of high-order schemes (such as the compact scheme) in compressible codes is very limited. Smith and Sankar (1991) evaluated the compact operator in both an Euler and Navier-Stokes solver. They documented a 40 – 50% reduction in the number of grid points required to model hovering rotor flows. Furthermore, they found that the accuracy of the compact scheme results were maintained when the number of grid points were reduced, in contrast to results obtained with a second-order scheme. Roach and Jenkins (1995) applied the compact scheme to the study of flow over a 65° delta wing. Compact differencing was used in two of the coordinate directions, with fourth-order, five-point central differences in the third direction. Comparison of computed oil-flow patterns with experiment showed that the fourth-order scheme provided an overall better comparison. Roach also confirmed an observation first made in this study: that a second-order boundary stencil yields better freestream conserving properties than a fourth-order boundary stencil. Ekaterinaris (1993) evaluated 3rd, 4th, and 5th-order upwind-biased differencing to assess the effects of spatial accuracy on the strength of leading-edge vortices. The results showed that higher accuracy yielded stronger vortices, with closer agreement between computed and measured surface pressures. Soh (1994) combined a wave solution method with a 2-D unsteady Navier-Stokes solver (with a compact scheme) to produce an integrated aeroacoustic code to predict far-field jet noise. The application of compact schemes to the Euler equations was documented by Abarbanel and Kumar (1988). A summary on the technique of compact differencing was presented by Lele (1992).

### III. The Time-Accurate Navier-Stokes (TANS) Model

In this chapter, a numerical model for the study of the temporal behavior of laminar, three-dimensional vortex breakdown in a tube is presented. This includes the description of the tube geometry and the tube grid, the specification of governing equations and boundary conditions, the transformation of the governing equations and boundary conditions from physical to computational coordinates, the discretization of the transformed governing equations and boundary conditions, and the solution procedure. Descriptions of the computational resources, flow visualization, and recorded data are also included.

#### 3.1 Geometry and Grid

A Cartesian and a cylindrical coordinate system will be referenced. The coordinate systems are shown in Figure 10a and 10b. The Cartesian system,  $(x, y, z)$ , is defined such that positive  $x$  is aligned with the tube centerline and pointed downstream. The  $y$  and  $z$  directions are in a crossplane normal to  $x$  and form a right-handed system. The velocity components are denoted by  $(u, v, w)$ . The cylindrical coordinate system,  $(\hat{z}, r, \theta)$ , aligns the  $\hat{z}$  direction with  $x$ . The  $r$  and  $\theta$  directions lie in the crossplane normal to  $\hat{z}$  such that  $\theta = 0$  corresponds to  $r = +y$ . The axial, radial and azimuthal velocity components are denoted by  $(\hat{w}, \hat{u}, \hat{v})$ .

The physical domain consists of a two-stage cylindrical tube of circular cross-section and varying radius, and is nearly identical to the geometry used by Beran and Culick (1992). This domain is shown in Figure 11. The radius of the inlet station is denoted by  $R_0$ . The radius of the first stage is given by

$$R(x) = R_0 + \alpha R_0 [\cos(2\pi x/x_1) - 1] \quad (0 \leq x \leq x_1) \quad (8)$$

where  $x_1$  is the length of the first stage. The parameter  $\alpha$  controls the amount of tube contraction. The values of  $\alpha$  and  $x_1$  are fixed for this work at 0.05 and 6.18 respectively. These parameter values were chosen to allow for comparison with results of Beran and



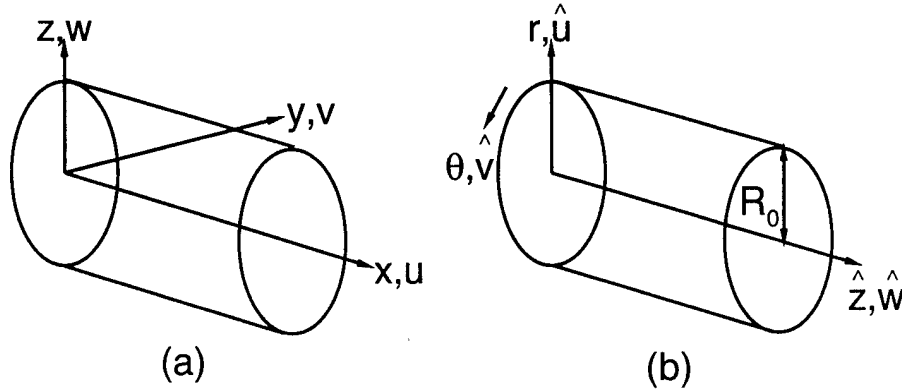


Figure 10. Coordinate systems: (a) Cartesian, (b) cylindrical.

Culick (1992). The second stage of the tube has a constant tube radius of  $R_0$

$$R(x) = R_0 \quad (x_1 < x \leq L) \quad (9)$$

where  $L$  denotes the tube length. Different values of  $R_0$  and  $L$  are evaluated in this study to determine their impact on the solution. The domain boundaries are denoted by  $s1$ ,  $s2$ , and  $s3$ , corresponding to the inflow, wall, and outflow boundaries, respectively.

The constriction in the first stage of the tube provides a favorable pressure gradient in the converging section, while an adverse gradient forms aft of the throat. Thus, the constriction keeps the breakdown from occurring near  $s1$ , where columnar conditions are enforced. This allows for flows that are consistent with those found in tube experiments. The experiments of Faler and Leibovich (1977) and Garg and Leibovich (1979) demonstrate that the flowfields upstream and far downstream of breakdown are quasi-cylindrical in nature. Quasi-cylindrical (QC) flows are defined to be nearly columnar, i.e., QC flows do not possess large axial gradients. Numerical simulations of breakdown in straight tubes assuming QC inlet conditions typically involve breakdown near the inlet. Such computations are not self-consistent with the specified inlet conditions, due to the large axial gradients induced by breakdown. Beran and Culick (1992) demonstrated that the upstream flow in the proposed geometry agrees well with numerical solutions of the QC equations.

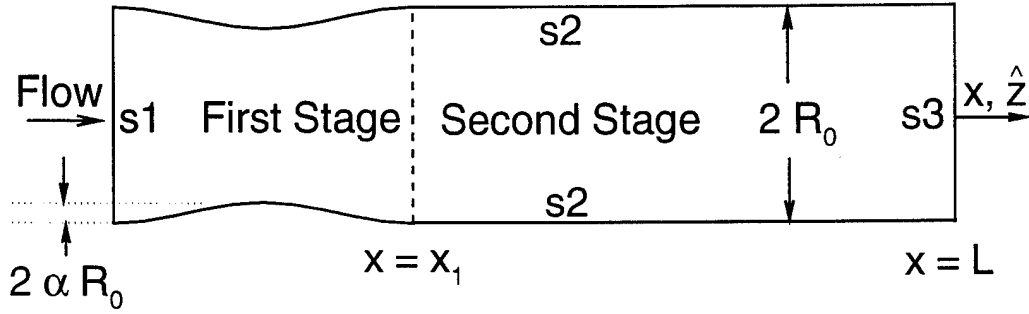


Figure 11. Schematic of tube geometry in an arbitrary  $(\hat{z}, r)$  plane.

A computational coordinate system is required to facilitate the use of finite-difference operations on equally spaced nodes. A generalized mapping transforms the physical coordinates  $(x, y, z)$  to the computational coordinates  $(\xi, \eta, \zeta)$ . This transformation is performed in Section 3.3. The node indices in the  $(\xi, \eta, \zeta)$  coordinates are denoted by  $(i, j, k)$  respectively. The number of nodes in the  $(\xi, \eta, \zeta)$  coordinate directions are  $(n_x, n_y, n_z)$  respectively. Two planes of the computational domain are shown in Figure 12. For simplicity, Figure 12 depicts a single-block grid. In the discussion below, a multiple-block crossplane grid structure is introduced.

The 2-D crossplane grids employed in this work have a unique structure; nodes are arranged in a nearly rectilinear fashion close to the tube center, while maintaining near orthogonality at the tube wall (Figure 13a). This accomplishes three goals: (1) allows for nearly constant grid resolution near the centerline, where the vortex core may migrate off-center during spiral breakdown; (2) avoids an approximate numerical treatment at the tube centerline (essentially moving such treatment towards the tube wall), and (3) provides nearly orthogonal node placement at the wall, reducing numerical errors associated with the specification of Neumann-type boundary conditions. To achieve this type of grid, a multiple-block structure in the crossplanes,  $(\eta, \zeta)$ , is used. The structure consists of an inner block surrounded by four outer blocks (Figure 13b). The outer blocks are physically connected to each other, but contain two edges each that are considered as branch cuts in the computational domain. These cuts are labeled 1-4 in Figure 13b. The parameters  $j1$  and  $j2$  define the node indices of  $\eta$  at the cuts, while  $k1$  and  $k2$  are the node indices of

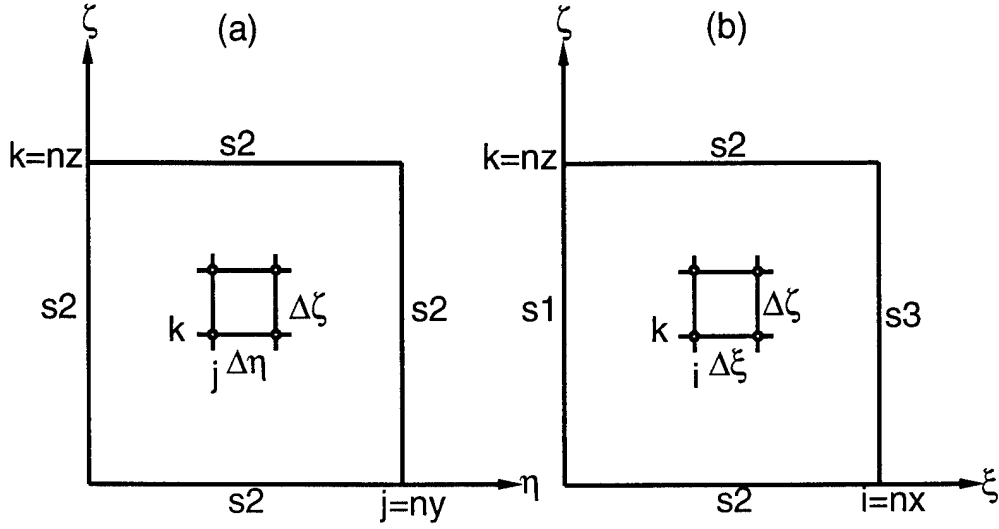


Figure 12. Schematics of a single-block computational domain: (a)  $(\eta, \zeta)$  crossplane, (b)  $(\xi, \zeta)$  crossplane.

$\zeta$  at the cuts. In Figure 13b,  $j_1 = k_1 = 6$ ,  $j_2 = k_2 = 36$ , and  $ny = nz = 41$ . The 2-D crossplane grid is generated using the grid generation software GRIDGEN, as described in Appendix C.

The 3-D grid is generated by placing the 2-D crossplane grids at the desired axial node locations. The crossplane node positions corresponding to each axial node are scaled such that the radial distances from the tube centerline to the wall nodes are equal to the local tube radius.

Clustering of axial node locations is used in this study to allow more axial nodes in the region aft of the tube throat (where breakdown is expected), while maintaining larger node spacings elsewhere. This helps reduce the overall computational effort by allowing fewer total nodes. The axial node locations are computed from  $x_i = x_{i-1} + \Delta x_i$ , where

$$\Delta x_i = \Delta x_0 (1 + \beta [\cos(2\pi x_{i-1}/x_2) - 1]) \quad (0 \leq x \leq x_2)$$

The parameters  $\beta$  and  $x_2$  control the amount and axial extent of clustering respectively. When  $x = 0$  or  $x > x_2$ ,  $\Delta x_i = \Delta x_0$ .

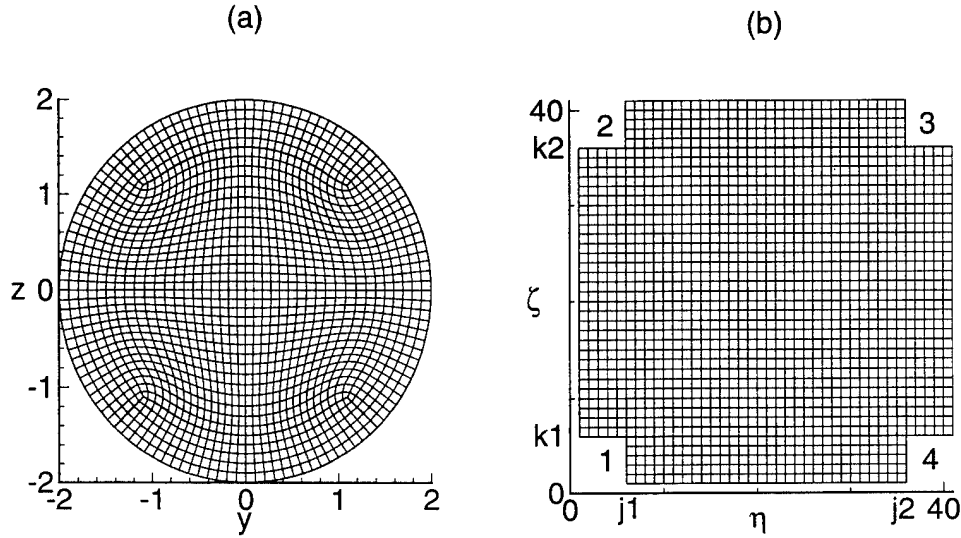


Figure 13. Crossplane grid for G1: (a) physical, (b) computational.

The form of  $\Delta x_i$  allows for a smooth transition from a relatively large axial node spacing at  $x = 0$ , to a minimum spacing at  $x = x_2/2$ , to an equally large node spacing at  $x = x_2$ . The clustered grids used in this work are generated with  $\beta = 1/4$  and  $x_2 = 10$ . This value of  $\beta$  provides a minimum axial node spacing of 0.1, which is about one-half the spacing in the non-clustered regions. The value of  $x_2$  places the minimum node spacing at  $x = 5$ , which is believed to be a reasonable location for flow disturbances to first occur.

Parameter values for all of the 3-D grids used in this work (designated G1–G13) are shown in Table 1. Grids with clustering are distinguished by the specification of  $x_2$  in Table 1, along with a nonzero value of  $\beta$ . Axial slices of grids G1 and G2 through  $z = 0$  are shown in Figure 14. Table 1 is repeated as Table 23 in Appendix G, where the run matrix and grids for this study are summarized.

### 3.2 Governing Equations

The Navier-Stokes equations are an accurate set of governing equations for simulating the flows of Newtonian fluids. The fluid is assumed to be a single-species perfect gas with no heat sources or external body forces. In addition, there are no chemical reac-

Table 1. 3-D grid parameters.

Grid	$nx$	$ny$	$nz$	$L$	$\Delta x_0$	$\beta$	$x_2$
G1	98	41	41	20	.206	0.0	-
G2	122	61	61	20	.200	.25	10
G3	172	61	61	30	.200	.25	10
G4	222	61	61	40	.200	.25	10
G5	146	41	41	30	.206	0.0	-
G6	98	61	61	20	.206	0.0	-
G7	51	61	61	20	.400	0.0	-
G8	101	61	61	20	.200	0.0	-
G9	201	61	61	20	.100	0.0	-
G10	51	61	61	10	.200	0.0	-
G11	201	61	61	40	.200	0.0	-
G12	101	41	41	20	.200	0.0	-
G13	101	81	81	20	.200	0.0	-

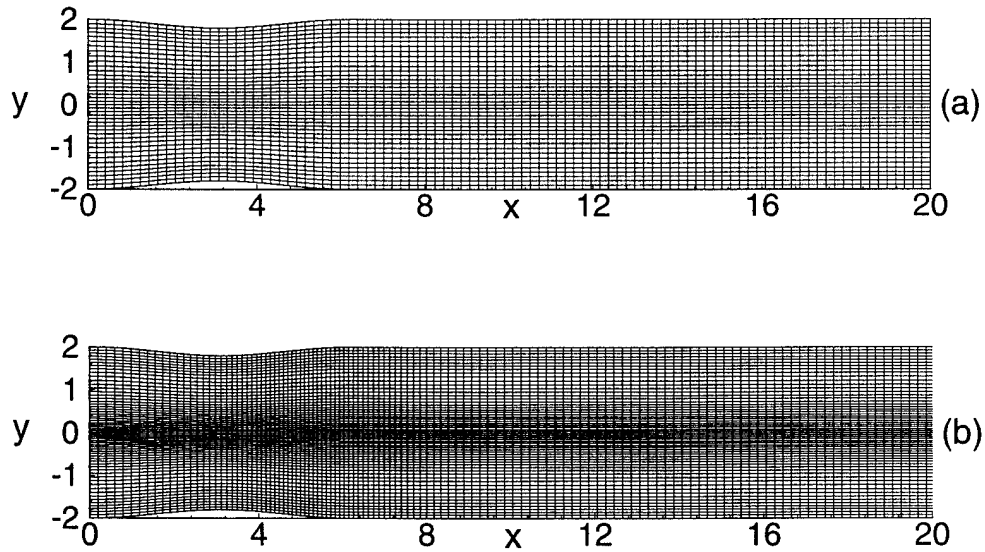


Figure 14. Axial slice of grids through  $z = 0$ : (a) G1, (b) G2.

tions and there are no electromagnetic effects. Given these assumptions, the Navier-Stokes equations are written below in terms of the fluid density,  $\rho$ , the Cartesian velocity components,  $(u, v, w)$ , and the pressure  $p$ . All variables are expressed in nondimensional form (details on the transformation from dimensional to nondimensional variables are contained in Appendix A).

$$\rho_t + \rho(u_x + v_y + w_z) + u\rho_x + v\rho_y + w\rho_z = 0 \quad (10)$$

$$u_t + uu_x + vu_y + wu_z + \frac{1}{\rho}p_x = \frac{1}{\rho} \left( \frac{\partial}{\partial x}\tau_{xx} + \frac{\partial}{\partial y}\tau_{xy} + \frac{\partial}{\partial z}\tau_{xz} \right) \quad (11)$$

$$v_t + uv_x + vv_y + wv_z + \frac{1}{\rho}p_y = \frac{1}{\rho} \left( \frac{\partial}{\partial x}\tau_{yx} + \frac{\partial}{\partial y}\tau_{yy} + \frac{\partial}{\partial z}\tau_{yz} \right) \quad (12)$$

$$w_t + uw_x + vw_y + ww_z + \frac{1}{\rho}p_z = \frac{1}{\rho} \left( \frac{\partial}{\partial x}\tau_{zx} + \frac{\partial}{\partial y}\tau_{zy} + \frac{\partial}{\partial z}\tau_{zz} \right) \quad (13)$$

$$p_t + up_x + vp_y + wp_z + \gamma p(u_x + v_y + w_z) = (\gamma - 1)\Phi - \nabla \cdot \vec{q} \quad (14)$$

The nondimensional shear stress tensor,  $\tau$ , and viscous dissipation,  $\Phi$ , are given by

$$\tau_{ij} = \frac{\mu}{Re} \left[ \left( \frac{\partial u_i}{\partial x_j} + \frac{\partial u_j}{\partial x_i} \right) - \frac{2}{3} \delta_{ij} \frac{\partial u_k}{\partial x_k} \right] \quad (i, j, k = 1, 2, 3) \quad (15)$$

and

$$\Phi = \nabla \cdot (\tau \cdot \vec{u}) - (\nabla \cdot \tau) \cdot \vec{u} \quad (16)$$

The nondimensional heat flux vector,  $\vec{q}$ , is defined as

$$\vec{q} = -\frac{\mu}{Pr Re M^2} \nabla T \quad (17)$$

where  $M$  is the reference Mach number based on the reference velocity,  $T$  is the temperature and  $Pr$  is the Prandtl number ( $Pr \equiv \mu_{ref} c_p / k_{ref} = 0.72$ ). The reference velocity,  $u'_{ref}$ , is defined as the axial velocity at the reference "point," taken to be at the juncture of the inflow and wall boundaries (the prime symbol is used to indicate that  $u'_{ref}$  is a dimensional quantity). Thus, the reference point is actually a set of points. However, since the flow at the inflow plane (which contains the reference point) is assumed to be axisymmetric, there is no ambiguity in the selection of reference quantities. All other flow quantities at the reference point are denoted with the subscript "ref." The Reynolds number  $Re$  and

Mach number  $M$  are defined as

$$Re \equiv \frac{u'_{ref} r_0}{\nu'_{ref}} \quad (18)$$

$$M \equiv u'_{ref} / c'_{ref} \quad (19)$$

where the length scale,  $r_0$ , is defined as the radius of the vortex core at the inflow boundary. [For example, with  $r_0$  as the length scale,  $R_0 = 2$  implies that the outer boundary is located at a radial distance equal to two times the vortex core radius, while  $L = 30$  implies that the outflow boundary is located a distance equal to 30 times the vortex core radius from the inflow boundary.]

Auxiliary equations, necessary to close the system of differential equations, are obtained by assuming a perfect gas and Sutherland's formula:

$$T = \frac{\gamma M^2 p}{\rho} \quad (20)$$

$$\mu = \frac{[1 + C_2]}{[T + C_2]} T^{\frac{3}{2}} \quad (21)$$

where  $C_2$  is a nondimensional constant defined in Appendix A. When  $Pr$  is fixed, we find the nondimensional relationship

$$k = \mu \quad (22)$$

The governing equations, in vector form, become

$$U_t + AU_x + BU_y + CU_z = D \quad (23)$$

where  $U \equiv (\rho, u, v, w, p)^T$  and

$$A = \begin{bmatrix} u & \rho & 0 & 0 & 0 \\ 0 & u & 0 & 0 & \frac{1}{\rho} \\ 0 & 0 & u & 0 & 0 \\ 0 & 0 & 0 & u & 0 \\ 0 & \gamma p & 0 & 0 & u \end{bmatrix} \quad B = \begin{bmatrix} v & 0 & \rho & 0 & 0 \\ 0 & v & 0 & 0 & 0 \\ 0 & 0 & v & 0 & \frac{1}{\rho} \\ 0 & 0 & 0 & v & 0 \\ 0 & 0 & \gamma p & 0 & v \end{bmatrix}$$

$$C = \begin{bmatrix} w & 0 & 0 & \rho & 0 \\ 0 & w & 0 & 0 & 0 \\ 0 & 0 & w & 0 & 0 \\ 0 & 0 & 0 & w & \frac{1}{\rho} \\ 0 & 0 & 0 & \gamma p & w \end{bmatrix} \quad D = \frac{1}{\rho} \begin{bmatrix} 0 \\ \frac{\partial}{\partial x}\tau_{xx} + \frac{\partial}{\partial y}\tau_{xy} + \frac{\partial}{\partial z}\tau_{xz} \\ \frac{\partial}{\partial x}\tau_{yx} + \frac{\partial}{\partial y}\tau_{yy} + \frac{\partial}{\partial z}\tau_{yz} \\ \frac{\partial}{\partial x}\tau_{zx} + \frac{\partial}{\partial y}\tau_{zy} + \frac{\partial}{\partial z}\tau_{zz} \\ \rho[(\gamma - 1)\Phi - \nabla \cdot \vec{q}] \end{bmatrix}$$

### 3.3 Transformation to Computational Coordinates

In this section, the governing equations are transformed to allow for computations over equally spaced nodes. The governing equations are rewritten in terms of computational coordinates  $(\xi, \eta, \zeta)$ , where  $x = x(\xi)$ ,  $y = y(\xi, \eta, \zeta)$  and  $z = z(\xi, \eta, \zeta)$ . Application of the chain rule to the spatial derivatives in the left-hand side of Eq. 23 results in

$$U_t + AU_\xi \xi_x + AU_\eta \eta_x + AU_\zeta \zeta_x + BU_\eta \eta_y + BU_\zeta \zeta_y + CU_\eta \eta_z + CU_\zeta \zeta_z = D \quad (24)$$

The viscous terms,  $D$ , are transformed to computational coordinates by application of the chain rule, and are found by first computing and storing the elements of the stress tensor,  $\tau$ , followed by the calculation of  $D$ . Eq. 24 can be written in the form

$$U_t + \mathcal{A}U_\xi + \mathcal{B}U_\eta + \mathcal{C}U_\zeta = D \quad (25)$$

where

$$\mathcal{A} = A\xi_x \quad \mathcal{B} = A\eta_x + B\eta_y + C\eta_z \quad \mathcal{C} = A\zeta_x + B\zeta_y + C\zeta_z$$

The metrics are evaluated from the following relations (Anderson et al. (1984)):

$$\begin{aligned} \xi_x &= 1/x_\xi & \xi_y &= 0 & \xi_z &= 0 \\ \eta_x &= -J(y_\xi z_\zeta - y_\zeta z_\xi) & \eta_y &= Jx_\xi z_\zeta & \eta_z &= -Jx_\xi y_\zeta \\ \zeta_x &= J(y_\xi z_\eta - y_\eta z_\xi) & \zeta_y &= -Jx_\xi z_\eta & \zeta_z &= Jx_\xi y_\eta \end{aligned}$$



where  $J = 1/\tilde{J}$  is the transformation Jacobian. The inverse transformation Jacobian,  $\tilde{J}$ , is given by

$$\tilde{J} = x_\xi (y_\eta z_\zeta - z_\eta y_\zeta) \quad (26)$$

The metrics  $(x_\xi - z_\zeta)$  are calculated using finite-difference approximations, where  $\Delta\xi = 1$ ,  $\Delta\eta = 1$ , and  $\Delta\zeta = 1$  are assumed for convenience. Details on the metric calculations are given in Section 3.6.

Eq. 25 has the same form as Eq. 23, implying that the incorporation of the transformation involves replacing the matrices  $A$ ,  $B$ , and  $C$  with  $\mathcal{A}$ ,  $\mathcal{B}$ , and  $\mathcal{C}$ , along with the application of the chain rule to  $D$ .

### 3.4 Boundary Condition Formulation

Boundary conditions are categorized as follows:

- inflow conditions (s1)
- wall conditions (s2)
- outflow conditions (s3)

Two conditions are formulated for the inflow and wall boundaries, while one condition is presented for the outflow boundary. Type 1 conditions consist of Inflow-1, Wall-1 and Outflow conditions. Type 2 conditions consist of Inflow-2, Wall-2 and Outflow conditions.

*3.4.1 Specification of Boundary Locations.* The specification of the boundary locations in both physical and computational domains is outlined in this section.

The specification of boundary locations in physical coordinates  $(x, y, z)$  is straightforward. The inflow conditions (s1) are evaluated at  $(0, y, z)$ , where  $y^2 + z^2 \leq R_0^2$ . Similarly, the outflow conditions (s3) are evaluated at  $(L, y, z)$ , where  $y^2 + z^2 \leq R_0^2$ . The wall boundary conditions are applied for  $0 < x < L$  such that  $y^2 + z^2 = R_0^2$  (it should be emphasized that  $x = 0$  and  $x = L$  are not included in the wall boundary condition).

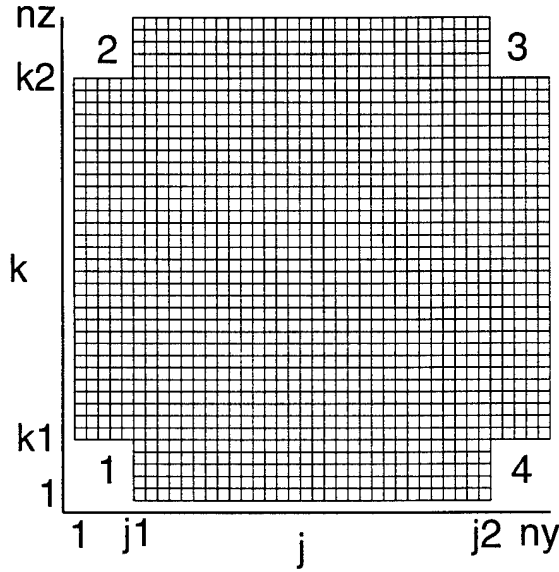


Figure 15. Schematic of crossplane grid in the computational domain.

Node indices are used in favor of computational coordinates to denote the boundary locations. Sets of node indices, denoted as  $\mathcal{I}^1$ ,  $\mathcal{I}^2$  and  $\mathcal{I}^3$  will be defined below as the nodes along  $s_1$ ,  $s_2$  and  $s_3$  respectively.

The specification of node indices in the crossplane is complicated by the multiblock nature of the grid structure. For convenience, node indices for a typical crossplane grid in the computational domain are presented in Figure 15. The following sets of crossplane indices  $(j, k)$  are defined to clarify their specification:

$$\mathcal{R}^1 = \{(j, k) : j = 1, \dots, ny; k = k1, \dots, k2\}$$

$$\mathcal{R}^2 = \{(j, k) : j = j1, \dots, j2; k = 1, \dots, k1 - 1\}$$

$$\mathcal{R}^3 = \{(j, k) : j = j1, \dots, j2; k = k2 + 1, \dots, nz\}$$

The complete set of crossplane node indices is formed from the union of  $\mathcal{R}^1$ ,  $\mathcal{R}^2$  and  $\mathcal{R}^3$ :

$$\mathcal{R}^c = \mathcal{R}^1 \cup \mathcal{R}^2 \cup \mathcal{R}^3 \quad (27)$$

Nodes along s1, the inflow boundary, are denoted by the set  $\mathcal{I}^1$ , defined as

$$\mathcal{I}^1 = \{(i, j, k) : i = 1; (j, k) = \mathcal{R}^c\} \quad (28)$$

Similarly, nodes along the outflow boundary (s3) are denoted by the set  $\mathcal{I}^3$ , defined as

$$\mathcal{I}^3 = \{(i, j, k) : i = nx; (j, k) = \mathcal{R}^c\} \quad (29)$$

The set of wall node indices is formed from the following sets of crossplane indices:

$$\begin{aligned} \mathcal{R}^4 &= \{(j, k) : j = 1; k = k1, \dots, k2\} \\ \mathcal{R}^5 &= \{(j, k) : j = ny; k = k1, \dots, k2\} \\ \mathcal{R}^6 &= \{(j, k) : j = j1, \dots, j2; k = 1\} \\ \mathcal{R}^7 &= \{(j, k) : j = j1, \dots, j2; k = nz\} \end{aligned}$$

The complete set of wall node indices for a given crossplane is formed from the union of  $\mathcal{R}^4 - \mathcal{R}^7$ :

$$\mathcal{R}^w = \mathcal{R}^4 \cup \mathcal{R}^5 \cup \mathcal{R}^6 \cup \mathcal{R}^7$$

The total set of wall node indices along s2 is denoted by  $\mathcal{I}^2$ , defined as

$$\mathcal{I}^2 = \{(i, j, k) : i = 2, \dots, nx - 1; (j, k) = \mathcal{R}^w\} \quad (30)$$

Indices at the wall/inflow juncture,  $i = 1$ , correspond to reference conditions, and are designated as

$$\mathcal{I}^{\text{ref}} = \{(i, j, k) : i = 1; (j, k) = \mathcal{R}^w\} \quad (31)$$

3.4.2 *Inflow-1.* The principle assumptions are that the flowfield is steady, axisymmetric and incompressible at the inflow plane, s1. For simplicity, the inlet axial velocity,  $\hat{w}$ , is chosen to be uniform:

$$\hat{w}(0, r, \theta) = 1 \quad (32)$$

This differs from flows exiting from a swirl-vane apparatus, which typically have a jet-like axial velocity profile. The effect of this axial velocity excess (or defect) on the vortex core is not explored in this work.

Boundary conditions on  $v$  and  $w$  (Cartesian velocity components) are obtained by specifying appropriate profiles for  $\hat{v}$  and  $\hat{u}$  (cylindrical velocity components). The following swirl velocity profile is characteristic of a Burger-type vortex and is appropriate for modeling the profiles obtained from a swirl-vane apparatus (Faler and Leibovich (1977)):

$$\hat{v}(0, r, \theta) = \mathcal{V}r^{-1}(1 - e^{-r^2}) = \Gamma r^{-1} \quad (33)$$

where  $\mathcal{V}$  is the vortex strength along s1 and  $\Gamma$  is the circulation (divided by  $2\pi$ ). The radial velocity component is assumed to vanish to reflect columnar flow at the inlet:

$$\hat{u}(0, r, \theta) = 0 \quad (34)$$

Transforming Eqs. 32-34 from the cylindrical system to the Cartesian coordinate system results in

$$u(0, y, z) = 1 \quad (35)$$

$$v(0, y, z) = -\hat{v}(0, r, \theta)\sin\theta \quad (36)$$

$$w(0, y, z) = \hat{v}(0, r, \theta)\cos\theta \quad (37)$$

where  $\sin\theta = z/r$ ,  $\cos\theta = y/r$  and  $r = \sqrt{y^2 + z^2}$ .

The inflow density profile is assumed to be uniform:

$$\rho(0, y, z) = 1 \quad (38)$$

A boundary condition on pressure is obtained by considering the axial momentum equation for inviscid flow:

$$u_t + uu_x + vu_y + wu_z + \frac{1}{\rho}p_x = 0 \quad (39)$$

Along the inflow plane,  $\rho = u = 1$ , and thus  $u_t$ ,  $u_y$  and  $u_z$  vanish, reducing Eq. 39 to

$$u_x(0, y, z) + p_x(0, y, z) = 0 \quad (40)$$

The continuity equation for incompressible flow in cylindrical coordinates is

$$\hat{u}_r + \frac{\hat{u}}{r} + \hat{w}_z = 0 \quad (41)$$

which can be simplified with Eq. 34 to obtain

$$\hat{w}_z(0, y, z) = u_x(0, y, z) = 0 \quad (42)$$

Substituting Eq. 42 into Eq. 40 results in

$$p_x(0, y, z) = 0 \quad (43)$$

Along  $s_1$ , the grid is constructed such that  $\eta_x = \zeta_x = 0$  (even if  $\alpha \neq 0$ ) and therefore application of the chain rule to  $p_x$  results in simply  $p_x = \xi_x p_\xi$ . Therefore, Eq. 43 can be written as

$$p_\xi(0, y, z) = 0 \quad (44)$$

The Inflow-1 boundary conditions are summarized in physical coordinates as

$$\begin{aligned} \rho(0, y, z) &= 1 \\ u(0, y, z) &= 1 \\ v(0, y, z) &= -\hat{v}(0, r, \theta)\sin\theta \\ w(0, y, z) &= \hat{v}(0, r, \theta)\cos\theta \end{aligned}$$

$$p_x(0, y, z) = 0$$

and in computational coordinates by

$$\rho_{(1,j,k)} = 1 \quad (45)$$

$$u_{(1,j,k)} = 1 \quad (46)$$

$$v_{(1,j,k)} = -\hat{v}_{(1,j,k)} \sin \theta_{(1,j,k)} \quad (47)$$

$$w_{(1,j,k)} = \hat{v}_{(1,j,k)} \cos \theta_{(1,j,k)} \quad (48)$$

$$p_{\xi(1,j,k)} = 0 \quad (49)$$

where  $(1, j, k) \in \mathcal{I}^1$  from Eq. 28.

**3.4.3 Inflow-2.** The primary difference between Inflow-1 and Inflow-2 is the inlet density profile. Inflow-1 assumes an incompressible ( $\rho = 1$ ) fluid state. Inflow-2 utilizes a non-uniform density profile based on columnar flow, which is enforced as a Dirichlet condition at the inlet.

$$\rho(0, y, z) = \rho_c(y, z)$$

The density profile,  $\rho_c$ , is obtained by solving the axisymmetric Navier-Stokes equations with the PAC algorithm (Appendix B.2) in a tube of short ( $L = 0.01$ ), but finite, axial extent. Inflow and outflow conditions of the short tube are enforced that dictate columnar flow. These conditions consist of fixed velocity components (Eqs. 32-34) with  $\rho_x = p_x = 0$ . The resulting columnar solution for density is defined as  $\rho_c$ .

Figure 16 shows Inflow-2 density profiles as vortex strength and Mach number are varied. The density at the centerline ( $r = 0$ ) is shown to decrease with increasing vortex strength and Mach number.

Morton (1989), studying unbounded vortices, used an inlet swirl velocity profile of the form

$$\hat{v} = \begin{cases} \mathcal{V}r(2 - r^2) & r \leq 1 \\ \mathcal{V}/r & r > 1 \end{cases}$$

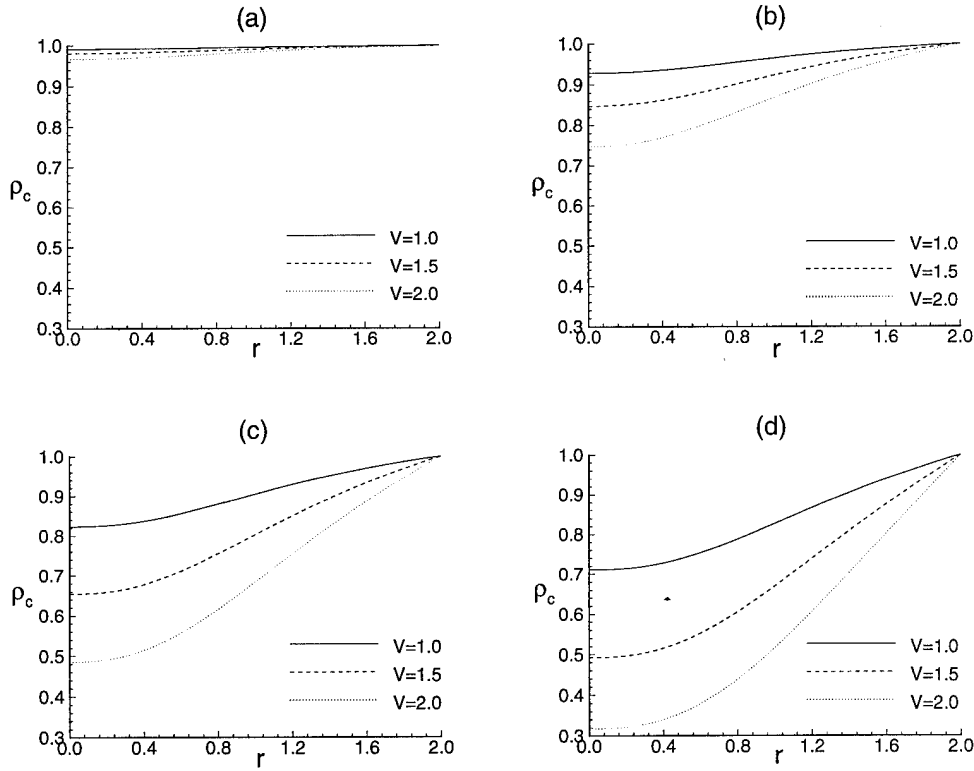


Figure 16. Inflow-2 density profiles for selected Mach numbers: (a)  $M = 0.1$ , (b)  $M = 0.3$ , (c)  $M = 0.5$ , (d)  $M = 0.7$ .

Morton (1989) also prescribed a non-uniform density profile assuming 2-D, compressible, columnar flow. The swirl momentum equation was utilized by Morton (1989) to obtain an expression for the internal energy at the inlet. Then, the axial momentum equation was used to solve for the inlet density.

Results of Morton's approach (provided by Morton only at the juncture of the inlet plane and centerline) are compared to the current approach for a wide range of Mach numbers in Table 2. The agreement is excellent, especially at the lower values of Mach number. The Mach number used in this study is  $M = 0.3$ . The PAC model was modified to allow for the different swirl velocity profile in order to obtain the comparison in Table 2.

The pressure for Inflow-2 is obtained by solving the steady, axial momentum equation. For steady, uniform axial flow at the inlet,  $u_y = u_z = 0$ , reducing the axial momentum

Table 2. Comparison of centerline ( $r = 0$ ) values of  $\rho_c$  between PAC model and results of Morton (1989).

$M$	$\rho_c$ (PAC)	$\rho_c$ (Morton)	percent difference
0.2	0.909	0.906	0.33%
0.4	0.693	0.688	0.72%
0.6	0.452	0.444	1.77%
0.8	0.269	0.255	5.20%

equation to

$$u_x + \frac{p_x}{\rho_c} = D_2 \quad (50)$$

where  $D_2$  is the second component of the vector  $D$ . In computational coordinates, Eq. 50 is written as

$$u_\xi + \frac{p_\xi}{\rho_c} = D_2/\xi_x \quad (51)$$

The Inflow-2 boundary conditions are summarized in physical coordinates as

$$\begin{aligned} \rho(0, y, z) &= \rho_c(y, z) \\ u(0, y, z) &= 1 \\ v(0, y, z) &= -\hat{v}(0, r, \theta)\sin\theta \\ w(0, y, z) &= \hat{v}(0, r, \theta)\cos\theta \\ u_x(0, y, z) + \frac{p_x(0, y, z)}{\rho_c(y, z)} &= D_2(0, y, z) \end{aligned}$$

and in computational coordinates as

$$\rho(1, j, k) = \rho_{c(j, k)} \quad (52)$$

$$u(1, j, k) = 1 \quad (53)$$

$$v(1, j, k) = -\hat{v}_{(1, j, k)}\sin\theta_{(1, j, k)} \quad (54)$$

$$w(1, j, k) = \hat{v}_{(1, j, k)}\cos\theta_{(1, j, k)} \quad (55)$$

$$u_{\xi(1, j, k)} + \frac{p_{\xi(1, j, k)}}{\rho_{c(j, k)}} = \frac{D_{2(1, j, k)}}{\xi_x} \quad (56)$$

where  $(1, j, k) \in \mathcal{I}^1$  from Eq. 28 and  $(j, k) \in \mathcal{R}^c$  from Eq. 27.



*3.4.4 Outflow.* Outflow conditions are chosen to reflect an assumed columnar flow state. This is a reasonable assumption when the outflow plane is sufficiently far downstream. As previously mentioned, the experiments of Faler and Leibovich (1977) and Garg and Leibovich (1979) demonstrate that flows far downstream of breakdown are quasi-cylindrical in nature, implying that axial variations in flow quantities are small. The columnar conditions employed here assume no axial variations. Columnar outflow conditions are also assumed in the works of Darmofal (1994) and Beran and Culick (1992).

The assumption of columnar flow at the outflow plane results in a complete set of outflow conditions:

$$\rho_x(L, y, z) = u_x(L, y, z) = v_x(L, y, z) = w_x(L, y, z) = p_x(L, y, z) = 0 \quad (57)$$

Since  $\eta_x = \zeta_x = 0$  at the outflow boundary, Eqs. 57 can be written in computational coordinates as

$$\rho_{\xi(nx,j,k)} = u_{\xi(nx,j,k)} = v_{\xi(nx,j,k)} = w_{\xi(nx,j,k)} = p_{\xi(nx,j,k)} = 0 \quad (58)$$

where  $(nx, j, k) \in \mathcal{I}^3$  from Eq. 29.

*3.4.5 Wall-1.* Wall boundary conditions are presented in this section for flows in a solid tube with slip. A straight wall ( $\alpha = 0$ ) is assumed for the Wall-1 conditions, with locally columnar flow prescribed at the wall.

The Wall-1 conditions are formulated to help define baseline grid requirements in Section 4.1. Their usefulness comes from the fact that, along with Inflow-1 conditions, steady breakdown solutions can be obtained. This allows for a “clean” assessment of the necessary grid resolution, since temporal errors can virtually be eliminated.

The absence of a wall boundary layer is likely to affect the location of breakdown, but it is not believed by the author to be a requirement for the development of breakdown or the resulting flow topology. Furthermore, when a constricted tube is used, a no-slip wall may result in regions of separated flow aft of the tube throat, which could complicate the flowfield and possibly contaminate the breakdown structures. For these reasons, and

for the reduced grid requirements allowed in the absence of a wall boundary layer, the slip wall is assumed. A slip wall is also used in the works of Darmofal (1994) and Beran and Culick (1992).

Dirichlet conditions are specified assuming locally columnar flow at the walls, i.e., the (reference) Dirichlet conditions at the inflow/wall juncture are specified at all wall points. The Wall-1 conditions are limited to straight ( $\alpha = 0$ ) tubes, since impermeability can not be enforced with these conditions if  $\alpha \neq 0$ . The conditions are written in physical coordinates along  $s_2$  ( $0 < x < L$  and  $y^2 + z^2 = R_0^2$ ) as

$$\rho(x, y, z) = \rho(0, y, z) = 1 \quad (59)$$

$$u(x, y, z) = u(0, y, z) = 1 \quad (60)$$

$$v(x, y, z) = v(0, y, z) = -(\Gamma(R_0)/R_0) \sin\theta \quad (61)$$

$$w(x, y, z) = w(0, y, z) = (\Gamma(R_0)/R_0) \cos\theta \quad (62)$$

$$p(x, y, z) = p(0, y, z) = 1/(\gamma M^2) \quad (63)$$

In computational coordinates, the Wall-1 conditions are written as

$$\rho(i, j, k) = \rho(1, j, k) = 1 \quad (64)$$

$$u(i, j, k) = u(1, j, k) = 1 \quad (65)$$

$$v(i, j, k) = v(1, j, k) = -(\Gamma_{(1, j, k)}/R_0) \sin\theta_{(1, j, k)} \quad (66)$$

$$w(i, j, k) = w(1, j, k) = (\Gamma_{(1, j, k)}/R_0) \cos\theta_{(1, j, k)} \quad (67)$$

$$p(i, j, k) = p(1, j, k) = 1/(\gamma M^2) \quad (68)$$

where  $(i, j, k) \in \mathcal{I}^2$  from Eq. 30 and  $(1, j, k) \in \mathcal{I}^{\text{ref}}$  from Eq. 31.

**3.4.6 Wall-2.** Boundary conditions are presented in this section that enforce impermeability at the slip wall for  $\alpha \neq 0$ . The flow at the wall is assumed to be steady, inviscid, and of constant temperature. In addition, it is assumed that the flow is compressible, but that the influence of compressibility is small.

Describing the wall surface in the form  $S(r, x) = 0$ , the impermeability condition is written as

$$\nabla S(r, x) \cdot \hat{\vec{u}} = 0$$

where

$$S(r, x) = r - R(x)$$

$$\hat{\vec{u}} = (\hat{u}, \hat{v}, \hat{w})^T$$

and  $R(x)$  is given by Eq. 8. Performing the dot product in cylindrical coordinates yields

$$\hat{u} - \frac{dR(x)}{dx} \hat{w} = 0$$

Defining  $\frac{dR(x)}{dx} \equiv -K(x)$ , results in

$$\hat{u} + K(x) \hat{w} = 0 \tag{69}$$

where

$$K(x) = \begin{cases} (2\pi\alpha R_0/x_1)\sin(2\pi x/x_1) & x \leq x_1 \\ 0 & x > x_1 \end{cases} \tag{70}$$

An expression for the swirl velocity,  $\hat{v}$ , at the wall can be obtained by considering that, in the absence of viscous losses, the wall is a streamsurface of the flow. The azimuthal momentum equation written in terms of the circulation,  $\Gamma$ , reduces to  $D\Gamma/Dt = 0$  along the wall for steady, inviscid flow. Thus, a fluid particle entering the physical domain at the inflow/wall juncture maintains a swirl velocity such that circulation remains constant. The condition that  $D\Gamma/Dt = 0$  is exact for incompressible flow, and is applied approximately here assuming that the effects of compressibility are small near the wall (Batchelor, 1967). Therefore, considering Eq. 33, we can write at the wall

$$\hat{v} = R_0 R(x)^{-1} \hat{v}_0 \tag{71}$$

where  $\hat{v}_0$  denotes the constant swirl velocity at the juncture of the inlet and wall surfaces.

Density is made proportional to pressure along  $s_2$  by prescribing the reference wall temperature. Then, from the perfect gas law,  $p/\rho$  is constant along the wall:

$$\frac{p}{\rho} = \frac{T}{\gamma M^2} = \frac{1}{\gamma M^2} \quad (72)$$

A third velocity condition is obtained from the compressible Bernoulli equation, valid for steady, inviscid flow along the wall streamsurface:

$$\frac{u^2 + v^2 + w^2}{2} + \frac{\gamma}{\gamma - 1} \frac{p}{\rho} = \text{constant}$$

This equation, along with Eq. 72, implies constant flow speed,  $\sqrt{u^2 + v^2 + w^2}$ , along  $s_2$ . The flow speed at the wall is evaluated from the inlet conditions, and is found to be  $\sqrt{1 + \hat{v}_0^2}$ . Expressed in terms of cylindrical velocity components, Bernoulli's equation applied along the wall yields

$$\hat{w}^2 + \hat{v}^2 + \hat{u}^2 = 1 + \hat{v}_0^2 \quad (73)$$

Substituting Eqs. 71 and 69 into Eq. 73 results in an expression for the axial velocity,  $u$ , along the wall:

$$u = \hat{w} = \sqrt{\frac{1 + \hat{v}_0^2 \left[ 1 - \left( \frac{R_0}{R(x)} \right)^2 \right]}{1 + K^2(x)}} \quad (74)$$

The wall pressure is determined by enforcing the conservation of momentum in the  $y$  and  $z$  directions. The  $y$  and  $z$  momentum equations for steady, inviscid flow are given by

$$uv_x + vv_y + ww_z + \frac{p_y}{\rho} = 0 \quad (75)$$

$$uw_x + vw_y + ww_z + \frac{p_z}{\rho} = 0 \quad (76)$$

Two different boundary conditions, Eqs. 75-76, are used due to the solution procedure, described in Section 3.6. The  $y$  momentum equation is used to solve for  $p$  in the  $\eta$ -sweep, while the  $z$  momentum equation is used to solve for  $p$  in the  $\zeta$ -sweep.

The Wall-2 boundary conditions in physical coordinates are summarized below for  $0 < x < L$  and  $y^2 + z^2 = R_0^2$ :

$$\frac{p}{\rho} = \frac{T}{\gamma M^2} = \frac{1}{\gamma M^2}$$

$$\hat{u} + K(x)\hat{w} = 0$$

$$\hat{v} = R_0 R(x)^{-1} \hat{v}_0$$

$$\hat{w} = \sqrt{\frac{1 + \hat{v}_0^2 \left[ 1 - \left( \frac{R_0}{R(x)} \right)^2 \right]}{1 + K^2(x)}}$$

$$uv_x + vv_y + ww_z + \frac{p_y}{\rho} = 0$$

$$uw_x + vw_y + ww_z + \frac{p_z}{\rho} = 0$$

The last two equations represent one boundary condition for pressure. Which equation is used depends on the location of the wall node. In computational coordinates, the above conditions are expressed as

$$\frac{p_{(i,j,k)}}{\rho_{(i,j,k)}} = \frac{1}{\gamma M^2} \quad (77)$$

$$\hat{u}_{(i,j,k)} + K_i \hat{w}_{(i,j,k)} = 0 \quad (78)$$

$$\hat{v}_{(i,j,k)} = R_0 R_i^{-1} \hat{v}_0 \quad (79)$$

$$\hat{w}_{(i,j,k)} = \sqrt{\frac{1 + \hat{v}_0^2 \left[ 1 - \left( \frac{R_0}{R_i} \right)^2 \right]}{1 + K_i^2}} \quad (80)$$

$$(uv_\xi \xi_x)_{(i,j,k)} + (v_\eta \Lambda_\eta)_{(i,j,k)} + (v_\zeta \Lambda_\zeta)_{(i,j,k)} + \frac{(p_\eta \eta_y + p_\zeta \zeta_y)_{(i,j,k)}}{\rho_{(i,j,k)}} = 0 \quad (81)$$

$$(uw_\xi \xi_x)_{(i,j,k)} + (w_\eta \Lambda_\eta)_{(i,j,k)} + (w_\zeta \Lambda_\zeta)_{(i,j,k)} + \frac{(p_\eta \eta_z + p_\zeta \zeta_z)_{(i,j,k)}}{\rho_{(i,j,k)}} = 0 \quad (82)$$

where  $R_i \equiv R(x_i)$ ,  $K_i \equiv K(x_i)$ ,  $(i, j, k) \in \mathcal{I}^2$  and

$$\Lambda_\eta = u\eta_x + v\eta_y + w\eta_z \quad (83)$$

$$\Lambda_\zeta = u\zeta_x + v\zeta_y + w\zeta_z \quad (84)$$

Eqs. 81 and 82 have been simplified to reflect the fact that  $\xi_y$  and  $\xi_z$  are zero for the grids developed in this work.

### 3.5 Discrete Boundary Conditions

The boundary conditions are approximated in discrete “delta” form in this section. The delta form implies that equations are written in terms of how the flow variables change from the known time level,  $n$ , to the unknown time level  $n + 1$ . For example,  $\Delta^n q$  refers to the change in an arbitrary flow quantity,  $q$ , between level  $n$  and  $n + 1$ , and is written as

$$\Delta^n q \equiv q^{n+1} - q^n \quad (85)$$

The spatial accuracy of the discrete form of derivative boundary conditions is first-order accurate during implicit sweeps, which is less than the spatial accuracy of the discrete interior equations. The reduction in formal accuracy is due to the solution procedure, discussed in Section 3.6. The discrete form of the governing equations (including boundary conditions) is written as a block-tridiagonal system of algebraic equations. To retain the tridiagonal form of the equations at the boundaries, two-point forward or backward differences are employed, which are first-order accurate.

Second-order accuracy is recovered at the end of each solution cycle by explicitly satisfying the boundary conditions using updated flow variables. For example, the outflow boundary condition for the density,  $\rho$ , is written in computational coordinates at the advanced time level as

$$\rho_{\xi}^{n+1}{}_{(nx,j,k)} = 0 \quad (86)$$

where  $(nx, j, k) \in \mathcal{I}^3$ . Eq. 86 is satisfied implicitly using a two-point backward difference:

$$\rho_{(nx,j,k)}^{n+1} - \rho_{(nx-1,j,k)}^{n+1} = 0$$

A second-order finite-difference formula involving  $\rho_{nx-2,j,k}^{n+1}$  is not used to approximate Eq. 86 implicitly, since this violates the tridiagonal structure of the discrete form of the equations. However, after the solution for  $\rho$  is obtained for every node from the current

solution cycle, the density at the outflow boundary is explicitly updated to second-order spatial accuracy from the three-point backward finite-difference discretization of Eq. 86:

$$3\rho_{(nx,j,k)}^{n+1} - 4\rho_{(nx-1,j,k)}^{n+1} + \rho_{(nx-2,j,k)}^{n+1} = 0 \quad (87)$$

Solving Eq. 87 for  $\rho_{(nx,j,k)}^{n+1}$  results in

$$\rho_{(nx,j,k)}^{n+1} = (4/3)\rho_{(nx-1,j,k)}^{n+1} - (1/3)\rho_{(nx-2,j,k)}^{n+1} \quad (88)$$

The value of  $\rho_{(nx,j,k)}^{n+1}$  provided by Eq. 88 is used to update the density at the outflow to second-order spatial accuracy.

Time accuracy of the discrete boundary conditions are exact unless otherwise noted. No unsteady boundary conditions are used in this study, therefore, there are no errors resulting from the discretization of temporal derivatives at the boundaries. Some boundary conditions do however employ “lagging” of one or more terms. A lagged term implies that it is considered approximately equal to it’s value at the previous time level to within an error of one order of magnitude.

*3.5.1 Inflow-1: Discrete Form.* The discrete forms of the Inflow-1 boundary conditions are presented in this section. The Inflow-1 boundary conditions in computational coordinates are summarized in Eqs. 45–49 of Section 3.4.2.

The discretization of Eqs. 45–49 into the delta form is straightforward, with  $p_\xi$  approximated using a two-point forward difference. The delta form is typically obtained by simply writing the boundary condition at time level  $n + 1$  and then subtracting from this the same condition at level  $n$ . Then, terms are grouped into the delta form using Eq. 85. For example, writing the Inflow-1 boundary condition for density at time levels  $n + 1$  and  $n$  yields

$$\rho_{(1,j,k)}^{n+1} = 1 \quad (89)$$

$$\rho_{(1,j,k)}^n = 1 \quad (90)$$

where  $(j, k) \in \mathcal{R}^c$ . Subtracting Eq. 90 from Eq. 89 results in

$$\Delta^n \rho_{(1,j,k)} = 0 \quad (91)$$

The remaining Inflow-1 conditions in delta form are

$$\Delta^n u_{(1,j,k)} = 0 \quad (92)$$

$$\Delta^n v_{(1,j,k)} = 0 \quad (93)$$

$$\Delta^n w_{(1,j,k)} = 0 \quad (94)$$

$$\Delta^n p_{(2,j,k)} - \Delta^n p_{(1,j,k)} = 0 \quad (95)$$

Eqs. 91–94 are exact, while Eq. 95 is first-order spatially accurate. Eqs. 91–95 are expressed in matrix form as

$$\begin{bmatrix} 0 & 0 & 0 & 0 & 0 \\ 0 & 0 & 0 & 0 & 0 \\ 0 & 0 & 0 & 0 & 0 \\ 0 & 0 & 0 & 0 & 0 \\ 0 & 0 & 0 & 0 & 1 \end{bmatrix} \Delta^n U_{(2,j,k)} - \begin{bmatrix} 1 & 0 & 0 & 0 & 0 \\ 0 & 1 & 0 & 0 & 0 \\ 0 & 0 & 1 & 0 & 0 \\ 0 & 0 & 0 & 1 & 0 \\ 0 & 0 & 0 & 0 & -1 \end{bmatrix} \Delta^n U_{(1,j,k)} = 0 \quad (96)$$

Eq. 96 is evaluated for all  $(j, k) \in \mathcal{R}^c$ .

**3.5.2 Inflow-2: Discrete Form.** The discrete form of the Inflow-2 boundary conditions are presented in this section. The Inflow-2 boundary conditions in computational coordinates are summarized in Eqs. 52–56 of Section 3.4.3.

Eqs. 52–56 are written in delta form as

$$\Delta^n \rho_{(1,j,k)} = 0 \quad (97)$$

$$\Delta^n u_{(1,j,k)} = 0 \quad (98)$$

$$\Delta^n v_{(1,j,k)} = 0 \quad (99)$$



$$\Delta^n w_{(1,j,k)} = 0 \quad (100)$$

$$\Delta^n u_{\xi(1,j,k)} + \frac{\Delta^n p_{\xi(1,j,k)}}{\rho_{c(j,k)}} = \frac{\Delta^n (D_2)_{(1,j,k)}}{\xi_x} \quad (101)$$

where the viscous term in Eq. 101 is lagged, resulting in the following approximation:

$$\Delta^n (D_2)_{(1,j,k)} = \Delta^{n-1} (D_2)_{(1,j,k)} + \mathcal{O}(\Delta t)^2$$

Therefore, Eq. 101 is written as

$$\Delta^n u_{\xi(1,j,k)} + \frac{\Delta^n p_{\xi(1,j,k)}}{\rho_{c(j,k)}} = \frac{\Delta^{n-1} (D_2)_{(1,j,k)}}{\xi_x} \quad (102)$$

Eqs. 97-100 and Eq. 102 are discretized and written in matrix form using two-point, forward differences for the terms  $u_\xi$  and  $p_\xi$ :

$$\begin{bmatrix} 0 & 0 & 0 & 0 & 0 \\ 0 & 0 & 0 & 0 & 0 \\ 0 & 0 & 0 & 0 & 0 \\ 0 & 0 & 0 & 0 & 0 \\ 0 & 1 & 0 & 0 & 1/\rho \end{bmatrix} \Delta^n U_{2,j,k} - \begin{bmatrix} 1 & 0 & 0 & 0 & 0 \\ 0 & 1 & 0 & 0 & 0 \\ 0 & 0 & 1 & 0 & 0 \\ 0 & 0 & 0 & 1 & 0 \\ 0 & -1 & 0 & 0 & -1/\rho \end{bmatrix} \Delta^n U_{1,j,k} = \begin{bmatrix} 0 \\ 0 \\ 0 \\ 0 \\ \frac{\Delta^{n-1} (D_2)_{1,j,k}}{\xi_x} \end{bmatrix} \quad (103)$$

Eq. 103 is evaluated at all crossplane nodes  $(j,k) \in \mathcal{R}^c$ .

**3.5.3 Outflow: Discrete Form.** The discrete forms of the outflow boundary conditions are presented in this section. The outflow boundary conditions in computational coordinates are summarized in Eqs. 58 of Section 3.4.4. Derivatives in Eqs. 58 are approximated using first-order, two-point backward finite differences. The remaining process of formulating the boundary conditions in delta and matrix form is similar to that described

in Sections 3.5.1 and 3.5.2. The result is

$$\begin{bmatrix} 1 & 0 & 0 & 0 & 0 \\ 0 & 1 & 0 & 0 & 0 \\ 0 & 0 & 1 & 0 & 0 \\ 0 & 0 & 0 & 1 & 0 \\ 0 & 0 & 0 & 0 & 1 \end{bmatrix} \Delta^n U_{nx,j,k} - \begin{bmatrix} 1 & 0 & 0 & 0 & 0 \\ 0 & 1 & 0 & 0 & 0 \\ 0 & 0 & 1 & 0 & 0 \\ 0 & 0 & 0 & 1 & 0 \\ 0 & 0 & 0 & 0 & 1 \end{bmatrix} \Delta^n U_{nx-1,j,k} = 0 \quad (104)$$

Eq. 104 is evaluated at all crossplane nodes  $(j, k) \in \mathcal{R}^c$ .

**3.5.4 Wall-1: Discrete Form.** The discrete forms of the Wall-1 boundary conditions are presented in this section. The Wall-1 boundary conditions in computational coordinates are summarized in Eqs. 64–68 of Section 3.4.5. Since all Wall-1 conditions are Dirichlet-type conditions, Eqs. 64–68 are written exactly in delta form as

$$\begin{bmatrix} 1 & 0 & 0 & 0 & 0 \\ 0 & 1 & 0 & 0 & 0 \\ 0 & 0 & 1 & 0 & 0 \\ 0 & 0 & 0 & 1 & 0 \\ 0 & 0 & 0 & 0 & 1 \end{bmatrix} \Delta^n U_{i,j,k} = 0 \quad (105)$$

Eq. 105 is evaluated at the wall nodes  $(i, j, k) \in \mathcal{I}^2$ .

**3.5.5 Wall-2: Discrete Form.** The discrete forms of the Wall-2 boundary conditions are presented in this section. The Wall-2 boundary conditions in computational coordinates are summarized in Eqs. 77–82 of Section 3.4.6.

Eqs. 77–82 can be expressed in delta form as

$$\Delta^n \rho - \gamma M^2 \Delta^n p = 0 \quad (106)$$

$$\Delta^n u = 0 \quad (107)$$

$$\Delta^n v = 0 \quad (108)$$

$$\Delta^n w = 0 \quad (109)$$

$$G^n \Delta^n \rho + \rho^n (u^n \Delta^n v_\xi \xi_x + \Lambda_\eta^n \Delta^n v_\eta + \Lambda_\zeta^n \Delta^n v_\zeta) + \Delta^n p_\eta \eta_y + \Delta^n p_\zeta \zeta_y = 0 \quad (110)$$

$$H^n \Delta^n \rho + \rho^n (u^n \Delta^n w_\xi \xi_x + \Lambda_\eta^n \Delta^n w_\eta + \Lambda_\zeta^n \Delta^n w_\zeta) + \Delta^n p_\eta \eta_z + \Delta^n p_\zeta \zeta_z = 0 \quad (111)$$

where  $G^n = u^n v_\xi^n \xi_x + v_\eta^n \Lambda_\eta^n + v_\zeta^n \Lambda_\zeta^n$  and  $H^n = u^n w_\xi^n \xi_x + w_\eta^n \Lambda_\eta^n + w_\zeta^n \Lambda_\zeta^n$ . The terms  $\Lambda_\eta$  and  $\Lambda_\zeta$  are defined in Eqs. 83 and 84 (Section 3.4.6). Eqs. 110-111 are first-order time accurate due to the linearization of the equations. For example, casting the nonlinear term,  $u^{n+1} v_x^{n+1}$  into the delta form is not possible unless one the terms is held constant over the time interval. This results in first-order accuracy in time. The linearized, approximate expression, choosing to hold  $u$  fixed over the time interval results in  $u^n \Delta^n v_x$ .

Eq. 110 is rewritten in terms of computational coordinates to yield

$$\frac{G^n}{\rho^n} \Delta^n \rho + \Lambda_\eta^n \Delta^n v_\eta + \frac{\eta_y}{\rho^n} \Delta^n p_\eta = -u^n \xi_x \Delta^n v_\xi - \Lambda_\zeta^n \Delta^n v_\zeta - \frac{\zeta_y}{\rho^n} \Delta^n p_\zeta \quad (112)$$

The right-hand-side terms are lagged to time level  $n - 1$  to first-order temporal accuracy.

$$\frac{G^n}{\rho^n} \Delta^n \rho + \Lambda_\eta^n \Delta^n v_\eta + \frac{\eta_y}{\rho^n} \Delta^n p_\eta = -u^n \xi_x \Delta^{n-1} v_\xi - \Lambda_\zeta^n \Delta^{n-1} v_\zeta - \frac{\zeta_y}{\rho^n} \Delta^{n-1} p_\zeta \equiv R H S_\eta \quad (113)$$

Similar manipulations to Eq. 111 result in

$$\frac{H^n}{\rho^n} \Delta^n \rho + \Lambda_\zeta^n \Delta^n w_\zeta + \frac{\zeta_z}{\rho^n} \Delta^n p_\zeta = -u \xi_x \Delta^{n-1} w_\xi - \Lambda_\eta^n \Delta^{n-1} w_\eta - \frac{\eta_z}{\rho^n} \Delta^{n-1} p_\eta \equiv R H S_\zeta \quad (114)$$

The Wall-2 boundary conditions are now written in matrix form at the wall nodes  $(i, j, k) \in \mathcal{I}^2$ . At  $j = 1$  and  $j = ny$ , the  $y$  momentum equation, Eq. 113, is used, while at  $k = 1$  and  $k = nz$ , the  $z$  momentum equation, Eq. 114, is used.

At  $j = 1$ , Eqs. 106, 107, 108, 109 and 113 are discretized using first-order forward differences and are written in matrix form as

$$\begin{bmatrix} 1 & 0 & 0 & 0 & -\gamma M^2 \\ 0 & 1 & 0 & 0 & 0 \\ 0 & 0 & 1 & 0 & 0 \\ 0 & 0 & 0 & 1 & 0 \\ \frac{G}{\rho} & 0 & -\Lambda^n_\eta & 0 & \frac{-\eta_y}{\rho} \end{bmatrix} \Delta^n U_{i,1,k} + \begin{bmatrix} 0 & 0 & 0 & 0 & 0 \\ 0 & 0 & 0 & 0 & 0 \\ 0 & 0 & 0 & 0 & 0 \\ 0 & 0 & 0 & 0 & 0 \\ 0 & 0 & \Lambda^n_\eta & 0 & \frac{\eta_y}{\rho} \end{bmatrix} \Delta^n U_{i,2,k} = \begin{bmatrix} 0 \\ 0 \\ 0 \\ 0 \\ RHS_\eta \end{bmatrix} \quad (115)$$

Eq. 115 is evaluated over  $2 \leq i \leq nx - 1$  and the set  $\mathcal{R}^4$  (Section 3.4.1). A similar condition holds at the wall nodes at  $j = ny$ . First-order backward finite differences are used to discretize the equations

$$\begin{bmatrix} 1 & 0 & 0 & 0 & -\gamma M^2 \\ 0 & 1 & 0 & 0 & 0 \\ 0 & 0 & 1 & 0 & 0 \\ 0 & 0 & 0 & 1 & 0 \\ \frac{G}{\rho} & 0 & \Lambda^n_\eta & 0 & \frac{\eta_y}{\rho} \end{bmatrix} \Delta^n U_{i,ny,k} + \begin{bmatrix} 0 & 0 & 0 & 0 & 0 \\ 0 & 0 & 0 & 0 & 0 \\ 0 & 0 & 0 & 0 & 0 \\ 0 & 0 & 0 & 0 & 0 \\ 0 & 0 & -\Lambda^n_\eta & 0 & \frac{-\eta_y}{\rho} \end{bmatrix} \Delta^n U_{i,ny-1,k} = \begin{bmatrix} 0 \\ 0 \\ 0 \\ 0 \\ RHS_\eta \end{bmatrix} \quad (116)$$

Eq. 116 is evaluated at  $2 \leq i \leq nx - 1$  and the set  $\mathcal{R}^5$ .

The boundary conditions at  $k = 1$  are discretized using first-order forward differences, resulting in

$$\begin{bmatrix} 1 & 0 & 0 & 0 & -\gamma M^2 \\ 0 & 1 & 0 & 0 & 0 \\ 0 & 0 & 1 & 0 & 0 \\ 0 & 0 & 0 & 1 & 0 \\ \frac{H}{\rho} & 0 & 0 & -\Lambda^n_\zeta & \frac{-\zeta_z}{\rho} \end{bmatrix} \Delta^n U_{i,j,1} + \begin{bmatrix} 0 & 0 & 0 & 0 & 0 \\ 0 & 0 & 0 & 0 & 0 \\ 0 & 0 & 0 & 0 & 0 \\ 0 & 0 & 0 & 0 & 0 \\ 0 & 0 & 0 & \Lambda^n_\zeta & \frac{\zeta_z}{\rho} \end{bmatrix} \Delta^n U_{i,j,2} = \begin{bmatrix} 0 \\ 0 \\ 0 \\ 0 \\ RHS_\zeta \end{bmatrix} \quad (117)$$

Eq. 117 is evaluated at  $2 \leq i \leq nx - 1$  and the set  $\mathcal{R}^6$ . Finally, at  $k = nz$ , first-order backward differences are used to discretize the equations to yield

$$\begin{bmatrix} 1 & 0 & 0 & 0 & -\gamma M^2 \\ 0 & 1 & 0 & 0 & 0 \\ 0 & 0 & 1 & 0 & 0 \\ 0 & 0 & 0 & 1 & 0 \\ \frac{H}{\rho} & 0 & 0 & \Lambda^n \zeta & \frac{\zeta_z}{\rho} \end{bmatrix} \Delta^n U_{i,j,nz} + \begin{bmatrix} 0 & 0 & 0 & 0 & 0 \\ 0 & 0 & 0 & 0 & 0 \\ 0 & 0 & 0 & 0 & 0 \\ 0 & 0 & 0 & 0 & 0 \\ 0 & 0 & 0 & -\Lambda^n \zeta & \frac{-\zeta_z}{\rho} \end{bmatrix} \Delta^n U_{i,j,nz-1} = \begin{bmatrix} 0 \\ 0 \\ 0 \\ 0 \\ RHS_\zeta \end{bmatrix} \quad (118)$$

Eq. 118 is evaluated at  $2 \leq i \leq nx - 1$  and the set  $\mathcal{R}^7$ .

### 3.6 Solution Procedure

The TANS solution procedure is described in this section. The spatial and temporal discretization of the governing equations is discussed in Section 3.6.1. The addition of explicit artificial dissipation to the scheme is discussed in Section 3.6.2. The sweeping strategy for the multiblock grid and the evaluation of explicit terms in the governing equations are discussed in Sections 3.6.3 and 3.6.4, respectively. A modification of the sweeping strategy is described in Section 3.6.5. Finally, the results of a freestream conservation check is presented in Section 3.6.6.

The solution procedure is a Beam-Warming, approximate-factorization scheme. The equations are solved in a nonconservative, implicit manner using either the Euler implicit (EI) scheme, the three-point backward scheme, or the trapezoidal scheme. Details concerning the development and application of the Beam-Warming algorithm are contained in Appendix F.

Temporal accuracy for the inviscid terms is first-order for the EI scheme and second-order for the three-point backward and trapezoidal schemes. The viscous terms are treated explicitly, implying first-order temporal accuracy for these terms.

**3.6.1 Spatial and Temporal Discretization.** Spatial accuracy is increased to fourth-order by replacing the traditional central-difference approximation with the more

accurate compact, or Padé, approximation (Lele, (1990)). The compact scheme approximation for the derivative of a scalar,  $u$ , with respect to  $x$  is given by

$$u_x = \frac{1}{2\Delta x} \left( \frac{\delta_x u}{S_x} \right) + \mathcal{O}(\Delta x^4) \quad (119)$$

where

$$\delta_x u \equiv u_{i+1} - u_{i-1} \quad S_x \equiv 1 + \delta_x^2/6 \quad \delta_x^2 u \equiv u_{i+1} - 2u_i + u_{i-1}$$

$S$ ,  $\delta$  and  $\delta^2$  denote discrete operators, while the subscript refers to the chosen coordinate direction. Section F.1 contains a derivation of the compact scheme approximation. It is of interest to note that for  $S = 1$ , the second-order, central-difference approximation is obtained.

Consistent with the boundary conditions, the scheme is written in the so-called delta form, where the correction,  $\Delta^n U \equiv U^{n+1} - U^n$  is computed at each time level. The superscripts denote time level, where  $n$  denotes the known time level, while  $n + 1$  refers to the unknown level. The general, approximately factored scheme (Appendix F) for the solution  $\Delta^n U$  is given by

$$\mathcal{X}\mathcal{Y}\mathcal{Z}\Delta^n U = \mathcal{R} \quad (120)$$

where

$$\mathcal{X} = \left[ I + \frac{\theta_1 \Delta t}{1 + \theta_2} \frac{\mathcal{A}^{n+1}}{2} \frac{\delta_\xi}{S_\xi} - \omega_i \delta_\xi^2 \right]$$

$$\mathcal{Y} = \left[ I + \frac{\theta_1 \Delta t}{1 + \theta_2} \frac{\mathcal{B}^{n+1}}{2} \frac{\delta_\eta}{S_\eta} - \omega_i \delta_\eta^2 \right]$$

$$\mathcal{Z} = \left[ I + \frac{\theta_1 \Delta t}{1 + \theta_2} \frac{\mathcal{C}^{n+1}}{2} \frac{\delta_\zeta}{S_\zeta} - \omega_i \delta_\zeta^2 \right]$$

and

$$\mathcal{R} = t1 + t2 + t3$$

$$t1 = \frac{\Delta t D^n + \theta_2 \Delta^{n-1} U}{1 + \theta_2}$$

$$t2 = -\omega_e \Delta t (\delta_\xi^4 + \delta_\eta^4 + \delta_\zeta^4) U^n$$

$$t3 = \frac{1}{2} \left[ (\theta_1 \mathcal{A}^{n+1} + (1 - \theta_1) \mathcal{A}^n) \frac{\delta_\xi}{\mathcal{S}_\xi} U^n + (\theta_1 \mathcal{B}^{n+1} + (1 - \theta_1) \mathcal{B}^n) \frac{\delta_\eta}{\mathcal{S}_\eta} U^n + (\theta_1 \mathcal{C}^{n+1} + (1 - \theta_1) \mathcal{C}^n) \frac{\delta_\zeta}{\mathcal{S}_\zeta} U^n \right] \left[ -\frac{\Delta t}{1 + \theta_2} \right]$$

Values of the pair  $(\theta_1, \theta_2)$  are  $(1, 0)$  for the EI scheme,  $(1/2, 0)$  for the trapezoidal scheme, and  $(1, 1/2)$  for the three-point backward scheme.

The  $\mathcal{A}$ ,  $\mathcal{B}$ , and  $\mathcal{C}$  matrices (defined in Section 3.2) are evaluated at time level  $n + 1$  to second-order accuracy to preserve the second-order temporal accuracy with which the inviscid terms are treated (Appendix F.3). The matrices are obtained through extrapolation, resulting in

$$(\mathcal{A}, \mathcal{B}, \mathcal{C})^{n+1} = (\mathcal{A}, \mathcal{B}, \mathcal{C})^n + (\mathcal{A}_t, \mathcal{B}_t, \mathcal{C}_t)^n \Delta t + \mathcal{O}(\Delta t^2) \quad (121)$$

For example,  $\mathcal{A}_t$ , refers to the partial derivative of the matrix,  $\mathcal{A}$ , with time,  $t$ . The elements of  $\mathcal{A}_t$ ,  $\mathcal{B}_t$ , and  $\mathcal{C}_t$  are evaluated to within an error of  $\mathcal{O}(\Delta t)$  since these terms are multiplied by  $\Delta t$  in Eq. 121. The evaluation of the elements of  $\mathcal{A}_t$ ,  $\mathcal{B}_t$ , and  $\mathcal{C}_t$  is straightforward. Nearly all of the elements consist of linear combinations of elements of the solution vector,  $U = (\rho, u, v, w, p)^T$ . Thus, for example,  $\mathcal{A}_{11} = \xi_x u$ , and therefore

$$\mathcal{A}_{t11}^n = \xi_x u_t^n = \xi_x \frac{\Delta^{n-1} u}{\Delta t} + \mathcal{O}(\Delta t)$$

$$\mathcal{A}_{11}^{n+1} = \mathcal{A}_{11}^n + \xi_x \Delta^{n-1} u + \mathcal{O}(\Delta t^2)$$

**3.6.2 Artificial Dissipation.** Explicit dissipation is necessary with the Beam-Warming scheme to suppress high-frequency oscillations in the solution. The damping term is spatially fourth-order in magnitude, allowing for the suppression of noise without formally degrading the spatial accuracy of the solution. The explicit damping coefficient,  $\omega_e$ , is defined above such that the explicit damping term is multiplied by  $\Delta t$ . This is done to insure steady-state consistency, (Desideri et al. (1978)). The damping level used in this study is  $\omega_e = 5/24$ . It was found that damping coefficients lower than  $5/24$  (e.g.,  $\omega_e = 1/8$ )

resulted in numerical instability and solution divergence. Pulliam (1984), suggests that values of  $\omega_e$  of  $\mathcal{O}(1)$  are typical.

The implicit damping coefficient,  $\omega_i$ , is set to zero for this work. Implicit damping is typically used to stabilize a scheme when large time steps are taken. However, for this work, the time-steps are small enough that implicit damping was found to be unnecessary.

**3.6.3 Sweeping Strategy.** The solution is updated in Eq. 125 following the solution of Eqs. 122–124 below, which represents the  $\xi$ ,  $\eta$  and  $\zeta$  sweeps respectively:

$$\left[ (\mathcal{S}_\xi)I + \frac{\theta_1 \Delta t}{1 + \theta_2} \frac{\mathcal{A}^{n+1}}{2} \delta_\xi \right] \Delta^n U_1 = (\mathcal{S}_\xi)(t1 + t3) + t2 \quad (122)$$

$$\left[ (\mathcal{S}_\eta)I + \frac{\theta_1 \Delta t}{1 + \theta_2} \frac{\mathcal{B}^{n+1}}{2} \delta_\eta \right] \Delta^n U_2 = (\mathcal{S}_\eta) \Delta^n U_1 \quad (123)$$

$$\left[ (\mathcal{S}_\zeta)I + \frac{\theta_1 \Delta t}{1 + \theta_2} \frac{\mathcal{C}^{n+1}}{2} \delta_\zeta \right] \Delta^n U = (\mathcal{S}_\zeta) \Delta^n U_2 \quad (124)$$

$$U^{n+1} = U^n + \Delta^n U \quad (125)$$

Note that  $\mathcal{S}_\xi$  is multiplied through Eq. 122 before solving the  $\xi$  sweep, and operates on all of the right-hand side terms except the damping term,  $t2$ . The damping term is excluded for consistency in comparing results to those obtained with the central-difference PAC scheme. Both the TANS and PAC models use the same fourth-order operator to provide numerical damping. If the TANS damping operator were modified by allowing  $\mathcal{S}$  to operate on it, then the damping operators, and the corresponding damping characteristics, would change.

The traditional method of sweeping in the  $\eta$  and  $\zeta$  directions is modified to allow for the presence of a multi-block grid structure (Section 3.1) in the  $\eta - \zeta$  plane. The  $\eta$  sweep is depicted in Figure 17a. Each horizontal line represents a collection of nodes. The algorithm computes  $\Delta^n U_2$  implicitly along each line by solving a  $5 \times 5$  block-tridiagonal system of  $5 \times ny$  equations.  $\Delta^n U_2$  is found along *primary* lines first (with wall boundary conditions imposed at  $j = 1$  and  $j = ny$ ) and then over *secondary* lines. The solid lines in



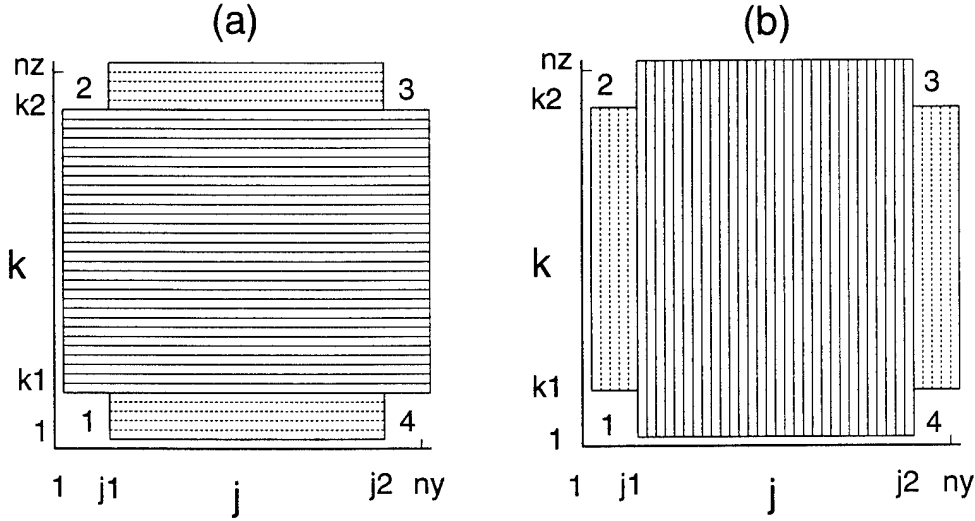


Figure 17. Illustration of sweeping strategy: (a)  $\eta$  sweep (b)  $\zeta$  sweep. Primary lines are solid, while secondary lines are dashed.

the figure are the primary lines and the dashed lines are the secondary lines. The conditions at the boundary nodes of secondary lines ( $j = j1$  and  $j = j2$ ) are found by equating them with the corresponding primary line solutions  $\Delta^n U_2$ , since corresponding nodes along the cuts share the same physical location. Therefore, when the primary lines are solved, so are the boundary nodes of the secondary lines. Thus, Dirichlet boundary conditions are enforced along secondary lines.

The  $\zeta$  sweep is depicted in Figure 17b. The algorithm solves for  $\Delta^n U$  implicitly along each vertical line, each involving the solution of a  $5 \times 5$  block-tridiagonal system of  $5 \times nz$  equations.  $\Delta^n U$  is found along primary lines first (with wall boundary conditions imposed at  $k = 1$  and  $k = nz$ ), and then over secondary lines. The conditions at the boundary nodes of secondary lines ( $k = k1$  and  $k = k2$ ) are known from the primary line solutions, analogous with the  $\eta$  sweep.

**3.6.4 Evaluation of Explicit Right-Hand Side Terms.** Spatial derivatives in  $t3$  are computed implicitly at time level  $n$  to fourth-order spatial accuracy. This can be accomplished in an efficient manner, since the resulting set of equations are tridiagonal.

For example, Eq. 119 is implemented as

$$u_{x,i+1} + 4u_{x,i} + u_{x,i-1} = (3/\Delta x)(u_{i+1} - u_{i-1})$$

Boundary conditions are required to complete the tridiagonal system. At boundaries s1, s2 and s3, second-order accurate, three-point forward/backward differences are used:

$$\begin{aligned}\bar{\delta}_x u_1 &\equiv -3u_1 + 4u_2 - u_3 \\ \underline{\delta}_x u_{nx} &\equiv 3u_{nx} - 4u_{nx-1} + u_{nx-2}\end{aligned}$$

The resulting system for  $u_x$  for becomes

$$\begin{bmatrix} 1 & & & & \\ & \ddots & & & \\ & & 1 & 4 & 1 \\ & & & \ddots & \\ & & & & 1 \end{bmatrix} \begin{bmatrix} u_{x,1} \\ \vdots \\ u_{x,i} \\ \vdots \\ u_{x,nx} \end{bmatrix} = \begin{bmatrix} \bar{\delta}_x u / 2\Delta x \\ \vdots \\ 3\delta_x u / \Delta x \\ \vdots \\ \underline{\delta}_x u / 2\Delta x \end{bmatrix}$$

which represents a constant matrix inversion problem for  $u_{x,i}$  with varying right-hand side terms. When considering solving many such systems along each line of nodes, the most efficient solution procedure is Lower/Upper Decomposition (LUD).

The  $\eta, \zeta$  crossplanes contain four grid cuts, which are treated as boundaries when performing implicit operations. For example, in the calculation of  $u_\eta$  along a secondary line  $k = k^*$ , where  $1 < k^* < k_1$ , the boundaries are at  $j = j_1$  and  $j = j_2$  (Figure 18). An overlapping of the nodes across the cuts is required to promote smooth solutions. At these internal boundaries, fourth-order central approximations are employed for the specification of boundary conditions. The stencil used is

$$u_\eta = (-u_{i,j+2,k} + 8u_{i,j+1,k} - 8u_{i,j-1,k} + u_{i,j-2,k})/12$$

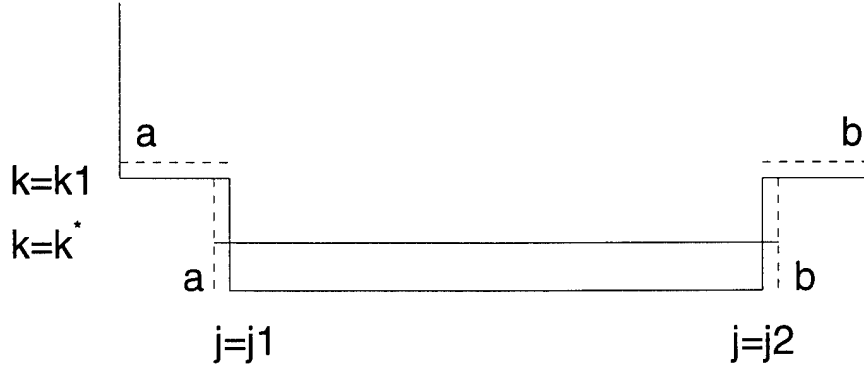


Figure 18. Schematic of computational domain showing treatment of cut boundaries.

which, for the current example at  $j = j1$ , would imply that points lying across the cut would be used as follows

$$u_{\eta} = (-u_{i,j1+2,k} + 8u_{i,j1+1,k} - 8u_{i,k,k1+1} + u_{i,k,k1+2})/12$$

The metrics and viscous terms,  $D$ , are calculated to fourth-order accuracy in the same manner as above. For these quantities, three-point backward conditions are specified at computational boundaries  $s1$ ,  $s2$  and  $s3$ , while the fourth-order approximation is used across the cuts.

**3.6.5 Modification of Sweeping Strategy.** The sweeping strategy discussed earlier was modified slightly to further improve the stability of the algorithm near the cuts. The modification involves overlapping a line of nodes at the cuts when sweeping along secondary lines. For example, in the  $\eta$  sweep along secondary lines between cuts 1 and 4, data from  $k = k1 + 1$  (horizontal dashed lines in Figure 18) is appended to the system consisting of nodes from  $j = j1$  to  $j = j2$ . The extended system solves from  $j = j1 - 1$  to  $j = j2 + 1$ .

Now the solution at the cut nodes depends on information from both sides of the cut. This is consistent with the treatment of the corresponding terms on the right-hand side.

*3.6.6 Freestream Conservation.* The ability of the numerical procedure to conserve a freestream was partially checked by solving for a uniform freestream with Dirichlet (no correction) boundary conditions at  $s_1$ ,  $s_2$  and  $s_3$ . The resulting temporal corrections,  $\Delta^n U$ , were found to be machine zero everywhere for 100 iterations over a wide range of time steps. It is of interest to note that employing a fourth-order-accurate boundary stencil (Lele (1992)) along the physical boundaries  $s_1$ ,  $s_2$  and  $s_3$  of the form

$$u_{\xi,1} + 3u_{\xi,2} = (1/6)(-17u_1 + 9(u_2 + u_3) - u_4)$$

resulted in freestream conservation errors.

### *3.7 Computational Resources and TANS Performance.*

*3.7.1 Computational Resources.* Computations and data visualization are performed on the following machines:

1. *DEC 4620/Alpha AXP Workstation (AFIT/ENY).* This scalar machine hosts both the TANS and PAC codes. As a dedicated machine, the DEC provides wall-clock throughput comparable to a heavily "loaded" Cray Y-MP. Its 380 Mbytes of memory and dual processors allow two "large" jobs (grid G2) to run concurrently.
2. *Cray C-90/161024 (Naval Oceanographic Office, Bay St. Louis, MS).* This 16 processor, vector machine is used to run the TANS code.
3. *Stardent ST-2000 Workstation, (AFIT/ENY).* This machine hosts the AVS graphics software which generates the flowfield visualization discussed in Section 3.8.
4. *DEC 3000/400 Workstation (AFIT/ENY).* This machine also hosts the AVS graphics software, however; its high-performance graphics hardware allows for faster imaging of the flow visualizations.
5. *Convex 220 (AFIT/ENY).* This machine is used to run the TANS code.

6. *Convex 3440 (Flight Dynamics Directorate: WL/FI)*. This machine supplements the DEC 4620 Workstation.
7. *Silicon Graphics IRIS-4D-80GT Workstation (WL/FIGC)*. This Workstation hosts the software package GRIDGEN.

*3.7.2 TANS Performance.* The TANS code consists of two major versions; one version uses second-order central differences while the other employs the fourth-order accurate compact scheme. The fourth-order version also has a vectorized version for use on the vector CRAY machines, and a scalar version for the DEC machine. The difference between the scalar and vector versions is in the data structure associated with the model's block solver. During each sweep, the scalar version treats data along lines of nodes one line at a time, while the vector version allows for solutions over many lines to be simultaneously obtained in a fully vectorized manner.

The performance of the TANS model is shown in Table 3 for the various machines and versions. The Data Processing Index (*DPI*) is defined as the amount of CPU time per iteration per node point. This metric is determined by timing the code on various machines for a given grid, then computing the metric based on the elapsed CPU time, number of time steps, and total number of grid points. The number of iterations used for the data in this study is 50. This number was found to be sufficient to minimize the effect of calculations which are performed only in the first iteration (e.g., reading in the grid and restart files and computing the metrics). *Mflops* is a measure of the number of floating-point operations (in millions) that the processor performs per second. This metric is a function of both the host machine and the code being run. The number of floating point operations per iteration is determined by the *hpm* utility on the Cray C-90. To avoid the uncertainty involved in computing *Mflops* based on both scalar and vector operations, the code is first recompiled to prohibit all optimizations. This typically results in about 1% or less of the operations being vector. The number of (scalar) operations is then recorded for one iteration. *Mflops* is then computed based on the number of floating-point operations per iteration and the CPU time required to compute a known number of iterations. The last column in the table shows the required CPU time to integrate to a nondimensional

time of  $t = 100$ , normalized by the time (40.5 hours) required for the second-order version running on the DEC 4620. The CPU times are computed assuming the baseline grids and associated time-steps for both the second and fourth-order versions of the code. The baseline grids for the second/fourth-order versions are G6/G1 respectively, with associated time steps of 0.03 and 0.04.

Table 3. Performance of the TANS code.

Computer/Version	$DPI$	$Mflops$	CPU ( $t = 100$ )	$\frac{CPU(t=100)}{CPU(DEC4620/2nd)}$
DEC 4620/2nd	1.20E-04	29	40.5 hours	1.000
DEC 4620/4th	2.05E-04	26	23.4 hours	0.577
CRAY YMP/2nd	2.29E-05	153	7.7 hours	0.190
CRAY C90/2nd	1.26E-05	279	4.2 hours	0.103
CRAY C90/4th	2.15E-05	237	2.5 hours	0.062

The required memory for the TANS code using grids G1/G2 is 9.8/18.8 million words.

### 3.8 Visualization.

The degree of difficulty in the visualization of a three-dimensional flowfield depends largely on the complexity of the large-scale flow structure. For example, if the flow is axisymmetric, data visualization is straightforward—only requiring contour plots on a plane that contains the vortex axis. Flow visualization is made more difficult when the flow is asymmetric, since no single plane gives a global description of the flow structure. In this case, one could consider displaying 3-D isosurfaces to help “visualize” the flow. These isosurfaces may prove to be useful if they are not greatly deformed. When isosurfaces are greatly deformed, however, interpretation of the flow becomes more difficult and sub-domains of the flow (such as recirculation regions) can become masked by the display of outer isosurfaces. This is a likely event for swirling flows that breakdown, since one encounters recirculation regions and (in the case of spiral breakdown) regions where the flow has a tendency to wrap around a common axis in a helical pattern.

It is therefore advantageous, for the case of swirling flows, to consider alternative means of flow visualization. Streaklines have been widely used to help visualize unsteady flowfields in experiments. The method chosen for this work utilizes discrete “material

points" that are introduced into the physical domain to create a discretized streakline. The material point positions are computed by integrating the current velocity field in time.

The material point positions are updated using Euler's method. The position of the  $i^{th}$  material point,  $\vec{x}_i$ , is governed by the ODE

$$\frac{d\vec{x}_i}{dt} = \vec{u}(\vec{x}_i, t) \quad (126)$$

where  $\vec{u} = (u, v, w)^T$  is the known velocity field. The ODE is integrated to first-order accuracy in time to advance the material point position

$$\vec{x}_i(t + \Delta t) \cong \vec{x}_i(t) + \vec{u}(\vec{x}_i(t), t)\Delta t \quad (127)$$

The velocity vector at the material point position,  $\vec{u}(\vec{x}_i(t), t)$ , is approximated to second-order spatial accuracy with the following Taylor series expansion

$$\vec{u}(\vec{x}_i) = \vec{u}_{\text{node}} + (\nabla \vec{u})_{\text{node}} \cdot (\vec{x}_i - \vec{x}_{\text{node}}) \quad (128)$$

where  $\vec{x}_{\text{node}}$  is the position of the node closest to the material point,  $\vec{u}_{\text{node}}$  is the velocity vector at the node, and  $(\nabla \vec{u})_{\text{node}}$  is the gradient of the velocity field at the node.  $(\nabla \vec{u})_{\text{node}}$  is approximated to second-order accuracy through central difference expressions.

The flow visualization method consists of two steps. In step 1 all the material point positions are computed every  $K^{th}$  iteration and stored in a file at the end of the run. Thus, the reader should note that the material point positions are computed as the TANS model executes. In step 2 the AVS software reads the file containing the material point positions. AVS then displays spheres on the workstation screen using the material point positions as the centroids of the spheres. A new set of spheres are displayed every  $K^{th}$  time step to create a dynamic flow visualization. The advantage of this two-step approach is that the dynamic display of the material points on the screen is much faster once the time integration computations are completed. In addition, step 2 can be performed on a remote system, separate from the system used to perform the time integration. The disadvantage

is that one must wait until the end of the time integration run to visualize the discrete streakline.

### 3.9 Recorded Data.

In addition to the material point visualization, several scalar quantities are saved every  $m^{th}$  iteration, where  $m$  is user specified. The first is the minimum axial velocity,  $Q$ , over all nodes. The second scalar is the maximum change in the solution vector,  $U$ , denoted  $\Delta^n U_{\max}$ . This global maximum is computed considering all five components of  $U$  and by considering all nodes. The remaining recorded data consists of the time histories of the velocity components  $(u, v, w)^T$  for a fixed centerline node, and the axial velocity along centerline nodes,  $u_c(x)$ , at the end of each run.

**3.9.1 Calculation of  $Q$ .** The quantity  $Q$  is defined by

$$Q \equiv \min_{i,j,k} [u_{i,j,k}] \quad (129)$$

**3.9.2 Calculation of  $\Delta^n U_{\max}$ .** The quantity  $\Delta^n U_{\max}$  is the maximum change in the solution vector over one iteration, and is defined by

$$\Delta^n U_{\max} \equiv \Delta^n (\rho, u, v, w, \gamma M^2 p)^T_{\max} \quad (130)$$

$$\equiv \max_{i,j,k} [\Delta^n \rho_{i,j,k}, \Delta^n u_{i,j,k}, \Delta^n v_{i,j,k}, \Delta^n w_{i,j,k}, \gamma M^2 \Delta^n p_{i,j,k}]^T \quad (131)$$

**3.9.3 Calculation of  $u_s$ ,  $v_s$ , and  $w_s$ .** The quantities  $u_s$ ,  $v_s$  and  $w_s$  are the velocity components at a fixed centerline node, and are defined by

$$u_s \equiv u(7, 0, 0) \quad (132)$$

$$v_s \equiv v(7, 0, 0) \quad (133)$$

$$w_s \equiv w(7, 0, 0) \quad (134)$$

The location  $x = 7$  is selected as a reasonable location, aft of the tube constriction, to expect flow disturbances to occur. Other locations along the centerline were not examined.



3.9.4 *Calculation of  $u_c(x)$ .* The centerline axial velocity  $u_c(x)$  is recorded at the end of each time-integration run and is defined by

$$u_c(x) \equiv u(x, 0, 0) \quad (0 \leq x \leq L) \quad (135)$$

3.10 *Definition of the  $L_2$  Norm.*

The  $L_2$  norm is used throughout this report to quantify results. The  $L_2$  norm of a vector  $\underline{x}$  consisting of  $n$  elements is given by:

$$L_2 \equiv \left[ \frac{1}{n} \sum_{i=1}^n x_i^2 \right]^{1/2} \quad (136)$$

#### *IV. Grid Requirements & Validation*

Baseline grid requirements and validation of the TANS model are outlined in this chapter.

In Section 4.1, node spacing and domain sizes are varied. Node spacings are varied to determine the value of the node spacings that, upon further reduction, have negligible impact on the solution. Solutions with such node spacings are said to be grid independent. The location of the outflow boundary is determined such that an increase in tube length has a negligible impact on the solutions. Finally, the influence of tube radius on the resulting solutions is discussed. It is found that solutions are sensitive to tube radius between  $R_0 = 2$  and  $R_0 = 3$ . However, it is demonstrated that solutions at  $R_0 = 2$  and low Mach number agree well with the incompressible results of Beran and Culick (1992).

Comparisons between PAC and TANS solutions are presented in Section 4.2. The results show that when the vortex strength is sufficiently small, steady, axisymmetric solutions are admitted by the TANS model, even in the presence of an asymmetric crossplane grid structure. The resulting steady, axisymmetric solutions produced by the TANS model agrees with the PAC solutions to a very high degree of accuracy. This ability to produce steady, axisymmetric TANS solutions is important, since it allows for the possibility of studying the genesis of three-dimensional behavior.

##### *4.1 Grid Requirements*

Grid requirements are primarily assessed with the second-order accurate, central-difference formulation of the TANS model. Using the second-order model provides a conservative assessment of the necessary node spacings, as well as a means of comparing the improved accuracy of the fourth-order model. However, it is found necessary to employ the compact scheme, with fourth-order spatial accuracy, to demonstrate convergence in solutions as the average radial node spacing is decreased.

The effects of axial node spacing, tube length, and radial node spacing for the second-order model are discussed in Sections 4.1.1–4.1.3 respectively. The effects of radial node spacing using the fourth-order compact scheme are discussed in Section 4.1.4, while the

Table 4. Run matrix for grid resolution study.

Run No.	$Re$	$\mathcal{V}$	$M$	$\Delta t$	$\alpha$	BC Type	Grid	Accuracy (Time/Space)
1	100	1.80	0.3	.030	0.00	1	G7	1st/2nd
2	100	1.80	0.3	.030	0.00	1	G8	1st/2nd
3	100	1.80	0.3	.030	0.00	1	G9	1st/2nd
4	100	1.80	0.3	.030	0.00	1	G10	1st/2nd
5	100	1.80	0.3	.030	0.00	1	G11	1st/2nd
6	100	1.80	0.3	.030	0.00	1	G12	1st/2nd
7	100	1.80	0.3	.030	0.00	1	G13	1st/2nd
8	100	1.80	0.3	.040	0.00	1	G1	2nd/4th
9	100	1.80	0.3	.025	0.00	1	G6	2nd/4th

effects of tube radius are discussed in Section 4.1.5. A discussion on the grid requirements for the PAC model is given in Section 4.1.6, while Section 4.1.7 provides a summary of the results of Section 4.1.

A summary of the model parameters for each run performed in this section is contained in Table 4. The vortex strength,  $\mathcal{V}$ , is set to 1.8 so that a bubble breakdown would develop, ensuring that the grid refinement is assessed for a flowfield representative of the flows of interest. The baseline grid established in this section is determined based on a relatively low  $Re$  of 100. Results at higher  $Re$ , presented in Chapter V, include the effects of further grid resolution and tube length.

The boundary conditions utilized are Inflow-1 and Wall-1, with  $\alpha = 0$ . These conditions are referred to as Type 1 boundary conditions. Specification of Type 2 conditions (Inflow-2 and Wall-2) can lead to unsteady solutions for  $\mathcal{V} = 1.8$ , even at Reynolds numbers as low as 100. Thus, for purposes of determining the necessary grid resolutions, the Type 1 conditions are employed. Determining adequate grid resolution based on unsteady flow data would be problematic, since temporal and spatial errors could not be systematically separated and analyzed.

For each run, Euler implicit time integration is performed until a convergence criterion of  $(\Delta^n U)_{\max} < 10^{-6} \Delta t$  is satisfied.

*4.1.1 Effects of Axial Node Spacing.* The effect of axial node spacing are presented by comparing the converged values of axial velocity along the tube centerline,  $u_c$ ,

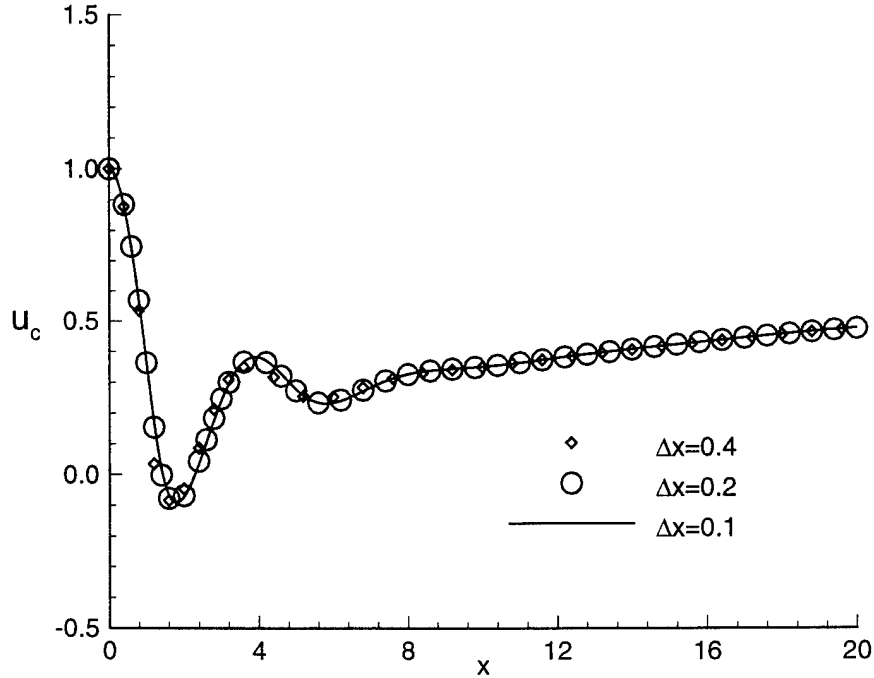


Figure 19. Effect of axial node spacing on centerline axial velocity for  $\mathcal{V}=1.8$ ,  $Re=100$  and  $M=0.3$ .

for Runs 1–3. Grids G7, G8, and G9 are used, which have 51, 101, and 201 axial nodes respectively, yielding axial node spacings,  $\Delta x$ , of 0.4, 0.2, and 0.1 respectively. The tube length, tube radius, and number of crossplane nodes are held fixed at  $L = 20$ ,  $R_0 = 2$ , and  $n_y = n_z = 61$ . Results are shown in Figure 19. It is observed that profiles of  $u_c$  for  $\Delta x = 0.2$  and 0.1 are nearly identical. At  $\Delta x = 0.4$ , the data appears to capture the first minimum value in the breakdown region ( $x \approx 2$ ) very well. Downstream ( $x \approx 4$ ), however, the axial velocity does not recover fully to that of the finer-grid solutions. For  $x > 7$ , all three solutions agree quite well. Based on these results, an axial node spacing of 0.2 is found to be sufficient to provide grid independence with respect to  $\Delta x$ .

The  $L_2$  norm (Section 3.10) of the difference in  $u_c$  between  $\Delta x = 0.4$  and 0.2 is  $2.0\text{E-}02$ . The  $L_2$  norm of the difference in  $u_c$  between  $\Delta x = 0.2$  and 0.1 is  $3.9\text{E-}03$ .

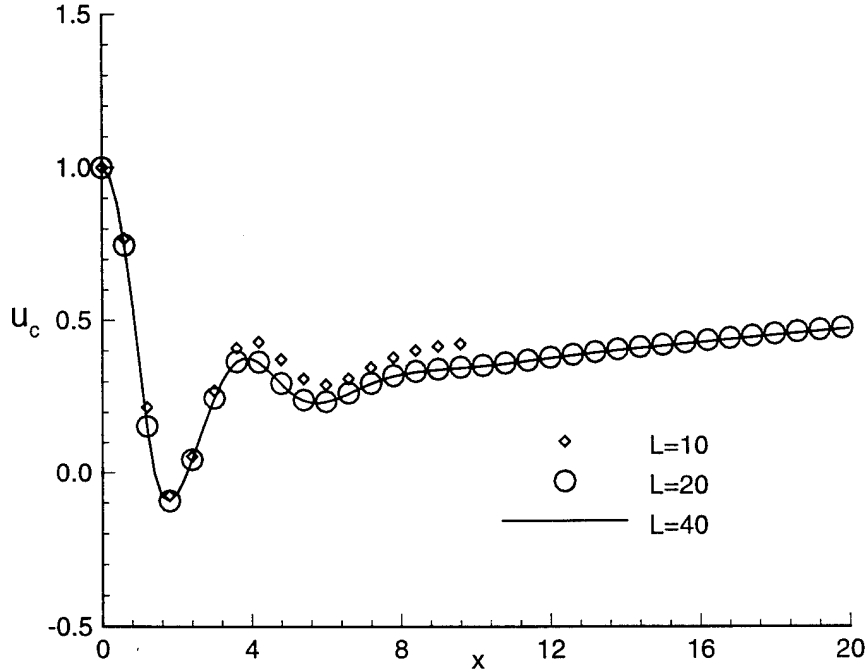


Figure 20. Effect of domain length on centerline axial velocity for  $\mathcal{V}=1.8$ ,  $Re=100$  and  $M=0.3$ .

*4.1.2 Effects of Tube Length.* Next, the tube length,  $L$ , is varied for  $R_0 = 2$ , and  $ny = nz = 61$ . The tube lengths considered are  $L=10, 20$ , and  $40$ , corresponding to grids G10, G8, and G11 respectively. Figure 20 shows the centerline axial velocity,  $u_c$ , for Runs 4, 2, and 5. When the tube length is 10, the axial velocity compares well with the solutions for the longer tubes near the breakdown region,  $x \approx 2$ . However, past  $x \approx 4$ ,  $u_c$  is significantly larger than that computed in the longer tubes. The solutions for tube lengths of 20 and 40 are shown to be in excellent agreement, with only a very slight variation in value past  $x = 10$ . From these results, and for this relatively low  $Re$  of 100, tube lengths greater than 20 provide a negligible improvement in accuracy. Therefore,  $L = 20$  is selected for the baseline grid.

The  $L_2$  norm of the difference in  $u_c$  between  $L = 10$  and  $L = 20$  is  $5.5E-02$ . The  $L_2$  norm of the difference in  $u_c$  between  $L = 20$  and  $L = 40$  is  $3.1E-03$ .

Another means of determining the necessary tube length comes from considering the outflow criticality. The concept of criticality is discussed in Section 2.1.1. If it can be shown that the outflow is supercritical, then by definition, disturbances at the outflow boundary are not capable of propagating upstream. This implies that any condition imposed at a supercritical outflow boundary should not impact the solution upstream. Thus, a suitable means of determining the outflow location would be to compute the flow criticality at each axial station to determine the location at which the flow transitions from subcritical flow (in the breakdown region) to supercritical flow aft of breakdown. This location could then be used as the outflow boundary.

One problem with this tailored approach of determining outflow location is that Benjamin's (1962) analysis for computing criticality is limited to axisymmetric, inviscid flows. Thus, three-dimensional flows and flows where  $Re$  is not sufficiently large are inconsistent with the analysis.

It should be noted that imposing the QC equations as an outflow boundary condition does not allow complete freedom in choosing an outflow location. Even though QC flows are necessarily supercritical, imposing QC conditions locally in a flow does not imply that the actual flow would have been supercritical at the outflow boundary. Furthermore, a supercritical outflow boundary implies that only axisymmetric disturbances cannot propagate upstream. Three-dimensional disturbances are still capable of upstream propagation in supercritical flows.

Given the lack of suitable methods to compute flow criticality for 3-D, viscous flows, and the uncertainty involved in specifying QC outflow conditions, numerical experimentation, as represented in Figure 20, remains a robust, simple method to determine the necessary tube length.

*4.1.3 Effects of Radial Node Spacing: Second-Order Accuracy.* Node spacing requirements in the crossplane are now considered. For  $L = 20$ ,  $R_0 = 2$  and  $nx = 101$ ,  $ny$  and  $nz$  are set to 41, 61 and 81, corresponding to grids G12, G8 and G13. Assuming nearly constant spacing, this corresponds to average radial step sizes,  $\Delta r$ , of  $1/10$ ,  $1/15$ , and  $1/20$ . Figure 21 shows the centerline axial velocities,  $u_c$ , for Runs 6, 2, and 7. The

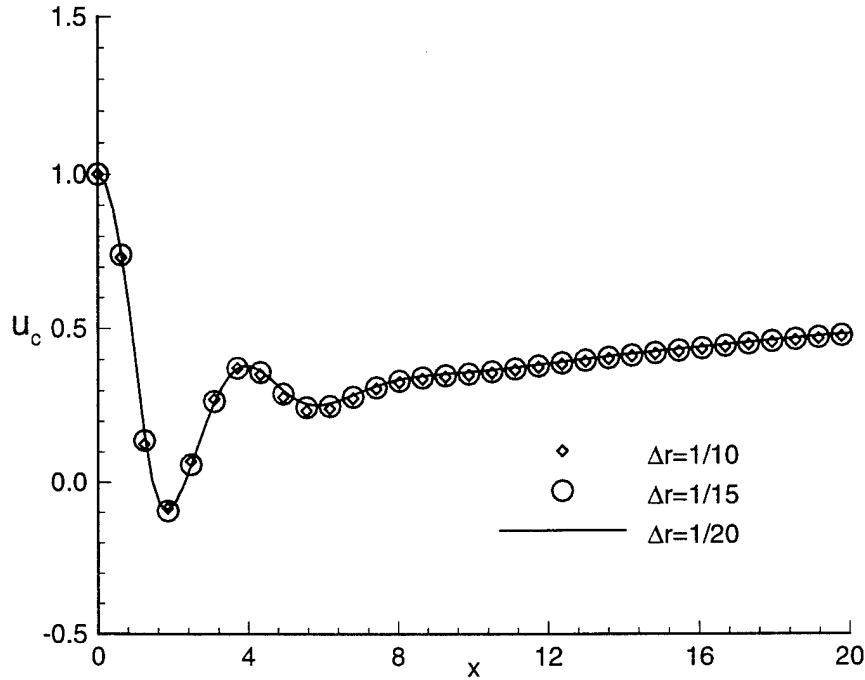


Figure 21. Effect of crossplane node spacing on centerline axial velocity for  $V = 1.8$ ,  $Re = 100$  and  $M = 0.3$ .

axial velocities are relatively insensitive to crossplane node spacing everywhere except in the region aft of the breakdown bubble.

An average radial node spacing of  $1/15$  is chosen, since it is apparent that only a minimal increase in accuracy occurs upon further refinement. However, in a strict sense, this spacing cannot be considered adequate in demonstrating grid independence. Further reductions in  $\Delta r$  are not considered, since simultaneously increasing  $n_y$  and  $n_z$  has a substantially larger impact on the computational work than does increasing  $n_x$ . This is true because two coordinate directions are involved when decreasing  $\Delta r$ , instead of one when decreasing  $\Delta x$ . Thus, choosing  $\Delta r = 1/15$  represents a compromise between solution accuracy and computational efficiency.

*4.1.4 Effects of Radial Node Spacing: Fourth-Order Accuracy.* In Section 4.1.3, an average radial node spacing of  $\Delta r = 1/15$  is chosen, even though the results showed some sensitivity to radial spacing at that value. In this section, the effect of the average radial spacing is reevaluated using the fourth-order version of the TANS model. Figure 22 shows the effect of crossplane node spacing for Runs 8 and 9 using the fourth-order scheme. Average radial spacings of  $1/10$  and  $1/15$ , corresponding to grids G1 and G6, are considered. The figure illustrates that the two grids yield nearly identical results, implying that  $\Delta r = 1/10$  is sufficient for grid independence. This is an improvement over the second-order accurate, central-difference scheme, where grid independence was not strictly achieved, even for  $\Delta r = 1/15$ .

The improvement in spatial accuracy is also evidenced by computing the  $L_2$  norms of the differences in  $u_c$ . The  $L_2$  norm of the difference in  $u_c$  between  $\Delta r = 1/15$  and  $1/20$  for the second-order model is  $7.2\text{E-}03$ . The  $L_2$  norm of the difference in  $u_c$  between  $\Delta r = 1/10$  and  $1/15$  is  $1.2\text{E-}03$ . Thus, greater accuracy can be achieved on coarser node spacings.

*4.1.5 Effects of Tube Radius.* An assessment of the effect of tube radius on centerline axial velocity using the Type 1 conditions is not performed. This is due to the author's belief that such an evaluation should incorporate the details of the tube wall geometry. That is, the Type 2 conditions ( $\alpha = 0$ ) should be used in this case, since these conditions are used throughout the remainder of the study. This was not an issue when considering the tube length, since the outflow boundary conditions are the same for Type 1 and Type 2.

The effect of the outer wall location has been assessed in other studies and it was found that  $R_0 = 2$  is sufficient. The analysis of Beran and Culick (1992) showed virtually no difference in minimum centerline axial velocity for  $R_0 = 2$  and  $R_0 = 3$  for  $Re$  between 250 and 2000 and for  $\alpha = 0.05$ . Salas and Kuruvila (1989) looked at vorticity profiles at a particular axial station of a straight tube for  $R_0 = 2$  and  $R_0 = 4$  and found the two profiles to be nearly identical for  $Re = 400$ .

The PAC model, however, using Type 2 boundary conditions, produces results which show some sensitivity to wall position. In particular, as  $R_0$  is increased from 2 to 3 (for



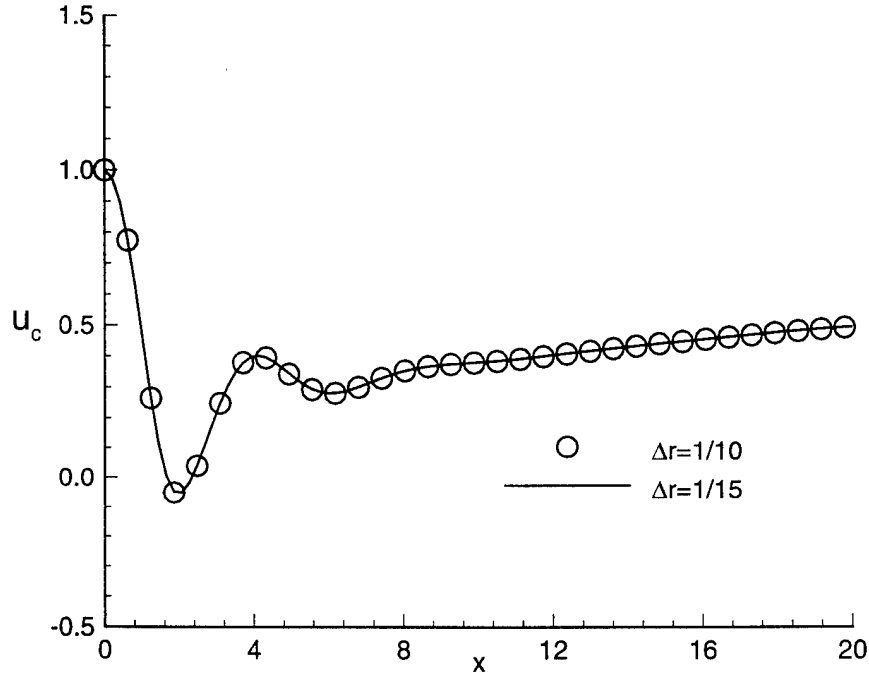


Figure 22. Effect of crossplane node spacing on centerline axial velocity for  $\mathcal{V} = 1.8$ ,  $Re = 100$ , and  $M = 0.3$  using the fourth-order compact scheme.

$M = 0.3$  and  $Re = 250$ ) the vortex strength corresponding to the first appearance of reversed flow moves from about  $\mathcal{V} = 1.55$  to  $\mathcal{V} = 1.3$ . However, the qualitative behavior of  $Q$  as  $\mathcal{V}$  is increased is similar; the primary effect of larger  $R_0$  is the shifting of the curve  $Q(\mathcal{V})$  laterally towards smaller  $\mathcal{V}$ . Similar trends in solution behavior were observed at  $M = 0.1$  for  $R_0 = 3$ .

To investigate the accuracy of the PAC results for  $R_0 = 2$ , incompressible results from Beran and Culick (1992) are used to compare against data from the PAC model for a low Mach number of 0.1 and  $R_0 = 2$ . The comparison as shown in Figure 23 is very favorable, with breakdown points ( $Q = 0$ ) of  $\mathcal{V} = 1.49$  and  $\mathcal{V} = 1.506$  for the published results and PAC model respectively. Below Mach numbers of 0.1, the PAC model yields spurious solutions. The effect of increasing Mach number from 0.1 to 0.3 with the PAC model moves the breakdown point from  $\mathcal{V} = 1.506$  to  $\mathcal{V} = 1.55$  (Figure 23). The preceding

comparison strongly suggests that the PAC model yields accurate results for  $R_0 = 2$ . The general trend in solution paths for  $R_0 = 2$  as Mach number is reduced shows convergence to the incompressible solution path.

The difference in solutions between  $R_0 = 2$  and  $R_0 = 3$  is most likely due to a decrease in vortex core pressure at the inflow plane as the wall location increases. The lower core pressures result from the necessity that pressure approximately satisfy the QC form of the radial momentum equation in the presence of a constant wall pressure. The lower pressures near the centerline appear to coincide with larger axial pressure gradients, which provides the physical mechanism to allow breakdown at smaller vortex strengths.

Thus, to decrease the solution sensitivity to changing  $R_0$ , it is necessary to allow the reference pressure to change as  $R_0$  is increased. This could be handled by specifying reservoir conditions, and by assuming that isentropic flow prevails such that the inlet/wall juncture maintains a constant total pressure. Then the reference pressure changes with  $R_0$ , through isentropic relations, as the local Mach number changes. Increasing  $R_0$  would then result in a decrease in the local Mach number and an increase in the static pressure at the reference point. This behavior is necessary in providing a nearly equivalent inlet pressure profile with changing  $R_0$ .

*4.1.6 Grid Requirements for PAC Model.* Grid requirements for the PAC model differ from the TANS model since the PAC code uses second-order, central-difference operators. The higher accuracy levels of the compact scheme can result in differences between the 2-D and 3-D solutions when the node spacings do not produce grid independence in each algorithm. Therefore, the average radial spacing for the PAC model should be comparable to the average radial spacing for the TANS model using central differences. This radial spacing is about  $1/15$ , which is approximately achieved using 32 radial nodes over a tube radius of 2.

The blocking strategy used by the PAC model requires that the total number of nodes multiplied by five must be evenly divisible by 16 (Beran (1995)). While 101 axial nodes and 32 radial nodes meets this requirement, earlier work considered the use of 24 radial nodes, which fails the requirement. The adopted number of axial nodes used in this

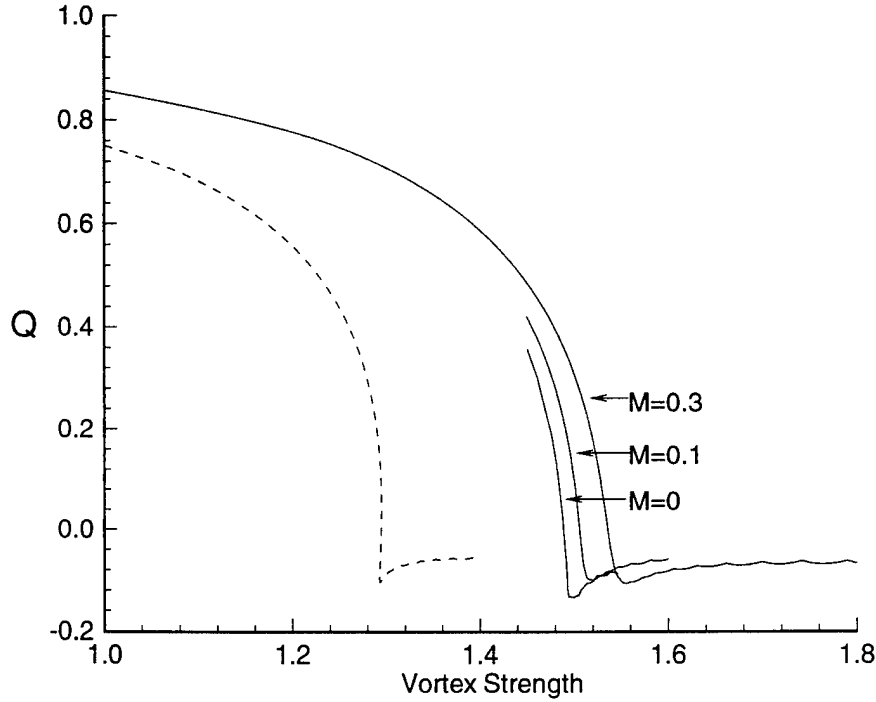


Figure 23. Comparison of 2-D Solution Paths between PAC model ( $M > 0$ ) and model used by Beran and Culick (1992) ( $M = 0$ ) for  $Re = 250$ . Solid lines represent data for  $R_0 = 2$  and the dashed line represents the PAC model result for  $M = 0.3$  and  $R_0 = 3$ .

study is 98 instead of 101, since the combination of 24 radial nodes and 98 axial nodes meets the above requirement. This is why the distinction is made, for example, between grids G1 and G12, and G6 and G8. Practically speaking, these grids should yield nearly equivalent results, but they are distinguished to provide an accurate account of the grid evaluation process.

In summary, the baseline grid for the PAC model consists of 98 axial nodes and 32 radial nodes for  $R_0 = 2$  and  $L = 20$ . This grid is designated g1. 2-D grid parameters are summarized in Table 5.  $nr$  is defined as the number of nodes in the radial direction.

2-D grids with  $nr = 32$  are used to generate initial conditions for 3-D grids with  $ny = nz = 41$ . Similarly, 2-D grids with  $nr = 48$  are generally used to generate initial

Table 5. 2-D grid parameters.

Grid	$nx$	$nr$	$L$	$\Delta x_0$	$\beta$	$x_2$
g1	98	32	20	.206	0.0	-
g2	122	48	20	.200	.25	10
g3	172	48	30	.200	.25	10
g4	222	48	40	.200	.25	10

conditions for 3-D grids with  $ny = nz = 61$ . The 3-D grids are constructed such that they share the same axial node locations as the 2-D grid from which the initial conditions are generated. This was done to simplify the 2-D/3-D interpolation process described in Appendix B.3.

*4.1.7 Summary of Grid Requirements.* In summary, the required grid ( $nx \times ny \times nz$ ) using central differences is at least  $101 \times 61 \times 61$  for a tube length of 20 and a radius of 2. This grid is designated G8. As shown in Section 4.1.4, this requirement can be reduced using the compact scheme to  $101 \times 41 \times 41$ . For compatibility with the PAC model (Section 4.1.6),  $nx$  is reduced slightly from 101 to 98. Therefore, the baseline grid for the fourth-order compact scheme is  $98 \times 41 \times 41$ , and is designated G1 in Section 3.1. The baseline grid for the central-difference scheme is  $98 \times 61 \times 61$ , and is designated as grid G6. In evaluating the compact scheme, no attempt was made to increase the axial node spacing, anticipating a requirement for smaller spacings at higher Reynolds numbers.

## 4.2 Validation

The validation process of the TANS model proceeded along two lines. First, the model is used to solve a variety of model problems. These model problems include the incompressible and compressible flows over a flat plate, unsteady Couette flow and unsteady heat conduction. The comparisons between the model output and the known solutions to the model problems are contained in Appendix D. Second, the TANS and PAC models are cross-validated for flow conditions that lead to steady, axisymmetric solutions of the TANS model.

It is shown in Chapter V that for  $Re = 100$ , steady and axisymmetric solutions are admitted by the TANS model when the vortex strength is at or below  $\mathcal{V} = 1.7$ . Under

Table 6. Summary of TANS run parameters for validation.

Run No.	$Re$	$\mathcal{V}$	$M$	$\Delta t$	$\alpha$	BC Type	Grid	Accuracy (Time/Space)
10	100	1.00	0.3	.030	0.05	2	G6	1st/2nd
11	100	1.70	0.3	.030	0.05	2	G6	1st/2nd

these conditions, solutions to the PAC and TANS models should match with a high degree of accuracy when computed with identical parameter values. Runs 10 and 11, summarized in Table 6, are computed to demonstrate that when the vortex strength is sufficiently small, the TANS and PAC models yield apparently identical steady and axisymmetric solutions, even in the presence of an asymmetric grid structure. Runs 10 and 11 are computed with the second-order spatially accurate version of TANS. Section 5.2 shows that similar agreement between the PAC and TANS models exist when the fourth-order model is utilized.

Initial conditions for Runs 10 and 11 are obtained from the PAC model solutions for  $\mathcal{V} = 1.0$  and  $1.7$  respectively. Cubic spline interpolation is used (Section B.3) to generate these initial conditions from the PAC solutions. Time integration is carried out by the TANS model until a steady-state convergence criterion of  $(\Delta^n U)_{\max} < 10^{-6} \Delta t$  is met.

Figure 24 shows the comparison between the TANS and PAC models for  $\mathcal{V} = 1.0$ . The two solutions yield a good match in all of the primitive variables. The value of  $(\Delta^n U)_{\max}$  at  $t = 0$  was quite small, approximately  $10^{-3}$ , indicating that the initial solution was indeed very close to the final solution of the TANS model. Results for  $\mathcal{V} = 1.7$  are shown in Figure 25. This vortex strength is near the point at which reversed flow occurs for  $M = 0.3$  and  $Re = 100$ . The comparison between the two solutions is good here as well.

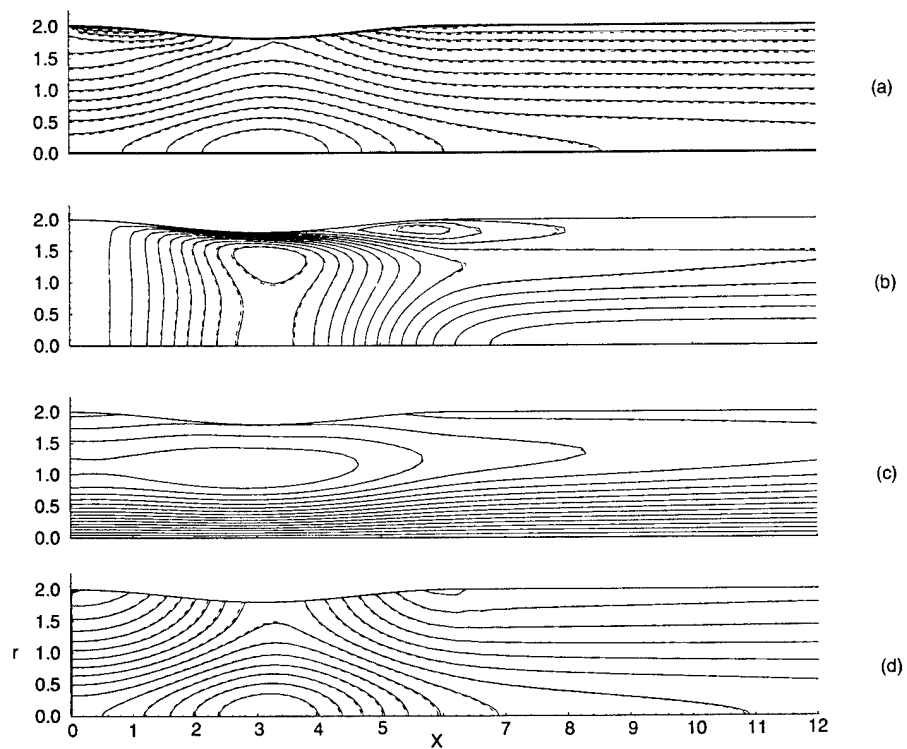


Figure 24. Comparison between TANS and PAC solutions for  $V=1.0$  (PAC model: dashed lines; TANS model: solid lines). Numbers in parenthesis indicate contour range: (a) density (0.907858,1.02033), (b) axial velocity (0.898258,1.30267), (c) crossplane velocity (0.0420968,0.631453), (d) pressure (7.28086,8.10293).

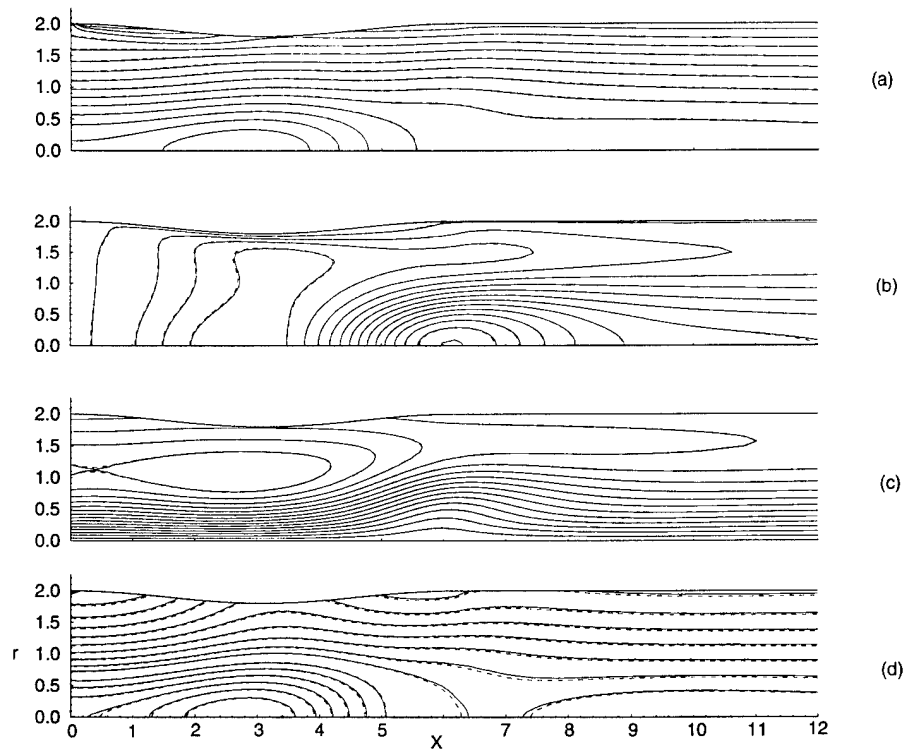


Figure 25. Comparison between TANS and PAC solutions for  $V=1.7$  (PAC model: dashed lines; TANS model: solid lines). Numbers in parenthesis indicate contour range: (a) density (0.791321,1.0409), (b) axial velocity (0.082124,1.38003), (c) crossplane velocity (0.0719934,1.0799), (d) pressure (6.58968,8.28171).

## V. Results.

The results presented in this chapter are divided into four sections; each section represents results at a different Reynolds number. Reynolds numbers of 100, 250, 500 and 1000 are considered in Sections 5.2 – 5.4 respectively. All results presented in this chapter are derived from the fourth-order spatially accurate version of the TANS model. Furthermore, three-point backward time integration is used in all runs to achieve second-order spatial accuracy of the inviscid terms. Viscous terms are treated explicitly, resulting in first-order temporal accuracy for these terms.

Runs at  $Re = 100$  are included for validation purposes, and to provide preliminary evidence of flow behavior.

Reynolds numbers of 250 and 500 are considered based on results of Beran and Culick (1992), who show that unique 2-D solutions exist at  $Re = 250$ , while a region of nonunique solutions exist at  $Re = 500$ . Similar results are found in this work. However, the region of nonunique solutions at  $Re = 500$  is very small, and therefore, only a limited examination is done at this Reynolds number. The region of nonuniqueness is greater at  $Re = 1000$ , and therefore this value of  $Re$  is chosen for examining time-asymptotic 3-D solutions in the presence of nonunique 2-D solutions.

### 5.1 Results for $Re = 100$ .

Four runs are presented at  $Re = 100$ . For each run, a distinct value of the vortex strength ( $\mathcal{V} = 1.0, 1.5, 1.7$ , and  $1.8$ ) is specified. A summary of run parameters for  $Re = 100$  is contained in Table 7.

Table 7. Summary of TANS run parameters for  $Re = 100$ .

Run No.	$Re$	$\mathcal{V}$	$M$	$\Delta t$	$\alpha$	BC	Grid	Accuracy (Time/Space)
12	100	1.00	0.3	.040	0.05	2	G1	2nd/4th
13	100	1.50	0.3	.040	0.05	2	G1	2nd/4th
14	100	1.70	0.3	.040	0.05	2	G1	2nd/4th
15	100	1.80	0.3	.040	0.05	2	G1	2nd/4th



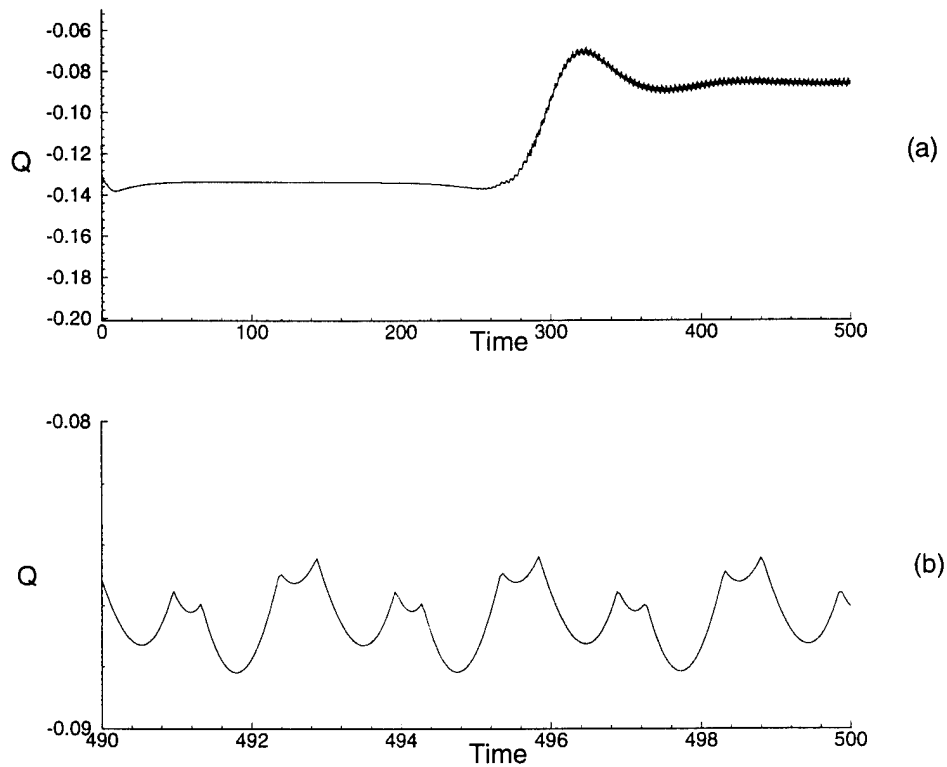


Figure 26.  $Q$  versus time for  $V=1.8$ : (a) global view, (b) magnified view near end of run.

Runs 12–14 ( $V = 1.0 - 1.7$ ) result in steady solutions which agree to a high degree of accuracy with the initial 2-D solutions obtained by the PAC model. Thus, the initially steady initial condition does not evolve in time to an asymmetric flow, even in the presence of an asymmetric grid structure. In Run 15 ( $V = 1.8$ ) the initially steady solution evolves into a periodic solution. Figure 26a shows a plot of  $Q$ , the minimum axial velocity (Section 3.9), as a function of time. Figure 26b shows a magnified view of the data near the end of the run, where the periodic nature of the solution is evident.

The unsmooth nature of the data, evident in Figure 26b, is believed by the author to be due to the fact that  $Q$  is not evaluated at a fixed point. Instead, the node where  $Q$  occurs can move about as the solution evolves in time, resulting in the unsmooth behavior in  $Q$ .

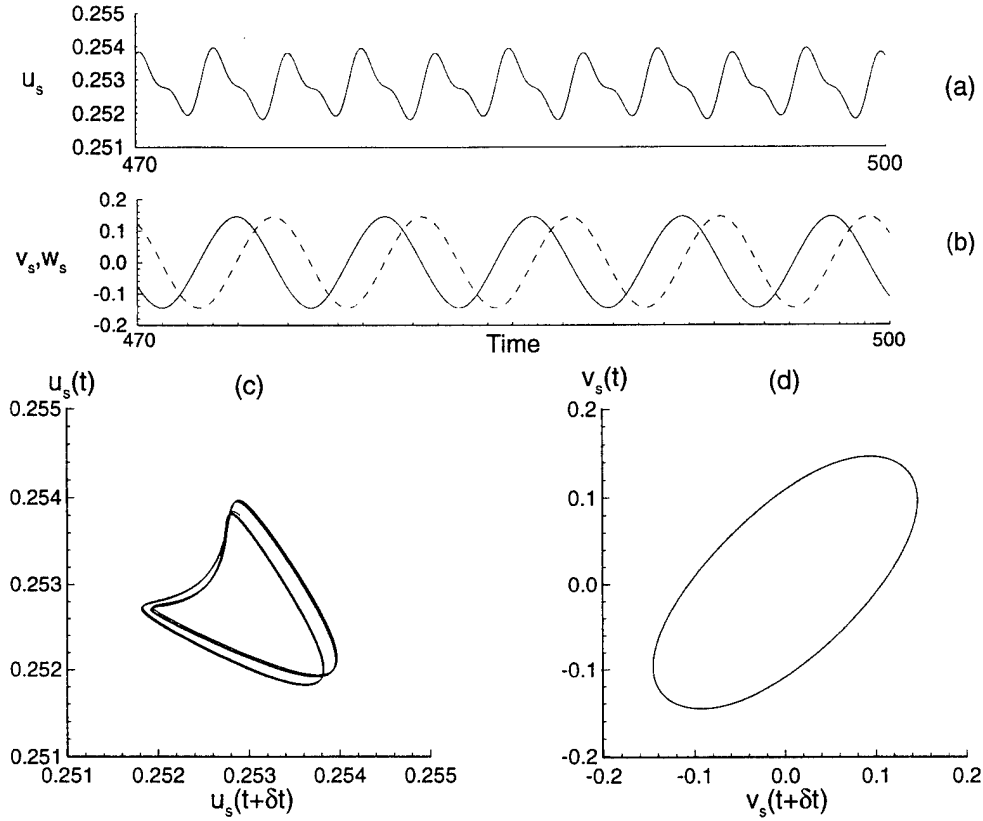


Figure 27. Evidence of periodic flow for  $\mathcal{V} = 1.8$  and  $Re = 100$ : (a)  $u_s(t)$ , (b)  $v_s(t)$ ; solid,  $w_s(t)$ ; dashed, (c) phase plot of  $u_s$ , (d) phase plot of  $v_s$ .

To better examine the smooth, periodic nature of the flow, the velocity components  $u_s$ ,  $v_s$ , and  $w_s$ , are plotted versus time in Figure 27a-b. These quantities, described in Section 3.9, are evaluated at a fixed centerline location of  $x = 7$ . The figures show that the solutions are smooth, and apparently periodic in nature.

Periodicity is better illustrated with phase plots; generated by plotting the functions  $u_s$ ,  $v_s$ , or  $w_s$ , at time  $t$  versus the same function at a later time  $t + \delta t$ . If a function is periodic, the phase plot will depict a closed path if more than one period of the data is included. The value of  $\delta t$  used here is 0.8. Phase plots of  $u_s$  and  $v_s$  are shown in Figures 27c-d, where the periodic nature of the flow is evident. The data represented in Figures 27c-d is from  $t = 470$  to  $t = 500$ .

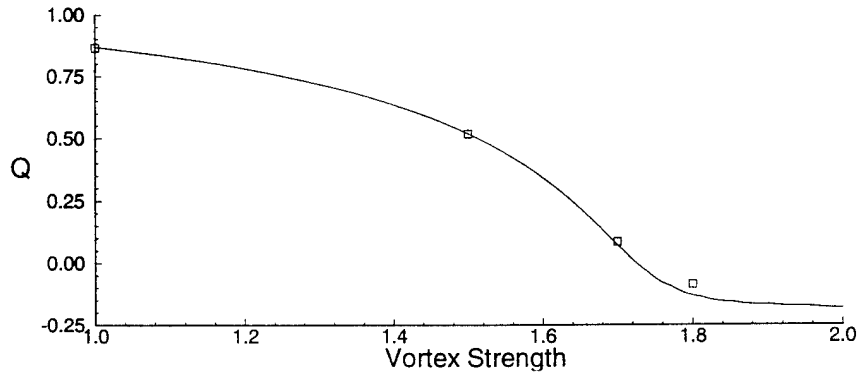


Figure 28. Minimum axial velocity,  $Q$ , versus vortex strength,  $\mathcal{V}$ , for  $Re = 100$ : PAC model (solid line) and TANS model (square symbols).

The change in solution type, from an equilibrium solution at  $\mathcal{V} = 1.7$ , to a periodic solution at  $\mathcal{V} = 1.8$ , is believed to be the result of passing a Hopf bifurcation point between  $\mathcal{V} = 1.7$  and  $\mathcal{V} = 1.8$ . Further examination of this type of bifurcation is performed in the next section, where similar behavior is found for  $Re = 250$ .

A summary of the results for  $Re = 100$  are shown in Figure 28. The solid line is a plot of  $Q$  versus  $\mathcal{V}$  corresponding to the steady, axisymmetric solutions obtained from the PAC model. The square symbols represent the time-asymptotic values of  $Q$  obtained from the TANS model. At  $\mathcal{V} = 1.0, 1.5$  and  $1.7$ , the time-asymptotic solution is steady, and agrees well with the PAC solution. At  $\mathcal{V} = 1.8$ , the value of  $Q$  is shown to be slightly higher than the value of  $Q$  obtained from the PAC model. This increase in minimum axial velocity near the onset of periodic flow is examined further in Section 5.2. Tabulated results for  $Re = 100$  are given in Table 8. The tabular value for  $Q$  at  $\mathcal{V} = 1.8$  is computed by averaging the peak values in the oscillation.

Table 8. Comparison of 2-D (PAC) and 3-D (TANS) minimum axial velocities for  $Re = 100$ .

$\mathcal{V}$	$Q$ (2-D)	$Q$ (3-D)
1.0	0.868	0.865
1.5	0.519	0.518
1.7	0.072	0.084
1.8	-0.131	-0.086

Table 9. Summary of TANS run parameters for  $Re = 250$ .

Run No.	$Re$	$\mathcal{V}$	$M$	$\Delta t$	$\alpha$	BC	Grid	Accuracy (Time/Space)
16	250	1.00	0.3	.040	0.05	2	G1	2nd/4th
17	250	1.50	0.3	.040	0.05	2	G1	2nd/4th
18	250	1.53	0.3	.040	0.05	2	G1	2nd/4th
19	250	1.55	0.3	.040	0.05	2	G1	2nd/4th
20	250	1.60	0.3	.040	0.05	2	G1	2nd/4th
21	250	1.65	0.3	.040	0.05	2	G1	2nd/4th
22	250	1.70	0.3	.040	0.05	2	G1	2nd/4th
23	250	1.80	0.3	.040	0.05	2	G1	2nd/4th
24	250	1.90	0.3	.040	0.05	2	G1	2nd/4th
25	250	2.10	0.3	.040	0.05	2	G1	2nd/4th
26	250	2.30	0.3	.040	0.05	2	G1	2nd/4th
27	250	1.50	0.3	.025	0.05	2	G2	2nd/4th
28	250	1.53	0.3	.025	0.05	2	G2	2nd/4th
29	250	1.53	0.3	.040	0.05	2	G5	2nd/4th
30	250	1.55	0.3	.025	0.05	2	G2	2nd/4th
31	250	1.55	0.3	.025	0.05	2	G1	2nd/4th

## 5.2 Results for $Re = 250$ .

A total of 16 runs are presented for  $Re = 250$ . A summary of run parameters for  $Re = 250$  is contained in Table 9. All runs are initialized with the axisymmetric PAC solution. Runs 16–26 comprise a sequence of runs computed on grid G1 where the vortex strength is steadily increased from 1.0 to 2.3. Runs 27–31 are presented to determine the solution sensitivity to grid resolution, tube length, and time step at selected vortex strengths. Second-order accurate, three-point-backward time integration is used. The time step,  $\Delta t$ , for runs using grids G1 and G5 is 0.04, while runs on the finer grid, G2, have a time step of 0.025. The reduction in time step from 0.04 with grid G1 to 0.025 with grids G2 is necessary to avoid solution divergence. Data presented next in Section 5.2.1 shows that between  $\mathcal{V}=1.0$  and  $\mathcal{V}=1.5$ , the initially steady, 2-D flow does not evolve in time to an asymmetric flow state, even in the presence of an asymmetric grid structure. Similar behavior is observed in Section 5.1 for vortex strengths up to 1.7. As  $\mathcal{V}$  is increased slightly to 1.53, the flow becomes three-dimensional and time periodic. As  $\mathcal{V}$  is further increased, the magnitude of the asymmetry also increases. This change in stability is attributed to the crossing of a supercritical Hopf bifurcation point between  $\mathcal{V} = 1.5$  and  $\mathcal{V} = 1.53$ .

In Section 5.2.2, the effect of emerging three-dimensional flow on  $Q$  is examined. In particular, results in Section 5.2.1 show that the 3-D, time-asymptotic values of  $Q$  computed at vortex strengths just past the Hopf point are significantly greater than their initial, 2-D values. Section 5.2.2 presents an analysis of the 3-D vorticity dynamics, including elements of the theoretical framework of vortex breakdown put forth by Brown and Lopez (1990), to correlate the observed behavior of  $Q$  with the emerging three-dimensional effects.

Flow visualizations using numerical streaklines are presented in Section 5.2.3 for selected vortex strengths.

*5.2.1 Evidence of a Hopf Bifurcation.* Evidence for a supercritical Hopf bifurcation is presented in this section. Flows computed before a critical value of  $\mathcal{V}$  are found to be steady and axisymmetric. Past the critical vortex strength, the computed flows are shown to be time-periodic and three-dimensional. A plot showing the agreement of axisymmetric and 3-D solutions at a vortex strength lower than the critical value is also presented.

The deviations of  $Q$  from the initial conditions are illustrated in Figures 29a-d for  $\mathcal{V}=1.5, 1.53, 1.55$ , and  $1.65$ . The solid lines in this figure represent results computed with the baseline grid G1. In Figure 29a ( $\mathcal{V}=1.5$ ), it is evident that no appreciable deviation from the initial condition is present. This appearance of a converged solution was confirmed by tracking  $\Delta^n U_{\max}$  at each iteration and observing a reduction to a minimum level near  $10^{-6}$ . At  $\mathcal{V}=1.53$  (Figure 29b), it is clear that the solution departs from the initial condition, as evident by the increase in  $Q$  as time increases. Eventually, the behavior of  $Q$  time asymptotes to time-periodic behavior, not discernable from the scales of the figure. At  $\mathcal{V}=1.55$  and  $1.65$  (Figures 29c-d), much larger deviations are evident.

The effects of grid resolution are also illustrated in Figure 29 by presenting results computed on grid G2. Grid G2 incorporates  $61^2$  nodes in each crossplane, as opposed to  $41^2$  for grid G1. This reduces the average radial node spacing from  $1/10$  to  $1/15$ . Furthermore, grid G2 uses axial clustering of nodes to achieve smaller node spacings just aft of the tube constriction. The minimum axial node spacing for grid G2 is  $0.1$  at  $x = 5$ , compared to a constant node spacing of  $0.2$  for grid G1.

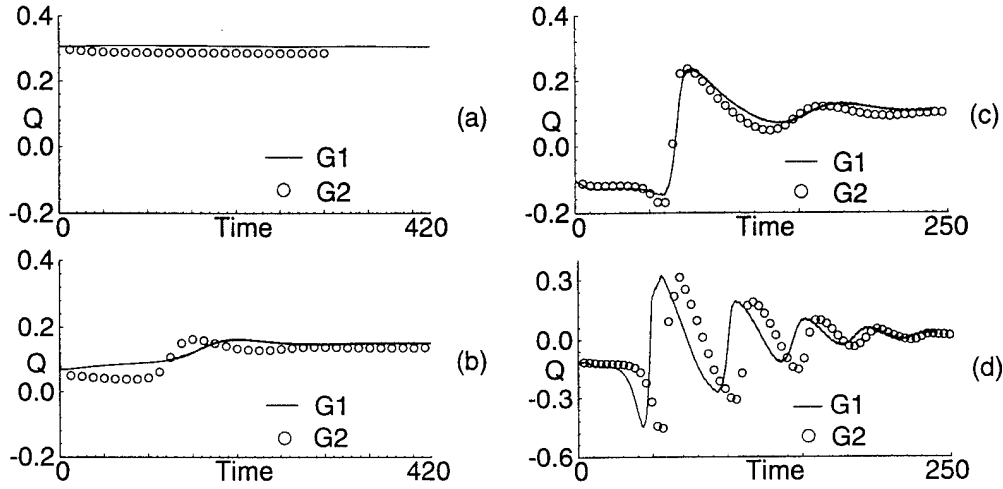


Figure 29.  $Q$  versus time for  $M = 0.3$  and  $Re = 250$ : (a)  $\mathcal{V} = 1.5$ , (b)  $\mathcal{V} = 1.53$ , (c)  $\mathcal{V} = 1.55$ , (d)  $\mathcal{V} = 1.65$ .

Figures 30a-d illustrate how grid refinement from G1 to G2 affects  $Q$ . At  $\mathcal{V} = 1.5$ , resolving the grid from G1 to G2 results in a slight decrease in the time-asymptotic value of  $Q$ . However, the flow remains steady and axisymmetric. At  $\mathcal{V} = 1.53$ , a more pronounced transient response is observed for the fine-grid G2; possibly representing a slight shift of the Hopf point to smaller values of vortex strength with grid refinement. The time-asymptotic behavior remains periodic (discussed later in this section), with time-asymptotic values of  $Q$  slightly less than the flow computed with grid G1. Thus, the Hopf bifurcation point remains in the range between  $\mathcal{V} = 1.5$  and  $\mathcal{V} = 1.53$ , even under grid refinement. The sensitivity to grid refinement appears to diminish as vortex strength is increased away from the Hopf point, as evident in Figure 29c. At  $\mathcal{V} = 1.65$ , refining the grid results in a small shift in time in the onset of the transient response. However, the time-asymptotic levels of  $Q$  show little impact.

Solution sensitivity to time step and tube length are illustrated in Figure 30. Figure 30a shows that reducing the time step from 0.04 to 0.025 (Runs 19,31), with grid G1, has a negligible influence on the transient behavior of  $Q$ . This suggests that the differences in  $Q$  evident in Figures 29a-d are due primarily to grid refinement and not to the reduction of the time step. The  $L_2$  norm of  $Q_{19} - Q_{31}$  is 5.87E-03, where the subscripts of  $Q$  denote

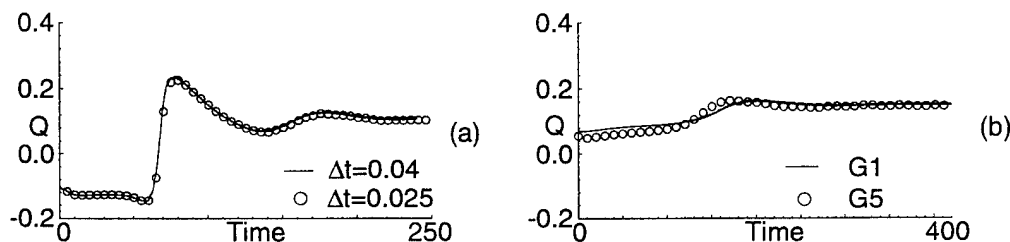


Figure 30. Effect of time step and tube length on  $Q$  for  $M = 0.3$  and  $Re = 250$ : (a) effect of time step for  $\nu = 1.55$ , (b) effect of tube length for  $\nu = 1.53$ .

the run number. The effect of tube length is shown in Figure 30b, where increasing the tube length,  $L$ , from 20 to 30 appears to have a small, but negligible effect on  $Q$ .

In summary, the data presented in Figure 29 suggests that grid G1 provides an acceptable level of accuracy to allow further presentation of the data. One notable exception where G1 may not be adequate is for transient flows computed very close to the Hopf point. In addition, the effect of further grid refinement and tube radius is not explored, owing to practical limits on computer resources.

A comparison of PAC and TANS solutions for a vortex strength below the Hopf point shows that both models produce steady, axisymmetric flows. The PAC and TANS solutions for Run 17 ( $\nu = 1.5$ ) are plotted in Figure 31, where it is evident that the two solutions are in excellent agreement. Furthermore, this result also demonstrates that solutions obtained from the fourth-order version of the TANS model agree with PAC solutions for conditions which lead to steady, axisymmetric solutions. Similar comparisons of solutions between the PAC model and the second-order version of the TANS model are given in Chapter 4.2.

The small differences in pressure contours near  $x = 8$  in Figure 31d are the likely result of the different relative discretization errors associated with the PAC and TANS models.

The relative agreement between PAC solutions and axisymmetric TANS solutions is quantified by computing the  $L_2$  norms (Section 3.10) of the differences between PAC and TANS primitive variables. The PAC solution is first interpolated onto the 3-D grid, using the cubic spline routine of Section B.3. This allows for both solutions to be compared on

Table 10. Quantification of the agreement between PAC solutions and axisymmetric TANS solutions.

Run	$L_2(\rho)$	$L_2(u)$	$L_2(v)$	$L_2(w)$	$L_2(p)$
17	1.12E-03	4.38E-03	2.58E-03	2.57E-03	4.89E-03
27	3.05E-04	2.27E-03	2.47E-03	2.43E-03	1.30E-03

the same grid, while also introducing interpolation error. The results are shown in Table 10 for Runs 17 and 27 ( $\mathcal{V} = 1.5$ ) using grids G1 and G2 respectively. The  $L_2$  norms are small for both runs, with a noticeable reduction in the  $L_2$  norms associated with the finer grid, G2.

The periodic nature of the flows are now examined. Figures 32 and 33 show  $v_s$ ,  $u_s$ , and  $w_s$  as a function of time. These quantities, defined in Section 3.9, denote the three velocity components evaluated along the centerline at a fixed axial location of  $x = 7$ . Figure 32 plots  $v_s(t)$  and  $w_s(t)$ . Oscillations in  $v_s$  and  $w_s$  indicate three-dimensional behavior, since these velocity components are identically zero along the centerline for axisymmetric flow. The starting times for the data are distinct, since different amounts of time are required to achieve time-asymptotic behavior. Harmonic oscillations in  $v_s$  and  $w_s$  first appear in Figure 32 at  $\mathcal{V} = 1.53$ , which coincides with the first temporal deviations in  $Q$  from the initial conditions in Figure 29.

The amplitudes of the oscillations in  $v_s$  and  $w_s$  are found in this case grow larger as  $\mathcal{V}$  is increased. However, this should not be interpreted as a general result, since the node from which data is collected is held fixed. If, for example, the axial position (where the maximum amplitude of the crossplane velocity components occur) starts at  $x = 9$  and moves upstream as  $\mathcal{V}$  is increased. Then,  $v_s$  and  $w_s$  may grow in amplitude until a certain vortex strength is reached, followed by a decrease in amplitude with increasing  $\mathcal{V}$ .

In the analysis to follow, a new parameter,  $\Omega$ , is introduced. This parameter represents the extreme values of the sum of  $v$  and  $w$  considering all of the centerline nodes. This parameter is found to increase monotonically as  $\mathcal{V}$  is increased. Oscillations in the axial velocity component,  $u_s$ , are shown in Figure 33. A discernable oscillation first appears at  $\mathcal{V} = 1.53$ , consistent with the first appearance of oscillations in  $v_s$  and  $w_s$  in Figure 32.



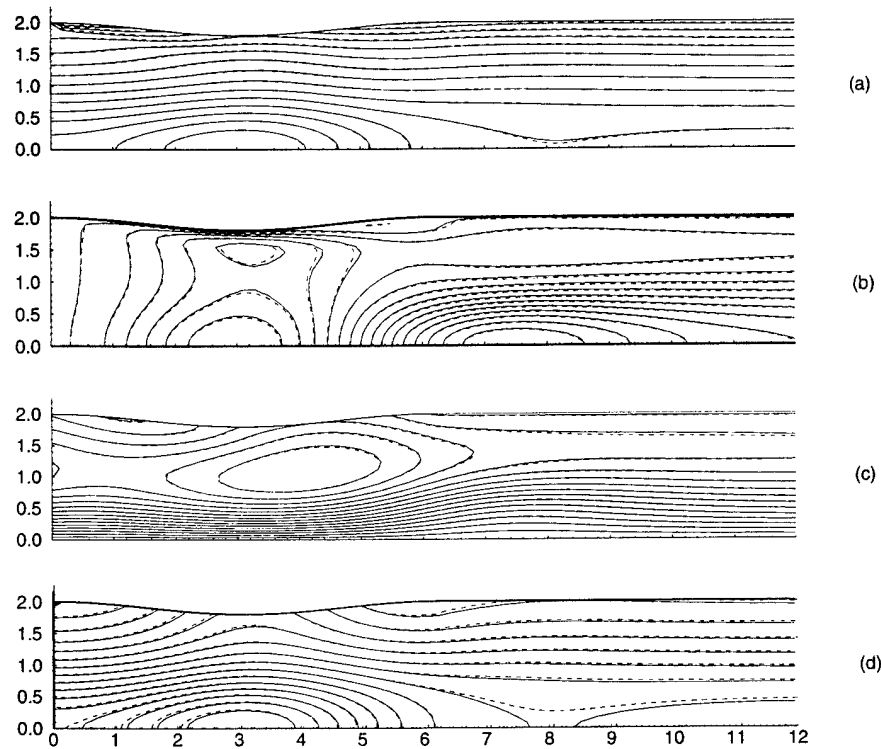


Figure 31. Comparison between TANS and PAC solutions for Run 17,  $V=1.5$  (PAC model: dashed lines; TANS model: solid lines). Numbers in parenthesis indicate contour range: (a) Density (0.819212,1.03179), (b) Axial Velocity (0.380704,1.36375), (c) Crossplane velocity (0.0677997,1.017), (d) Pressure (6.70018,8.21738).

The amplitudes of the oscillations in axial velocity are a factor of 30 smaller than those of  $v_s$  and  $w_s$ .

While Figures 32 and 33 are good for showing the temporal nature of the solutions, phase plots are better suited to demonstrate periodicity. Phase plots for the same vortex strengths and times considered in Figures 32 and 33 are presented in Figures 34–37. Phase plots of  $w_s$  are not included, since this quantity is similar to  $v_s$  when lagged in time, and would therefore provide redundant information.

Plots of  $u_s(t)$  in Figures 34–37 show that, for solutions for vortex strengths less than 2.3, the axial velocities are not evolved sufficiently to the point where pure time-periodic motion is evident. The effect of numerical errors may also play a role in this observation,

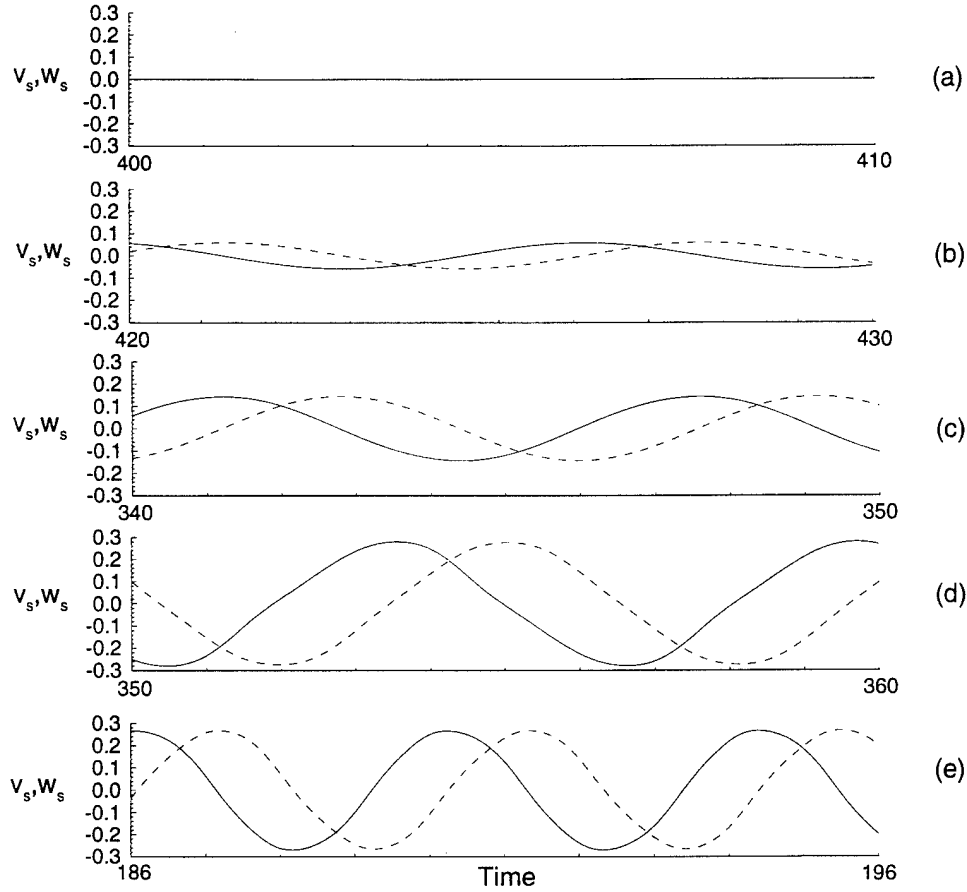


Figure 32. Crossplane velocity components  $v_s$  (solid lines) and  $w_s$  (dashed lines) versus time: (a)  $\mathcal{V} = 1.5$ , (b)  $\mathcal{V} = 1.53$ , (c)  $\mathcal{V} = 1.55$ , (d)  $\mathcal{V} = 1.65$ , (e)  $\mathcal{V} = 2.3$ .

owing to the relatively small amplitudes involved. However, periodic motion is strongly indicated for  $v_s$  at each vortex strength.

At  $\mathcal{V} = 2.3$ , periodic behavior is evident for all three velocity components. The period of  $u_s(t)$  here *appears* (from Figure 33e) to be about half of that for  $v_s(t)$  and  $w_s(t)$ . However, upon examination of the data with the aid of the phase plot representation, it is found that the period of  $u_s(t)$  matches that of  $v_s(t)$  and  $w_s(t)$  to a high degree of accuracy. Figure 37a shows the closed path for  $u_s(t)$  with two “branches” in very close proximity. By inspecting the data, it is found that one period of the motion corresponds to traveling completely along both branches. The observed period of  $u_s(t)$  is found to be 4.16, the same

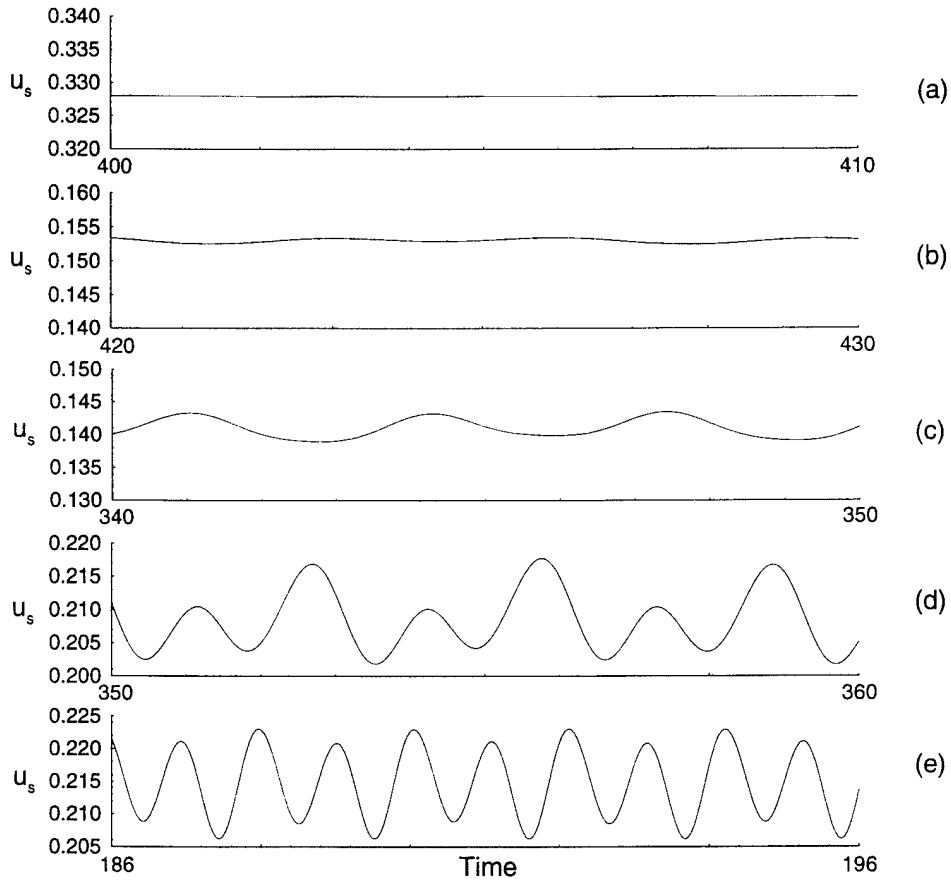


Figure 33. Axial velocity component  $u_s$  versus time: (a)  $\mathcal{V} = 1.5$ , (b)  $\mathcal{V} = 1.53$ , (c)  $\mathcal{V} = 1.55$ , (d)  $\mathcal{V} = 1.65$ , (e)  $\mathcal{V} = 2.3$ .

as the period of  $v_s(t)$ . These periods are found by taking the difference in time between peak values in the raw data.

Two new parameters are now defined to aid in illustrating the effect of the Hopf bifurcation. To identify directly the onset of three-dimensionality, a global parameter,  $H$ , is constructed, which is defined to be the maximum absolute value of  $d\hat{v}/d\theta$ .  $H$  departs from zero when the flow is asymmetric. Flow unsteadiness and asymmetry are characterized by another parameter,  $\Omega$ , which is defined as the minimum and maximum values of  $v_s(t) + w_s(t)$ . By definition,  $\Omega$  is zero for an axisymmetric flow.  $\Omega$  characterizes the “degree” of flow unsteadiness by representing the largest amplitude of the time-periodic wave,  $v_s(t) + w_s(t)$ , along the centerline. Flow periodicity is demonstrated in Figures 32–37.

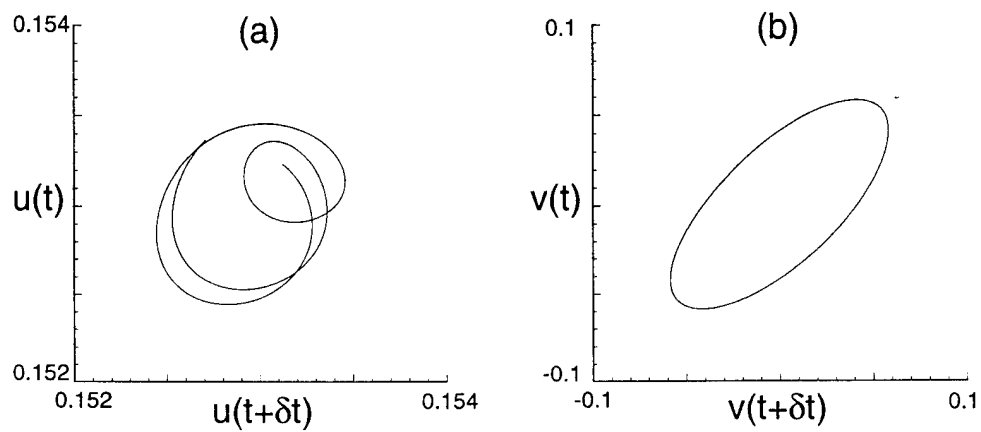


Figure 34. Phase plot for  $\mathcal{V} = 1.53$ : (a)  $u_s(t)$ , (b)  $v_s(t)$ .

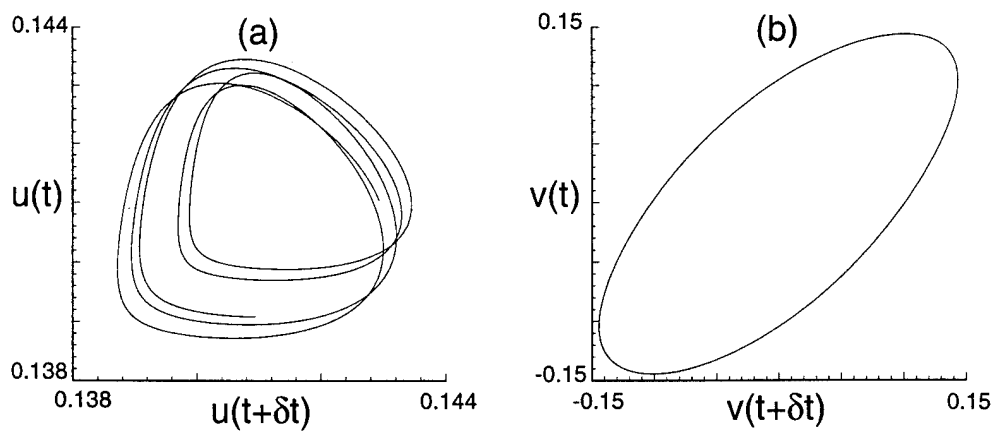


Figure 35. Phase plot for  $\mathcal{V} = 1.55$ : (a)  $u_s(t)$ , (b)  $v_s(t)$ .

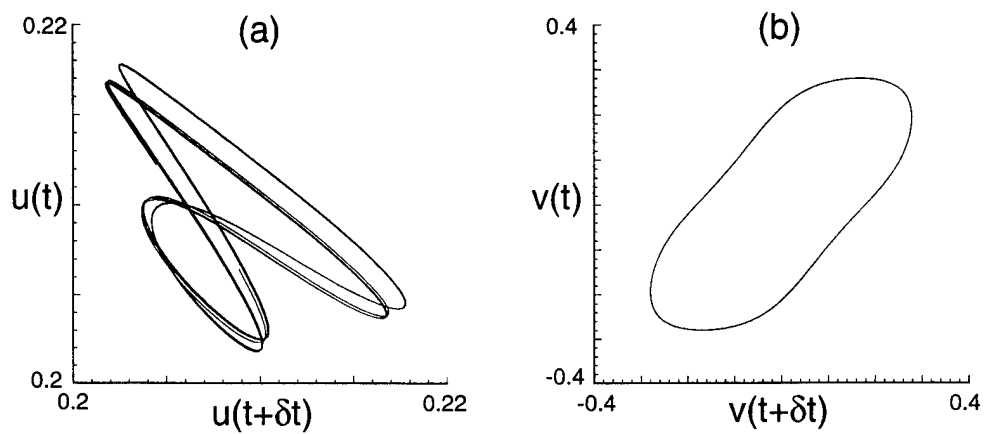


Figure 36. Phase plot for  $\mathcal{V} = 1.65$ : (a)  $u_s(t)$ , (b)  $v_s(t)$ .

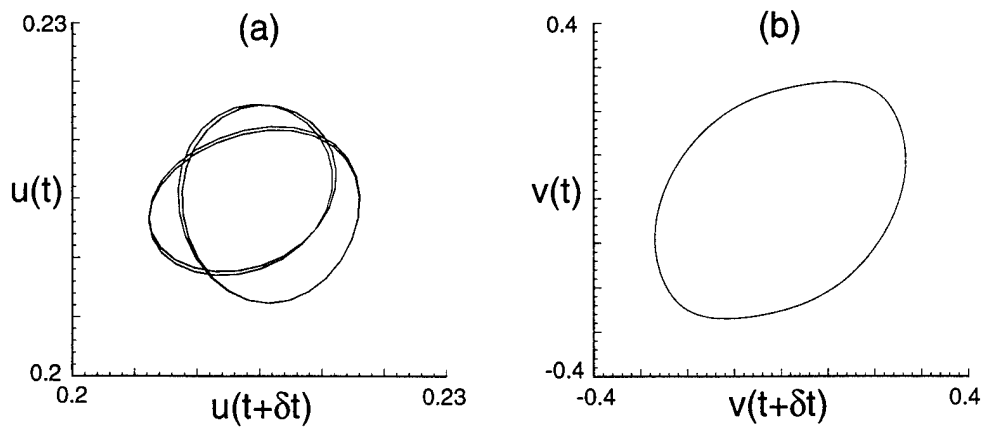


Figure 37. Phase plot for  $\mathcal{V} = 2.3$ : (a)  $u_s(t)$ , (b)  $v_s(t)$ .

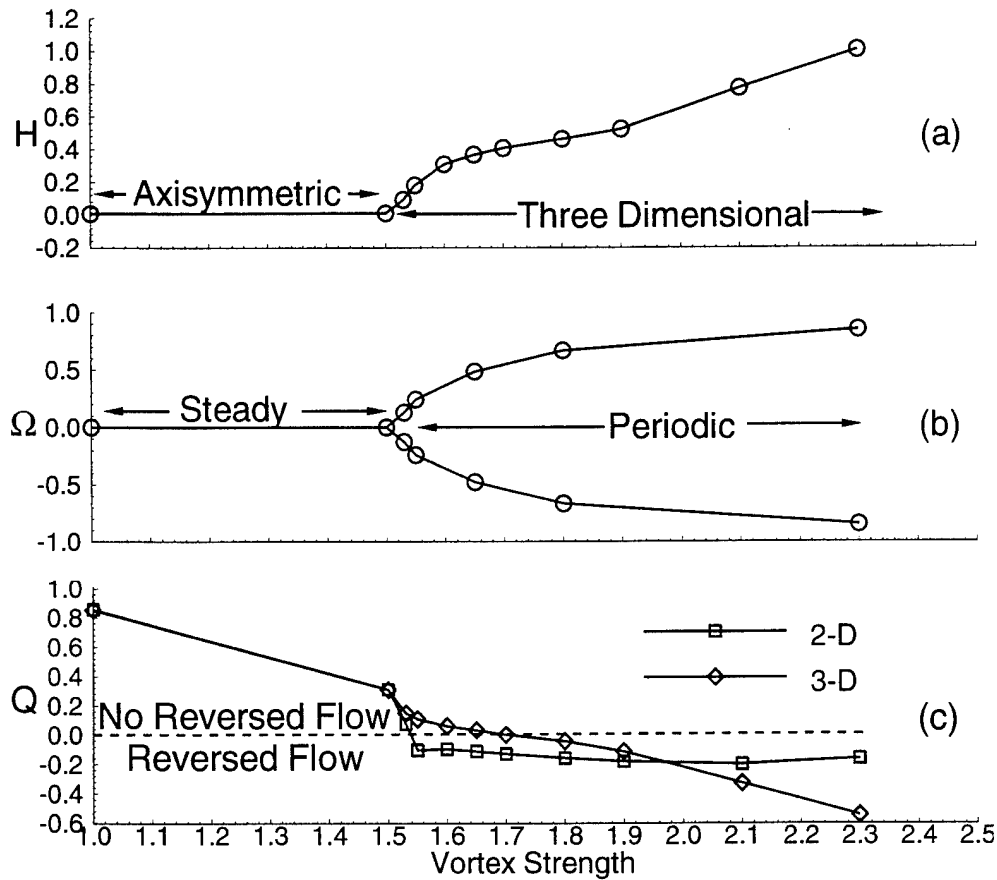


Figure 38. Evidence of a Hopf bifurcation for  $M = 0.3$  and  $Re = 250$ .

The nature of the Hopf bifurcation is illustrated in Figure 38. In Figure 38a,  $H$  abruptly departs from zero between  $V = 1.5$  and  $V = 1.53$ . Within this range of  $V$ , fully 3-D solutions bifurcate from the branch of 2-D solutions when the 2-D solutions become physically unstable.

The onset of asymmetric flow is coincident with the onset of flow unsteadiness. Figure 38b shows that  $\Omega$  departs from zero at the same value of  $V$  that the flow becomes asymmetric. Thus, Figures 38a and 38b demonstrate that flow unsteadiness and asymmetry are intimately linked. The loss of stability to time-periodic flow is evidence for a Hopf bifurcation between  $V = 1.5$  and  $V = 1.53$ . The bifurcation is supercritical, since the amplitude of the disturbance, characterized by  $\Omega$ , grows as  $V$  is increased past the Hopf

Table 11. Summary of computed flow parameters for  $Re = 250$ . Solutions denoted by an asterisk (\*) are computed with grid G2.

$\mathcal{V}$	$H$	$\Omega$	$Q$ (2-D)/(3-D)	Period
1.00	.0076	0.0/0.0	.856/ .852	-
1.50	.0101	-.002/.001	.310/ .307	-
1.50*	.0081	-.002/.001	.303/ .285	-
1.53	.0922	-.127/.127	.077/ .149	6.40
1.53*	.1283	-.164/.164	.063/ .135	6.40
1.55	.1800	-.241/.241	-.102/ .109	6.40
1.65	.3665	-.478/.482	-.111/ .034	6.16
1.65*	.4270	-.494/.493	-.111/ .020	6.13
1.80	.4626	-.666/.667	-.157/-.042	5.76
2.30	1.006	-.847/.849	-.159/-.544	4.16

point. A general depiction of the supercritical Hopf bifurcation is given in Figure 69 of Section B.1.

The initial and time-asymptotic values of  $Q$  are shown in Figure 38c. The Hopf point occurs prior to the appearance of reversed flow; thus, loss of stability is not a consequence of a gross structural change in the flowfield. Also, Figure 38c shows a region in  $\mathcal{V}$  where 2-D flows with bubble-type breakdown evolve into 3-D, unsteady flows with no reversed flow. An examination of this evolution to positive values of  $Q$  (no breakdown) is presented in the next section.

Data from selected points of Figure 38 are shown in Table 11, along with the tabulated periods of the solutions. The effect of grid refinement (for  $\mathcal{V} = 1.5$  and 1.53) on the time-asymptotic behavior is also shown. At  $\mathcal{V} = 1.53$ , an increase in  $H$  and  $\Omega$  is evident as the solution is resolved from grid G1 to G2, indicative of a slight shift in the Hopf point in the direction of smaller vortex strength. The Hopf point remains, however, somewhere in the range between  $\mathcal{V} = 1.5$  and  $\mathcal{V} = 1.53$ . Time integration for the other vortex strengths with grid G2 to their time-asymptotic solutions were not performed, due to the high computational expense.

A comparison between 2-D and 3-D velocity fields further illustrates the departure from axisymmetric behavior. Figure 39a-d compares velocity vectors from the axisymmetric initial conditions to the planar projected velocity field for the 3-D time-asymptotic

solutions. The left column contains the 2-D results while the right column contains the 3-D results. The two rows correspond to different vortex strengths. Figures 39a and 39c compare velocity vectors for  $\mathcal{V} = 1.5$ . Here we see that both solutions depict axisymmetric flow. A region of mild axial flow deceleration is evident between  $x = 6$  and  $x = 10$ . Figures 39b and 39d compare vectors for  $\mathcal{V} = 1.53$ . The axial deceleration evident at  $\mathcal{V} = 1.5$  has increased in severity, as shown in Figure 39b, but the flow still has no region of reversed flow. Furthermore, the region of decelerated flow has moved farther upstream. The movement of flow disturbances upstream with increasing vortex strength is also observed in the tube experiments of Faler and Leibovich (1977). The first signs of asymmetry are evident in Figure 39d. The asymmetry is characterized by the appearance of a component of velocity in the  $y$  direction along the centerline  $y = 0$ .

Figures 40 and 41 show comparisons of velocity vectors at higher vortex strengths. Figure 40a and 40c, corresponding to  $\mathcal{V} = 1.65$ , show a pronounced difference between 2-D and 3-D velocity fields. The 2-D flow is now reversed at this vortex strength, as evidenced in the figure between  $x = 6$  and  $x = 7$  for  $y = \pm 1/2$ . The 3-D flow, however, is not reversed. However, it is evident from the velocity vectors that the flow is more asymmetric in nature than at lower vortex strengths. This is apparent from the sharp deflection of the velocity vectors in Figure 40c near  $x = 6$  and  $y = 0$ . At  $\mathcal{V} = 1.8$ , the 2-D solution has a region of reversed flow that has expanded in both radial and axial extent from that at  $\mathcal{V} = 1.65$ , as evident in Figure 40b. The corresponding 3-D flow in Figure 40d, however, has changed little in appearance from the solution depicted in Figure 40c. The time-asymptotic value of  $Q$  for this run from Table 11 is -0.042, indicating reversed flow. However, the particular slice of data in Figure 40d does not bear evidence of the reversed flow. The small region of reversed flow is most likely found at a slice in the  $x - y$  plane not containing the centerline, i.e., where  $z \neq 0$ .

The breakdown region continues to move upstream as  $\mathcal{V}$  increases to 2.3 in Figure 41. The range of abscissa values in this figure are lowered to accommodate the forward movement of the breakdown regions.

The 3-D flows shown in Figure 41c and 41d depict a noticeable region of reversed flow. The vectors generally mark a circular region which enclose a center point where the



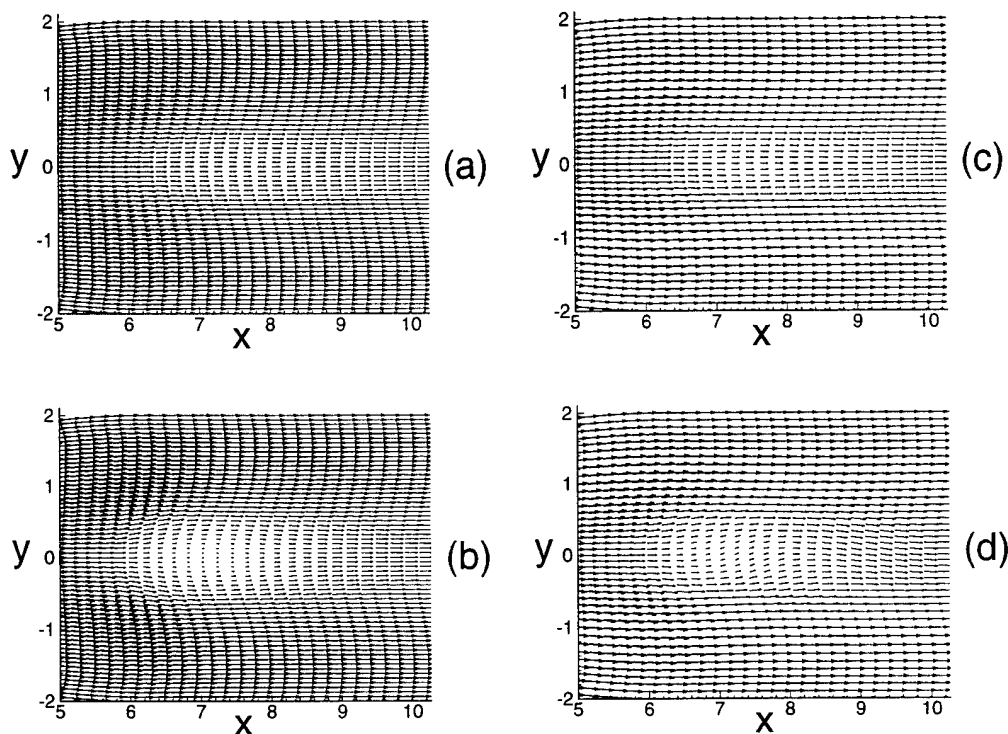


Figure 39. Velocity vectors in  $x = \hat{z}, y = r$  plane (2-D) or  $x, y$  plane (3-D): (a)  $\mathcal{V} = 1.5$  (2-D), (b)  $\mathcal{V} = 1.53$  (2-D), (c)  $\mathcal{V} = 1.5$  (3-D), (d)  $\mathcal{V} = 1.53$  (3-D).

planar-projected velocity vector vanishes. The position of this center point approximately identifies the current spatial position where the vortical core, deflected off-axis at some upstream location, intersects the  $x - y$  plane. Visualization of this behavior is presented later in Section 5.2.3.

The 2-D velocity vector plots are very informative, however, much information is lost when trying to depict 3-D behavior. The primary difficulty lies in the fact that no single plane in the 3-D flowfield can be isolated to depict the general flowfield. This is why the streaklines advocated in Section 3.8 are presented later in Section 5.2.3.

**5.2.2 The Effect of Three-Dimensionality on  $Q$ .** Results of the previous section shows that when the vortex strength is specified between  $\mathcal{V} = 1.53$  and  $\mathcal{V} = 1.9$ , the time-asymptotic values of  $Q$  are higher than the value of  $Q$  corresponding to the initial axisymmetric solution.

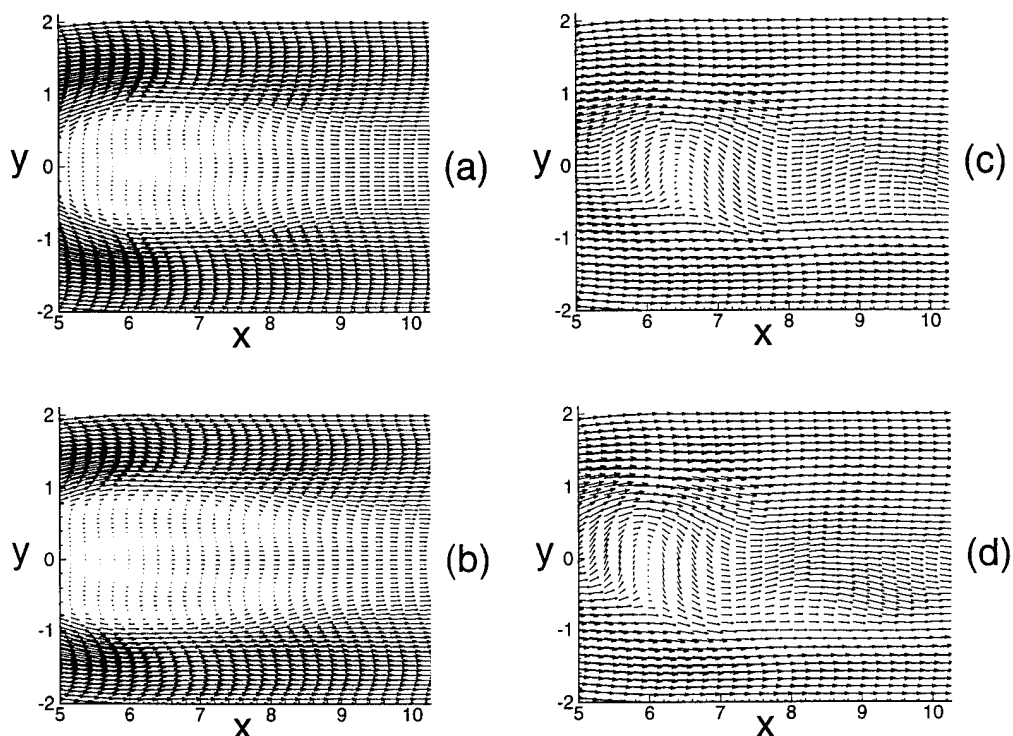


Figure 40. Velocity vectors in  $x = \hat{z}, y = r$  plane (2-D) or  $x, y$  plane (3-D): (a)  $\mathcal{V} = 1.65$  (2-D), (b)  $\mathcal{V} = 1.8$  (2-D), (c)  $\mathcal{V} = 1.65$  (3-D), (d)  $\mathcal{V} = 1.8$  (3-D).

This observed effect of three-dimensionality on  $Q$  requires further explanation. In particular, it is desired to establish a correlation between the increase in  $Q$  levels (at swirl values near the Hopf point) to certain asymmetric terms in the governing equations. To accomplish this requires the application of concepts put forth by Brown and Lopez (1990), along with an extension of an analysis of the 3-D vorticity transport equation performed by Darmofal (1993).

Brown and Lopez (1990) established a link between the production of negative azimuthal vorticity in axisymmetric flow and the extent of axial flow deceleration: negative azimuthal vorticity is a necessary condition for the deceleration of the axial flow, (Section 2.1.1.2). In particular, the more negative the azimuthal vorticity, the smaller  $Q$  becomes. Consequently, it is anticipated that the minimum azimuthal vorticity,  $\hat{\eta}_m$ , for the 3-D flow would be greater (less negative) than that of the initial 2-D flow. This is

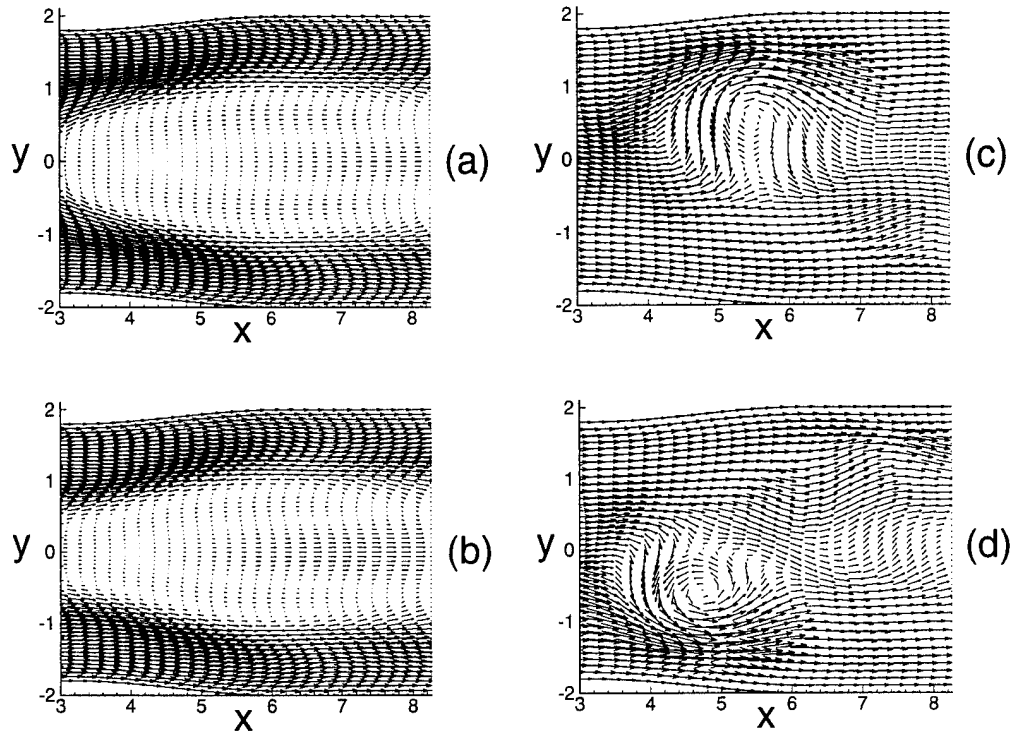


Figure 41. Velocity vectors in  $x = \hat{z}, y = r$  plane (2-D) or  $x, y$  plane (3-D): (a)  $\mathcal{V} = 2.1$  (2-D), (b)  $\mathcal{V} = 2.3$  (2-D), (c)  $\mathcal{V} = 2.1$  (3-D), (d)  $\mathcal{V} = 2.3$  (3-D).

indeed the case, as shown in Table 12. At  $\mathcal{V} = 1.5$ , the value of  $\hat{\eta}_m$  is virtually the same for 2-D and 3-D flow, allowing for some error due to calculating  $\hat{\eta}_m$  from discrete data. This point lies before the Hopf bifurcation. Beyond the Hopf point,  $\hat{\eta}_m$  is greater in the 3-D flow than for the initial 2-D flow. The data in the figure does not correlate, however, the trend at higher vortex strengths, where the paths of  $Q$  cross. Thus, the discussion is limited to vortex strengths near the bifurcation point. However, since the theory is only strictly valid for steady, axisymmetric flow, the movement away from steady, axisymmetric flow as  $\mathcal{V}$  is increased reduces the applicability of the theory. Therefore, it is of little concern that the behavior of  $\hat{\eta}$  at the higher vortex strengths is inconsistent. With this established, an attempt is made to correlate the increase in  $Q$  with the physical mechanisms associated with the production of positive azimuthal vorticity in the 3-D flows.

Table 12. Comparison of minimum azimuthal vorticities for 2-D and 3-D flows.

$\mathcal{V}$	$\hat{\eta}_m$ (2-D)	$\hat{\eta}_m$ (3-D)	$\Delta\hat{\eta}_m(\%)$
1.50	-1.0	-.99	1.0
1.53	-1.4	-1.3	7.1
1.55	-2.0	-1.4	30.0
1.65	-2.9	-1.9	34.5
1.80	-3.6	-2.4	33.3
1.90	-4.0	-2.8	30.0
2.10	-4.3	-3.7	13.9

A numerical evaluation of asymmetric terms in the governing equations is performed to help explain the increase of 3-D azimuthal vorticity levels. The following analysis assumes that compressibility and viscous effects are not important in identifying how positive azimuthal vorticity is produced. Then, the vorticity equation is written as

$$\frac{D\vec{w}}{Dt} = \vec{w} \cdot \nabla \vec{u} \quad (137)$$

where  $\vec{u} \equiv (\hat{w}, \hat{u}, \hat{v})^T$ . The azimuthal component of Eq. 137 can be expanded and written as

$$\frac{D\hat{\eta}}{Dt} = \hat{\xi} \frac{\partial \hat{v}}{\partial r} + \hat{\zeta} \frac{\partial \hat{v}}{\partial z} + \frac{\hat{u}\hat{\eta}}{r} + \frac{\hat{\eta}}{r} \frac{\partial \hat{v}}{\partial \theta} \quad (138)$$

Eq. 138 is in terms of the material derivative of  $\hat{\eta}$ ; therefore, a Lagrangian viewpoint is adopted in the discussion below. Darmofal (1993) identified how each of the first three terms on the right-hand-side of Eq. 138 contribute to the production or decay of  $\hat{\eta}$  for axisymmetric flow. The analysis is in terms of how vorticity stretching and tilting contribute to the production of azimuthal vorticity and, subsequently, breakdown.

Along the same lines, the contribution from the new terms present for 3-D flows (e.g. the fourth term on the right-hand-side of Eq. 138) may provide the mechanism that produces a positive azimuthal vorticity contribution. The effect of three-dimensionality on the above equations is evident by the terms  $\frac{\partial \hat{w}}{\partial \theta}$  and  $\frac{\partial \hat{u}}{\partial \theta}$  in the definitions of  $\hat{\xi}$  and  $\hat{\zeta}$  respectively.  $\hat{\xi}$  and  $\hat{\zeta}$  in turn, affect the first two terms on the right-hand side of Eq. 138. Lastly, the fourth term in Eq. 138 is included for 3-D flow. Thus, the first, second, and fourth term on the right-hand side of Eq. 138 contain direct contributions from 3-D effects.

At  $\mathcal{V} = 1.53$  and  $t = 420$ , the three terms in question are numerically evaluated at the point where azimuthal vorticity is minimum. The second and fourth terms are negligible in comparison to the dominant first term,  $\hat{\xi} \frac{\partial \hat{v}}{\partial r}$ . Inspection of how the swirl velocity,  $\hat{v}$ , changes with radial position reveals that  $\frac{\partial \hat{v}}{\partial r}$  is positive throughout the flow. Since  $\frac{\partial \hat{v}}{\partial r}$  is also positive throughout a 2-D flow, this quantity is not important in the current context. Therefore, it is postulated that the effect of three-dimensionality on radial vorticity,  $\hat{\xi}$ , plays a key role in understanding the emergent 3-D flow behavior. A region consisting of a positive net change in radial vorticity must exist in order to correlate the observed change in  $Q$ . In particular, if  $\hat{\xi}$  has a positive net change from 2-D to 3-D flow, then from Eqn. 138,  $\frac{D\hat{\eta}}{Dt}$  also has a positive net change. Therefore,  $\hat{\eta}$  becomes larger in the region where azimuthal vorticity is minimum, which implies by the theory of Brown and Lopez (1990) that  $Q$  must increase from 2-D to 3-D flow.

Contour plots of  $\hat{\xi}$  are shown in Figure 42. Solid contours denote positive values, dashed are negative. Figures 42a-b show the contours for the axisymmetric and 3-D solutions respectively, while Figure 42c shows the net effect of the evolution from 2-D to 3-D. The figure clearly shows the development of a region of positive radial vorticity. Furthermore, the asymmetric term,  $\frac{1}{r} \frac{\partial \hat{w}}{\partial \theta}$ , is found to be the dominant term in the calculation of  $\hat{\xi}$  from Eq. 2 of Section 2.1.1.2.

In summary, the computed flowfield at  $\mathcal{V} = 1.53$  is used to evaluate how three-dimensional terms in the vorticity transport equation contribute to the net production of positive azimuthal vorticity in the region where the azimuthal vorticity is minimum. The effect of this net increase corresponds to an increase in  $Q$  as the flow evolves from its 2-D initial condition to the 3-D flow. The principal contributing factor to the net increase in  $\hat{\eta}$  is found to be an increase in radial vorticity.

**5.2.3 Flow Visualization.** Flowfield visualization is performed by calculating the numerical equivalent of streaklines. Five material points are introduced into the flowfield at the inflow boundary. One point (white) lies initially on the tube centerline, the others (grey scaled) lie on the  $y$  and  $z$  axes at distances of  $\pm 0.1$  from the centerline. Every  $K$ th iteration ( $K$  is user specified), five new material points are introduced into the flowfield

where the first five points were initialized, thereby simulating a numerical equivalent of dye-injection in experiments. The positions of these material points are computed in time from the evolving velocity field using a first-order-accurate Euler time integration.

Snapshots of the time-asymptotic streaklines are shown in Figure 43; the tube geometry is omitted for clarity. Vortex strengths of 1.5, 1.53, 1.65, 1.8 and 2.3, corresponding to Runs 17, 18, 21, 23 and 26, are considered. Vortex strengths not included in the visualization are found to be similar to the types of disturbances presented, and are therefore omitted. All flows have a base rotation in the clockwise direction when viewed in the positive  $x$  direction. Material points are only computed in the inner grid block. If a particle convects out of the inner block, its position is no longer tracked. This situation only occurs for the highest vortex strength considered.

At  $\mathcal{V} = 1.5$  (Figure 43a), before the Hopf point, the vortex core swells at an axial location of about  $x = 6$ . The swelling of the core occurs symmetrically, illustrating the effect of axial flow deceleration. At  $\mathcal{V} = 1.53$  (Figure 43b), beyond the Hopf point, an asymmetric disturbance occurs upstream of the initial swelling at  $x = 6$  for  $\mathcal{V} = 1.5$ . The upstream movement of flow disturbances with increasing  $\mathcal{V}$ , evident between Figures 43a and 43b, is in agreement with experimental evidence (Faler and Leibovich, 1977). The axial deceleration along with a rotation of the disturbance produces rings of material points which subsequently convect downstream. The direction of rotation is clockwise (looking downstream); consistent with the base vortical flow. The initial disturbance near  $x = 5$  appears as a swelling of the vortex core, which is of greater radial extent than that observed at  $\mathcal{V} = 1.5$ .

When  $\mathcal{V}$  is increased to 1.65 (Figure 43c), the material points deflect off-axis in a more coherent structure, as shown in Figure 43c. A swelling of the vortex core is evident before the material points deflect off-axis as a group. This structure also rotates about the centerline with the same direction as the base flow. The flow at this vortex strength contains no reversed flow. However, the flow has nearly stagnated along the centerline, as evidenced by a time-asymptotic value of  $Q$  of 0.034.

A further increase in vortex strength to  $\mathcal{V} = 1.8$  (Figure 43d) "tightens" the coherent structure, while moving the disturbance farther upstream. A slight region of reversed flow exists just downstream of the position where the material points deflect off-axis.

The flows depicted in Figure 43 do not have the tightly wrapped helical form of spiral-type breakdown. Instead, these flow structures have more in common with what Faler and Leibovich (1977) term "type 6." Type 6 disturbance is described as a low Reynolds number disturbance, characterized as a gentle, off-axis deflection of the central dye filament. The deflection is of nearly constant azimuthal location until the disturbance reaches a sufficiently large radial extent, at which time the structure rotates about the centerline in the direction of the base flow. The type 6 disturbance contains no reversed flow, consistent with the flows in Figure 43b-c, and therefore it is technically not considered as a form of breakdown. The flow depicted in Figure 43d does contain a small region of reversed flow, and therefore is believed to be an intermediate form between the type 6 disturbance and the spiral breakdown.

There are some differences, however, between the computed flow structures and the type 6 disturbance. First, the type 6 disturbance has been found to nearly reach the tube wall in the experiments of Faler and Leibovich (1977). Flows in Figure 43 do not possess such a large radial extent. Second, Faler and Leibovich (1977) state that when the disturbance nears the tube wall, noticeable oscillations are evident which break up the dye filament. Such a disruption is not evident in the computed flows, since the flow disturbances do not approach the tube wall.

Characteristics of flow Types 3-5 are not evident in Figure 43. Types 3 and 4 contain regions of flow recirculation, which are not evident in the flows in Figure 43, or by their positive (or slightly negative) time-asymptotic values of  $Q$ . The type 5 (double helix) form is not evident as well, since there is no indication that the material points deflect off axis to form the characteristic triangular pattern observed in experimental dye traces.

At the largest value of vortex strength considered,  $\mathcal{V} = 2.3$ , (Figure 44) the material points deflect off axis in a well defined helical-type structure, consistent with spiral-type breakdown. Figure 44 depicts the spiral breakdown at four different times which span the

period of rotation of the deflected particles. The rotation of the structure is the same as the base vortical flow, but the sense of winding of the helix is opposite that of the base flow. This observation is consistent with observations made in the experiment of Brücker. Downstream of the point where the material points deflect off the centerline axis, a limited region of reversed flow exists. Regions of reversed flow also exist in experimentally observed spiral breakdowns.

The period of rotation of the helical structure, as well as for the other 3-D structures at lower vortex strengths, is at least approximately equal to the period identified in Table 11. The period is substantiated by plotting material points at four different times in the time-periodic cycle for  $\mathcal{V} = 2.3$ . Due to computational constraints, new material points were “injected” into the flow every 10 iterations (0.4 seconds). Therefore, material points at a time of 4 seconds were easily obtainable, which is close to the tabulated period of rotation (4.16) of the spiral structure. The similarity between Figure 44a and Figure 44d approximately confirms the period of rotation.

Finally, the spiral breakdown in Figure 44 can be compared to the corresponding planar projected velocity field given in Figure 41 of Section 5.2.1. Figure 44c corresponds in time to the velocity field in Figure 41. Consider a slice in Figure 44c through  $z = 0$ . The material points initially deflect towards the negative  $y$  and  $z$  directions, eventually intersecting the  $x - y$  slice from below near  $x = 5$  and  $y = -1/2$ . This location in the  $x - y$  plane corresponds to the center of the planar velocity field evident in Figure 41.



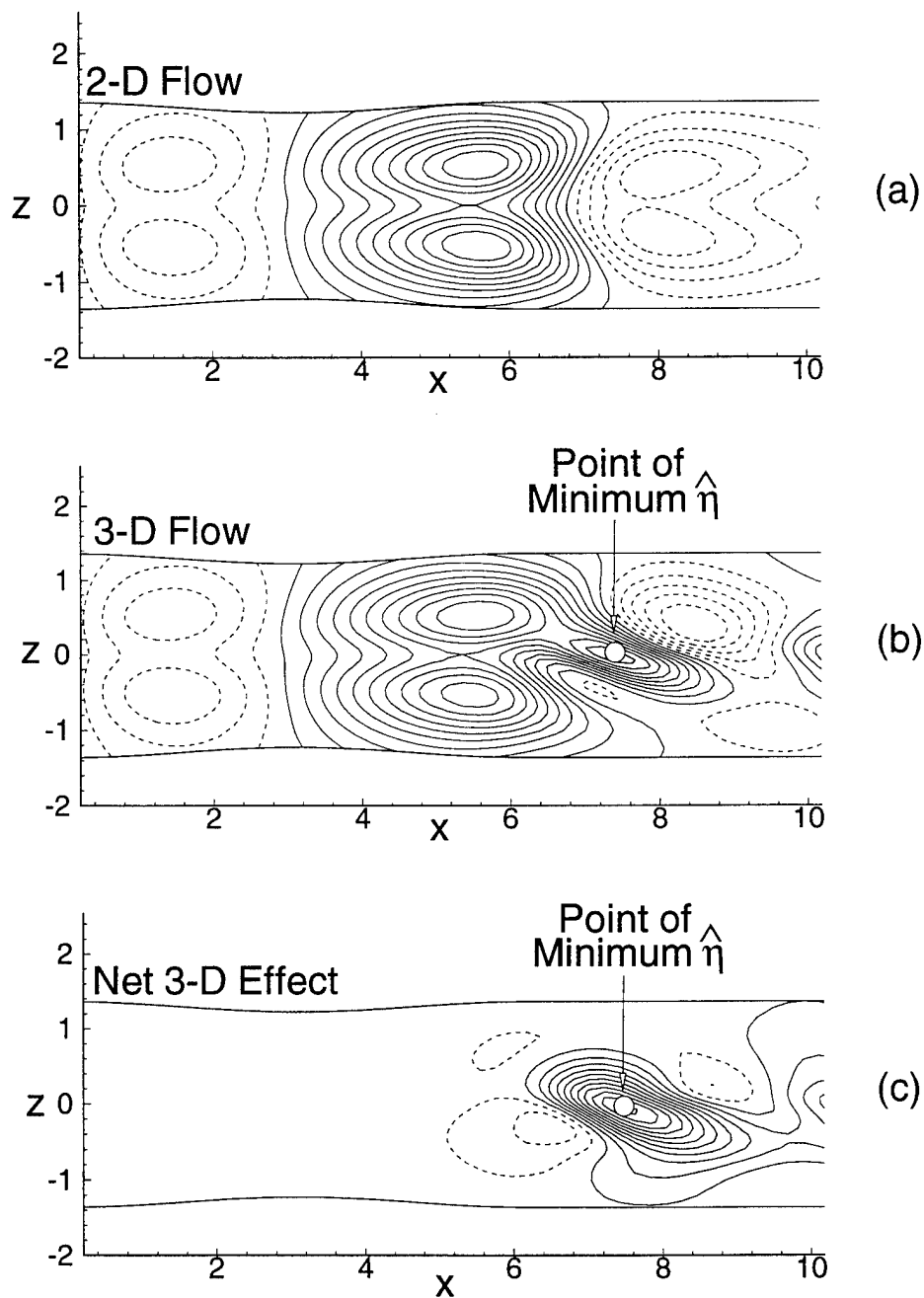


Figure 42. Contours of radial vorticity,  $\hat{\xi}$ , at  $y = 0.3$  for  $\mathcal{V} = 1.53$ . Solid lines denote positive contour values; dashed denote negative values. Numbers in parentheses indicate contour range: (a) axisymmetric flow  $(-0.09, 0.24)$ , (b) 3-D, time-asymptotic flow  $(-0.11, 0.22)$ , (c) Net perturbation from the axisymmetric flow  $(-0.10, 0.29)$ .

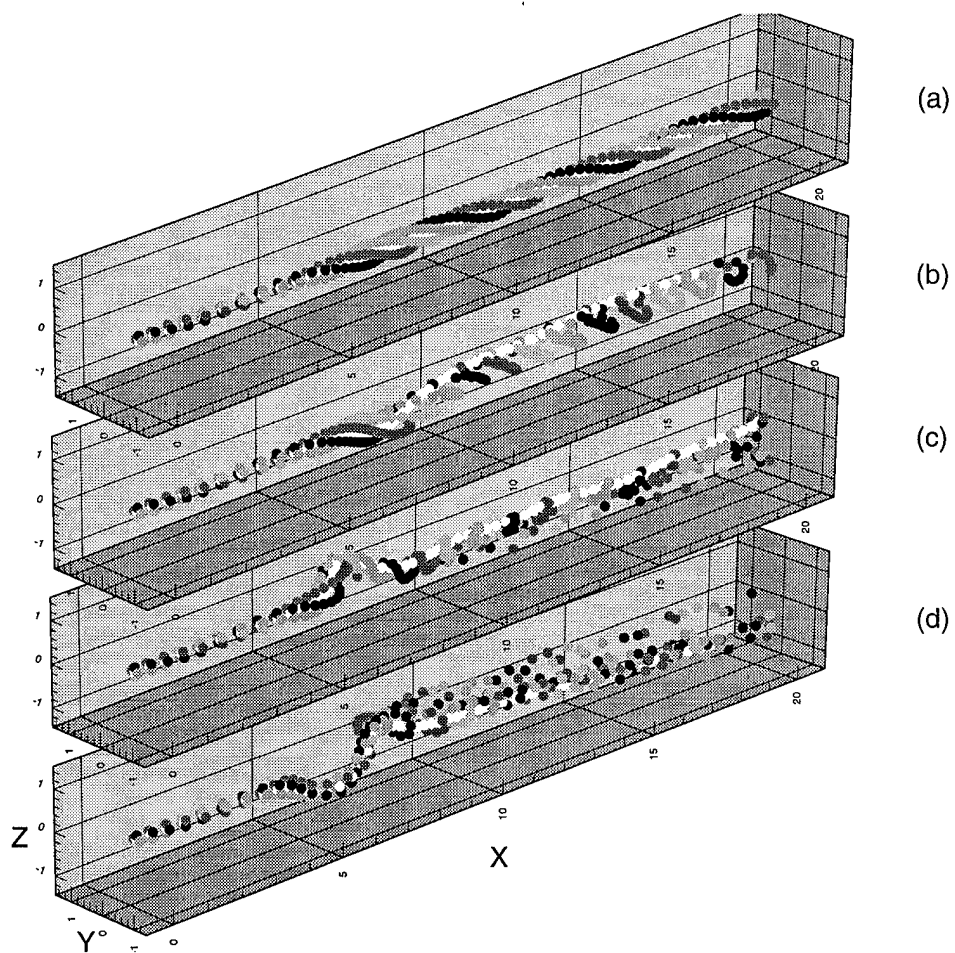


Figure 43. Particle traces showing development of three-dimensionality with increasing vortex strength: (a)  $\mathcal{V} = 1.5$ , (b)  $\mathcal{V} = 1.53$ , (c)  $\mathcal{V} = 1.65$ , (d)  $\mathcal{V} = 1.8$ .

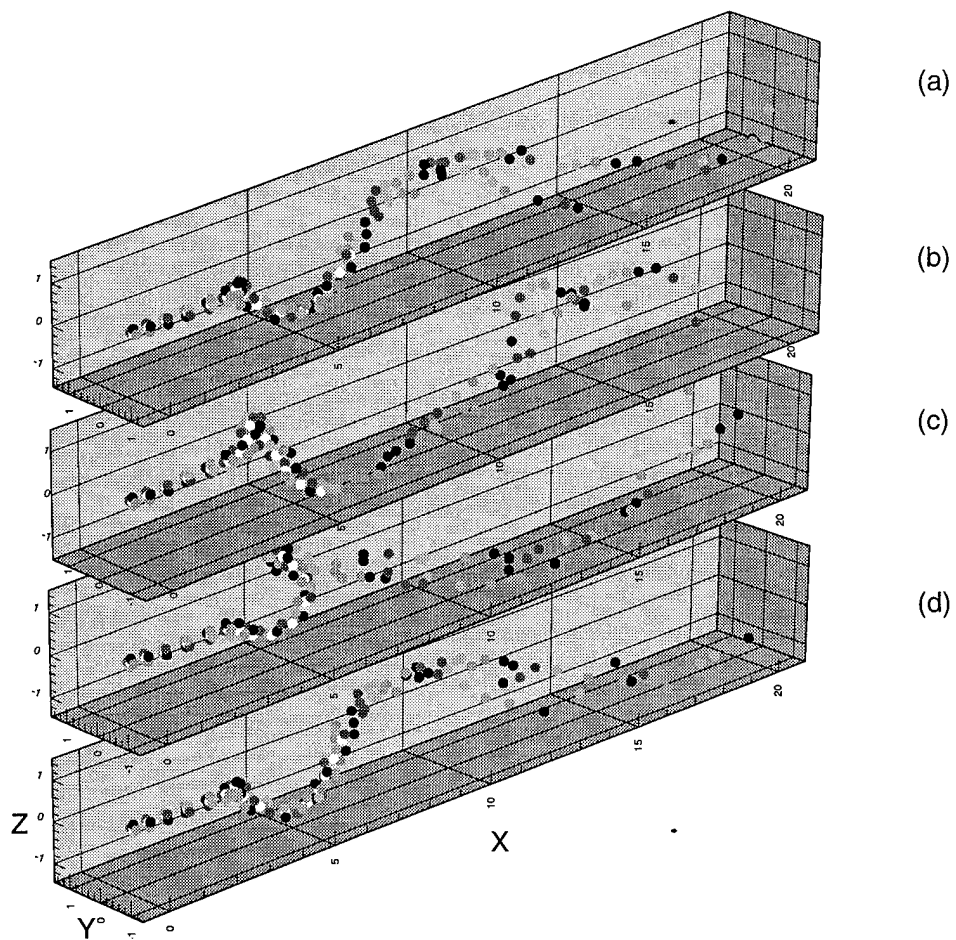


Figure 44. Particle traces showing periodic rotation of flow structure for  $\mathcal{V} = 2.3$ : (a)  $t = 426$ , (b)  $t = 427.2$ , (c)  $t = 428.8$ , (d)  $t = 430$ .

### 5.3 Results for $Re = 500$ .

In contrast to the axisymmetric solution paths for  $Re = 100$  and  $Re = 250$ , axisymmetric solution paths at  $Re = 500$  contain folds, resulting in *primary* and *secondary* limit points (Section B.1). The behavior of flows with vortex strengths prescribed near these solution folds is briefly presented in this chapter. A more detailed investigation is deferred until Section 5.4, where flows at  $Re = 1000$  are considered.

Results in Section 5.3.1 show that equilibrium solutions occur when the vortex strength is prescribed to be less than the primary limit point. In particular, the specification of three nonunique, axisymmetric initial conditions (at a vortex strength between the primary and secondary limit points) lead to three apparently identical time-asymptotic solutions which are steady and axisymmetric. When the vortex strength is prescribed to be greater than the primary limit point, a periodic, three-dimensional solution develops. The change in solution behavior is attributed to a Hopf bifurcation, believed by the author to lie at, or in very close proximity to the primary limit point. A similar change in solution stability near the primary limit point is found in Section 5.4 for  $Re = 1000$ .

The growth and decay of asymmetric flow is briefly examined in Section 5.3.2 to assess if such asymmetries are traveling upstream and contradicting the prescribed axisymmetric inflow conditions.

**5.3.1 Solution Behavior Near the Primary Limit Point.** In this section, four time-integrated solutions are obtained from the TANS model. The first three solutions are obtained by specifying nonunique, axisymmetric initial conditions, corresponding to a solution along the upper stable branch, the unstable branch, and the lower stable branch (Section B.1). The fourth solution is obtained by specifying a vortex strength slightly greater than the primary limit point.

The region of nonunique, axisymmetric PAC solutions is shown in Figure 45 for  $Re = 500$ . The chosen initial conditions for the TANS model are denoted with square symbols in the figure, with the corresponding TANS model parameters for these runs summarized in Table 13. The time-asymptotic values of  $Q$  are denoted with diamond symbols in the figure. The three runs at  $\mathcal{V} = 1.49$  are designated  $\mathcal{V} = 1.49^{s+}$ ,  $\mathcal{V} = 1.49^{s-}$ ,

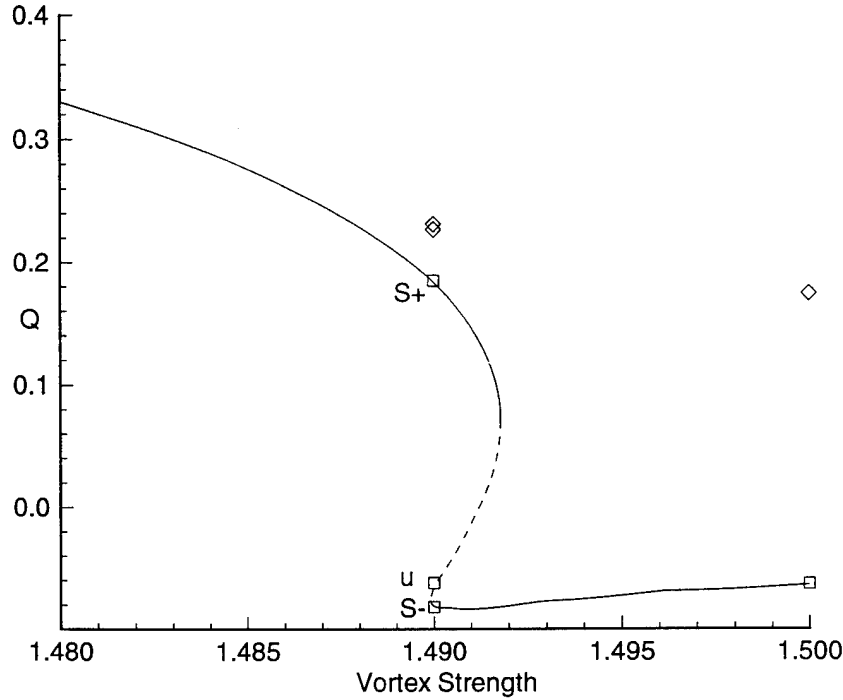


Figure 45. Axisymmetric solution path for  $Re = 500$  and  $M = 0.3$ : Stable branches; solid lines; unstable branch; dashed line; TANS initial conditions; square symbols.

and  $\mathcal{V} = 1.49^u$ , corresponding to the upper stable branch, the lower stable branch, and the unstable branch respectively. The primary and secondary limit points are encountered at  $\mathcal{V}_p = 1.4918$  and  $\mathcal{V}_s = 1.4899$  respectively.

The three runs computed before the primary limit point all migrate to apparently identical solutions near the initial condition at  $\mathcal{V} = 1.49^{s+}$ . It is believed by the author that differences in grid resolution are responsible for the differences in the three time-

Table 13. Summary of TANS model parameters for  $Re = 500$ .

Run No.	$Re$	$\mathcal{V}$	$M$	$\Delta t$	$\alpha$	BC	Grid	Accuracy (Time/Space)
32	500	$1.49^{s+}$	0.3	.040	0.05	2	G1	2nd/4th
33	500	$1.49^{s-}$	0.3	.040	0.05	2	G1	2nd/4th
34	500	$1.49^u$	0.3	.040	0.05	2	G1	2nd/4th
35	500	1.50	0.3	.040	0.05	2	G1	2nd/4th

Table 14. Summary of results for  $Re = 500$ .

Run No.	$\mathcal{V}$	$H$	$Q$
32	$1.49^{s+}$	0.010197	0.22685
33	$1.49^{s-}$	0.010198	0.22691
34	$1.49^u$	0.010194	0.23126
35	1.50	0.119011	0.17422

asymptotic solutions and the initial condition at  $\mathcal{V} = 1.49^{s+}$ . This issue is dealt with in more detail in Section 5.4.2.1. At  $\mathcal{V} = 1.5$ , the time-asymptotic value of  $Q$  (diamond symbol) is significantly larger than the initial value of  $Q$  (square symbol). This observation is consistent with results at  $Re = 100$  and  $Re = 250$  for solutions computed past the Hopf bifurcation point.

The minimum axial velocity component,  $Q$ , for Runs 32–34 is plotted versus time in Figure 46a. It is evident in all three runs,  $\mathcal{V} = 1.49^{s+}$ ,  $\mathcal{V} = 1.49^{s-}$ , and  $\mathcal{V} = 1.49^u$ , that the flow temporally evolves from a negative to a positive value of  $Q$ , indicating the elimination of a reversed flow region. The time-asymptotic solutions are found to be steady, since  $\Delta^n U_{\max}$  converges to values near  $10^{-6}$  at the end of these runs. The time-asymptotic solutions are also found to be axisymmetric by computing the values of  $H$ . The global parameter  $H$  characterizes the degree of flow asymmetry and is defined as the maximum absolute value of  $d\hat{v}/d\theta$ . The time-asymptotic values of  $H$  for each run are given in Table 14. The small values of  $H$  indicate that the solutions are virtually axisymmetric. Furthermore, it is found that small errors interpolation errors, as well as errors in computing  $H$  with discrete data, contribute greatly to the given values of  $H$ . For example, the value of  $H_2$ , corresponding to  $H$  for the initial (PAC) solution, interpolated onto the 3-D grid for  $\mathcal{V} = 1.49^{s+}$  is 0.00908. This is approximately 89% of the total value of  $H$ .

The fourth run (Run 35), computed at a vortex strength just past  $\mathcal{V}_p$ , is found to be time-periodic and three-dimensional.  $Q$  is plotted for this run in Figure 46b. Examination of the behavior of  $Q$  and  $\Delta^n U_{\max}$ , along with the computation of  $H$  in Table 14, indicates that the time-asymptotic behavior of Run 33 is unsteady and three-dimensional. Plots of  $v$ , and  $w$ , are shown in Figure 47a, with the corresponding phase plot of  $v$ , shown in

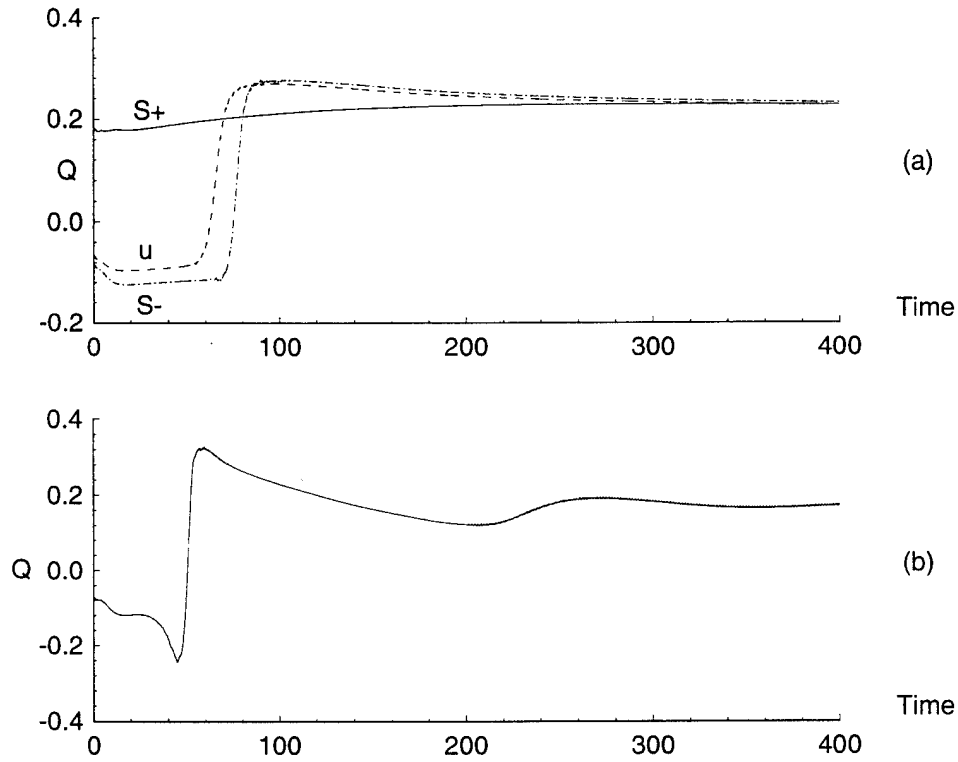


Figure 46.  $Q$  versus time for  $Re = 500$ : (a)  $\mathcal{V} = 1.49^{s+}$  (solid line),  $\mathcal{V} = 1.49^{s-}$  (dot-dash), and  $\mathcal{V} = 1.49^u$  (dashed), (b)  $\mathcal{V} = 1.5$ .

Figure 47b, where  $\delta t = 0.8$ . The periodic nature of  $v_s$  is evident in the figure. The phase plot of  $w_s$  is not shown, owing to the similarity between  $v_s$  and  $w_s$ . The axial velocity component  $u_s$  is found to be nearly steady in time, with no indications of periodic behavior.

The preceding results indicate that a distinct change in solution character occurs when  $\mathcal{V}$  is increased slightly from 1.49 to 1.50. All three solutions at  $\mathcal{V} = 1.49$  are steady and axisymmetric, while at  $\mathcal{V} = 1.5$  the flowfield is periodic and three-dimensional. In between the vortex strengths of 1.49 and 1.5 lies the primary limit point at  $\mathcal{V}_p = 1.4918$ . Thus, there is strong evidence that a Hopf bifurcation point lies at, or in very close proximity to, the primary limit point.

To further illustrate the change in solution behavior, a new parameter is introduced.  $\Omega_1$  is defined as the sum of  $v_s$  and  $w_s$ , where  $v_s$  and  $w_s$  are crossplane velocity components at a centerline location of  $x = 7$ . Figure 48 shows plots of  $\Omega_1$  versus time for the four runs

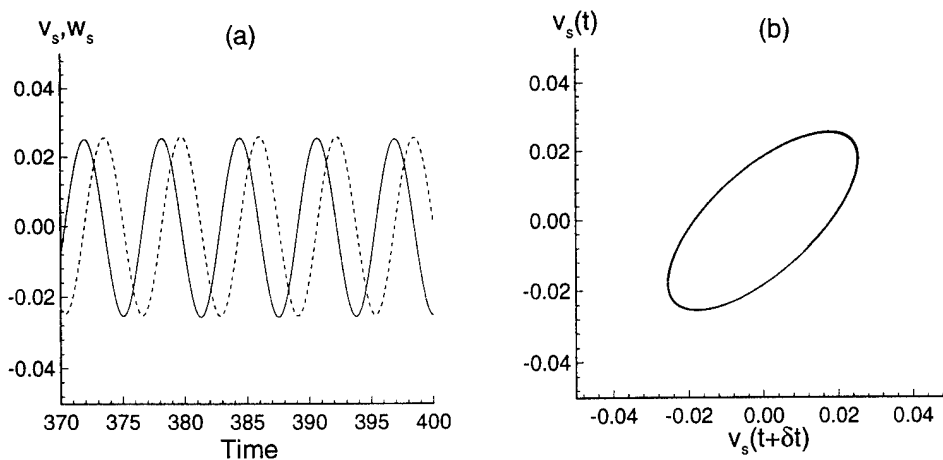


Figure 47. Periodic behavior of flow computed at  $\mathcal{V} = 1.5$  and  $Re = 500$ : (a)  $v_s$  (solid) and  $w_s$  (dashed) versus time, (b) phase plot of  $v_s$  for  $t = 370$  to  $t = 400$ .

at  $\mathcal{V} = 1.49$  and  $1.5$ . By comparing this figure to Figure 46, we see that for  $\mathcal{V} = 1.49^u$  and  $\mathcal{V} = 1.49^s$ , an asymmetric disturbance develops in Figure 48b-c which is coincident in time with the migration of  $Q$  from reversed to nonreversed flow. However, as time marches on, these disturbances decay and vanish. At  $\mathcal{V} = 1.5$ , a similar disturbance appears in Figure 48d which has almost twice the maximum amplitude as the other disturbances. The feature that distinguishes the flow at  $\mathcal{V} = 1.5$  from the other three is the reformation of an asymmetric disturbance near  $t = 200$ , which emerges after the transient disturbance vanishes. Figure 48 illustrates that asymmetric disturbances which appear at  $\mathcal{V} = 1.49$  do not survive, indicating stability to this type of disturbance. On the other hand, the flow computed past the primary limit point appears to be unstable to asymmetric disturbances, resulting in unsteady and three-dimensional flow.



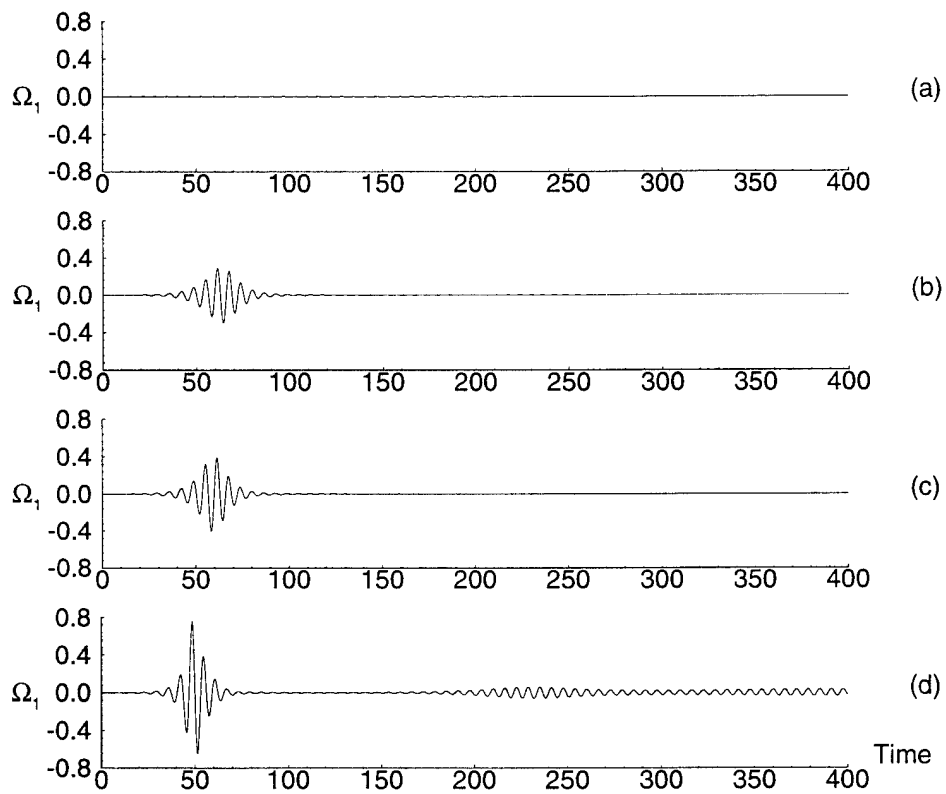


Figure 48.  $\Omega_1$  versus time for  $Re = 500$ : (a)  $\mathcal{V} = 1.49^{s+}$ , (b)  $\mathcal{V} = 1.49^u$ , (c)  $\mathcal{V} = 1.49^{s-}$ , (d)  $\mathcal{V} = 1.5$ .

### 5.3.2 *The Growth and Decay of Asymmetric Flow Near the Inflow Boundary.*

The development and decay of asymmetric flow for a fixed observation point is illustrated the last section in Figure 48b-c. Also of interest to this study is the movement of asymmetric disturbances. In particular, if an asymmetric disturbance is formed, it may be possible for the disturbance to propagate upstream. If this occurs, the disturbance could reach the inflow boundary, violating the assumption of axisymmetric inflow conditions.

The upstream propagation of asymmetric waves near the supercritical inflow boundary would require that asymmetric waves have a negative group velocity in supercritical flow. The criticality of axisymmetric waves is discussed in Section 2.1.1, however, little is known about the group velocity of asymmetric waves. The general conclusion of the few experimental investigations aimed at determining the group velocity of asymmetric waves (summarized by Leibovich (1984)) is that the group velocity of asymmetric waves in supercritical flow is positive, i.e. directed downstream.

To investigate how the developed asymmetries propagate in the runs considered here, a new parameter,  $\Omega_2(x, t)$  is created. This function is defined as the absolute value of the sum  $v(x, t) + w(x, t)$  along the centerline.  $\Omega_2(x, t)$  is plotted in Figure 49 at various times for Run 32. The selected times coincide with times when the maximum (positive) values of  $\Omega_1$  occur in Figure 48b. In Figure 49a, the data for times corresponding to increasing levels of the disturbance are shown, while in Figure 49b the (subsequent) times of the decaying disturbance are shown. Each line corresponds to a different time level, with alternating solid and dashed lines used to help delineate between them. The figure clearly shows the development and subsequent decay of the asymmetric disturbance. In addition, the most important observation in the current context is that the asymmetric disturbance is found to propagate downstream, consistent with the above-mentioned experimental findings. Thus, this limited investigation shows that the inflow assumption of axisymmetry is not being compromised.

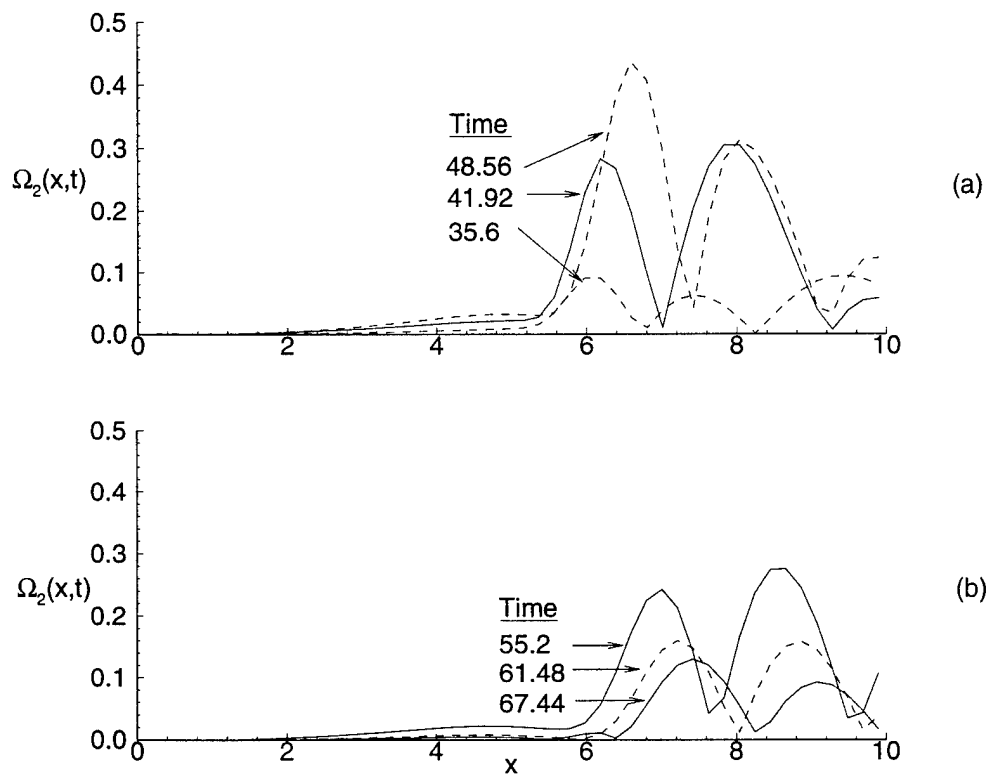


Figure 49. Growth and decay of asymmetric disturbance  $\Omega_2(x,t)$  versus  $x$  for various times: (a)  $t = 35.6, 41.92, 48.56$ , (b)  $t = 55.2, 61.48, 67.44$ .

#### 5.4 Results for $Re = 1000$ .

Results for flows at  $Re = 1000$  are presented in this section, with TANS run parameters summarized in Table 15.

The axisymmetric solution paths are shown in Section 5.4.1, using three different axisymmetric grids to assess solution sensitivity to node spacing and tube length. Initial conditions to the TANS model are selected from these axisymmetric solution paths.

Flows with vortex strengths prescribed to be less than the primary limit point are discussed in Section 5.4.2. In particular, three initial conditions are selected; one from each of the upper stable branch, lower stable branch and the unstable branch of axisymmetric solutions. Time-integration from these initial conditions, in the presence of a three-dimensional geometry, result in three nearly-equivalent time-asymptotic flows which are all axisymmetric and steady. Results for three different 3-D grids are shown to illustrate solution sensitivity to node spacing and tube length.

Flows with vortex strengths prescribed to be greater than (but close to) the primary limit point are presented in Section 5.4.3. These flows are found to be periodic and asymmetric, providing evidence of a Hopf bifurcation. A summary of Sections 5.4.2 and 5.4.3 is given in Section 5.4.4, along with further evidence indicating that a supercritical Hopf bifurcation occurs at or near the primary limit point. The loss of periodic flow as vortex strength is further increased past the Hopf point is discussed in Section 5.4.5.

Solution sensitivity to tube length for vortex strengths beyond the primary limit point is discussed in Section 5.4.6. The results indicate that a tube length of  $L = 20$  is sufficient for flows computed near the primary limit point. However, solutions for  $V = 1.7$ , computed for both  $L = 20$  and  $L = 30$  indicate that a tube length of at least  $L = 30$  is required. Based on this result, solutions computed past the primary limit point are obtained with  $L = 30$ .

Flow visualization is presented in Section 5.4.7. Flow disturbances visualized with numerical streaklines are found to be similar in form to those encountered at  $Re = 250$ .

Table 15. Summary of TANS run parameters for  $Re = 1000$ .

Run No.	$Re$	$\mathcal{V}$	$M$	$\Delta t$	$\alpha$	BC	Grid	Accuracy (Time/Space)
36	1000	1.475 <sup>s+</sup>	0.3	.040	0.05	2	G1	2nd/4th
37	1000	1.475 <sup>s-</sup>	0.3	.040	0.05	2	G1	2nd/4th
38	1000	1.475 <sup>u</sup>	0.3	.040	0.05	2	G1	2nd/4th
39	1000	1.475 <sup>s+</sup>	0.3	.025	0.05	2	G2	2nd/4th
40	1000	1.475 <sup>s-</sup>	0.3	.025	0.05	2	G2	2nd/4th
41	1000	1.475 <sup>u</sup>	0.3	.025	0.05	2	G2	2nd/4th
42	1000	1.47 <sup>s+</sup>	0.3	.025	0.05	2	G3	2nd/4th
43	1000	1.47 <sup>s-</sup>	0.3	.025	0.05	2	G3	2nd/4th
44	1000	1.47 <sup>u</sup>	0.3	.025	0.05	2	G3	2nd/4th
45	1000	1.50	0.3	.025	0.05	2	G3	2nd/4th
46	1000	1.60	0.3	.025	0.05	2	G3	2nd/4th
47	1000	1.70	0.3	.025	0.05	2	G3	2nd/4th
48	1000	1.90	0.3	.025	0.05	2	G3	2nd/4th
49	1000	1.90	0.3	.025	0.05	2	G4	2nd/4th
50	1000	2.10	0.3	.025	0.05	2	G3	2nd/4th

5.4.1 *Axisymmetric Solutions for  $Re = 1000$ .* Axisymmetric solutions from the PAC model are presented in this section to assess the impact of grid resolution and tube length. The axisymmetric solution paths are shown in Figure 50, where Figure 50a gives a “global” view and Figure 50b provides a “magnified” view near the region of solution nonuniqueness. The outer solid line (corresponding to the largest primary limit point,  $\mathcal{V}_p$ ) represents solutions computed with the  $98 \times 32$  (baseline) grid, g1. The dashed line illustrates the effect of grid refinement to  $122 \times 48$  nodes (grid g2). The inner solid line shows the effect of increasing the domain length from  $L = 20$  to  $L = 30$  using grid g3. The global view, Figure 50a, suggests that the effect of grid refinement and domain length are very small. However, the magnified view, Figure 50b, more clearly shows the acute sensitivity to both node spacing and domain length near the primary limit points.

Increasing the grid resolution (g1 to g2) results in a decrease in  $\mathcal{V}$  at the primary limit. The primary and secondary limit points for solutions on g1 are given by  $\mathcal{V}_p = 1.48052$  and  $\mathcal{V}_s = 1.46422$  respectively. For solutions computed on g2, the limit points are located at  $\mathcal{V}_p = 1.47685$  and  $\mathcal{V}_s = 1.45844$ . Increasing the domain length  $L$  also results in a decrease in the primary limit point. Solutions computed on g3 have a primary limit point  $\mathcal{V}_p = 1.47435$  and a secondary limit point  $\mathcal{V}_s = 1.45844$ .

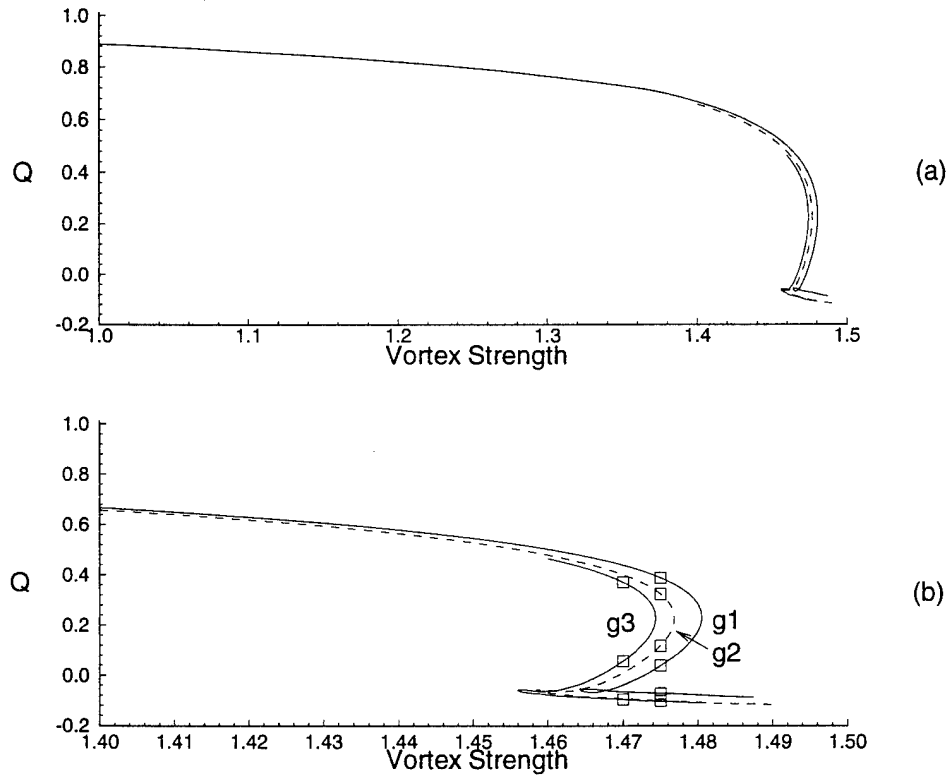


Figure 50. 2-D solution paths for  $Re = 1000$  and  $M = 0.3$ : (a) global view, (b) magnified view. Square symbols denote selected initial conditions for the TANS model.

Runs performed on grid g3 ( $L = 30$ ) are done so at a slightly smaller value of vortex strength than those runs considered with grids g1 and g2, due to the decrease in the primary limit points. The selected vortex strength for initial conditions computed on g1 and g2 is  $\mathcal{V} = 1.475$ , while a vortex strength of  $\mathcal{V} = 1.47$  is selected for initial conditions computed on grid g3.

Given the above locations of the primary and secondary limit points, it appears that the separation in  $\mathcal{V}$  between these points increases with increasing Reynolds number. At  $Re = 500$ , the primary and secondary limit points are separated by a distance of only 0.0019. This distance grows to 0.015 at  $Re = 1000$ ; a factor of 8 increase.

Compressibility appears to diminish the region of nonuniqueness. Beran and Culick (1992) report limit point separations ( $M = 0$ ) of about 0.012 and 0.04 for  $Re = 500$

and  $Re = 1000$  respectively, consistent with the observed trend with Reynolds number. However, these limit point separations for  $M = 0$  are much greater (for the same Reynolds number) as those reported here for  $M = 0.3$ . Morton (1989) similarly observed that increasing  $M$  in 2-D flows result in smaller regions of nonunique solutions, eventually leading to Mach numbers where only unique 2-D solutions exist.

*5.4.2 Solutions for Vortex Strengths Less Than  $V_p$ .* Solutions computed at vortex strengths below the primary limit point are presented in this section. In particular, three initial conditions, corresponding to solutions on the upper stable branch, lower stable branch and the unstable branch are considered. In addition, these three runs are repeated for grids G1, G2 and G3, and are discussed in Sections 5.4.2.1- 5.4.2.3 respectively. The initial conditions for Runs 36-44 are denoted with square symbols in Figure 50b. These runs are performed to determine if nonunique, axisymmetric initial conditions lead to nonunique solutions of the 3-D governing equations.

*5.4.2.1 Solutions Computed On Grid G1.* Figure 51 shows plots of  $Q$  as a function of time for Runs 36-38, which are computed with grid G1. Inspection of the time-asymptotic solutions indicates that all three solutions are steady and axisymmetric. Solution nonuniqueness, present in the 2-D solutions, is lost when time integration is performed with the three-dimensional governing equations.

The three solutions converge at a value of  $Q$  which is somewhat higher (7.2%) than the initial value of  $Q$  corresponding to the upper stable branch. There are at least two possible explanations for why the solutions did not converge near one of the three initial conditions. First, the difference between initial and final values of  $Q$  (i.e., for Run 34) may be attributed to differences in grid resolution between the PAC and TANS models. Second, it may be possible that there exists another stable solution near the one computed by the PAC model. Of these two possible explanations, the first seems the most likely, and is investigated below. The second explanation is not investigated. However, for incompressible flows, Beran and Culick (1992), Darmofal (1994) and Lopez (1994) do not observe disconnected branches of steady, axisymmetric solutions.

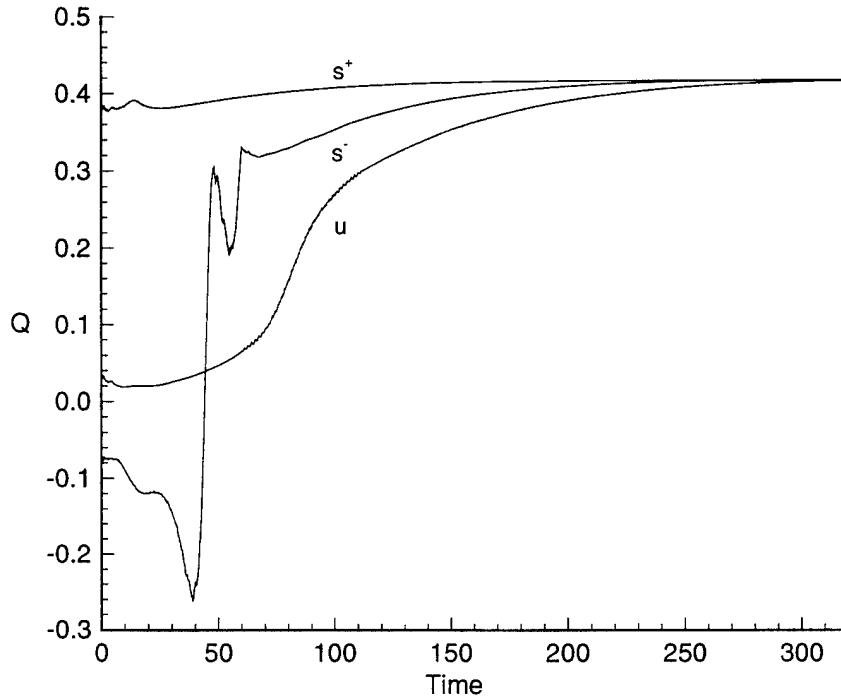


Figure 51.  $Q$  versus time for Runs 36-38 (grid G1).

The PAC model is second-order accurate (spatially) while the TANS model is fourth-order accurate. The higher accuracy of the TANS model generally allows for larger node spacings over those used by the PAC model. In particular, comparing grids g1 and G1, the average radial node spacings are about 0.0645 and 0.1 respectively. Increasing the radial node spacing to 0.086 with the PAC model and recomputing the 2-D solution for the upper stable branch results in a larger value of  $Q$ , which is much closer to the time-asymptotic value achieved by the TANS model. Changing the axial node spacing has a minimal effect on  $Q$ . Therefore, it is suspected that a lack of crossplane grid resolution in the TANS model is responsible for the deviation away from the initial (2-D) value of  $Q$ .

A scenario in which different node spacings are used in models of different spatial accuracies is depicted in Figure 52. The conceptual behavior of  $Q$  with the average radial node spacing,  $\Delta r$ , is illustrated, where decreasing  $\Delta r$  is equivalent to increasing  $1/\Delta r$ . It



has generally been observed in this study that increasing  $1/\Delta r$  results in a decrease in  $Q$  until a converged value is reached. The finer grid resolution allows for better definition of the decelerated region and minimizes the effects of numerical viscosity. The two curves in the figure correspond to the fourth-order model (TANS) and the second-order model (PAC). The radial node spacings of the PAC and TANS models are denoted  $\Delta r_2$  and  $\Delta r_4$  respectively. It is evident from the figure that if  $1/\Delta r_2 = 1/\Delta r_4$ , the TANS model will produce a more accurate (or equal) value of  $Q$  over the PAC model. Furthermore, convergence with the TANS model is achieved with a larger radial spacing. However, having two different radial spacings can lead to different values of  $Q$ , if grid convergence has not been achieved in one or both models. A lack of grid resolution can result in a slightly higher value,  $Q = Q_4$ , in the TANS model over the initial condition,  $Q = Q_2$ . Finally, it is evident that agreement in  $Q$  between the TANS and PAC models is a strong indication that *both* models are employing sufficiently resolved grids. This is the case for  $Re = 250$ , where initial and final values of  $Q$  agreed to within 1% for flows computed on G1 (Figure 29a). More of a deviation in  $Q$  is evident for grid G2 in Figure 29a, since g1 (and not g2) is used to compute the initial solution.

The conclusion to be drawn from the preceding discussion is that the baseline grid, G1, is not adequate for resolving the 3-D flowfield at  $Re = 1000$ , due primarily to a lack of sufficient grid resolution in the crossplane.

*5.4.2.2 Solutions Computed On Grid G2.* This section presents results where the three runs performed in the last section are better resolved by changing from grid G1 to grid G2. Runs 36-38 are recomputed on grid G2 and are denoted as Runs 39-41. Grid G2 decreases the average radial spacing by increasing the number of crossplane nodes from  $41^2$  to  $61^2$ , and by clustering axial nodes. The minimum axial spacing for G2 is about 0.1 at  $x = 5$ , whereas the constant axial spacing for G1 is about 0.2. Figure 53 compares  $Q$  as a function of time for the three initial conditions at  $V = 1.475$  with grid G2. Generally, the behavior of  $Q$  is similar to the behavior observed in the previous three runs. However, all three runs are converging to a final value of  $Q$  which is within about 1% of the initial  $Q$  computed on the upper stable branch. Longer run times are apparently required to show

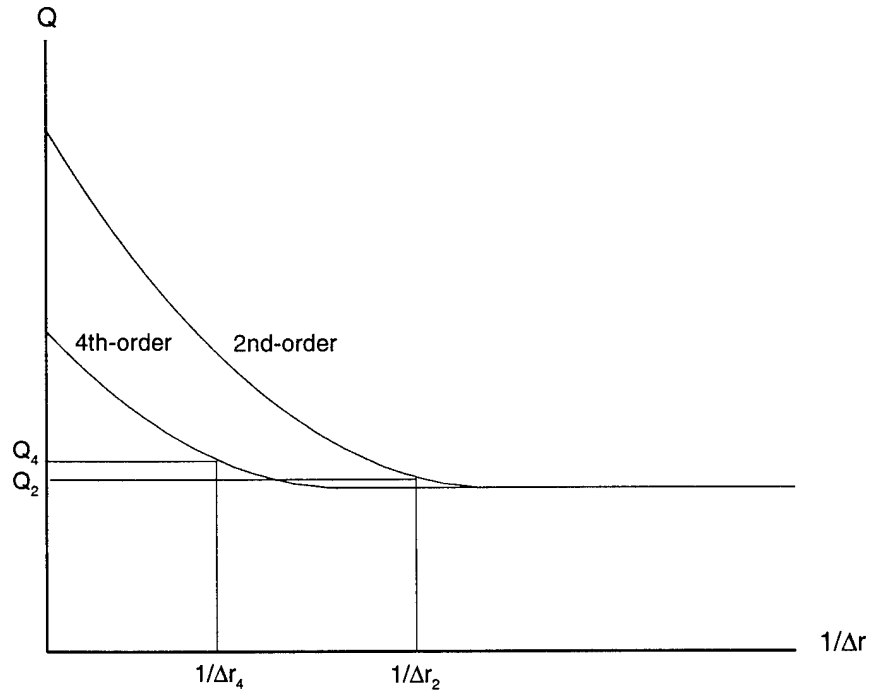


Figure 52. Schematic representation of grid convergence for second and fourth-order schemes.

full convergence of the three solutions. However, these runs were not carried out further in time, since sufficient convergence is evident on the coarser grid, G1.

*5.4.2.3 Solutions Computed On Grid G3.* The effect of domain length on the temporal behavior of  $Q$  is assessed by repeating the previous three runs using grid G3, which extends the tube length from  $L = 20$  to  $L = 30$  with node spacings held fixed. The results are shown in Figure 54. Despite the slight differences in initial conditions ( $V = 1.47$ ) from runs computed on G2, the qualitative behavior of  $Q$  as a function in time remains basically the same as that observed in Runs 36–38. Therefore, it is concluded that grid G2 is adequate for resolving the flowfields for  $Re = 1000$ , at least for vortex strengths below the primary limit point.

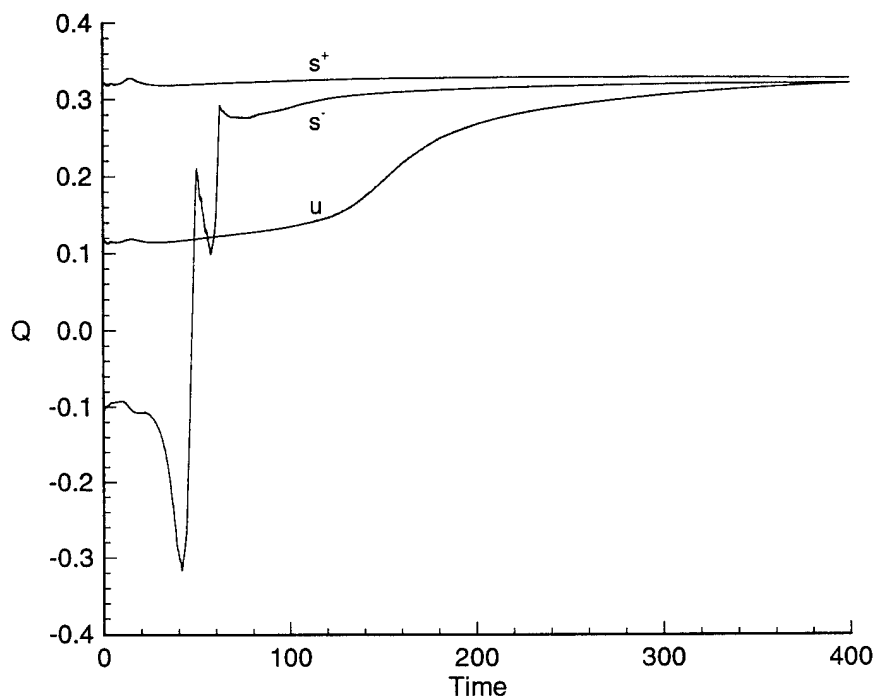


Figure 53.  $Q$  versus time for runs 39-41 (grid G2).

5.4.3 *Solutions for Vortex Strengths Greater than  $\mathcal{V}_p$ .* Time histories of  $Q$  are presented in this section for flows with vortex strengths greater than  $\mathcal{V}_p = 1.47435$ . In particular, vortex strengths of  $\mathcal{V} = 1.5$  and  $\mathcal{V} = 1.6$  are considered using grid G3.

The deviations from the initial conditions are illustrated in Figure 55, where  $Q$  is plotted versus time for  $\mathcal{V} = 1.5$  and  $1.6$ . In Figure 55a ( $\mathcal{V}=1.5$ ) it is evident that an appreciable deviation from the initial condition is present—similar to the transient that developed from the initial condition at  $\mathcal{V} = 1.47^{+-}$ . The initial axisymmetric flow at  $\mathcal{V} = 1.5$  has reversed flow, since the initial value of  $Q$  is negative. The time-asymptotic value of  $Q$  at  $\mathcal{V} = 1.5$  is positive, indicating the absence of reversed flow. Eventually, the behavior of  $Q$  time asymptotes to periodic behavior, which is not discernable from the scales of the figure (time periodicity is discussed later in Section 5.4.4). Furthermore, an

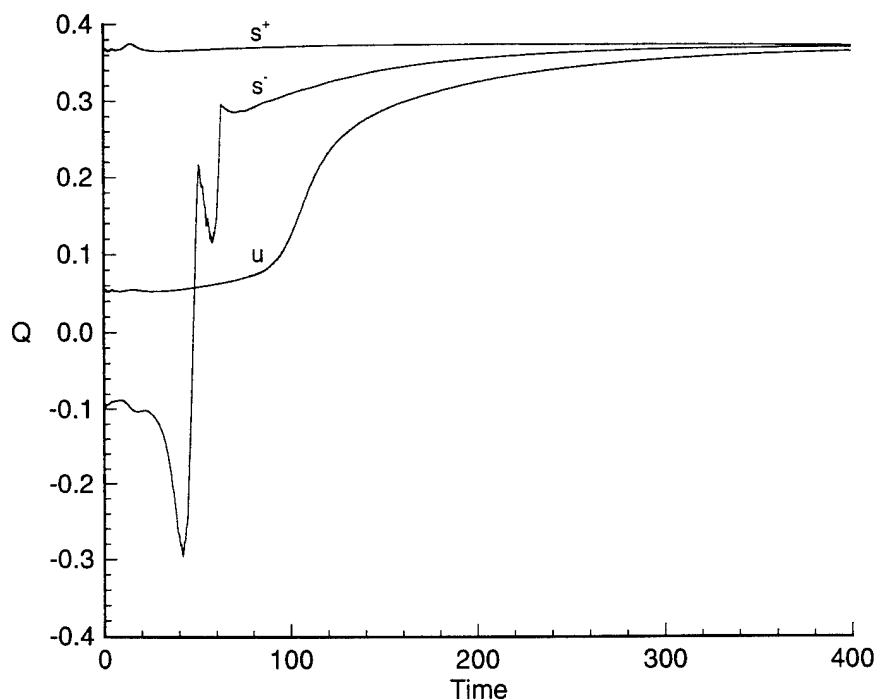


Figure 54.  $Q$  versus time for Runs 42-44 (grid G3).

overall increase in  $Q$ , consistent with results at  $Re = 250$ , is evident. This increase in  $Q$  was correlated with the production of radial vorticity in Section 5.2.2.

Figure 55b shows the behavior of  $Q$  for  $\mathcal{V} = 1.6$ . Here the initial and final values of  $Q$  are negative, with time-periodic behavior developing near the end of the run. Thus, there exists a small region in  $\mathcal{V}$  between at least 1.5 and 1.6 where initially symmetric and reversed flows time-asymptote to 3-D flows without reversed flow. This behavior is also evident at  $Re = 250$  for flows computed past the Hopf bifurcation near  $\mathcal{V} = 1.53$ .

**5.4.4 Evidence of a Hopf Bifurcation Near the Primary Limit Point.** In Section 5.4.2, the behavior of  $Q$  for solutions computed before the primary limit are presented, claiming these flows to be steady and axisymmetric. In Section 5.4.3,  $Q$  values are presented for solutions computed after the primary limit point, claiming these flows

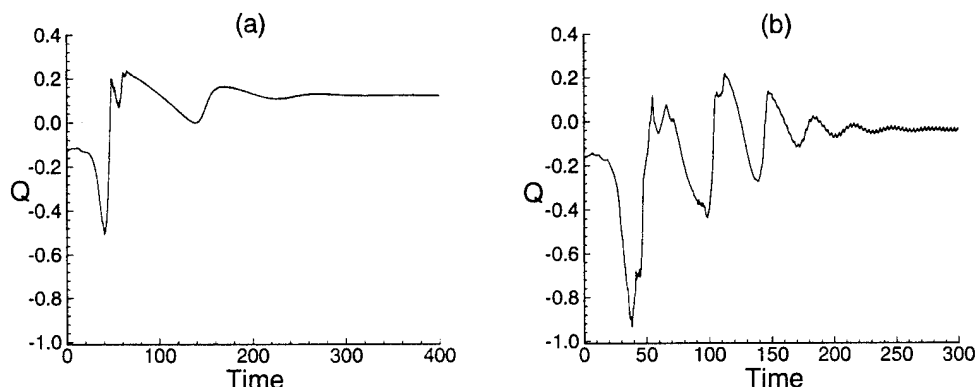


Figure 55.  $Q$  versus time for  $M = 0.3$  and  $Re = 1000$ : (a)  $\mathcal{V} = 1.5$ , (b)  $\mathcal{V} = 1.6$ .

to be three-dimensional and periodic. In this section, these claims are substantiated by presenting the nature of the solutions before and after the primary limit point.

Flows computed before the primary limit point are steady and axisymmetric. Runs 36–44 are found to be steady by monitoring the value of  $\Delta^n U_{\max}$  and observing the steady reduction of this parameter to levels near  $10^{-6}$ . The flows are found to be axisymmetric by computing the value of  $H$  at the end of each run.  $H$  is a global parameter, defined as the maximum absolute value of  $d\hat{v}/d\theta$ . Typical values of  $H$  are found to be about 0.0084 for Runs 42–44.

The periodic nature of flows computed past  $\mathcal{V}_p$  is illustrated in Figures 56–57. Figure 56 contains plots of  $v_s$  and  $w_s$ , where nonzero values of  $v_s$  and  $w_s$  indicate three-dimensional flow. At  $\mathcal{V} = 1.47^{s+}$ , both  $v_s$  and  $w_s$  are virtually zero, indicating an axisymmetric flow. Slightly beyond the primary limit point at  $\mathcal{V} = 1.5$  and  $1.6$ , a periodic oscillation in  $v_s$  and  $w_s$  is observed. The axial velocity component,  $u_s$ , (Figure 57) is also observed to be unsteady at  $\mathcal{V} = 1.6$ , however, any axial velocity fluctuations for  $\mathcal{V} = 1.5$  were too small to detect.

Phase plots of  $u_s$  and  $v_s$  for  $\mathcal{V} = 1.5$  and  $1.6$  are presented to further assess the periodicity of these flows. Figure 58 shows phase plots for  $\mathcal{V} = 1.5$  and  $1.6$  for  $\delta t = 0.5$ . Only the crossplane velocity component,  $v_s$ , is shown for  $\mathcal{V} = 1.5$ , owing to the time-independence of  $u_s$ . The crossplane velocity component,  $v_s$ , is found to be nearly perfectly

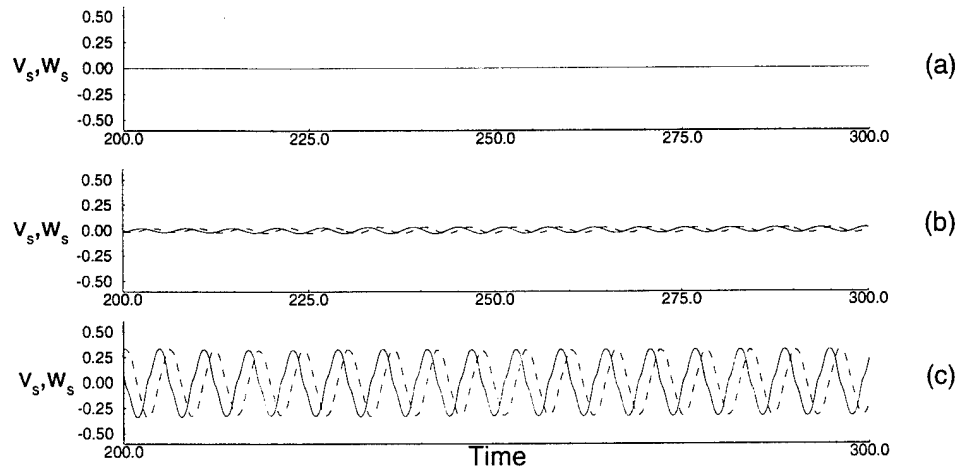


Figure 56. Crossplane velocity components  $v_s$  and  $w_s$  versus time for  $Re = 1000$  ( $v_s(t)$  (solid);  $w_s(t)$  (dashed)): (a)  $\mathcal{V} = 1.47^{*+}$ , (b)  $\mathcal{V} = 1.5$ , (c)  $\mathcal{V} = 1.6$ .

periodic, with between 7-9 periods of data depicted in the figure. Periodicity is not strictly observed in  $u_s$  for  $\mathcal{V} = 1.6$ . There are at least two possible explanations for this result. First, the amplitude of the oscillation in  $u_s$  is much smaller than that of  $v_s$ , making it more susceptible to numerical errors. Second, the axial velocity component has been found to take longer to reach a time-asymptotic state, which can cause a phase plot to drift.

Finally, the nature of the Hopf bifurcation is illustrated in a manner similar to results for  $Re = 250$ , Section 5.2. Plots of the parameters  $H$ ,  $\Omega$ , and  $Q$  for flows computed before and after  $\mathcal{V}_p$  are shown in Figure 59. Data presented in the figure is taken from computations on grid G3, and is summarized in Table 16. Figures 59a-b show that flows computed before the primary limit point at  $\mathcal{V}_p = 1.47435$  are axisymmetric and steady. Flows computed after the primary limit point are both three-dimensional and periodic. The loss of stability of equilibrium solutions to time-periodic solutions is evidence for a Hopf bifurcation.

The fact that  $\Omega$  steadily increases from zero near  $\mathcal{V}_p$  is evidence for the supercritical type of Hopf bifurcation (Section B.1). Figure 59c shows that the path of axisymmetric solutions branch off near the primary limit point to form a branch of three-dimensional flows. Solutions on the branch of 3-D flows near the primary limit point do not contain

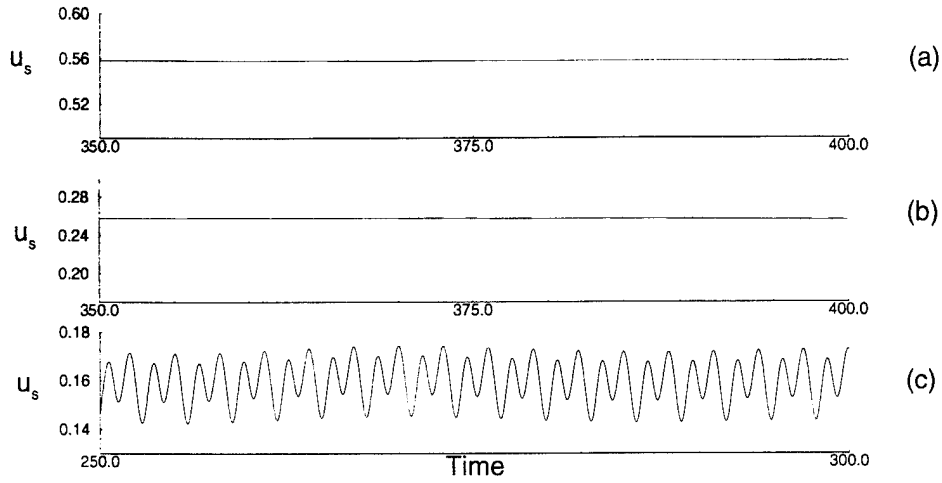


Figure 57. Axial velocity component  $u_s$  versus time for  $Re = 1000$ : (a)  $\mathcal{V} = 1.47^{s+}$ , (b)  $\mathcal{V} = 1.5$ , (c)  $\mathcal{V} = 1.6$ .

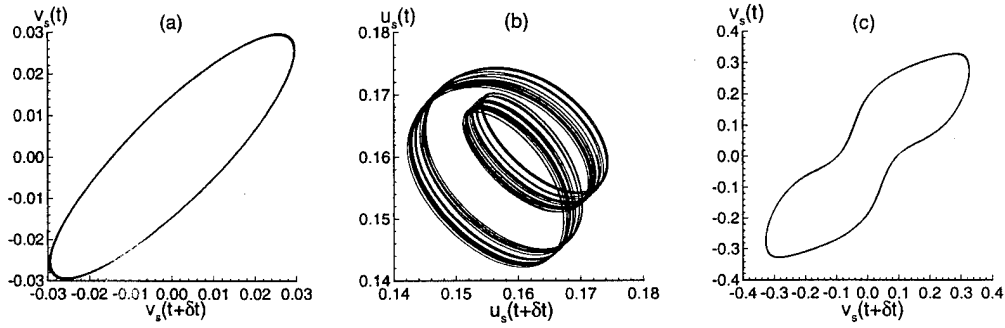


Figure 58. Phase plots for  $\mathcal{V} = 1.5$  and  $1.6$ : (a)  $v_s(t)$ ,  $\mathcal{V} = 1.5$ , (b)  $u_s(t)$ ,  $\mathcal{V} = 1.6$ , (c)  $v_s(t)$ ,  $\mathcal{V} = 1.6$ .

reversed flow. Reversed flow is not achieved until the vortex strength is increased to  $\mathcal{V} = 1.6$ .

**5.4.5 Results for Further Increases in  $\mathcal{V}$ .** Further increases in vortex strength past  $\mathcal{V} = 1.6$  yield two significant changes in temporal behavior from the periodic solutions computed between  $\mathcal{V} = 1.5$  and  $\mathcal{V} = 1.6$ . The first change is the appearance of a large-scale, periodic fluctuation in the time-asymptotic value of  $Q$ . The second change is the loss of time-periodic behavior in the velocity components  $u_s$ ,  $v_s$  and  $w_s$ . These changes are attributed to additional bifurcations of the flow. The observed changes in flow behav-

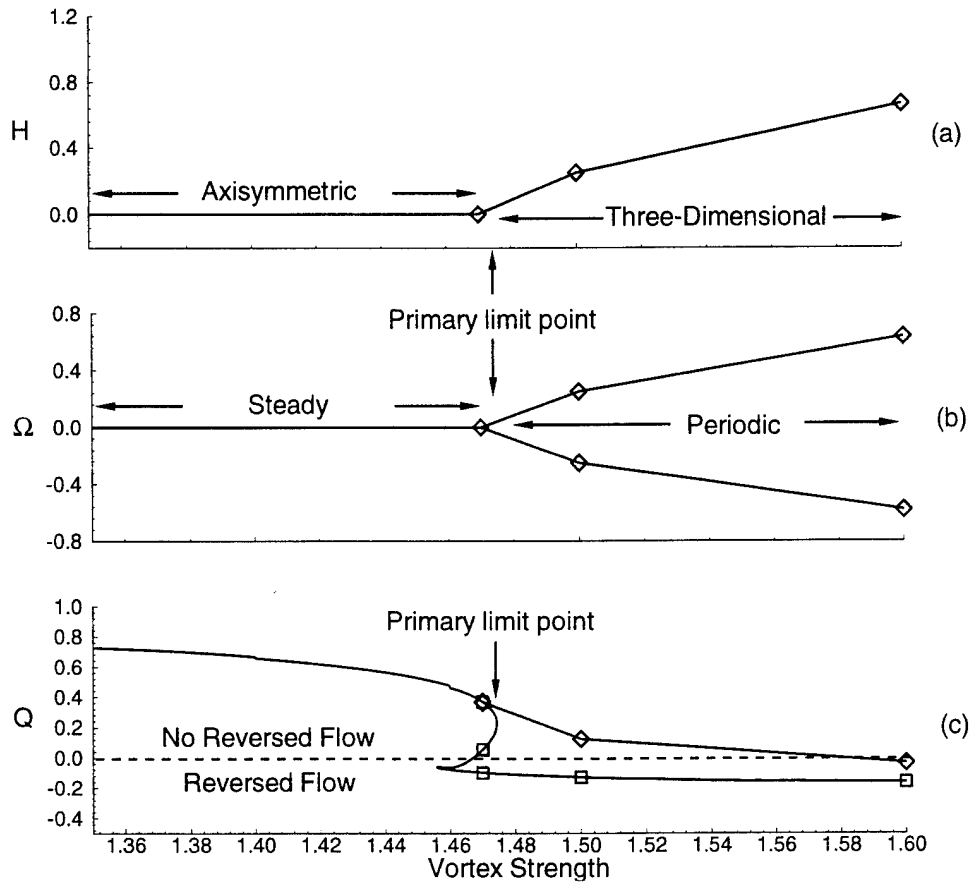


Figure 59. Evidence of a Hopf bifurcation near the primary limit point for  $Re = 1000$ .

ior are also discussed in light of results of Lopez (1994), who computed time-dependent, axisymmetric solutions under similar conditions and geometry.

The behavior of  $Q$  for  $\mathcal{V} = 1.7, 1.9$  and  $2.1$  is shown in Figure 60. In contrast to the time-asymptotic nature of  $Q$  at lower values of  $\mathcal{V}$ ,  $Q$  shown here consists of both a small and large-scale oscillation. The large-scale oscillation is clearly evident in the figure, with the smaller scale oscillation barely visible. At  $\mathcal{V} = 2.1$ ,  $Q$  appears to have lost any large-scale periodic behavior.

The velocity components  $u$ ,  $v$ , and  $w$ , for  $\mathcal{V}$  greater than  $1.6$  are no longer periodic. Figure 61 shows that the crossplane velocity components  $v$ , and  $w$ , are nearly periodic in nature for  $\mathcal{V} = 1.7$  and  $1.9$ . However, periodicity is totally lost at  $\mathcal{V} = 2.1$ , consistent with the irregular behavior of  $Q$  at this vortex strength. For  $\mathcal{V} = 1.7$  and  $1.9$ , Figure 62 depicts



Table 16. Summary of computed flow parameters for  $Re = 1000$ .

$\mathcal{V}$	$H$	$\Omega$	$Q$ (2-D)/(3-D)	Period
1.47 <sup>s+</sup>	.0084	-0.0001/0.0001	.369/ .371	-
1.47 <sup>u</sup>	.0084	-0.0001/0.0002	.056/ .364	-
1.47 <sup>s-</sup>	.0084	-0.0003/0.0004	-.098/ .369	-
1.50	.2491	-0.2513/0.2513	-.128/ .124	6.05
1.60	.6653	-0.5080/0.5080	-.159/-.032	6.05

a fundamental change in the behavior of the axial velocity component  $u_s$  over the behavior at lower values of  $\mathcal{V}$ . High frequency oscillations in  $u_s$  are observed which are superimposed on a lower frequency oscillation. The period associated with the lower frequency behavior is about 24 time units, which is about a factor of four over the period of 6.05 for  $u_s$ ,  $v_s$  and  $w_s$  at  $\mathcal{V} = 1.6$ . At  $\mathcal{V} = 2.1$ , periodicity is lost in  $u_s$ , as it is in  $Q$ ,  $v_s$  and  $w_s$ .

Phase plots for the three vortex strengths are shown in Figure 63. Figure 63a-d confirms that flows computed at  $\mathcal{V} = 1.7$  and 1.9 are found to be nearly periodic in  $v_s$  and  $w_s$  and aperiodic in  $u_s$ . A further increase in  $\mathcal{V}$  to 2.1 results in aperiodic behavior in both  $u_s(t)$  and  $v_s(t)$ , as evident in Figure 63e-f.

The preceding plots of  $Q$  and the velocity components indicate changes in solution behavior between  $\mathcal{V} = 1.6$  and 1.7, and between  $\mathcal{V} = 1.9$  and 2.1. The occurrence of additional bifurcations from the original Hopf bifurcation near the primary limit point is the most likely explanation for these changes in solution behavior. The classification of such secondary bifurcations is beyond the scope of this work.

The results of Lopez (1994) provide additional information which may help correlate the observed loss of stability of periodic solutions. Lopez (1994) studied the time-dependent behavior of axisymmetric solutions for  $Re = 250$  to 1000 and for similar vortex strengths considered in this work. The tube geometry is identical to the geometry used in this work, with similar node spacings. Lopez (1994) found that for  $Re = 1000$ , both steady and unsteady axisymmetric solutions coexist for vortex strengths beyond  $\mathcal{V} \approx 1.63$ . The branch of 2-D, unsteady solutions is computed up to  $\mathcal{V} = 1.7$ . The appearance of this unsteady branch of axisymmetric solutions corresponds well with the development of large-amplitude oscillations observed in this study starting at  $\mathcal{V} = 1.7$ . This may be another example of

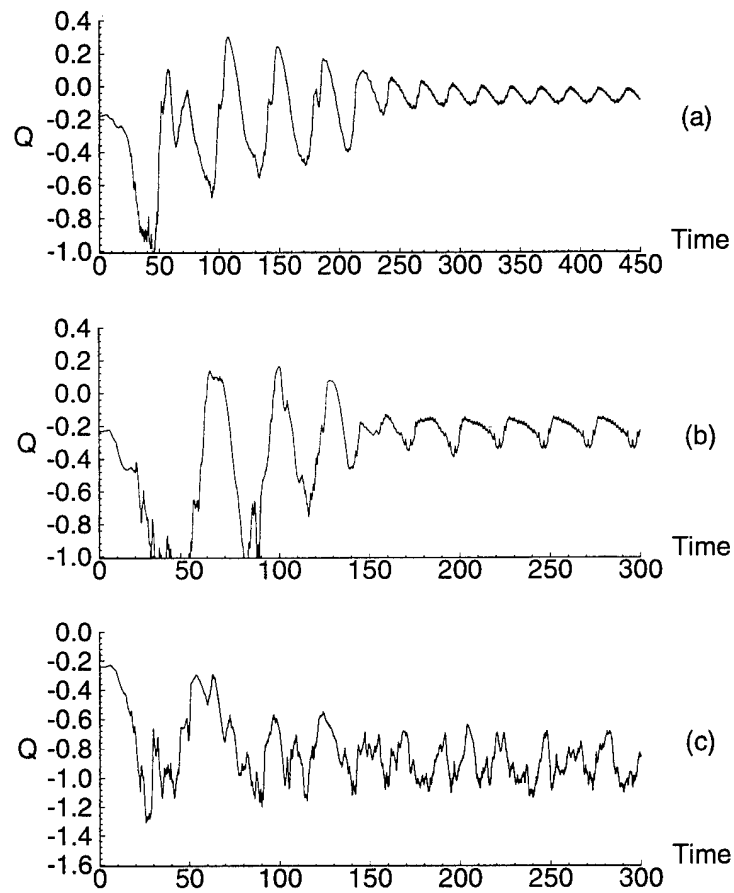


Figure 60.  $Q$  versus time for  $Re = 1000$  and  $M = 0.3$ : (a)  $\mathcal{V} = 1.7$ , (b)  $\mathcal{V} = 1.9$ , (c)  $\mathcal{V} = 2.1$ .

how changes in the underlying axisymmetric solution space can also correspond to changes in the 3-D solution space. The first example is the close proximity of the primary limit point, evident in paths of axisymmetric solutions, to the Hopf bifurcation observed in 3-D flows.

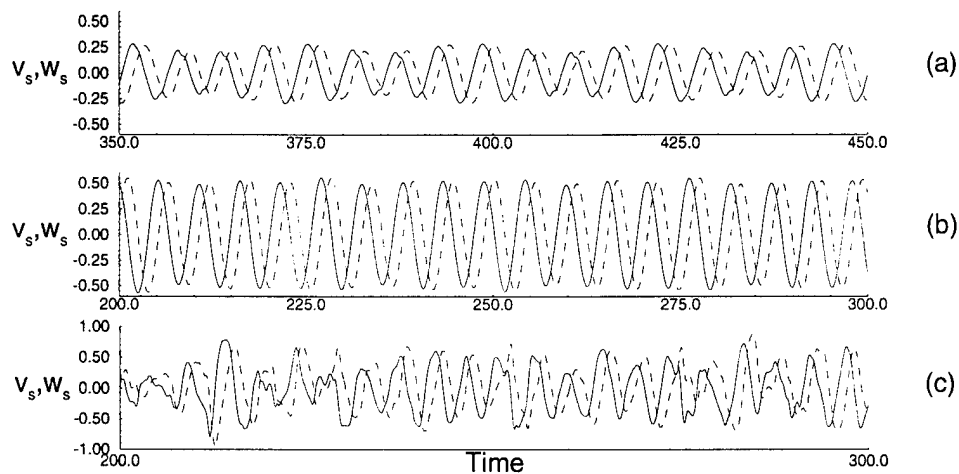


Figure 61. Crossplane velocity components  $v_s$  and  $w_s$  versus time for  $Re = 1000$  ( $v_s(t)$  (solid);  $w_s(t)$  (dashed)): (a)  $Nu = 1.7$ , (b)  $Nu = 1.9$ , (c)  $Nu = 2.1$ .

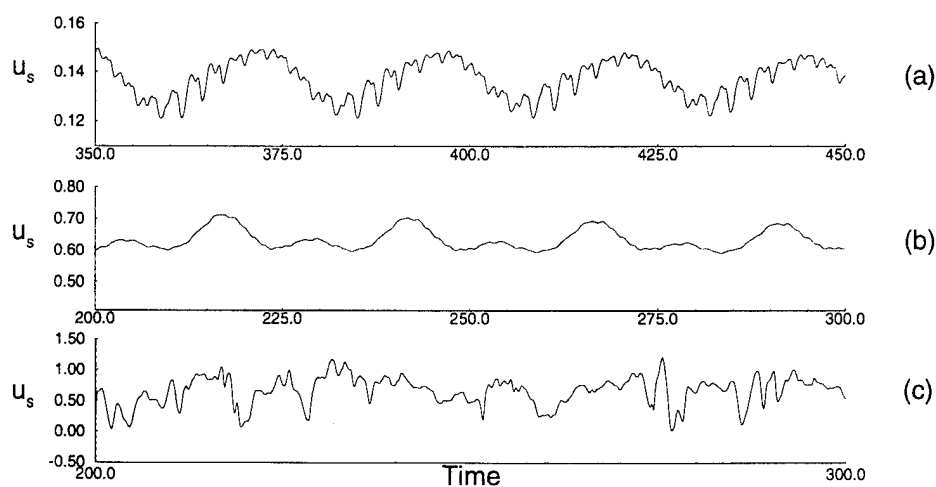


Figure 62. Axial velocity component  $u_s$  versus time for  $Re = 1000$ : (a)  $Nu = 1.7$ , (b)  $Nu = 1.9$ , (c)  $Nu = 2.1$ .

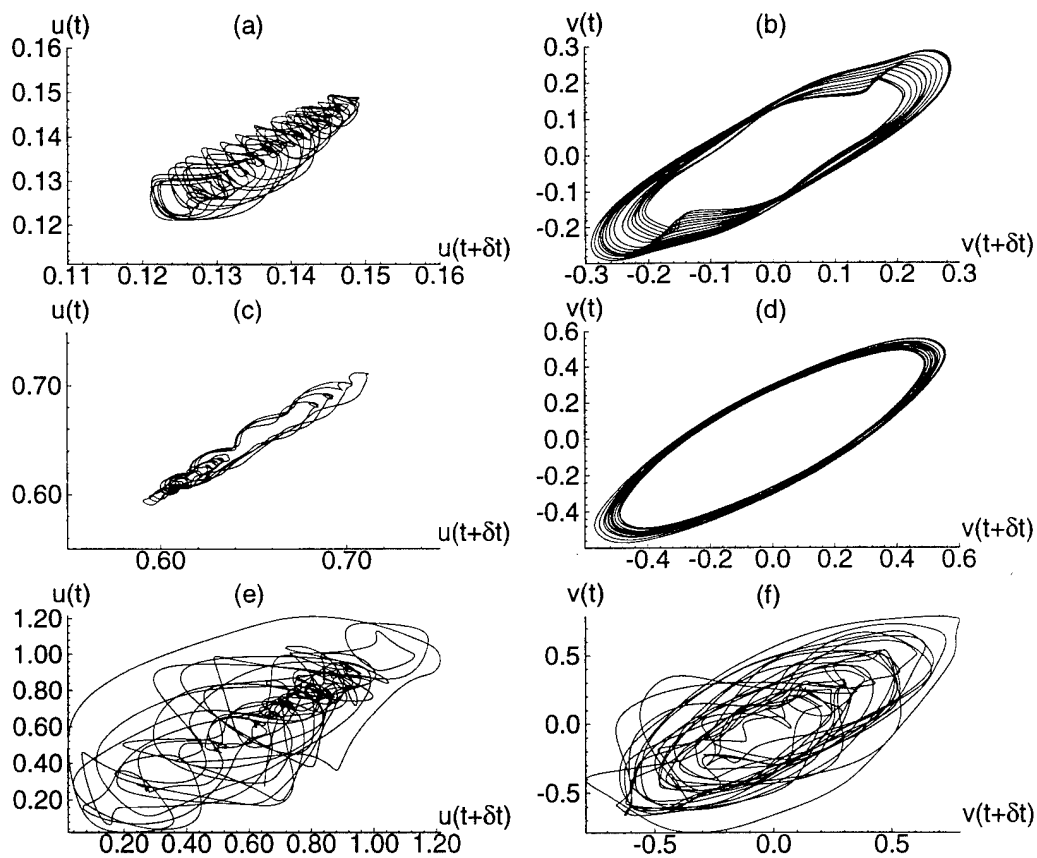


Figure 63. Phase plots showing loss of periodic behavior: (a)  $u_s$ ,  $\mathcal{V} = 1.7$ , (b)  $v_s$ ,  $\mathcal{V} = 1.7$ , (c)  $u_s$ ,  $\mathcal{V} = 1.9$ , (d)  $v_s$ ,  $\mathcal{V} = 1.9$ , (e)  $u_s$ ,  $\mathcal{V} = 2.1$ , (f)  $v_s$ ,  $\mathcal{V} = 2.1$ .

*5.4.6 Solution Sensitivity to Tube Length.* The results of Section 5.4.2.3 show that a tube length of  $L = 20$  is adequate for computing flows when  $\mathcal{V} < \mathcal{V}_p$  and  $Re = 1000$ . Results in this section show that a further extension in tube length to  $L = 30$  is required at higher vortex strengths.

Figure 64 shows the effect of further increases in tube length. From inspection of Figure 64a, it appears that a tube length of  $L = 20$  is adequate for  $\mathcal{V} = 1.5$ . This result is consistent with the results of Section 5.4.2.3, where a tube length of  $L = 20$  is found to be sufficient for  $\mathcal{V} = 1.47$ . However, a substantial solution impact is evident at  $\mathcal{V} = 1.7$ , where the tube length is increased from  $L = 20$  to  $L = 30$ . This observed sensitivity to tube length prompted all runs computed past the primary limit point to be run with a tube length of 30. A further extension of the tube to  $L = 40$  is considered in Figure 64c for  $\mathcal{V} = 1.9$ , where it is evident that only small deviations in  $Q$  occur when the tube is lengthened. Therefore, it is concluded that runs at  $Re = 1000$  generally require tube lengths of  $L = 20$  for vortex strengths up to the primary limit point. A tube length of  $L = 30$  is adequate for vortex strengths greater than the primary limit point.

The solution sensitivity to tube length at  $\mathcal{V} = 1.7$  is most likely the result of the flow transitioning from subcritical to supercritical between  $x = 20$  and  $x = 30$ . If the flow is subcritical at  $x = 20$ , then small, axisymmetric disturbances introduced by the downstream boundary condition may propagate upstream, affecting the transient solution. Increasing the tube length allows the flow to make the transition to supercritical before the outflow boundary is encountered. Then, since the flow is supercritical, disturbances can only convect downstream.

The observed sensitivity to tube length at  $\mathcal{V} = 1.7$  is consistent with the 2-D results presented by Darmofal (1994), where for  $Re = 1000$  and similar node spacings, flow criticality was computed for a converging tube similar to the one used in this study. At the onset of breakdown, the flow is subcritical in the (axial) vicinity of reversed flow, and does not recover to supercritical flow until approximately  $x = 24$ .

*5.4.7 Flow Visualization for  $Re = 1000$ .* The types of flow disturbances observed at  $Re = 1000$  are similar to the disturbances documented at  $Re = 250$  in Section 5.2. The

recognizable disturbances are the Type 6 disturbance and the spiral (Type 2) mode of breakdown. Detailed descriptions of these flow types are contained in Section 5.2.

Particle traces for flows at  $\mathcal{V} = 1.47^{*+}$ , 1.5 and 1.6 are shown in Figure 65. An axisymmetric flow is evident in Figure 65a, where a mild region of axial flow deceleration occurs near  $x = 5$ . This vortex strength is slightly below the primary limit point, where flows are found to be steady and axisymmetric. The first sign of asymmetric behavior is evident in Figure 65b for  $\mathcal{V} = 1.5$ . This value of the vortex strength lies just past the primary limit point, where flows are found to be periodic and three dimensional. This flow is void of reversed flow, and is therefore not a form of breakdown. The disturbance is most similar to the Type 6 disturbance documented by Faler and Leibovich (1977). A slightly higher value of vortex strength yields the disturbance shown in Figure 65c. The axial deceleration is greater here, resulting in reversed flow. Furthermore, there is visual evidence of a more coherent off-axis deflection of the particles. Downstream of the initial disturbance, the particles are scattered in a much more random fashion than in Figure 65b.

Further increases in vortex strength lead to the formation of the spiral mode of vortex breakdown, shown in Figure 66. Figures 66a-b represent intermediate forms of breakdown, not easily characterized by one of the documented forms observed by Faler and Leibovich (1977). The spiral mode, Figure 66c, is characterized as a sharp, off-axis deflection of the central particle trace into a helical-type structure. This structure rotates about the tube centerline in a periodic fashion in the same sense as the base vortical flow. The sense of winding of the helical structure, is however, opposite to the swirling direction of the base flow.

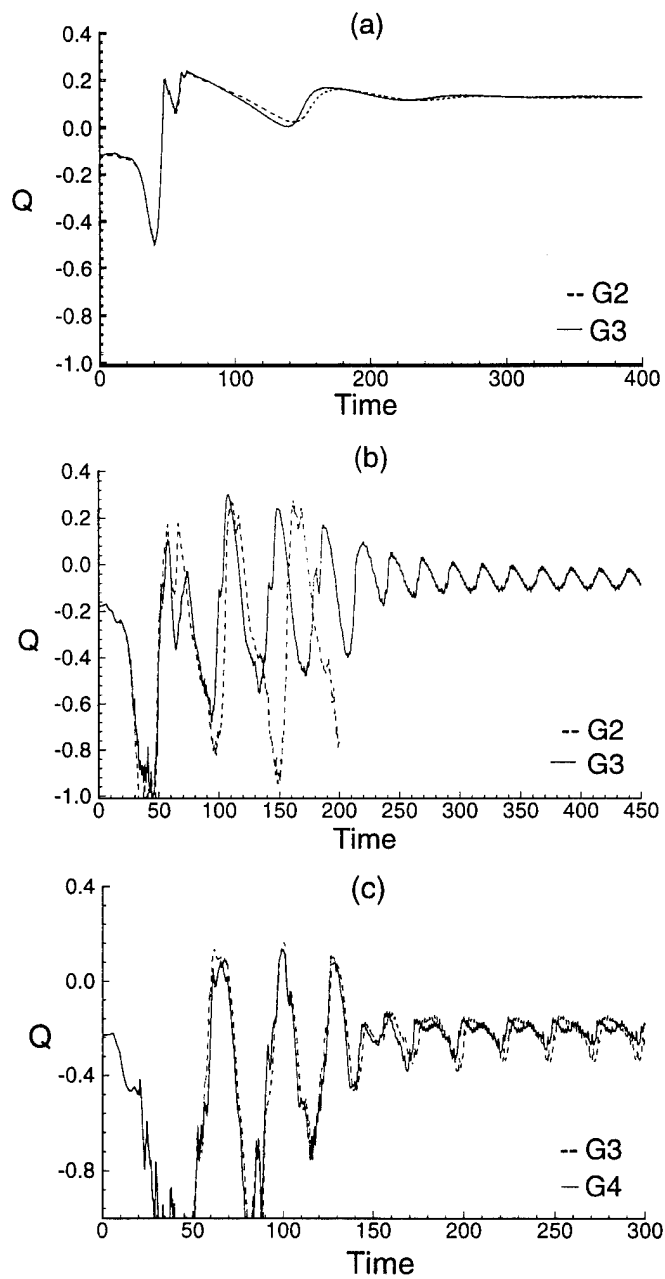


Figure 64. Sensitivity of  $Q(t)$  to tube length: (a)  $\nu = 1.5$ ,  $L = 20$  (dashed),  $L = 30$  (solid), (b)  $\nu = 1.7$ ,  $L = 20$  (dashed),  $L = 30$  (solid), (c)  $\nu = 1.9$ ,  $L = 30$  (dashed),  $L = 40$  (solid).

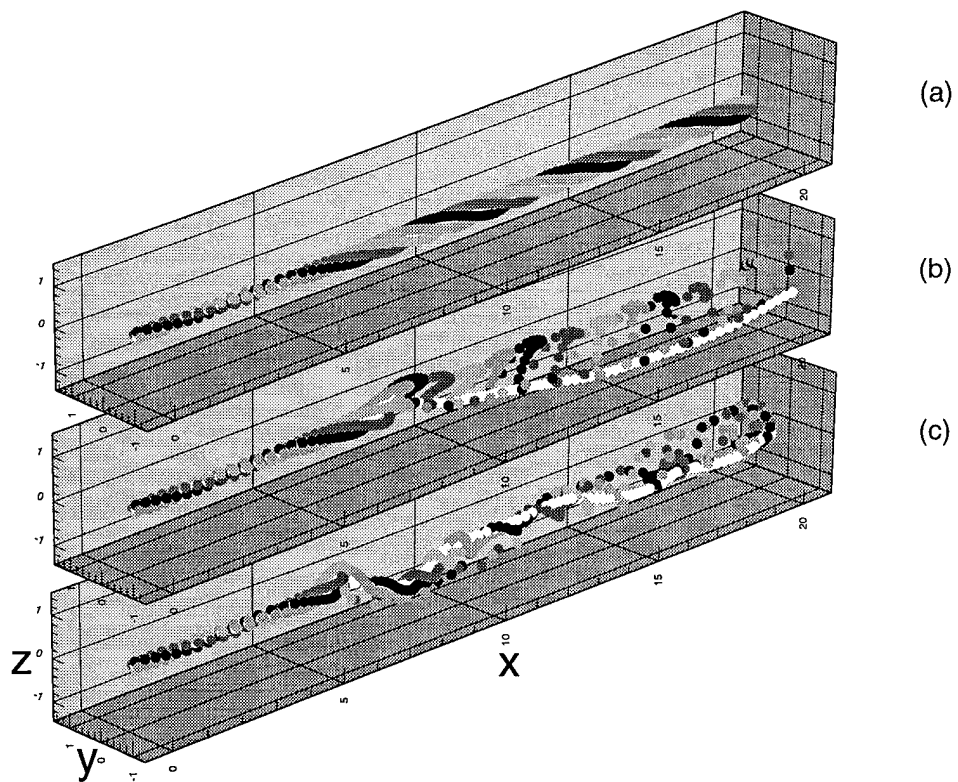


Figure 65. Particle traces showing development of three-dimensionality with increasing vortex strength: (a)  $\mathcal{V} = 1.47^+$ , (b)  $\mathcal{V} = 1.5$ , (c)  $\mathcal{V} = 1.6$ .



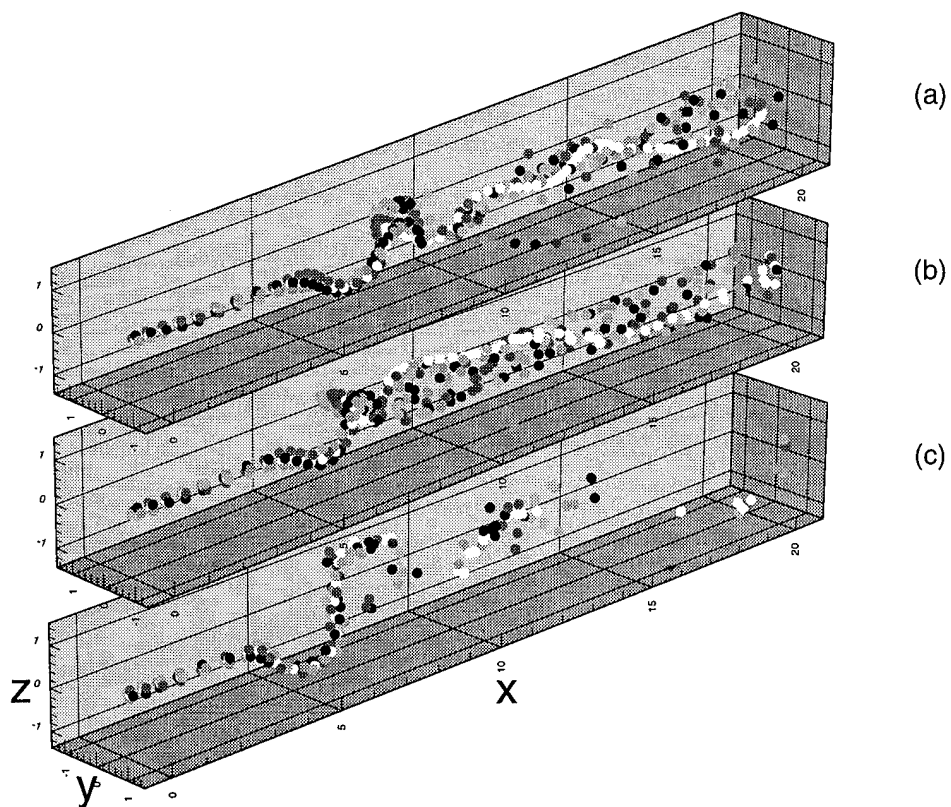


Figure 66. Particle traces showing evolution of the spiral mode of vortex breakdown as vortex strength is increased: (a)  $\mathcal{V} = 1.7$ , (b)  $\mathcal{V} = 1.9$ , (c) spiral breakdown,  $\mathcal{V} = 2.1$ .

## VI. Summary.

Results of Chapter V are summarized in this chapter, along with a discussion on the utility of the TANS model.

The TANS model is discussed in Section 6.1. Topics include the demonstrated utility of the compact scheme and the multiblock grid structure.

A review of the results at  $Re = 250$ , where solution nonuniqueness is not evident in the 2-D solutions, is contained in Section 6.2. Results at  $Re = 500$  and 1000, where 2-D solution nonuniqueness is found, is reviewed in Section 6.3. The types of flow disturbances encountered in this study are related to those found in the experiment of Faler and Leibovich (1977) in Section 6.4. Finally, a summary of quantified results is presented in Section 6.5.

### 6.1 The TANS Model.

The unique features of the TANS model include the incorporation of the fourth-order compact scheme, discussed in Section 6.1.1, and the ability of the model to compute solutions over a specific type of multiblock grid (Section 6.1.2).

*6.1.1 The Compact Scheme.* Previous works using the compact scheme in Euler and Navier-Stokes solvers are summarized in Chapter 2.2. These works include the application of the compact scheme to compressible, 3-D, and unsteady flows. Previous applications of the compact scheme to solvers employing multiple-block grids are not found. Therefore, it is believed by the author that this study represents the first application of the compact scheme to 3-D, compressible and unsteady flows in the presence of a multiblock grid.

The development of the compact scheme version of the TANS model was not one of the original goals of this work. However, as the study progressed, it was evident that the time-accurate computation of 3-D grid-independent solutions was too computationally demanding for standard second-order schemes. The computational requirements in this study are driven primarily by the long amounts of time required for solutions to reach

their time-asymptotic behavior. The compact scheme allows fewer nodes to be used in the crossplane, with similar levels of spatial accuracy. This greatly relieves the computational requirements of the study and allows more runs to be computed in a given amount of time.

The practical benefits of using the fourth-order model over the second-order model are primarily due to two factors. First, it was found in this study that similar levels of accuracy are achieved when  $61^2$  crossplane nodes (grid G6) are used with the second-order model and  $41^2$  crossplane nodes (grid G1) are used with the fourth-order model. Thus, fewer nodes can be used with the fourth-order model with similar levels of spatial accuracy. Second, the larger radial node spacing associated with the fourth-order model allows the solution to remain stable at a larger time step. The maximum time step allowed with the second-order model using grid G6 is at least 0.03, while the maximum time step of the fourth-order model for grid G1 is at least 0.04. However, it should be noted that when both models use the same grid, a larger time step can be used with the second-order model. For example, the maximum time step of the second-order model using grid G1 is at least 0.06. Thus, some robustness in time step is sacrificed with the fourth-order model. However, in this study, the allowance of the larger radial node spacing recovered this loss, resulting in a net increase in the maximum allowable time step from about 0.03 to about 0.04.

The overall savings in CPU time for the C-90 computer is computed assuming grids G6/G1 and time steps 0.03/0.04 for the second/fourth-order models respectively. The required CPU time to integrate to  $t = 100$  is 4.2 hours for the second-order model and 2.5 hours for the fourth-order model (Section 3.7). This corresponds to an overall savings in CPU time using the compact scheme of 42%. Section 3.7 provides TANS performance information for both the second and fourth-order versions of the model.

The preceding comparison of CPU time may seem unjust, since different grids are used in computing the required CPU times. However, the intent is to show the required CPU time to compute a solution to a given final time on grids which provide similar levels of spatial accuracy. In this light, the preceding comparison of CPU time is justified, since the CPU times are based on grids which yield similar levels of accuracy for their respective schemes. The other seemingly unfair aspect of the above comparison is that different time steps are involved. The intent is to use the maximum allowable solution-independent time

step. The higher time step associated with the compact scheme is a direct result of the coarser spacings in the crossplane grid.

In this study, the larger allowable time steps associated with the compact scheme are adequate in providing solutions which are nearly independent of time step. The time steps used are also specified to be very close to the maximum stable time step. That is, the maximum (solution-independent) time step in this study is less than, but in close proximity to, the time step in which solution stability is lost. This is generally an undesirable situation, especially if only a steady-state solution is sought. However, since time-accurate solutions are desired in this study, this situation is of less concern. In general, however, the time step for solution-independence may be much less than the time step associated with loss of stability. In these cases, increasing the time step (upon implementing the compact scheme) may not be possible if independence in time step is desired, resulting in less net savings of CPU time for the compact scheme than that cited above. About 22% of the 42% reduction of CPU time is due to the reduced number of nodes, and factoring in the difference in code efficiencies. The remaining 20% is achieved by running at a larger time step, made possible by the greater crossplane node spacing.

The data processing index (DPI) of the fourth-order version of the TANS model is (coincidentally) 42% larger than the central-difference formulation. Much of the extra computations in the compact scheme come from computing the viscous terms to fourth-order accuracy. It would be of interest to study the effect of allowing the viscous terms to be computed to second-order accuracy, assessing the loss of accuracy against improved efficiency.

Finally, a stability analysis of the compact scheme was not performed in this study. However, the observed requirement of smaller time steps for the compact scheme (over a second-order scheme) is confirmed by Lele (1992). Lele (1992) computed the explicit stability limits for two model problems, and generally found that the time step becomes more restrictive as the spatial accuracy of the scheme increases. The most restrictive time step for an explicit scheme was associated with spectral methods (Lele (1990)). The fourth-order compact scheme was found to have a time step restriction which lies between the limit associated with second-order schemes and spectral methods.

*6.1.2 The Multiblock Grid.* The crossplane grids employed in this work have a unique structure; nodes are arranged in a nearly rectilinear fashion close to the tube center, while maintaining near orthogonality at the tube wall. This accomplishes three goals: (1) allows for nearly constant grid resolution near the centerline, where the vortex core migrates off-center during spiral breakdown, (2) avoids an approximate numerical treatment at the tube centerline (essentially moving such treatment towards the tube wall), and (3) provides nearly orthogonal node placement at the wall, reducing numerical errors associated with the specification of Neumann-type boundary conditions. To achieve this type of grid, a multiblock structure in the crossplanes is used. The structure consists of an inner block surrounded by four outer blocks.

The primary benefit of the multiblock grid is the elimination of an approximate solution treatment at the tube centerline, moving such treatment radially outward toward the tube wall.

Finite difference methods may alternately use a radial-type grid for resolving a circular crossplane. Node positions of a radial grid lie at the intersection of radial lines emanating from the tube centerline, and circles drawn concentrically about the centerline. A centerline node is mapped from a point in physical space to a line in the crossplane computational space. Solution sweeps in the radial direction fail to uniquely compute the solution along the centerline, typically requiring an averaging of values to determine a unique centerline solution.

The multiblock grid used in this study eliminates the approximate treatment of the centerline solution. Instead, cuts in the computational domain are used to allow the grid to transition from a nearly rectilinear arrangement of nodes near the centerline, to an arrangement similar to a radial grid near the tube wall.

Results from Appendix C.2 show that there is a negligible effect upon the solution when the grid is rotated. This symmetry in the grid structure greatly inhibits the tendency of a flow to produce flow asymmetries when the true physical behavior is axisymmetric. In fact, the most notable feature of the grids developed for this study is their ability to yield nearly perfect axisymmetric solutions when the node arrangement is asymmetric.

## 6.2 Summary of Results for $Re = 250$ : The Hopf Bifurcation in the Presence of Unique Axisymmetric Solutions.

The results of Section 5.2 are summarized in this section.

Evidence of a Hopf bifurcation is summarized in Section 6.2.1, along with substantiating evidence from experimental observations. The correlation between the emergence of three-dimensional behavior and the observed increase in the time-asymptotic values of  $Q$  is summarized in Section 6.2.2. Finally, a summary of the effects of grid resolution, tube length and tube radius are given in Section 6.2.3.

*6.2.1 Evidence of a Hopf Bifurcation.* Axisymmetric flows at  $Re = 250$  are found to be unique, consistent with the results of Beran and Culick (1992). These axisymmetric solutions are used as initial conditions to the 3-D TANS model. When the vortex strength is prescribed to be less than a critical value, axisymmetric initial conditions remain steady and axisymmetric when time integrated with the 3-D TANS model. When the vortex strength is prescribed to be greater than the same critical value, the initially steady and axisymmetric solutions evolve in time to flows which are time-periodic and three-dimensional. The change in solution stability about the critical vortex strength is attributed by the author to a Hopf bifurcation. The type of Hopf bifurcation is supercritical, based on results presented in Section 5.2.1.

The existence of a Hopf bifurcation for 3-D swirling flows in tubes is not unexpected, based on the experiments of Garg and Leibovich (1979) and Leibovich (1984). Garg and Leibovich (1979) studied the spectral characteristics of breakdown flowfields using power spectrum techniques. They state in their conclusions that the wake regions are unstable to nonaxisymmetric disturbances, producing coherent (periodic) low frequency oscillations. Similarly, Leibovich (1984) postulates the emergence of an asymmetric ( $n = 1$ ) disturbance with an amplitude  $S(z, t)$ , where  $z$  is the axial coordinate. Leibovich (1984) cites the presence of a coherent periodic signal in the spectra of disturbances measured by Singh and Uberoi (1976) and Garg and Leibovich (1979), and suggests that the nonaxisymmetric amplitude  $S(z, t)$  grows out of this instability as a Hopf bifurcation. The instability to which Leibovich refers is the presumed instability of finite-amplitude axisymmetric waves

to asymmetric disturbances. These findings by Garg and Leibovich (1979) and Leibovich (1984) concerning the emergence of three-dimensional, time-periodic flow are consistent with the discovery of the Hopf bifurcation in this study.

#### 6.2.2 *The Relationship Between the Emergence of Three-Dimensional Flow and $Q$ .*

The values of  $Q$  for vortex strengths prescribed slightly beyond the critical value migrate in time from a negative (reversed flow) initial value to a positive (no reversed flow) time-asymptotic value. This overall increase in  $Q$  is correlated in Section 5.2.2 with a production of radial vorticity in the vicinity of the point of minimum axial velocity. The production of positive radial vorticity coincides with an increase in the minimum azimuthal vorticity through the azimuthal component of the vorticity equation. Elements of the theory of Brown and Lopez (1990) provide that the production of negative azimuthal vorticity is a necessary condition for the deceleration of the axial flow. Thus, a net increase in azimuthal vorticity, according to the theory, corresponds to a net increase in  $Q$ . The emergence of three-dimensional flow coincides with a net increase in both radial and azimuthal vorticity, which implies a higher value of  $Q$ .

The observed increase in  $Q$  from axisymmetric to 3-D flows also correlates with a framework of breakdown postulated by Leibovich (1984). Leibovich (1984) presented a scenario under which the emergence of the spiral mode of breakdown could be explained. In this scenario, the growth of axisymmetric disturbances in the vicinity of breakdown eventually lead to the instability of these disturbances to asymmetric waves. The gain in energy of the spiral mode is postulated to come at the expense of energy in the axisymmetric mode. Results in this study support this scenario. Flows computed past the Hopf bifurcation are asymmetric, resulting from the loss of stability of axisymmetric flow to 3-D disturbances. Furthermore, the emergence of asymmetric flow weakens the amplitude of the axisymmetric waves, as evidenced by an increase in the minimum axial velocity,  $Q$ .

6.2.3 *Assessment of Grid and Geometry Effects:  $Re = 250$ .* Grid G1, the baseline grid, is found to be adequate in resolving the flowfield at  $Re = 250$ . Grid G1 consists of  $98 \times 41 \times 41$  nodes, where the 98 axial nodes are equally spaced to yield an axial node spacing of about 0.2. The average radial node spacing for grid G1 is 0.1.

A tube length of  $L = 20$  is found to be adequate at this Reynolds number. Results for  $\mathcal{V} = 1.53$  show virtually no difference in  $Q$  between flows computed with a tube length of  $L = 20$  and  $L = 30$ .

An admitted limitation of this work is the lack of computations at values of the tube radius larger than  $R_0 = 2$ . This limitation is due to the additional demands on computer resources required to resolve larger tubes. Typical values of  $R_0$  in experiments are near  $R_0 = 3$ .

Tube radius effects are not believed to be significant at vortex strengths near the observed bifurcation point. Planar projected velocity vectors shown in Section 5.2 (Figures 39–41) reveal that the resulting flow disturbances at these vortex strengths ( $\mathcal{V} = 1.5$  to  $\mathcal{V} = 1.65$ ) are very limited in radial extent. Therefore, it is unlikely that the position of the radial boundary is degrading these solutions. Furthermore, flows at vortex strengths as high as  $\mathcal{V} = 1.8$  are found to contain flow disturbances which are contained to within a radial extent of unity.

Flows at the highest vortex strengths considered in this work may be impacted by a change in tube radius, however. The flow disturbances evident in Figure 41d consist of a large region of reversed flow. This region oscillates off-axis about the tube centerline, resulting in flowfield disturbances that are relatively close to the tube wall. A second, more indirect, tube wall effect may also exist for the higher vortex strengths. As the vortex strength is increased, the value of  $Q$  generally decreases, resulting in stronger and larger reversed flow regions. Considering flow continuity, larger axial velocity components are required to exist between the region affected by the reversed flow and the tube wall. It is more likely in these high vortex-strength cases that the region of high axial velocity is impacted by further increases in tube radius.

### *6.3 Summary of Results for $Re = 500$ and $Re = 1000$ : Hopf Bifurcation in the Presence of Nonunique Axisymmetric Solutions.*

The results for  $Re = 500$  and  $Re = 1000$  are summarized in this section.



The role of the primary limit point is discussed in Section 6.3.1. In particular, it is postulated, based primarily on the results of this study, that the loss of stability to time-periodic flow and the change in flow criticality are nearly simultaneous events. A summary of the effects of grid resolution, tube length and tube radius for  $Re = 1000$  are given in Section 6.3.2.

*6.3.1 The Role of the Primary Limit Point.* The axisymmetric flows computed in this study at  $Re = 500$  and  $Re = 1000$  contain solution folds, resulting in primary and secondary limit points. Results of Beran and Culick (1992) and Lopez (1994) also show nonunique axisymmetric solutions at these Reynolds numbers; both studies predict the first appearance of a limit point at  $Re = 360$ .

When the vortex strength is prescribed to be less than the primary limit point, the resulting time-asymptotic solutions are found to be steady and axisymmetric. In particular, when three nonunique initial conditions are time-integrated with the TANS model, all three initial conditions time-asymptote to the solution corresponding to the initial condition of the upper stable branch.

When the vortex strength is prescribed to be greater than the primary limit point, the resulting time-asymptotic solutions are found to be time-periodic and three-dimensional. Therefore, it is postulated that a Hopf bifurcation occurs at, or in very close proximity to, the primary limit point.

The precision to which the locations of the Hopf and primary limit points can be shown to be coincident is limited primarily by the selected values of  $\mathcal{V}$ . An upper bound on the computed difference in  $\mathcal{V}$  between the location of the Hopf point and the primary limit point is equal to the greater of the two differences  $\mathcal{V}_2 - \mathcal{V}_p$  and  $\mathcal{V}_p - \mathcal{V}_1$ , where axisymmetric, equilibrium solutions are obtained at  $\mathcal{V}_1$  and three-dimensional, time-periodic solutions are obtained at  $\mathcal{V}_2$ .

In this study, the smallest difference in  $\mathcal{V}$  where the change in stability was observed is at  $Re = 500$ , where  $\mathcal{V}_2 = 1.5$  and  $\mathcal{V}_1 = 1.49$ . The primary limit point for  $Re = 500$  occurs at  $\mathcal{V}_p = 1.4918$ . Thus, the maximum difference in  $\mathcal{V}$  between the location of the Hopf bifurcation and the primary limit point is  $1.5 - 1.4918 = 0.0082$  at  $Re = 500$ . This very

small difference in  $\mathcal{V}$  is believed to be ample justification to claim that the Hopf point and the primary limit point are in very close proximity. At  $Re = 1000$ , the maximum difference between the Hopf bifurcation point and the primary limit point is 0.02565. Additional runs would be required to determine if this maximum difference at  $Re = 1000$  could be reduced.

The location of the primary limit point in an axisymmetric solution space has been associated with the appearance of critical flow. Beran and Culick (1992) found that for sufficiently high Reynolds numbers, a parabolized version of the axisymmetric governing equations, known as the quasi-cylindrical (QC) equations, agree well with solutions of the Navier-Stokes equations when the vortex strength is below the primary limit point, but fail to converge to a solution as the vortex strength is increased towards the primary limit point. The failure point of the parabolic QC equations is believed by Hall (1972) to be the approximate point at which critical flow develops. Thus, the work of Beran and Culick (1992) and Hall (1972) suggest that the flow transitions from supercritical flow to subcritical flow at a vortex strength which is approximately equal to the primary limit point.

This relationship is somewhat evident in the work of Darmofal (1994), where the criticality of axisymmetric flows is computed by solving the stationary perturbation equations of Hall (1972). Visual inspection of Darmofal's plots of  $Q$  versus  $\mathcal{V}$  show that the slope of  $Q$  at flow criticality is nearly infinite, which implies that the critical point and the limit point are at least approximately coincident. However, a definite relationship between flow criticality and the location of a primary limit point cannot be obtained from this work, since the absence of a continuation procedure precludes the computation of a limit point.

The results of this study add further insight into the role of the primary limit point. The results presented in Chapter V demonstrate to within a precision of 0.0082 in  $\mathcal{V}$ , that the Hopf bifurcation point and the primary limit point are coincident. Therefore, given the results cited above, it is postulated by the author that, to within close proximity in  $\mathcal{V}$ , the loss of stability to time-periodic flow (via the Hopf bifurcation) and the occurrence of critical flow are coincident events. This relationship between the primary limit point and the loss of stability to periodic flow is believed by the author to be previously unreported in the literature.

It is of interest to contrast the role of the primary limit point for 3-D flows to the role associated with axisymmetric solutions. For axisymmetric flows, the primary limit point is associated with values of  $Q$  which are positive. However, a slight increase in  $\mathcal{V}$  above the primary limit point brings about large differences in solution behavior, due to the sudden drop of solutions from the upper to lower stable branch. Thus, a slight increase in  $\mathcal{V}$  from  $\mathcal{V}_p$  in 2-D flows results in a dramatic change in solution character—from flows with no reversed flow to flows with reversed flow.

Results in this study indicate that 3-D flows do not undergo this large change in flow structure as the primary limit point is crossed. Instead, flows computed just past the primary limit point are still void of reversed flow. (The correlation of the emerging three-dimensionality with the increase in  $Q$  from axisymmetric levels is treated in Section 5.2.2.) In 3-D flows, therefore, the primary turning point is not readily associated with imminent breakdown, as it is generally perceived in axisymmetric flows. For example, Figure 59c in Section 5.4 shows that the primary limit point is at  $\mathcal{V}_p = 1.47435$ , whereas reversed flow is not achieved until approximately  $\mathcal{V} = 1.6$ . In general, the effect of three-dimensionality delays the formation of reversed flow, requiring generally larger values of vortex strength to achieve breakdown than in axisymmetric flows.

*6.3.2 Assessment of Grid and Geometry Effects:  $Re = 1000$ .* Grid G1 ( $98 \times 41 \times 41, L = 20$ ), the baseline grid, is found to be inadequate in resolving the flowfield at  $Re = 1000$ , due primarily to a lack of resolution in radial node spacing. Grid G2 is found to be adequate at  $Re = 1000$  when the vortex strength is prescribed to be less than the primary limit point. Grid G2 consists of  $122 \times 61 \times 61$  nodes, where the 122 axial nodes are clustered to yield a minimum axial node spacing of about 0.1 near  $x = 5$ . The average radial node spacing for grid G2 is 0.066. Further refinements in node spacing from grid G2 were not explored, due to the requirement of excessive computational resources.

A tube length of  $L = 30$  is generally found to be necessary when the vortex strength is greater than the primary limit point. Results for  $\mathcal{V} = 1.9$  show only minor differences in  $Q$  between flows computed with a tube length of  $L = 30$  and  $L = 40$ .

The possible shortcomings of tube radius, described in Section 6.2.3 for  $Re = 250$ , is equally applicable when  $Re = 1000$ .

#### 6.4 Relationship Between Observed Types of Flow Structures with Experiments.

A summary of the observed types of flow disturbances is given in this section, along with a discussion on how these disturbances relate to those found in the experiment of Faler and Leibovich (1977), referred to here as *FL*.

A map showing the experimentally observed axial positions of the Types 0–6 disturbances as a function of the Reynolds number,  $Re_{FL}$ , and the swirl parameter,  $\Omega_{FL}$ , is reproduced from Faler and Leibovich (1977) in Figure 67. The abscissa represents the axial position where the disturbance begins. In the context of this study, it is only important to note the relative axial positions at which the flow disturbances occur. The ordinate,  $Re$ , and  $\Omega$  in Figure 67 are referred to in this study by  $Re_{FL}$  and  $\Omega_{FL}$  respectively.  $Re_{FL}$  and  $\Omega_{FL}$  are defined differently than  $Re$  and the vortex strength,  $\mathcal{V}$ , used in this study.

The numbers in Figure 67 correspond to the disturbance type. Types 0 and 1 refer to bubble forms of breakdown. Type 2 is the spiral form of breakdown, which is observed in this study. Types 3, 4 and 5, are intermediate forms of disturbances which generally occur at lower Reynolds numbers and vortex strengths between the Type 2 and Type 6 disturbances. Numbers surrounded by short horizontal lines represent the observed axial movement of that particular disturbance. Multiple branches for a given  $\Omega_{FL}$  indicate that multiple types of breakdown were observed with fixed values of the flow parameters.

In attempting to correlate the results in this study to Figure 67, a consistent set of parameters must be defined. In particular, differences in definitions between  $\Omega_{FL}$  and  $\mathcal{V}$  must be accounted for, as well as differences between  $Re_{FL}$  and  $Re$ .

$\Omega_{FL}$  and  $\mathcal{V}$  differ in definition by the reference velocity used to normalize them from dimensional to nondimensional quantities.  $\Omega_{FL}$  is normalized by the average axial velocity in the axial jet produced by the experimental apparatus.  $\mathcal{V}$  is normalized by the reference

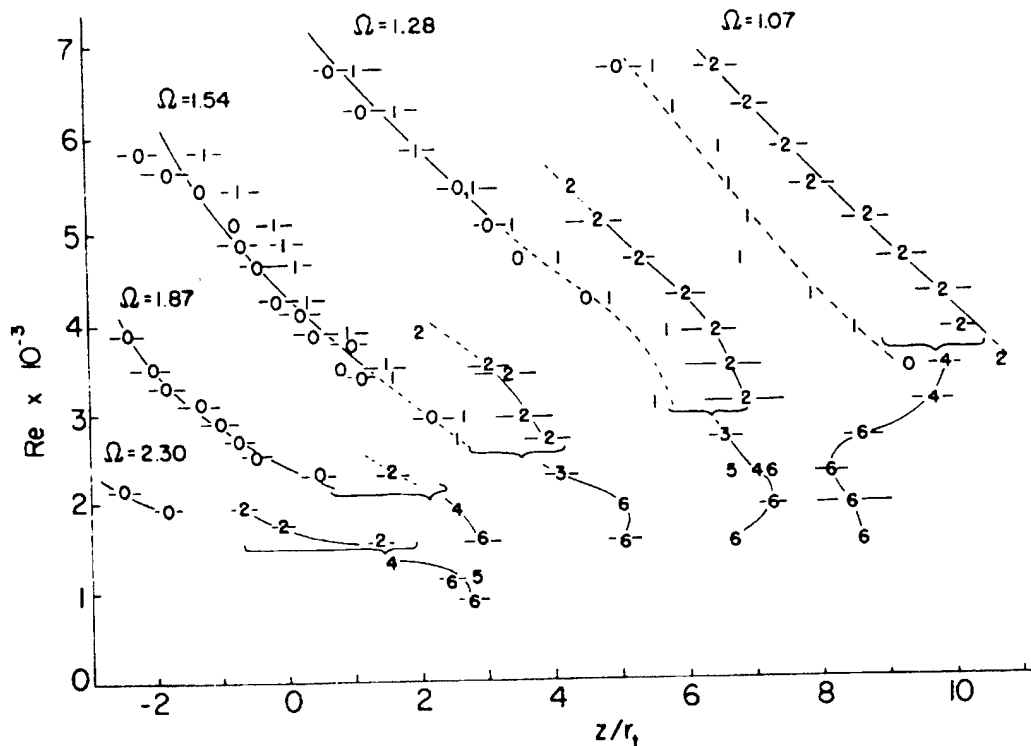


Figure 67. Plot of the axial position (abscissa) of flow disturbances as a function of  $Re_{FL}$  and the swirl parameter  $\Omega_{FL}$  (Faler and Leibovich (1977)).

axial velocity, taken as the uniform axial velocity at the inlet.

$$\mathcal{V} = \frac{\mathcal{V}'}{u'_{ref}} \quad \Omega_{FL} = \frac{\mathcal{V}'}{\bar{W}}$$

where  $\mathcal{V}'$  is the dimensional vortex strength and  $\bar{W}$  is the average axial velocity used by FL. To reconcile these differences in definition,  $\Omega_{FL}$  is adjusted to reflect a reference velocity corresponding to the axial velocity at the tube wall. This definition should provide a more favorable comparison between  $\Omega_{FL}$  and  $\mathcal{V}$ . In addition, selecting the reference velocity away from the vortex core region is consistent with the nature of naturally occurring jets in vortices over delta wings. In these cases, the axial velocity far removed from core values correspond to freestream values.

Measured velocity data in  $FL$  indicate that the strength of the axial jet generally increases with  $Re_{FL}$ . Thus, the differences in  $\Omega_{FL}$  and  $\mathcal{V}$  are believed to be greater at higher

Reynolds numbers. Increases in the axial velocity from wall values to average values are found to range between 25% at  $Re_{FL} = 3220$  to near 50% at  $Re_{FL} = 6000$ . Therefore, as a crude way to correlate the swirl parameters,  $\Omega_{FL}$  at the higher values of  $Re_{FL}$  should be multiplied by a factor of about 1.5; and by a factor of about 1.25 at lower Reynolds numbers.

Two corrections are needed to correlate the Reynolds numbers. The first correction is required for the same reason as above;  $Re_{FL}$  is based on average axial velocity, whereas  $Re$  is based on the wall reference value. The second correction is required because of differences in reference length.

$$Re = \frac{u'_{ref} r_0}{\nu} \quad Re_{FL} = \frac{\bar{W} D}{\nu}$$

where  $D$  is the diameter of the tube used by FL. The length scales  $D$  and  $r_0$  differ by a factor of about 6. Overall then,  $Re_{FL} \approx 9Re$  at the higher Reynolds numbers in Figure 67, whereas  $Re_{FL} \approx 7.5Re$  at lower Reynolds numbers.

Flows performed in this study at  $Re = 250$  and  $Re = 1000$  are compared to the disturbances in Figure 67.  $Re = 250$  is roughly equivalent, given the above corrections, to  $Re_{FL} = 1875$ . Similarly,  $Re = 1000$  is roughly equivalent to  $Re_{FL} = 9000$ . Values of  $\Omega_{FL}$  then roughly span from  $\mathcal{V} = 1.33$  to  $\mathcal{V} = 2.8$  at  $Re_{FL} = 1875$ . At  $Re_{FL} = 9000$ , the values of  $\Omega_{FL}$  roughly span from  $\mathcal{V} = 1.6$  to  $\mathcal{V} = 2.8$  (although the highest Reynolds number considered by FL is 7000).

The Types 3, 4 and 5 forms of breakdown are not observed in this study. This is believed to be due to the selected values of  $Re$  of this study. Figure 67 shows that these forms of breakdown occur between  $Re_{FL} = 2000$  and  $Re_{FL} = 3500$ , which corresponds to  $Re = 266$  to  $Re = 388$ , given the above corrections. Reynolds numbers,  $Re$ , of 250 and 1000 were heavily investigated in this study. These values were selected primarily because they correspond to axisymmetric solution paths without and with limit points.

At  $Re = 250$  (Section 5.2), increasing vortex strength from that which produces steady, axisymmetric flow results in a gradual progression of a three-dimensional flow structure. At relatively low vortex strengths near  $\mathcal{V} = 1.5$  to 1.65, the solutions contain no

reversed flow, and the form of the disturbance is most similar to the Type 6 disturbance documented by *FL*. As vortex strength is further increased, the gentle off-axis deflection of the central material points evolves into a more coherent and sharper deflection. Eventually, at  $\mathcal{V} = 2.3$ , the deflection of the material points is very abrupt, and the material points deflect off-axis in a very coherent corkscrew shape. This form of flow disturbance is very similar to the Type 2 (spiral) mode of breakdown.

A similar progression of flows is evident in Figure 67 for  $Re_{FL} = 1875$ . The Type 6 is evident in the figure for  $\mathcal{V} = 1.33$  ( $\Omega_{FL} = 1.07$ ) to  $2.3$  ( $\Omega_{FL} = 1.87$ ). Past  $\mathcal{V} = 2.3$ , the spiral form of breakdown is indicated in the figure.

At  $Re = 1000$  (Section 5.4) a vortex strength of  $\mathcal{V} = 1.5$  yields a structure again similar to the Type 6 form found in *FL*. Steadily increasing  $\mathcal{V}$  finally yields a Type-2 spiral at  $\mathcal{V} = 2.1$ .

In Figure 67,  $Re_{FL} = 9000$  is not considered in the figure. However, if the data is extrapolated, a spiral form of breakdown would be expected from  $\mathcal{V} = 1.6$  ( $\Omega_{FL} = 1.07$ ) to  $\mathcal{V} = 1.92$  ( $\Omega_{FL} = 1.28$ ). In this study, the spiral is not fully formed until  $\mathcal{V} = 2.1$ .

Any further comparisons between flow types found in this study to their location in Figure 67 would be problematic. Several other factors, including differences in tube geometry, inflow axial velocity profiles, the absence of slip in the TANS model, and compressibility will all effect the types and breakdown and the conditions necessary for development. Overall however, the observance of flows in this study generally coincide with the forms found in *FL*, once the parameters are defined in a consistent manner.

Absent in this study is the observance of the bubble form of breakdown. While the observance of this form is not expected for  $Re = 250$ , based on Figure 67, it is expected for  $Re = 1000$  at the higher vortex strengths. The most likely reason for the inability of the model to form the bubble breakdown is that the tube wall is influencing the breakdown structure at the higher vortex strengths.

Table 17. Summary of quantified results.

Category	Quantified Data	Result	Section
Axisymmetric Soln. of TANS Model	Cubic Spline Interp.	4th-Order Accuracy	B.3
	Calculation of $H$	$H_{2D} = 0.89H$	5.3
	Agreement of 2D/3D Flows	$L_2 < 2.5E - 03$	5.2
Spatial Accuracy	Model Problem: Steady	$L_2 < 5.8E - 03$	D.1
	Axial Resolution	$L_2 < 4.0E - 03$	4.1
	Radial Res.: 2nd-Order	$L_2 < 7.2E - 03$	4.1
	Radial Res.: 4th-Order	$L_2 < 1.3E - 03$	4.1
	Domain Length	$L_2 < 3.1E - 03$	4.1
Temporal Accuracy	Model Problem: Unsteady	$L_2 < 2.7E - 03$	D.4
	Time Step Resolution	$L_2 < 5.9E - 03$	5.2

### 6.5 A Summary Assessment of Numerical Accuracy.

Quantified assessments of numerical accuracy performed in this study are summarized in this section. These assessments are categorized into three areas: spatial accuracy, temporal accuracy, and the accuracy of axisymmetric solutions of the TANS model.

The summary is presented in Table 17. The three categories are listed in the first column of the table. The second column lists specific examples of quantified data used to assess accuracy. The third column lists the specific quantified result, while the fourth column provides the section where more details of the quantification can be found.

The first category addresses the ability of the TANS model to compute axisymmetric solutions. The first set of quantified data verifies that the cubic spline interpolation method is fourth-order spatially accurate at interior nodes. Nodes near a boundary are at worst case second-order accurate. The second item shows that values of  $H$  presented in this study contain a substantial contribution from axisymmetric data. This is a likely consequence of small interpolation errors and discrete errors in computing  $H$ . The example given in the table shows that 89% of the value of  $H$  (for a specific run) is attributed to the value associated with the initial axisymmetric solution ( $H_{2D}$ ). Therefore, the change in  $H$  due to asymmetries is generally smaller than the value of  $H$  indicates. The third item indicates that the  $L_2$  norm of the difference of TANS and PAC solutions (computed over the entire domain) is quite small.



The second category addresses the spatial accuracy of solutions computed in Chapter IV, where the baseline grid is determined. The most important observation here is that the  $L_2$  norms for the radial resolution are larger with the second-order scheme, even when larger node spacings are used with the compact scheme.

The third category addresses the temporal accuracy of a model problem and of two solutions computed with different time steps.  $L_2$  norms here are also quite small.

## *VII. Conclusions and Recommendations.*

### *7.1 Conclusions.*

The important conclusions of this study are summarized in this chapter, and are related to the stated objectives in Section 1.1. In addition, questions raised in Chapter I are answered in light of the study results and conclusions.

The conclusions of this study which directly relate to the study objectives are summarized as follows:

- For fixed Mach and Reynolds numbers and increasing vortex strength, a critical vortex strength is identified, where initially steady, axisymmetric solutions first lose stability to 3-D, time-periodic solutions. The identification of these critical vortex strengths satisfy Objective 1 of Section 1.1.
- The loss of stability of equilibrium flows to time-periodic flows are attributed to Hopf bifurcations, evidenced for  $M = 0.3$  at  $Re = 100, 250, 500$  and  $1000$ . The Hopf bifurcations are found to be of the supercritical type. The identification of the bifurcation type satisfies Objective 2 of Section 1.1.
- The role of the primary limit point is further defined in this study. Previous (axisymmetric) work has established a correspondence between the primary limit point and a change in flow criticality, implying that flow criticality signals the emergence of axisymmetric breakdown. This study establishes a link between the location of the primary limit point, and the location of a Hopf bifurcation point. Thus, it is postulated that the change in flow criticality is associated with the loss of stability of equilibrium flows. The identification of a Hopf bifurcation point near the primary limit point satisfies Objective 3 of Section 1.1.
- Flow types computed in this study are found to most closely resemble either the Type 6 disturbance or the spiral (Type 2) form of breakdown, following the classification of Faler and Leibovich (1977). Bubble breakdowns are not observed for the parameter range considered in this study (Section 7.2.2). The comparison of the computed flow

disturbances with the experiments of Faler and Leibovich (1978) satisfies Objective 4 of Section 1.1.

Further conclusions can be drawn from the results of this study that surpass the stated objectives in Section 1.1.

- Flows computed just past the critical vortex strength are found to have larger values of the minimum axial velocity than the initially axisymmetric flow. This observation is correlated to the emergence of 3-D contributions from the vorticity equation, and from elements of the theory of Brown and Lopez (1990). The observed increase in  $Q$  from axisymmetric to 3-D flows also correlates with a framework of breakdown postulated by Leibovich (1984). Leibovich (1984) presented a scenario under which the emergence of the spiral mode of breakdown could be explained. In this scenario, the growth of axisymmetric disturbances in the vicinity of breakdown eventually lead to the instability of these disturbances to asymmetric waves. The gain in energy of the spiral mode is postulated to come at the expense of energy in the axisymmetric mode. Results in this study support this scenario. Flows computed past the Hopf bifurcation are asymmetric, resulting from the loss of stability of axisymmetric flow to 3-D disturbances. Furthermore, the emergence of asymmetric flow weakens the amplitude of the axisymmetric waves, as evidenced by an increase in the minimum axial velocity,  $Q$ .
- An investigation in Section 5.3 shows that a flow asymmetry produced in a supercritical flow convects downstream. This result implies that the group velocity of the asymmetric disturbances in the supercritical flow is positive, which is in agreement with experimental evidence (Leibovich (1984)). This result also demonstrates that the specification of axisymmetric inflow conditions in this study are not compromised by the upstream movement of flow asymmetries.
- The implementation of fourth-order compact operators allows for a practical savings in computer CPU time of approximately 42%. The savings result from the requirement of fewer nodes to resolve the flow to similar levels of accuracy, and from a corresponding increase in the maximum allowable time step.

The results and conclusions obtained from this study are now utilized to answer the five questions posed in Chapter I.

- Questions 1 and 2: under what conditions are the assumptions of steady, axisymmetric flow valid? The results of this study show that steady, axisymmetric flows are stable to three-dimensional disturbances when the vortex strength is prescribed to be less than the identified critical value. Thus, the assumption of steady and axisymmetric flow is valid below this critical value of vortex strength.
- Question 3: how does the steady, axisymmetric solution branch bifurcate onto a solution branch of three-dimensional flows? Flows computed before a critical value of vortex strength are steady and axisymmetric, while just beyond the critical value the flows are found to be three-dimensional and time-periodic. The loss of stability of equilibrium solutions to time-periodic solutions are evidence for a Hopf bifurcation. The Hopf bifurcations are found to be of the supercritical type.
- Question 4: does the nonuniqueness of the 2-D solution paths play a role in the structure of 3-D solution paths? The specification of nonunique, axisymmetric initial conditions did not lead to nonunique 3-D solutions. Instead, the nonunique initial conditions lead to one unique time-asymptotic solution. This behavior was observed for both  $Re = 500$  and  $Re = 1000$ . However, the appearance of nonunique 2-D solutions coexists with the appearance of a primary limit point. The next question posed addresses the role of the primary limit point.
- Question 5: does the criticality of 2-D flows have any bearing on the nature of the 3-D solution space? The works of Beran and Culick (1992) and Darmofal (1994) demonstrate that the location of the primary limit point in a 2-D solution space is at least approximately coincident with a change in flow criticality. The results of this work show that to within 0.0082 in vortex strength, the location of the Hopf bifurcation point and the primary limit point are coincident. Therefore, the author postulates that the change in flow criticality and the loss of stability due to the Hopf bifurcation are nearly simultaneous events.

## 7.2 Recommendations.

Recommendations for future work are outlined in this section. Section 7.2.1 contains suggestions for improving the performance and accuracy of the TANS model. Specific recommendations on how the code could be modified to allow for a more direct comparison with tube experiments are provided in Section 7.2.2. Section 7.2.3 contains recommendations of how additional studies in tubes could provide valuable information on discretization requirements for flows over wings. Finally, Section 7.2.4 outlines recommendations to extend the model to allow for time-varying circulation.

*7.2.1 Improvements to TANS Model.* Four recommendations are given to improve the performance or accuracy of the TANS model.

The first recommendation is to consider evaluating the viscous terms, which appear explicitly in the TANS model, to 2nd-order spatial accuracy. Then, the reduction in spatial accuracy could be weighed against the substantial reduction in the required CPU time.

The second recommendation is to consider a similarity transformation of the matrix form of the governing equations (Pulliam (1985)). A similarity transformation would reduce the overall computational workload considerably by replacing the solution of a block tridiagonal system of equations with a block diagonal system of equations. Pulliam (1985) quantifies the computational savings for 2-D flow, predicting savings as high as 40%. Computational savings for 3-D codes are expected to be higher. The penalty for performing the diagonalization, however, using the three-point backward scheme, is a reduction to first-order temporal accuracy. This reduction in temporal accuracy could then be weighed against the decrease in the required CPU times to determine if the modification is warranted. Also, depending on the extent of CPU time reduction, a decrease in the time step could be investigated, regaining some temporal accuracy at the expense of additional computations.

The third recommendation is to consider treating the viscous terms implicitly. This would increase the temporal accuracy associated with the viscous terms from first to second-order accuracy. The first recommendation could also be done in conjunction with

this modification by using second-order operators in the left-hand-side of the governing equations, instead of the compact operator.

For flows at higher reference Mach numbers (past  $M = 0.3$ ), it is recommended that the governing equations be reformulated into conservative form when the local Mach number is found to exceed unity. The formation of large axial velocities, along with high values of vortex strength can produce local Mach numbers that are considerably higher than the freestream value. For example, numerical results (Visbal (1995)) show that the large axial jets associated with delta wing flows can produce supersonic flow in the vortical core when the freestream Mach number is greater than 0.3. However, the current implementation of the TANS model does not model this large axial jet at the inflow, although large axial velocity components are produced naturally through the tube constriction.

*7.2.2 Further Validation.* It is recommended that the TANS model be modified to allow for a direct comparison with a tube experiment, such as the experiment of Brücker (1993) or Faler and Leibovich (1977). Such a direct validation could not be performed in this study, primarily due to differences in the tube geometry. The required modifications to the model would include the specification of the tube geometry of the chosen experiment, specification of a no-slip wall (with appropriate changes in grid resolution near the wall), and formulation of representative inflow conditions (including the modeling of an axial jet). Specification of representative inflow conditions would be the biggest challenge of the required modifications. Inflow conditions on velocity would need to be available from experimental results. The density would be set to reference conditions, and the Mach number set to a sufficiently low value, for consistency with the incompressible flow of water in the experiments. The specification of an inflow pressure condition is unclear, however, depending on the chosen experimental geometry, the specification of a columnar inflow condition on pressure may be adequate.

It is also recommended that additional runs with the current TANS model be performed. These runs would focus on determining why the bubble form of breakdown was not observed in this study. The bubble form is generally expected to occur (with increasing

likelihood) as Reynolds number and vortex strength are increased. However, increasing both of these parameters to levels where the bubble is likely to appear did not result in bubble breakdown. Thus, further increases in either Reynolds number or vortex strength are not likely to produce a bubble breakdown. The effect of grid resolution is not likely to be an inhibitor to the bubble form, since transient bubble breakdowns were observed in this study. The only remaining model parameter which may affect the appearance of the bubble breakdown is the tube radius,  $R_0$ . It is recommended that the tube radius be increased to at least  $R_0 = 3$ , with corresponding increases in the number of crossplane node points such that crossplane grid resolution remains constant. Such a large tube radius was not considered in this study, due to the excessive demands on computer resources.

*7.2.3 Additional Studies with the Tube Geometry.* In addition to the physical information that breakdown in a tube provides, valuable information for those performing breakdown calculations over delta wings can be efficiently obtained.

Breakdown in tubes can provide guidance on the necessary grid resolution and time step needed to model the vortical core over wings. This information could be obtained at a substantial savings in computational cost. It is estimated, based on the fine grids used by Visbal (1993A), that the grid requirements for a delta wing are at least a factor of four over the requirement in tubes. It must be noted, however, that a large portion of the nodes used in wing computations are placed to resolve the boundary layer near the wing surface. Breakdown in tubes is limited to providing information on the necessary resolution required in the vortex core.

A more important role for 3-D computations in tubes may be in establishing how grid resolution affects the appearance of spurious steady and unsteady numerical solutions. There have been several studies which address solution nonuniqueness in axisymmetric flows (Beran and Culick (1992), Lopez (1994), Leibovich and Kribus (1990)). However, few studies (other than the current study) have considered nonuniqueness in 3-D vortical flows. Visbal (1995) (and references within) discuss solution nonuniqueness as it appears over a  $75^\circ$  delta wing. For angles-of-attack between  $27^\circ$  and  $32^\circ$ , solution nonuniqueness is evident in the computations of Visbal (1995). Within this range, for a final angle-

of-attack of  $30^\circ$ , different initial values of angle-of-attack lead to at least four different time-asymptotic behaviors of the computed lift coefficient. However, the development of spurious solutions could not be ruled out as a possible explanation of the different solutions. Further refinement in the grid over the wing is not always practical, given the enormous number of required grid nodes. In addition, the nondimensional times required for these solutions to reach time-asymptotic values are in the thousands, assuming a vortex core length scale. Therefore, it is proposed that a determination of the effects of grid resolution on the development of spurious, nonunique solutions can be performed more efficiently by the TANS model developed in this work, assuming the spurious solutions are the result of inadequate grid resolution.

Lastly, breakdown in tubes may be an efficient alternative to full wing calculations for studying the unsteady pressure fluctuations present during tail-buffeting. Breakdown in tubes could provide guidance for the necessary grid and time-step resolution required to adequately resolve the frequency and amplitudes of coherent pressure fluctuations found in experiments.

*7.2.4 Time-Varying Circulation.* It is recommended that the TANS model be modified to allow for the time-dependent behavior of the inlet circulation. Then, the dynamic movement of vortex breakdown position can be simulated, similar to that observed over pitching delta wings.

The axial position of breakdown over delta wings is highly dependent on the instantaneous angle-of-attack and its temporal derivatives. The time scale associated with the dynamic movement of breakdown position is relatively large, resulting in a larger time lag between the wing motion and the aerodynamic response than that present without breakdown. This lag corresponds to larger phase shifts in the wing lift and pitching moment, reducing the aircraft's maneuvering performance.

Specification of a time-dependent inflow condition for circulation can ultimately result in information on the time scales associated with breakdown movement, rate effects, and possible control strategies.



The first step is to collect data on the dynamic response of the breakdown position to changes in circulation, and compare this behavior to available data collected over delta wings. If there is sufficient agreement in the dynamic behaviors, more studies are justified.

These additional studies would involve strategies for either inhibiting breakdown, or decreasing the dynamic lags associated with breakdown. These strategies would be rated according to both their performance and their practical implementation on delta-wing geometries.

The types of control strategies could include traditional blowing techniques, which have received much attention in the literature, or acoustic techniques, which have received less attention. An acoustic control technique would involve the generation of pressure waves at controlled values of amplitude and frequency. The selected frequency would generally correspond to the (assumed) frequency associated with the instability of the breakdown position. The effects of driving the instability with the generated pressure waves could be studied to determine if such a technique is feasible in affecting the dynamic response of the breakdown movement.

### Appendix A. The Navier-Stokes Equations.

The Navier-Stokes equations are an accurate set of governing equations for the simulation of Newtonian fluids. In this Appendix, the dimensional form of the governing equations are nondimensionalized, resulting in Eqs. 10-14 of Section 3.2. Development of the Navier-Stokes equations abound in the literature. For example, refer to Anderson et al. (1984).

#### A.1 Dimensional Equations of Motion.

The fluid is assumed to be a single-species perfect gas with no heat sources or body forces. In addition, there are no chemical reactions or electromagnetic effects. Given these assumptions, the dimensional Navier-Stokes equations are written below in nonconservative form in terms of the fluid density,  $\rho'$ , the velocity components in the  $x', y'$  and  $z'$  directions,  $(u', v', w')$ , and the pressure  $p'$ . Primes are used here to denote dimensional quantities.

$$\rho'_{t'} + \rho'(u'_{x'} + v'_{y'} + w'_{z'}) + u'\rho'_{x'} + v'\rho'_{y'} + w'\rho'_{z'} = 0 \quad (139)$$

$$u'_{t'} + u'u'_{x'} + v'u'_{y'} + w'u'_{z'} + \frac{1}{\rho'}p'_{x'} = \frac{1}{\rho'} \left( \frac{\partial}{\partial x'} \tau'_{x'x'} + \frac{\partial}{\partial y'} \tau'_{x'y'} + \frac{\partial}{\partial z'} \tau'_{x'z'} \right) \quad (140)$$

$$v'_{t'} + u'v'_{x'} + v'v'_{y'} + w'v'_{z'} + \frac{1}{\rho'}p'_{y'} = \frac{1}{\rho'} \left( \frac{\partial}{\partial x'} \tau'_{y'x'} + \frac{\partial}{\partial y'} \tau'_{y'y'} + \frac{\partial}{\partial z'} \tau'_{y'z'} \right) \quad (141)$$

$$w'_{t'} + u'w'_{x'} + v'w'_{y'} + w'w'_{z'} + \frac{1}{\rho'}p'_{z'} = \frac{1}{\rho'} \left( \frac{\partial}{\partial x'} \tau'_{z'x'} + \frac{\partial}{\partial y'} \tau'_{z'y'} + \frac{\partial}{\partial z'} \tau'_{z'z'} \right) \quad (142)$$

$$p'_{t'} + u'p'_{x'} + v'p'_{y'} + w'p'_{z'} + \gamma p'(u'_{x'} + v'_{y'} + w'_{z'}) = (\gamma - 1)[\Phi' - \nabla \cdot \vec{q}'] \quad (143)$$

Subscripts are used here to represent differentiation and  $t'$  is the dimensional time. The components of the shear stress tensor,  $\tau'$ , is given by

$$\tau'_{ij} = \mu' \left[ \left( \frac{\partial u'_i}{\partial x'_j} + \frac{\partial u'_j}{\partial x'_i} \right) - \frac{2}{3} \delta_{ij} \frac{\partial u'_k}{\partial x'_k} \right] \quad (i, j, k = 1, 2, 3) \quad (144)$$

where  $\mu'$  is the fluid viscosity and

$$\delta_{ij} = \begin{cases} 1 & i = j \\ 0 & i \neq j \end{cases}$$

This description of the shear stress components incorporates Stokes' hypothesis, which assumes that the second coefficient of viscosity,  $\lambda'$ , equals  $-\frac{2}{3}\mu'$ . The viscous dissipation function,  $\Phi'$ , is given by

$$\Phi' = \nabla \cdot (\boldsymbol{\tau}' \cdot \vec{u}') - (\nabla \cdot \boldsymbol{\tau}') \cdot \vec{u}' \quad (145)$$

where <sup>1</sup>  $\vec{u}' \equiv (u', v', w')^T$ . Finally, the heat flux vector,  $\vec{q}'$  is given by

$$\vec{q}' = -k' \nabla T' \quad (146)$$

where  $k'$  is the coefficient of thermal conductivity and  $T'$  is the temperature.

Eqs. 139-143 are five equations with eight unknowns,  $(\rho', u', v', w', p', T', \mu', k')$ . Three auxiliary equations are required to close the system. The first equation comes from the perfect gas law

$$p' = \rho' R T' \quad (147)$$

where  $R$  is the universal gas constant. Two other equations are required to write the transport properties  $(\mu', k')$  in terms of the remaining variables. For low temperature gases, Sutherland's formula provides a very accurate <sup>2</sup> approximation for  $\mu'$

$$\mu' = C_1' \frac{T'^{3/2}}{T' + C_2'} \quad (148)$$

where  $C_1'$  and  $C_2'$  are dimensional constants. The thermal conductivity,  $k'$ , is related to  $\mu'$  by assuming that the Prandtl number, defined as

$$Pr = \frac{c_p \mu'}{k'} \quad (149)$$

<sup>1</sup>A superscript  $T$  cited herein denotes the vector transpose operator, not temperature.

<sup>2</sup>Eq. 148 is accurate to  $\pm 2\%$  for air if  $T \in [300^\circ \text{ R}, 3240^\circ \text{ R}]$  (White (1974)).

is constant throughout the fluid and equal to 0.72. The specific heats,  $c_v$  and  $c_p$ , and the ratio  $\gamma \equiv \frac{c_p}{c_v} = 1.4$  are also assumed constant for a perfect gas. Eqs. 147-149 allow  $(T', \mu', k')$  to be written in terms of the remaining unknowns  $(\rho', u', v', w', p')$ , resulting in five equations with five unknowns.

### A.2 Dimensional Equations of Motion in Vector Form.

The dimensional equations are now cast in vector form for compatibility with the formulation of the solution procedure presented in Section 3.6. In vector form, Eqs. 139-143 can be written as

$$U'_{t'} + A'U'_{x'} + B'U'_{y'} + C'U'_{z'} = D' \quad (150)$$

where  $U' \equiv (\rho', u', v', w', p')^T$  and

$$A' = \begin{bmatrix} u' & \rho' & 0 & 0 & 0 \\ 0 & u' & 0 & 0 & \frac{1}{\rho'} \\ 0 & 0 & u' & 0 & 0 \\ 0 & 0 & 0 & u' & 0 \\ 0 & \gamma p' & 0 & 0 & u' \end{bmatrix} \quad B' = \begin{bmatrix} v' & 0 & \rho' & 0 & 0 \\ 0 & v' & 0 & 0 & 0 \\ 0 & 0 & v' & 0 & \frac{1}{\rho'} \\ 0 & 0 & 0 & v' & 0 \\ 0 & 0 & \gamma p' & 0 & v' \end{bmatrix}$$

$$C' = \begin{bmatrix} w' & 0 & 0 & \rho' & 0 \\ 0 & w' & 0 & 0 & 0 \\ 0 & 0 & w' & 0 & 0 \\ 0 & 0 & 0 & w' & \frac{1}{\rho'} \\ 0 & 0 & 0 & \gamma p' & w' \end{bmatrix} \quad D' = \frac{1}{\rho'} \begin{bmatrix} 0 \\ \frac{\partial}{\partial x'} \tau'_{x'x'} + \frac{\partial}{\partial y'} \tau'_{x'y'} + \frac{\partial}{\partial z'} \tau'_{x'z'} \\ \frac{\partial}{\partial x'} \tau'_{y'x'} + \frac{\partial}{\partial y'} \tau'_{y'y'} + \frac{\partial}{\partial z'} \tau'_{y'z'} \\ \frac{\partial}{\partial x'} \tau'_{z'x'} + \frac{\partial}{\partial y'} \tau'_{z'y'} + \frac{\partial}{\partial z'} \tau'_{z'z'} \\ \rho'(\gamma - 1)[\Phi' - \nabla \cdot \vec{q}'] \end{bmatrix}$$

### A.3 Nondimensionalization of Equations of Motion.

The governing equations are now cast in nondimensional form after specifying appropriate length and velocity scales. The selected length scale is the radius of the vortex core at the inflow boundary,  $r_0$ . The velocity scale is the axial velocity,  $u'_{ref}$ , at the reference point, which is located at the intersection of the tube wall and the inflow boundary. The nondimensional (unprimed) variables are defined as

$$x = \frac{x'}{r_0} \quad y = \frac{y'}{r_0} \quad z = \frac{z'}{r_0}$$

$$\rho = \frac{\rho'}{\rho'_{ref}} \quad p = \frac{p'}{p'_{ref}} \quad T = \frac{T'}{T'_{ref}}$$

$$u = \frac{u'}{u'_{ref}} \quad v = \frac{v'}{u'_{ref}} \quad w = \frac{w'}{u'_{ref}}$$

$$\mu = \frac{\mu'}{\mu'_{ref}} \quad k = \frac{k'}{k'_{ref}} \quad t = \frac{t'}{t'_{ref}}$$

where

$$p'_{ref} \equiv \rho'_{ref} u'^2_{ref} \quad T'_{ref} \equiv 293.166^\circ K \quad t'_{ref} \equiv \frac{r_0}{u'_{ref}} \quad M \equiv \frac{u'_{ref}}{c'_{ref}}$$

and  $c'_{ref}$  is the reference speed of sound.

Substitution of the nondimensional variables into Eqs. 139-143 results in:

$$\rho_t + \rho(u_x + v_y + w_z) + u\rho_x + v\rho_y + w\rho_z = 0 \quad (151)$$

$$u_t + uu_x + vv_y + ww_z + \frac{1}{\rho}p_x = \frac{1}{\rho} \left( \frac{\partial}{\partial x}\tau_{xx} + \frac{\partial}{\partial y}\tau_{xy} + \frac{\partial}{\partial z}\tau_{xz} \right) \quad (152)$$

$$v_t + uv_x + vv_y + ww_z + \frac{1}{\rho}p_y = \frac{1}{\rho} \left( \frac{\partial}{\partial x}\tau_{yx} + \frac{\partial}{\partial y}\tau_{yy} + \frac{\partial}{\partial z}\tau_{yz} \right) \quad (153)$$

$$w_t + uw_x + vw_y + ww_z + \frac{1}{\rho}p_z = \frac{1}{\rho} \left( \frac{\partial}{\partial x}\tau_{zx} + \frac{\partial}{\partial y}\tau_{zy} + \frac{\partial}{\partial z}\tau_{zz} \right) \quad (154)$$

$$p_t + up_x + vp_y + wp_z + \gamma p(u_x + v_y + w_z) = (\gamma - 1)\Phi - \nabla \cdot \vec{q} \quad (155)$$

As a result of the nondimensionalization, the  $(\gamma - 1)$  term is no longer present in the heat conduction term in Eq. 155. The nondimensional shear stress tensor,  $\tau$ , and viscous dissipation,  $\Phi$ , are given by

$$\tau_{ij} = \frac{\mu}{Re} \left[ \left( \frac{\partial u_i}{\partial x_j} + \frac{\partial u_j}{\partial x_i} \right) - \frac{2}{3} \delta_{ij} \frac{\partial u_k}{\partial x_k} \right] \quad (i, j, k = 1, 2, 3) \quad (156)$$

and

$$\Phi = \nabla \cdot (\tau \cdot \vec{u}) - (\nabla \cdot \tau) \cdot \vec{u} \quad (157)$$

where the Reynolds number is defined as  $Re \equiv \frac{\rho'_{ref} u'_{ref} r_0}{\mu'_{ref}}$ . The nondimensional heat flux vector becomes

$$\vec{q} = -\frac{\mu}{Pr Re M^2} \nabla T \quad (158)$$

The auxiliary equations, Eqs. 147-148, become

$$p = \frac{\rho T}{\gamma M^2} \quad (159)$$

$$\mu = \frac{[1 + C'_2/T'_{ref}]}{[T + C'_2/T'_{ref}]} T^{\frac{3}{2}} \quad (T'_{ref} = 293.166^\circ K, C'_2 = 110.4^\circ K) \quad (160)$$

Eq. 160 can be rewritten as

$$\mu = \frac{[1 + C_2]}{[T + C_2]} T^{\frac{3}{2}} \quad (C_2 = 0.3766) \quad (161)$$

For fixed  $Pr$  we find that

$$k = \mu \quad (162)$$

#### A.4 Final Form of Equations of Motion.

The final form of the nondimensional equations of motion are written in vector form from Eqs. 151-155:

$$U_t + AU_x + BU_y + CU_z = D \quad (163)$$

where  $U \equiv (\rho, u, v, w, p)^T$  and

$$A = \begin{bmatrix} u & \rho & 0 & 0 & 0 \\ 0 & u & 0 & 0 & \frac{1}{\rho} \\ 0 & 0 & u & 0 & 0 \\ 0 & 0 & 0 & u & 0 \\ 0 & \gamma p & 0 & 0 & u \end{bmatrix} \quad B = \begin{bmatrix} v & 0 & \rho & 0 & 0 \\ 0 & v & 0 & 0 & 0 \\ 0 & 0 & v & 0 & \frac{1}{\rho} \\ 0 & 0 & 0 & v & 0 \\ 0 & 0 & \gamma p & 0 & v \end{bmatrix}$$

$$C = \begin{bmatrix} w & 0 & 0 & \rho & 0 \\ 0 & w & 0 & 0 & 0 \\ 0 & 0 & w & 0 & 0 \\ 0 & 0 & 0 & w & \frac{1}{\rho} \\ 0 & 0 & 0 & \gamma p & w \end{bmatrix} \quad D = \frac{1}{\rho} \begin{bmatrix} 0 \\ \frac{\partial}{\partial x} \tau_{xx} + \frac{\partial}{\partial y} \tau_{xy} + \frac{\partial}{\partial z} \tau_{xz} \\ \frac{\partial}{\partial x} \tau_{yx} + \frac{\partial}{\partial y} \tau_{yy} + \frac{\partial}{\partial z} \tau_{yz} \\ \frac{\partial}{\partial x} \tau_{zx} + \frac{\partial}{\partial y} \tau_{zy} + \frac{\partial}{\partial z} \tau_{zz} \\ \rho[(\gamma - 1)\Phi - \nabla \cdot \vec{q}] \end{bmatrix}$$

The fundamental effect of the nondimensionalization is to replace  $\mu'$  with  $\frac{\mu}{Re}$  and replace  $(\gamma - 1) k'$  with  $\frac{\mu}{Pr Re M^2}$ .

## Appendix B. The Pseudo-Arclength Continuation (PAC) Model.

### B.1 Definitions

The following are frequently used terms in the context of nonlinear systems (Seydel (1988)), such as the Navier-Stokes equations in discrete form.

- *Solution branch (or path)*: Consider a nonlinear system governed by

$$q_t + F(q; \lambda) = 0 \quad (164)$$

where  $F$  is a set of  $n$  nonlinear, algebraic equations dependent on  $q$  and  $\lambda$ ,  $q$  is an  $n$ -component array of unknowns and  $\lambda$  is a free parameter. In the present context  $\lambda$  represents the vortex strength,  $\mathcal{V}$ . Solutions characterized by a scalar norm,  $N$ , and plotted versus  $\lambda$  usually comprise continua which appear as smooth curves. Such curves are referred to as solution branches.

Different types of solution branches can occur. For example, solutions may represent a steady-state condition of the system, where  $q_t = 0$ . These solutions are typically referred to as equilibrium solutions. Another type of solution can exist in which equilibrium is not achieved, resulting in time-dependent behavior ( $q_t \neq 0$ ). The most common example of such solutions are periodic solutions. In addition, both equilibrium and nonequilibrium solutions can be either stable or unstable.

Stable equilibrium solutions are usually defined by drawing a solid line in a diagram depicting  $N$  versus  $\lambda$ . Unstable equilibrium are denoted with dashed lines. Stable periodic solutions are denoted with solid circles, whereas unstable periodic solutions are denoted with open circles.

- *Limit (or turning) point*: A limit point refers to a particular point on a solution branch where a fold occurs, resulting in multiple solutions for a given value of  $\lambda$ . In Figure 68, limit points are found at  $\lambda = \lambda_1$  and  $\lambda = \lambda_2$ . As  $\lambda$  is increased along branches  $a$  and  $b$ , the first limit point encountered is at  $\lambda_2$ , which is referred to in this work as the *primary* limit point. The second limit point encountered is at  $\lambda_1$ , and is referred to as the *secondary* limit point.



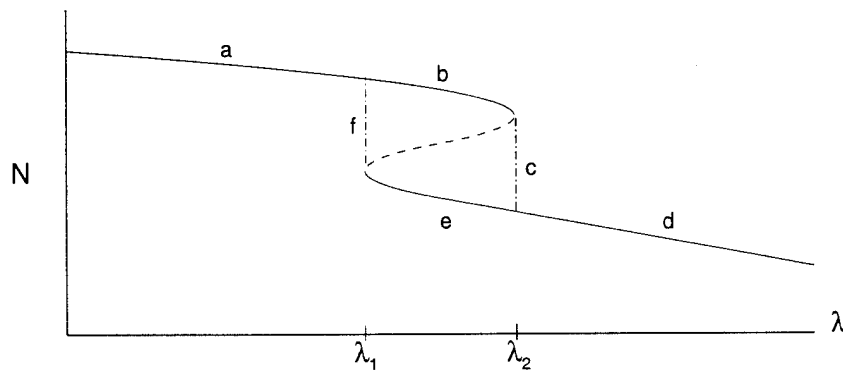


Figure 68. A representative solution branch depicting turning points: stable path (solid line); unstable path (dashed line) and jump in solution space (dash-dot line).

- *Upper/Lower Stable Branch and Unstable Branch:* In Figure 68, the upper stable branch is defined by the paths *a* and *b*. As  $\lambda$  is increased along branch *b*, the primary limit point is encountered at  $\lambda_2$ . The unstable branch is depicted by the dashed line between  $\lambda_1$  and  $\lambda_2$ . The secondary limit point is found at  $\lambda_1$ . The lower stable branch is defined by the paths *e* and *d*. The branch between the two limit points is unstable since it is known that encountering a simple fold along a stable branch results in a change of stability in the solutions past the limit point (Seydel, 1988). Similarly, increasing  $\lambda$  past the secondary limit point, the solution path changes from unstable to stable.

It is known in this study that the upper branch, representing solutions of the PAC model, are stable (Beran (1994)). The term “stable” and “unstable” referring, in the present context, to stability of the axisymmetric solutions.

- *Nonunique solutions:* Nonunique solutions occur in cases depicted in Figure 68 for  $\lambda$  between  $\lambda_1$  and  $\lambda_2$ , where two stable solutions and one unstable solution exist.
- *Hysteresis:* Hysteresis can occur when a solution space contains regions of nonunique solutions. For example, in Figure 68, as  $\lambda$  is increased, the physically realizable solutions are found along the path *a – b – d*. However, the solution would travel

along the path  $d - e - a$  as  $\lambda$  is decreased. This results in a hysteresis loop around the portion of the solution space where nonunique solutions exist.

- *Bifurcation point:* A bifurcation point refers to a specific value of  $\lambda$  where two (or more) solution paths intersect. Bifurcation points are usually associated with a change in solution stability. *Simple* bifurcations involve the intersection of exactly two solution branches. A necessary condition for a simple bifurcation to occur is

$$|F_q| \equiv \left| \frac{\partial F_i}{\partial q_j} \right| = 0 \quad (165)$$

where  $F_q$  is the Jacobian matrix. Thus, we see that a simple bifurcation occurs when the determinant of  $F_q$  vanishes. In practice, simple bifurcations are found numerically by detecting a change in the sign of  $|F_q|$ .

- *Hopf Bifurcation:* A bifurcation in which a time-invariant, equilibrium solution evolves into a periodic, time-varying solution. Seydel (1988) identifies the two classic types of Hopf bifurcation. The first is the *supercritical* Hopf bifurcation (Figure 69a). With the supercritical type, stable periodic orbits (filled circles) encircle a region of unstable equilibrium solutions (dashed lines). In addition, the “magnitude” associated with the periodic behavior increases from zero at the bifurcation point,  $\lambda_1$ , with steadily increasing magnitude as  $\lambda$  moves away from the bifurcation point. Thus, supercritical bifurcations are classified as a *soft loss of stability*. The second type (Figure 69b) is called a *subcritical* Hopf bifurcation. This type has a region of unstable periodic solutions (open circles) encircling stable equilibrium (solid lines). The subcritical Hopf bifurcation is also known as a *hard loss of stability*, due to the abrupt change in solution character as  $\lambda$  crosses the bifurcation point at  $\lambda_2$ . Solutions undergo a large transition from stable equilibrium to large-amplitude, periodic behavior. Between  $\lambda_1$  and  $\lambda_2$ , one of two stable solutions are possible: a stable equilibrium solution or a stable periodic solution.

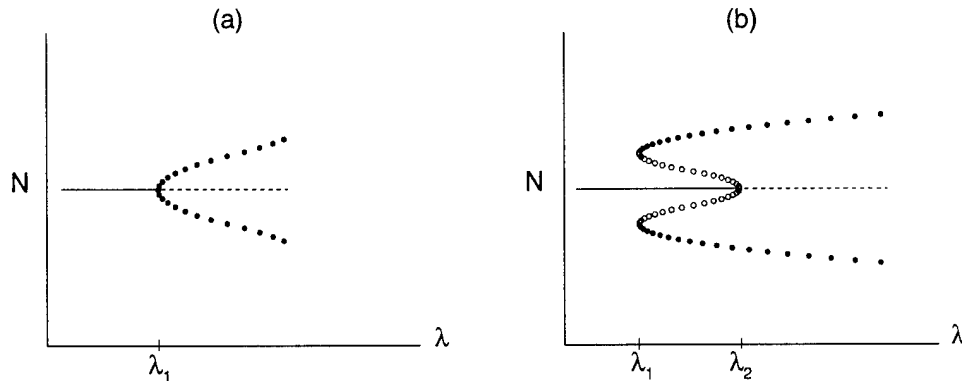


Figure 69. Graphical representation of Hopf bifurcations: (a) supercritical, (b) subcritical. Stable periodic solutions; solid circles: unstable periodic solutions; open circles. From Seydel, 1988.

## B.2 The Pseudo-Arclength Continuation Model.

A brief outline of the PAC model is given in this section. This very general and robust approach is used to compute steady, axisymmetric, and compressible base flows. The application of PAC to the computation of axisymmetric, incompressible flows is described by Beran and Culick (1992).

The PAC model, developed by Beran (1994), is designed to be modular in the sense that a user of the model need only define and implement the necessary governing equations and boundary conditions. Elements of the Jacobian matrix are computed numerically, allowing the PAC model to be written generically for virtually any set of governing equations. For this study, the author's contribution to the PAC model, discussed in Sections B.2.2 and B.2.3, consisted of modifying the compressible, axisymmetric Navier-Stokes equations (written for Cartesian coordinates) to allow for computations over a generalized grid. The author also defined and implemented the boundary conditions into the PAC code.

**B.2.1 The PAC Method.** The PAC model requires that the governing equations be written in discrete form and cast as a nonlinear system of equations given by Eq. 164. While other methods can be used to solve Eq. 164, Newton's method is used in this study for its systematic and efficient ability to compute 2-D base flows. Newton's method, a general method for solving non-linear systems of equations, requires an initial guess,  $q^i$ ,

which must be sufficiently close to the solution of interest. An improved solution,  $q^{i+1}$ , is calculated from the Newton iterate

$$F_q(q^i; \lambda) (q^{i+1} - q^i) = -F(q^i; \lambda) \quad (166)$$

Newton iterates are repeated until a suitable convergence criterion is met.

The PAC method allows for the efficient calculation of a solution which is considered “close” to an existing solution. A close solution refers to one in which a parameter,  $\lambda$ , is slightly varied from its previous value. The advantage of PAC over some other types of continuation is that solutions can be found near limit points, where the Jacobian matrix becomes singular. The point  $P_1$  is a known steady-state solution point on what could be an otherwise unknown path of solutions (Figure 70). The PAC algorithm computes the tangent vector  $T$ . The user specifies the distance from  $P_1$ , along  $T$ , to the point  $P_2$ , where a normal-direction search path is formed. The point  $P_2$  serves as the initial guess for Newton’s method for an extended set of equations, consisting of the governing equations, plus an additional equation which constrains the search to a line normal to  $T$  at  $P_2$ . Thus, the *predictor* step determines  $P_2$ . The *corrector* step is Newton’s method, which solves the extended set of equations to limit the search to the line  $\overline{P_3 - P_2}$ . The desired solution is denoted as point  $P_3$ . The ordinate in Figure 70,  $N$ , represents a user-defined scalar measure of the solution  $q$ . For this work, the minimum axial velocity,  $Q$ , is chosen, since Beran and Culick (1992) found that this scalar effectively identified solution folds.

**B.2.2 Governing Equations.** The governing equations are the compressible Navier-Stokes equations written in cylindrical coordinates. Derivatives in the azimuthal ( $\theta$ ) direction vanish to honor the assumption of axisymmetry. The equations are written in nonconservative, nondimensional form and are nondimensionalized in the same manner as the three-dimensional equations. This nondimensionalization is described in Appendix A.

$$\rho \hat{u}_r + \hat{u} \rho_r + \frac{\rho \hat{u}}{r} + \rho \hat{w}_z + \hat{w} \rho_z = 0 \quad (167)$$

$$\rho \hat{u} \hat{u}_r + \rho \hat{w} \hat{u}_z - \frac{\rho \hat{v}^2}{r} + p_r - \frac{1}{r} [(r \hat{\tau}_{11})_r + (r \hat{\tau}_{13})_z] + \frac{\hat{\tau}_{22}}{r} = 0 \quad (168)$$

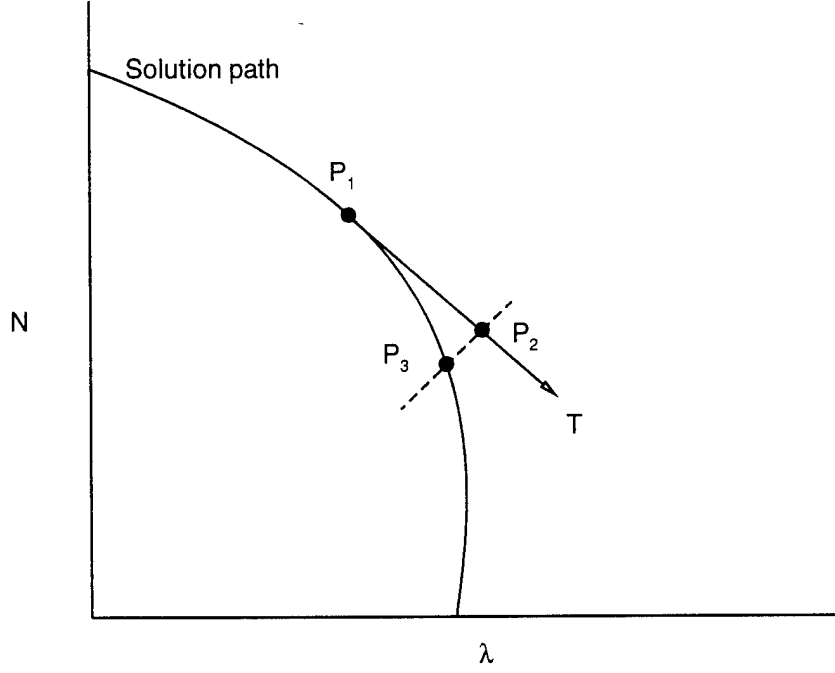


Figure 70. Graphical representation of the pseudo-arclength continuation solution procedure.

$$\rho \hat{u} \hat{v}_r + \frac{\rho \hat{u} \hat{v}}{r} + \rho \hat{w} \hat{v}_z - \frac{1}{r} [(r \hat{\tau}_{12})_r + (r \hat{\tau}_{23})_z] - \frac{\hat{\tau}_{12}}{r} = 0 \quad (169)$$

$$\rho \hat{u} \hat{w}_r + \rho \hat{w} \hat{w}_z + p_z - \frac{1}{r} [(r \hat{\tau}_{13})_r + (r \hat{\tau}_{33})_z] = 0 \quad (170)$$

$$\hat{u} p_r + \hat{w} p_z + \gamma (\nabla \cdot \vec{u}) p - (\gamma - 1) (\hat{\Phi} - \nabla \cdot \hat{\vec{q}}) = 0 \quad (171)$$

where

$$\vec{u} = (\hat{u}, \hat{v}, \hat{w})^T$$

The components of the symmetric stress tensor,  $\hat{\tau}$ , are given by

$$\begin{aligned} \hat{\tau}_{11} &= \frac{\mu}{Re} [-(2/3)(\nabla \cdot \vec{u}) + 2\hat{u}_r] \\ \hat{\tau}_{22} &= \frac{\mu}{Re} [-(2/3)(\nabla \cdot \vec{u}) + 2\hat{u}/r] \\ \hat{\tau}_{12} &= \frac{\mu}{Re} [\hat{v}_r - \hat{v}/r] \end{aligned}$$

$$\begin{aligned}
\hat{\tau}_{23} &= \frac{\mu}{Re} \hat{v}_z \\
\hat{\tau}_{13} &= \frac{\mu}{Re} [\hat{w}_r + \hat{u}_z] \\
\hat{\tau}_{33} &= \frac{\mu}{Re} [-(2/3)(\hat{u}_r + \hat{u}/r) + (4/3)\hat{w}_z]
\end{aligned}$$

where  $\hat{\tau}_{21} = \hat{\tau}_{12}$ ,  $\hat{\tau}_{31} = \hat{\tau}_{13}$ ,  $\hat{\tau}_{32} = \hat{\tau}_{23}$ . The viscous dissipation,  $\hat{\Phi}$ , is defined as

$$\hat{\Phi} = \frac{-2\mu(\nabla \cdot \vec{u})^2}{3Re} + \frac{2\mu}{Re} (e_{11}^2 + e_{22}^2 + e_{33}^2) + \frac{4\mu}{Re} (e_{12}^2 + e_{13}^2 + e_{23}^2)$$

where the elements of the symmetric strain tensor,  $e$ , are given by

$$\begin{aligned}
e_{11} &= \hat{u}_r \\
e_{12} &= (\hat{v}_r - \hat{v}/r)/2 \\
e_{13} &= (\hat{w}_r + \hat{u}_z)/2 \\
e_{22} &= \hat{u}/r \\
e_{23} &= \hat{v}_z/2 \\
e_{33} &= \hat{w}_z
\end{aligned}$$

Finally, the divergence of the heat flux vector,  $\hat{\vec{q}}$ , is expanded, resulting in

$$\nabla \cdot \hat{\vec{q}} = -\frac{1}{Pr Re M^2 (\gamma - 1)} [\mu (T_r/r + T_{rr} + T_{zz}) + T_r \mu_r + T_z \mu_z]$$

Eqs. 167–171 reduce to five equations in five unknowns,  $(\rho, \hat{u}, \hat{v}, \hat{w}, p)$ , when the assumption of a perfect gas and Sutherland's law are incorporated (Chapter III: Eqs. 20–21).

The discretization of Eqs. 167–171 involves first writing the equations in computational coordinates, where  $\xi$  and  $\eta$  refer to the computational coordinates in the  $\hat{z}$  and  $r$  directions respectively. Derivatives are approximated using second-order-accurate, central-difference approximations at interior nodes and second-order, three-point formulas at boundaries.

Fourth-order damping terms are added to the above equations, analogous with the TANS model. The damping term has the form

$$\omega_{\xi} \Delta t \delta^4 U_{\xi} + \omega_{\eta} \Delta t \delta^4 U_{\eta}$$

where  $U \equiv (\rho, \hat{u}, \hat{v}, \hat{w}, p)^T$ . The form of the damping term allows for different damping levels for the streamwise and radial directions. This is done to allow for greater consistency with the TANS model. The PAC model is only capable of supplying damping in the radial and axial directions, while the TANS model supplies damping in two crossplane directions,  $y$  and  $z$ , and the axial direction. One can think of the damping applied in  $y$  and  $z$  as being realigned into radial and azimuthal components. In this light, we see that the TANS model will provide greater levels of damping over the PAC model if damping coefficients are equivalent. To compensate for the lack of azimuthal damping in the PAC model, we set  $\omega_{\eta} = 2\omega_{\xi}$ . This provided better comparisons between the two models.  $\omega_{\xi}$  is set equal to the explicit damping coefficient used in the TANS model,  $\omega_e$ .

*B.2.3 Boundary Conditions.* The boundary conditions for the TANS and PAC model are identical, except for differences in implementation and coordinate systems. The TANS model solution is in the delta form, requiring the boundary conditions to be formulated in the delta form as well. The PAC model requires that the boundary conditions be written in the same form as the governing equations, i.e., in the form  $F(q; \lambda) = 0$ . All but two of the inflow, outflow, and wall boundary conditions can be easily deduced by referring to the boundary condition description in Section 3.4. The first exception is the pressure condition for Inflow-2. The axial momentum equation is solved in both models to find an expression for pressure at the inlet. The PAC model solves Eq. 170, instead of the steady form of Eq. 11. The second exception is the Wall-2 condition for pressure. The TANS model solves the steady form of Eqs. 12–13, which represent the conservation of momentum in the  $y$  and  $z$  directions. The PAC model solves the radial momentum equation, Eq. 168.

The PAC model requires boundary conditions along the tube centerline. The centerline values of radial and azimuthal velocity must vanish since the centerline is both a

streamline and a line of symmetry:

$$\hat{u}(0, z) = 0$$

$$\hat{v}(0, z) = 0$$

The remaining variables are constrained to be smooth and symmetric about the centerline by enforcing that the corresponding radial derivatives vanish:

$$\hat{w}_r(0, z) = 0$$

$$\rho_r(0, z) = 0$$

$$p_r(0, z) = 0$$

### *B.3 Solution Interpolation Between 2-D and 3-D Grids*

This subsection describes the cubic spline interpolation routine (Press et al. (1989)), which takes axisymmetric data from the PAC model and interpolates it onto a 3-D grid. The cubic spline interpolation method has several features that make it a good choice for this problem. First of all, the method requires that first derivatives be continuous across the boundary between two intervals of data. This is a requirement for most applications where the tabulated data source is a physical process. Second, the method inherently creates interpolating polynomials of low (third) degree. Some other methods (e.g., Lagrange polynomial method) create interpolating polynomials that are the degree of the number of tabulated points minus one. This can lead to the undesirable result of large variations (or “wiggles”) in the polynomial behavior between data points. Third, the method yields high, fourth-order accuracy. Finally, the numerical procedure is very efficient and straightforward, even when the tabulated points are not equally spaced. The cubic spline algorithm was adapted from Press et al. (1989), with supplemental error analysis supplied by the author.

*B.3.1 Cubic Spline Interpolation.* The tabulated function is written as  $y_j = y(r_j)$ ,  $j = 1, \dots, N$ , where the independent variable  $r$  denotes the radial coordinate. For  $r \in$



$(r_j, r_{j+1})$ , let  $r_1 \equiv r - r_j$  and  $r_2 \equiv r_{j+1} - r$  such that  $\Delta r = r_1 + r_2 = r_{j+1} - r_j$ . The goal is to construct an interpolating polynomial between  $r_j$  and  $r_{j+1}$ . The value of  $y(r)$  is approximated by writing a Taylor series about  $y_j$

$$y(r) = y_j + r_1 y'_j + \frac{r_1^2}{2} y''_j + \frac{r_1^3}{6} y'''_j + \mathcal{O}(r_1^4) \quad (172)$$

where primes denote differentiation. The central idea of cubic spline interpolation is to guarantee continuity in the first derivatives of the interpolating polynomial, and to use this continuity to calculate  $y''$ . Thus, with some foresight, Eq. 172 is written in terms of only the function,  $y$ , and its second derivative  $y''$ . Utilizing Taylor series, the following expressions are obtained

$$y'_j = [y_{j+1} - y_j - (\Delta r^2/2)y''_j - (\Delta r^3/6)y'''_j]/\Delta r + \mathcal{O}(\Delta r^3) \quad (173)$$

$$y'''_j = [y''_{j+1} - y''_j]/\Delta r + \mathcal{O}(\Delta r) \quad (174)$$

Eqs. 173-174 are substituted into Eq. 172 and simplified with the relations  $A \equiv r_2/\Delta r$  and  $B \equiv r_1/\Delta r$  to obtain

$$y(r) = Ay_j + By_{j+1} + Cy''_j + Dy''_{j+1} + \mathcal{O}(r_1^4, r_1\Delta r^3, r_1^3\Delta r) \quad (175)$$

where

$$C \equiv \frac{1}{6}(A^3 - A)(r_{j+1} - r_j)^2 \quad D \equiv \frac{1}{6}(B^3 - B)(r_{j+1} - r_j)^2$$

Since  $r_1$  can vary between 0 and  $\Delta r$ , the truncation error will be greatest when  $r_1 = \Delta r$ , allowing Eq. 175 to be written as

$$y(r) = Ay_j + By_{j+1} + Cy''_j + Dy''_{j+1} + \mathcal{O}(\Delta r^4) \quad (176)$$

The second derivatives,  $y''$ , are evaluated by requiring that the first derivatives be continuous between the boundaries of the intervals  $(r_{j-1}, r_j)$  and  $(r_j, r_{j+1})$ . This conditions allows

for  $y''$  to be calculated from  $j = 2$  to  $j = N - 1$  as

$$ay''_{j-1} + by''_j + cy''_{j+1} = d \quad (177)$$

where

$$\begin{aligned} a &= (r_j - r_{j-1})/6 & b &= (r_{j+1} - r_{j-1})/3 \\ c &= (r_{j+1} - r_j)/6 & d &= \frac{y_{j+1} - y_j}{r_{j+1} - r_j} - \frac{y_j - y_{j-1}}{r_j - r_{j-1}} \end{aligned}$$

Boundary conditions are required at  $j = 1$  and  $j = N$  to complete the tridiagonal system represented in Eq. 177. Three boundary conditions have been implemented. The three conditions correspond to linear, parabolic, and cubic behavior at the end points. The formal truncation error within a boundary interval grows from fourth, to third, to second-order as the boundary condition changes from cubic, to parabolic, and then to linear behavior respectively. Once  $y''$  is calculated, the value of  $y$  at any given point,  $r$ , in the range of the tabulated data can be found from Eq. 176.

*B.3.2 Validation.* The cubic spline algorithm written for this work was validated by comparison with data from the software package MathCAD (1988). The algorithm was also tested to verify the order-of-accuracy of the method for various test functions. A summary of the results are shown in Tables 18 and 19. Three different functions are presented in Table 18. Table 19 compares results from a fifth-degree polynomial tested with the three different boundary conditions. Errors in the tables are calculated by subtracting the known value of the function at the evaluated point from the interpolated value. The constant node spacing,  $\Delta r$ , is given by

$$\Delta r = \frac{r_{\max} - r_{\min}}{N - 1}$$

where  $r_{\max}$  and  $r_{\min}$  are the maximum and minimum values of the independent variable,  $r$ . The functions shown in the tables are evaluated at the point  $(r_0 - \Delta r/2)$ , with values of  $r_0$  given in Table 18. For the fifth-degree polynomial,  $r_0 = 1$ ,  $r_{\min} = 0$ , and  $r_{\max} = 1$ . The data verifies fourth-order truncation errors with possible exceptions of second or third-

Table 18. Cubic spline results.

Function	$r_0$	$r_{\min}$	$r_{\max}$	$N$	Error	Factor
$y=\sin(r)$	$\pi/2$	0	$2\pi$	257	9.4506369(-10)	-
				513	5.9063088(-11)	16.00092
$y=\exp(r)$	1.6875	-3	3	257	4.1979460(-09)	-
				513	2.6394087(-10)	15.90487
$y=\text{erf}(r)$	0.5	0	1	257	2.6637581(-12)	-
				513	1.6642243(-13)	16.00600

Table 19. Effect of boundary conditions:  $y = r^5 + r^4 + r^3 + r^2 + r + 1$ .

Boundary Condition	$N$	Error	Factor
linear	257	2.7925307(-05)	-
	513	6.9813671(-06)	3.99998
parabolic	257	1.9288001(-07)	-
	513	2.4153221(-08)	7.98568
cubic	257	8.6388230(-10)	-
	513	5.4085625(-11)	15.97249

order truncation errors near boundaries. The errors are evaluated by considering a halving of the spacing and checking the corresponding reduction in error (under heading of Factor in the tables). Factors of 4, 8, and 16 therefore represent second, third, and fourth-order truncation errors respectively. The accuracy of the method is important since truncation error due to interpolation must be of the same or higher order of magnitude than the truncation error of the second-order PAC model. The error analysis and the tests represented in Table 19 show that in the worst case (at the boundaries), the error will be second order, the same as the error introduced by the PAC model. Away from the boundaries the interpolation introduces fourth-order inaccuracies, which are much smaller than second-order errors produced by the PAC model. Thus, the interpolation scheme does not degrade the formal spatial accuracy of the base flows computed by the PAC model.

**B.3.3 Restart File Generation.** The process of taking the axisymmetric data from the PAC model and using it to create a *restart* file to initiate the TANS model computations is mechanized into one algorithm. This algorithm reads the 2-D and 3-D grid files and the 2-D restart file. The 2-D restart file contains the solution vector  $U = (\rho, \hat{u}, \hat{v}, \hat{w}, p)^T$ . The code first checks that the axial locations coincide for the two grids, and that the tube

radius at each axial location match. Then for each axial node, the second derivatives for the interpolating polynomial are computed. Then the radial position of each 3-D grid point (at that axial location) are evaluated and the cubic spline interpolation performed. A linear boundary condition is chosen along the centerline  $r = 0$ , consistent with the centerline boundary conditions enforced in the PAC model. At the tube wall, the cubic boundary condition is enforced. The process is repeated for each axial node and for each element of the solution vector. Then the radial and swirl velocities,  $(\hat{u}, \hat{v})$ , are transformed into the velocities in the  $y$  and  $z$  directions. This transformation is given by

$$v = (y\hat{u} - z\hat{v})/R$$

$$w = (z\hat{u} + y\hat{v})/R$$

where  $R = \sqrt{y^2 + z^2}$ . The velocity components  $v$  and  $w$  are set to zero at the centerline,  $R = 0$ . The output of the algorithm is a 3-D restart file containing the interpolated solution vector  $U = (\rho, u, v, w, p)^T$  valid at the 3-D grid points.

### *Appendix C. Grid Generation*

A description of the grid generation procedure and the method used to access grid quality are described in this Appendix. Section C.1 contains an overview of the grid construction process, which utilizes the software package GRIDGEN. Grid quality is assessed in Section C.2 by performing a grid rotation study, which demonstrates that there is no significant asymmetry in the grid structure.

#### *C.1 Grid Construction.*

The positions of the grid points in the  $(\eta, \zeta)$  planes are generated by the GRIDGEN software, Version 8 (Steinbrenner (1990)). GRIDGEN is designed to be a user-friendly, robust grid generation tool capable of generating 3-D, multiple-block grids. The primary customers of GRIDGEN are typically those requiring grid generation about complex geometries, such as a full aircraft configuration. The GRIDGEN software package consists of four distinct components, referred to as GRIDBLOCK, GEN2D, GEN3D, and VUE3D.

The basic procedure to generate a 3-D grid using GRIDGEN involves three steps. First, GRIDBLOCK specifies the blocking strategy for the grid. This includes the specification of the number of blocks, the location of the interfaces and their shapes, and the number of nodes. GRIDBLOCK initializes the gridpoints along the 2-D domains that make up the sides of the blocks. These gridpoints are determined from transfinite interpolation (TFI) methods. Second, GEN2D refines the domain gridpoints using standard elliptic partial differential equation (PDE) solvers. This refinement can only occur within each block. That is, GEN2D does not have the capability to perform multiple-block iteration. Finally, GEN3D initializes the 3-D grid with TFI using the gridpoints developed along the domains as boundary conditions. GEN3D then uses elliptic PDE solvers to smooth the interior points of the blocks. GEN3D has a multiple-block mode that helps smooth out points at block interfaces. VUE3D is a utility program that allows the user to visualize the grid.

The grids developed for this work contain five blocks. The inner block is prescribed to initially have a circular shape in the  $(y, z)$  crossplane, located concentrically with the

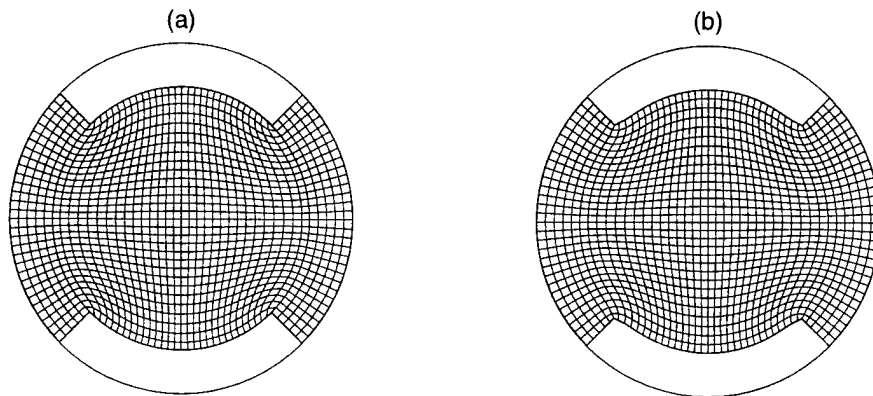


Figure 71. Typical crossplane grids: (a) initial grid, (b) final grid.

outer tube wall. The radius of this inner block is set at 1.5. The outer blocks are arranged as shown in Figure 71a. This crossplane is generated by GEN2D. To allow GRIDGEN to iterate over this crossplane in multiple-block mode, a 3-D geometry is created. This geometry resembles a short tube that has the crossplane structure of Figure 71a. The number of crossplanes (i.e., axial nodes) used is eleven. With this short tube geometry, the interior crossplane nodes can be determined using the GEN3D multiple-block mode. Then, the crossplane that is halfway down the length of the tube (Figure 71b) is selected as the crossplane grid. Figures 71a and 71b illustrate how GEN3D smooths out the interfaces between the inner and outer blocks. The final grid is constructed one crossplane at a time, by scaling the final crossplane grid to the local tube radius.

### C.2 Assessment of Grid Quality.

Grid quality is verified in two ways. First, the grid metrics and Jacobian contours are plotted and visually inspected for smoothness. Second, a grid rotation study is performed. This is done to insure that there is no asymmetry in the grid structure that may preferentially bias a solution in a particular radial direction, promoting an asymmetric solution in cases where the flow is physically axisymmetric.

The grid rotation study utilizes a swirling, columnar flow in a tube of very short axial extent. A 3-D grid consisting of 3 axial nodes is constructed by taking the crossplane grid from G1 (at  $x = 0$ ) and duplicating this grid over three equally-spaced axial nodes. In this way, fixed boundary conditions are enforced along the inflow and outflow planes to provide conditions for swirling, columnar flow. The inflow conditions enforce zero axial and radial velocity with pressure initialized to the reference value and  $\rho = 1$ . The specified swirl velocity at the inflow and outflow is of the form

$$\hat{v} = \frac{V}{(r - r^*)} \left( 1 - e^{-(r - r^*)^2} \right)$$

where

$$r - r^* = \sqrt{(y - y^*)^2 + (z - z^*)^2} \quad y^* = z^* = 1/2$$

The parameter  $r^*$  was introduced to provide an asymmetric profile, essentially moving the vortex core off axis to  $(y^*, z^*)$ . This is done to move the vortex core close to a corner point (e.g.,  $j = j2$  and  $k = k2$ ), providing a region of strong flow gradients. It is believed by the author that this provides a better test of the model's ability to compute accurately near a corner node, as well as show that the effects of grid rotation are negligible. The axial and radial components of velocity are prescribed to be zero at the wall, while the wall swirl velocity is set equal to the inflow value. Pressure is prescribed to be the reference pressure and  $\rho = 1$ . The solution is then iterated until converged.

Solutions are obtained for grids rotated at angles of  $\theta = 0, 90, 180$ , and  $270$  degrees. The upper right quadrant of the grid corresponding to  $\theta = 0$  is shown in Figure 72a. Corresponding contour plots of pressure for all four rotation angles are shown in Figure 72b. The contour plots are virtually identical for each rotation angle, indicating that the grid is sufficiently "unbiased." The figure also illustrates that solutions near the grid block interfaces are "seamless" in that the underlying multiblock grid structure is not evident from the solutions.

In an attempt to quantify the errors due to grid rotation, pressures are compared at two points in the crossplane. The two points are selected based on visual inspection of Figure 72b, where the greatest differences between pressure contours appear to occur near

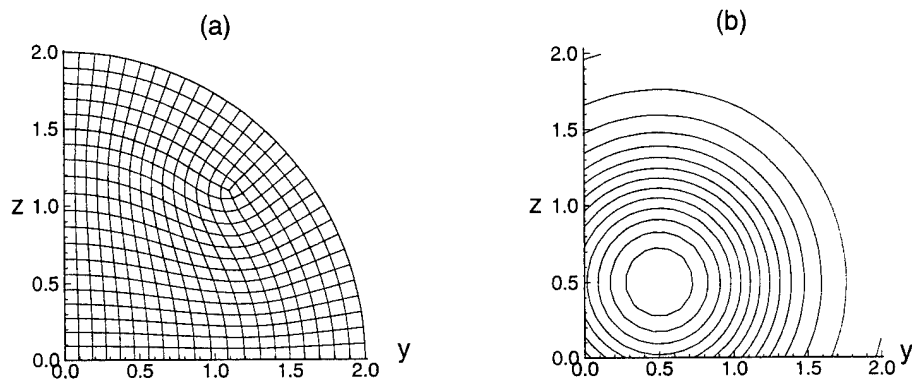


Figure 72. Results of grid-rotation study: (a) grid ( $\theta = 0$ ), (b) coalesced pressure contours correspond to grids rotated at angles of 0, 90, 180, and 270 degrees.

Table 20. Pressure values at two points in the crossplane for various grid rotation angles.

	$\theta$	Pressure
$p_{32,32}$	$0^\circ$	7.63129
	$90^\circ$	7.63131
	$180^\circ$	7.63137
	$270^\circ$	7.63125
$p_{36,36}$	$0^\circ$	7.76475
	$90^\circ$	7.76528
	$180^\circ$	7.76485
	$270^\circ$	7.76529

$y = z = 0.85$ . The closest node to this location is at  $j = k = 32$ . The second point is selected to be a corner node at  $j = k = 36$  ( $y = z \approx 1.06$ ). Table 20 shows the pressures at these points for each rotation angle.

The greatest relative error encountered at these two points occurs at the point  $j = k = 36$ , between pressures at  $\theta = 0^\circ$  and  $270^\circ$ . The magnitude of this error is 0.00054. The pressure over the entire crossplane ranges from  $p_{j,k_{\min}} = 7.52005$  to  $p_{j,k_{\max}} = 7.91945$ . Defining a normalized pressure error as

$$\Delta p \equiv \frac{(p_{36,36})_{270^\circ} - (p_{36,36})_{0^\circ}}{p_{j,k_{\max}} - p_{j,k_{\min}}}$$

gives  $\Delta p = 0.001352$ .



### *Appendix D. TANS Validation.*

The solution procedures and results of four test flows are described in this Appendix. The first two test flows, described in Sections D.1 and D.2, are incompressible and compressible flat plate flow. These checkcases are used to verify the steady-state accuracy of the TANS solutions. The remaining two test flows are unsteady Couette flow and unsteady heat conduction. These checkcases, described in Sections D.3 and D.4, validate the time-accuracy of the model.

Results in this appendix are obtained with the second-order, central difference version of the TANS model using a simplified version which allows for conventional, single-block grids. Two-dimensional flows are simulated with the 3-D TANS model by specifying that the velocity component and all derivatives in one of the coordinate directions vanish, yielding essentially 2-D flow. This coordinate direction is referred to as the *transparent* direction. Grid requirements are reduced by specifying only three nodes in the transparent direction.

#### *D.1 Incompressible Flow over a Flat Plate.*

Steady flow over a flat plate (at zero incidence) is simulated to verify that the model accurately converges to a known steady solution. It is an approximate comparison since the TANS model is formulated to simulate compressible flows whereas the test flow is incompressible. To minimize the impact of this difference, the TANS model is run at a low Mach number ( $M = 0.2$ ) and the boundary conditions are formulated for incompressible flow. In addition, the comparison is approximate since the exact solution is known only in the limit as  $Re \rightarrow \infty$ . Therefore, the TANS model is only expected to yield reasonable comparisons to the test flow for sufficiently large  $Re$ ; assumed here to be 10000.

The solution to incompressible flow over a flat plate was first obtained by Blasius in 1908, (White (1974)). Blasius formulated a similarity solution for the axial velocity,  $u$ , of the form

$$u(x, z) = f'(\eta), \quad \eta = \eta(x, z)$$

to obtain the governing equation

$$f''' + ff'' = 0 \quad (178)$$

where

$$u = f'(\eta) \quad \text{and} \quad \eta = z\sqrt{\frac{Re}{2x}}$$

The quantity  $x$  is the nondimensional freestream coordinate and  $z$  is the nondimensional distance normal to the flat plate. The boundary conditions are

$$f(0) = f'(0) = 0, \quad f'(\infty) = 1$$

The above relations are in nondimensional form, where  $Re$  is based on the constant freestream velocity and plate length. No closed-form analytic solution to Eq. 178 has been found. Instead, the Blasius solution is computed by numerically integrating Eq. 178 using a fourth-order Runge-Kutta method to obtain  $f'$ . The Reynolds number,  $Re$ , is required to obtain the solution  $u(x, z)$  from the similarity law. Thus, for a given  $Re$ , the Blasius solution is found and used to compare to the axial velocities produced by the TANS model.

TANS model solutions are obtained over the region  $(0 < x < 2)$  and  $(0 < z < 0.15)$  using constant node spacing. The number of axial and normal nodes is 101. The  $y$  direction is chosen as the transparent direction, requiring that the corresponding velocity component,  $v$ , vanish.

The boundary conditions consist of inflow, outflow, wall, and freestream conditions. The inflow conditions are  $\rho = u = 1$  with  $v = w = 0$ . The pressure is initialized to the nondimensional reference pressure,  $P_{ref}$ , which has a value of  $\frac{1}{\gamma M^2}$ . The freestream conditions are the same as the inflow conditions except that  $w_z = 0$  from the incompressible continuity equation. The outflow conditions dictate that  $(\cdot)_{xx} = 0$  for all five dependent variables. At the adiabatic wall, uniform density is enforced and the boundary-layer assumption dictates that  $p_z = 0$ .

For  $Re = 10000$  and  $M = 0.2$ , the TANS model was run until the maximum change in pressure over one iteration was less than  $10^{-5}$ . Velocities obtained from the TANS model

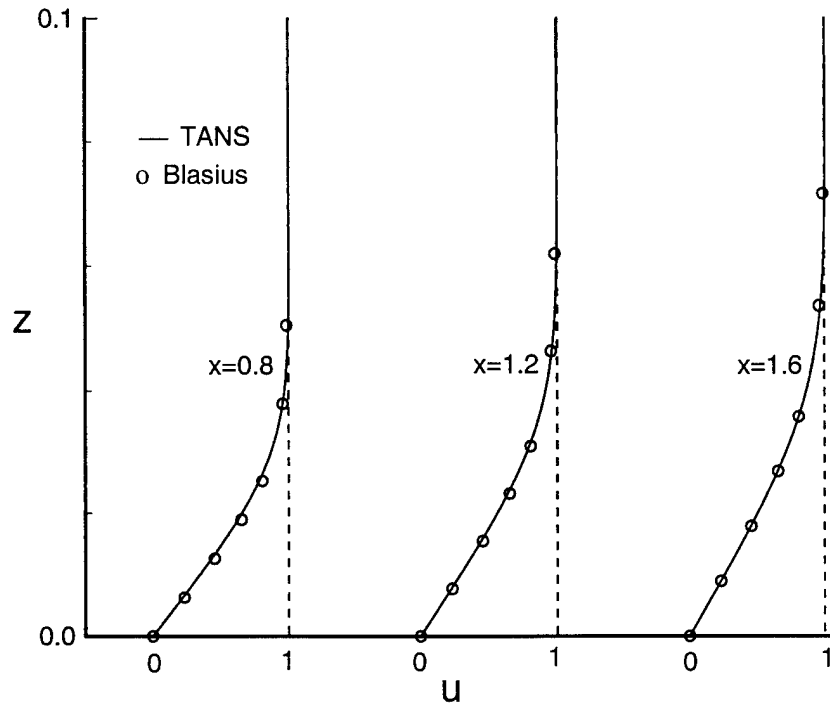


Figure 73. Comparison of streamwise velocity profiles for steady, flat-plate flow for  $Re = 10000$  and  $M = 0.2$ . Blasius solution from Eq. 178.

are compared to the Blasius profiles in Figure 73. The two solutions are shown to be in excellent agreement.

The  $L_2$  norms (Section 3.10) of the difference in  $u$  between the TANS model and the Blasius solution, corresponding to data at  $x = 0.8$ ,  $x = 1.2$  and  $x = 1.6$  are  $3.0E-03$ ,  $3.9E-03$  and  $5.7E-03$  respectively.

#### D.2 Compressible Flow over a Flat Plate.

This test flow is used to verify that the TANS model accurately predicts a steady-state temperature field. This augments the incompressible flat plate flow, where steady-state velocities are validated. A constant temperature wall is assumed in this case. Three wall temperatures, corresponding to the known adiabatic wall temperature and  $\pm 1\%$  of the

adiabatic temperature are specified. The result expected by the author is that when the adiabatic wall temperature is applied, the resulting temperature profile in  $z$  should result in a zero-slope (adiabatic) condition at the wall. A change in the heat flux at the wall should also occur when temperatures are specified above and below the adiabatic temperature. In addition, temperature profiles,  $T(z)$ , at a chosen axial station are compared for the three wall temperatures to an exact relation referred to as the Crocco-Busemann relation.

The geometry and parameter values for this flow are the same as the incompressible case, except the freestream Mach number is increased to 0.5 and  $Pr = 1$ . The wall pressure condition is found by solving the  $z$ -momentum equation for  $p_z$ .

The nondimensional adiabatic wall temperature,  $T_{aw}$ , can be expressed, for  $Pr = 1$ , as

$$T_{aw} = \frac{T'_{aw}}{T'_{ref}} = 1 + \frac{(\gamma - 1)}{2} M^2 \quad (179)$$

where the reference conditions are in the freestream flow.

The 2nd Crocco-Busemann relation (White, 1974), given in nondimensional form as

$$T = T_w + (T_{aw} - T_w)u - \left[\left(\frac{\gamma - 1}{2}\right)M^2\right]u^2 \quad (180)$$

relates the axial velocity,  $u$ , to the temperature. It is valid for compressible and incompressible boundary layers for constant  $c_p$ ,  $Pr = 1$ , and zero axial pressure gradient. The analytically determined temperature gradient at the wall can be obtained by differentiating Eq. 180 with respect to  $z$  and evaluating at  $z = 0$ . Given that  $u = 0$  at  $z = 0$ , this results in

$$\left(\frac{\partial T}{\partial z}\right)_w = (T_{aw} - T_w) \left(\frac{\partial u}{\partial z}\right)_w = -q_w/k \quad (181)$$

where the subscript  $w$  denotes wall conditions and  $q_w$  is the wall heat flux. Inspection of Eq. 181 reveals that the wall temperature gradient is zero when the wall maintains the adiabatic wall temperature, or  $T_w = T_{aw}$ . Furthermore, it is evident that the sign of the wall heat flux and the wall temperature gradient changes depending upon whether the wall temperature is higher or lower than the adiabatic temperature. Thus, the following

behavior should be observed from the TANS model:

$$\left(\frac{\partial T}{\partial z}\right)_w \begin{cases} = 0 & T_w = T_{aw} \\ < 0 & T_w > T_{aw} \\ > 0 & T_w < T_{aw} \end{cases}$$

The wall temperature chosen are  $T_w = T_{aw}$ ,  $T_w = 1.01T_{aw}$  and  $T_w = 0.99T_{aw}$ .

The solid lines in Figure 74 shows the resulting TANS temperature profiles for the three wall temperatures, while the open circles show the results from the Crocco relation. A change in sign of the heat-flux at the wall occurs around the adiabatic wall temperature, while at the adiabatic wall temperature we see an adiabatic temperature profile.

The insert to Figure 74 plots the computed wall temperature gradient versus the wall temperature. This figure shows the path crossing zero temperature gradient at a temperature that is virtually at the adiabatic temperature. Physically, the TANS model is correctly predicting that, for  $Pr = 1$ , the adiabatic wall temperature due to frictional heating equals the reference stagnation temperature, corresponding to a recovery factor of unity.

The differences in temperature near the edge of the thermal boundary layer are due to about a 2% overshoot (from freestream) in the TANS model axial velocity, which is used in the Crocco-Busemann relation to find  $T$ . This error in  $u$ , denoted as  $\epsilon$ , is amplified by a factor of 2 due to the  $u^2$  term in Eq. 180, and from considering the binomial expansion of  $u^2$  written in the form  $(1 + \epsilon)^2$ . Furthermore, the differences in temperature appear large due to the scaling of the figure. In fact, the error between  $T$  from the Crocco-Busemann relation and the model is at most  $0.004T_{aw}$  (i.e., the spacing between 2 minor tick marks in the figure). The comparison near the wall is quite favorable, however, where both the TANS model and Eq. 180 correctly predict the change in sign of the heat flux. The  $L_2$  norms of the temperature difference between the TANS model and the Crocco relation are  $1.9\text{E-}03$ ,  $1.7\text{E-}03$  and  $1.4\text{E-}03$  for  $T_w/T_{aw} = 1.01$ ,  $1.0$  and  $0.99$  respectively.

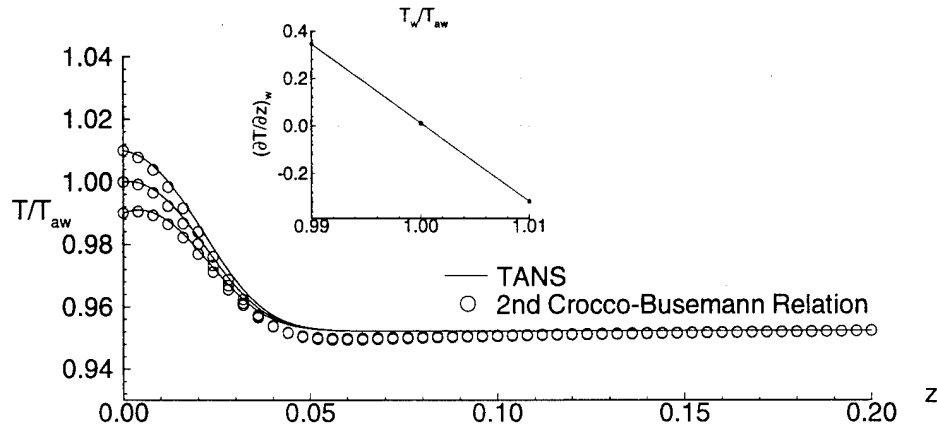


Figure 74. Temperature profiles for compressible, flat-plate flow for  $Re = 10000$  and  $M = 0.5$ . Second Crocco-Busemann relation from Eq. 180.

### D.3 Unsteady Couette Flow.

Unsteady Couette flow is simulated with the TANS model to verify the time accuracy of the computed velocity field. A nearly identical checkcase is given by Beam and Warming (1978), who used this type of flow to help validate the original Beam-Warming algorithm.

Couette flow refers to the incompressible, steady flow between two parallel, infinite, and adiabatic plates that are a distance  $h$  apart. The upper plate is stationary while the lower plate moves with uniform speed,  $U_0 = u'_{ref}$ . Unsteady Couette flow refers to the transition between the no-flow state, existing before the lower plate is set into motion, and the final steady-state flow that ultimately develops.

An exact solution for the axial velocity profile,  $u$ , for unsteady Couette flow (Schlichting, 1955) is given as

$$u = \frac{u'}{U_0} = \sum_{n=0}^{\infty} \operatorname{erfc}[2n\eta_1 + \eta] - \sum_{n=0}^{\infty} \operatorname{erfc}[2(n+1)\eta_1 - \eta] \quad (182)$$

which is approximated by truncating the asymptotic series to

$$u \cong \operatorname{erfc}(\eta) - \operatorname{erfc}(2\eta_1 - \eta) + \operatorname{erfc}(2\eta_1 + \eta) - \operatorname{erfc}(4\eta_1 - \eta) + \operatorname{erfc}(4\eta_1 + \eta) \quad (183)$$

where

$$\eta = \frac{z'}{2\sqrt{\nu t}} \quad (184)$$

$$\eta_1 = \frac{h}{2\sqrt{\nu t}} \quad (185)$$

and  $z'$  is the dimensional coordinate normal to the plates. The truncation of Eq. 182 to Eq. 183 results in errors in  $u$  less than  $10^{-11}$ .

The boundary conditions for this one-dimensional problem consist of upper and lower plate conditions. Define  $h$  as the length scale such that  $z = z'/h$ . For  $t \leq 0$ ,  $u = 0$  for all  $z \in [0, 1]$ . For  $t > 0$ ,  $u = 1$  at  $z = 0$  and  $u = 0$  at  $z = 1$ . The TANS model requires the conditions  $v = 0$ ,  $w = 0$ , and  $p_z = 0$  at  $z = 0$  and  $z = 1$ . The derivatives in the  $x$  and  $y$  directions must also vanish to simulate one-dimensional flow.

The number of unevenly spaced nodes in the  $z$  direction,  $n_z$ , is 11, while three nodes in the  $x$  and  $y$  directions are used. The node locations in the  $z$  direction are given by

$$z_k = (k - 1)r^{k-1}\Delta z_0 \quad (k = 1, \dots, 11)$$

where  $r = 1.1$  and  $\Delta z_0 = 0.038554328$ . Unequally spaced nodes were used to help validate the inclusion of the grid metric calculations in the early development of the model.

The Reynolds number for this calculation based on  $h$  is 6.2 and the Mach number is 0.09. The nondimensional time step ( $\Delta t = 0.00464$ ) is taken from results of Beam and Warming (1978), who comment that the comparison was less favorable for Courant numbers <sup>1</sup> away from unity. The Courant number for this calculation is approximately 1.3.

Figure 75 shows the excellent comparison between the solution from Eq. 183 and the TANS solution.

The  $L_2$  norms of the difference in the velocities,  $u$ , between the TANS model and the exact relation are less than 4.2E-03 for the five time levels in the figure.

---

<sup>1</sup>Courant number is defined as  $\nu = c' \frac{\Delta t}{\Delta z}$ .

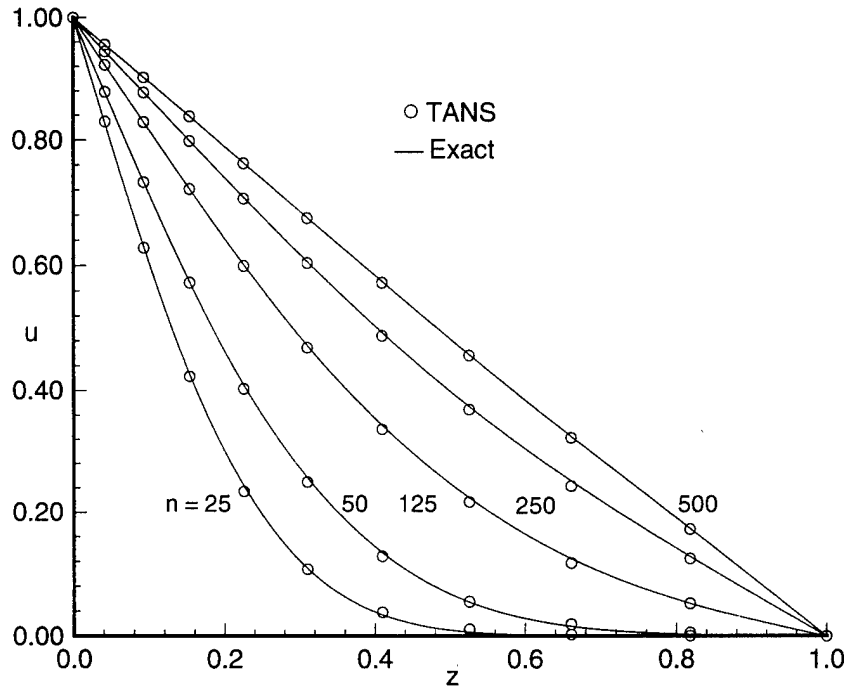


Figure 75. Formation of Couette flow for  $Re_h = 6.2$  and  $M = 0.09$ . Exact solution from Eq. 183.  $t = n\Delta t$ .

#### D.4 Unsteady Heat Conduction.

So far, two steady flows have been considered; comparing the steady velocities and temperature to known solutions. The Couette flow helped to validate the time accuracy of a the velocity field. The remaining checkcase extends the validation of time accuracy to the energy equation.

A flat plate immersed in a motionless fluid is considered. At  $t \leq 0$  the plate temperature is defined to be the reference temperature, or  $T = 1$  for  $t \leq 0$ . At  $t = 0$ , the plate is impulsively heated the to  $T_w$ . The TANS model is used to predict the temperature above the plate,  $T(t, z)$ , where  $z$  is the distance normal to the plate. This is similar to the Couette flow problem, where instead of impulsively moving the plate it is impulsively heated. The difference, however, is that for this problem there is no upper plate, that



is, the dimensional temperature satisfies  $T_{ref}$  as  $z \rightarrow \infty$ . To model this problem, a new nondimensionalization is considered. This is necessary to avoid singular behavior with the current nondimensionalization when the flow is at rest. The new nondimensionalization defines the reference velocity as

$$u'_{ref} \equiv \frac{\alpha}{L}$$

where  $L$  is the reference length and  $\alpha$  is the thermal diffusivity

$$\alpha \equiv \frac{k}{\rho c_p}$$

The reference length  $L$  is defined to be one-third the normal distance from the plate to the edge of the finite computational domain. With no flow, the continuity and momentum equations are satisfied identically. The governing equations reduce to the energy equation. When the above nondimensionalization is substituted into Eqs. 139-143, (the dimensional equations of motion) the resulting equations are exactly that given by Eqs. 10-14 only if the following is true:

$$Pr = 1 \quad Re = 1 \quad M^2 = \frac{1}{\gamma}$$

In other words, an artifice is established under this nondimensionalization that allows for the TANS model to solve this problem (without modification) given the above definitions for the flow parameters  $Pr$ ,  $Re$ , and  $M$ .

The nondimensional energy equation under the above assumptions reduces to

$$T_t = \gamma \alpha T_{zz} \tag{186}$$

which is the classic heat conduction equation with the  $\gamma$  term introduced by the current nondimensionalization. The exact solution to Eq. 186 follows from a solution from the problem of the suddenly accelerated plate, given by Schlichting (1955) as

$$f''(\eta) + 2\eta f'(\eta) = 0 \quad f(0) = 1 \quad f(\infty) = 0 \tag{187}$$

where

$$f = [T - T_{ref}]/[T_w - T_{ref}] \quad (188)$$

$$\eta = \frac{z}{2\sqrt{\gamma t}} \quad (189)$$

The analytical solution to Eq. 187 is

$$f = \text{erfc}(\eta) \quad (190)$$

The TANS model requires an outer boundary that is sufficiently far away from the wall to model the boundary condition at infinity. The procedure to obtain the data from the TANS model involves selecting a target value of  $\eta$  to achieve at some preselected outer boundary. Then from Eq. 189, the maximum run time that can be safely obtained without violating the upper boundary condition can be estimated. In other words, the thermal boundary layer grows with time, and yet the TANS model requires a boundary parallel to the plate and at a finite distance from the plate. Therefore, the TANS simulation will only be valid during a particular window of time.

Boundary conditions for the 1-D problem consist of specifying the wall temperature ( $T_w = 1.2T_{ref}$ ) and setting  $u = v = w$  everywhere. The number of equally spaced nodes in the  $z$  direction is 31. The nondimensional time step is  $\Delta t = 0.001$ .

The comparison of temperature profiles between Eq. 190 and the results of the TANS model is shown in Figure 76. The agreement is excellent, and as expected, the agreement lessens slightly as time increases, due to the movement of the thermal boundary layer towards the outer boundary.

The effect of the outer boundary is also evident in the  $L_2$  norms of the differences between the TANS and exact temperatures. The smallest  $L_2$  norm occurs for  $n = 50$ , and is given by 1.2E-03. The norm steadily increases with time, reaching a value of 2.6E-03 at  $n = 250$ .

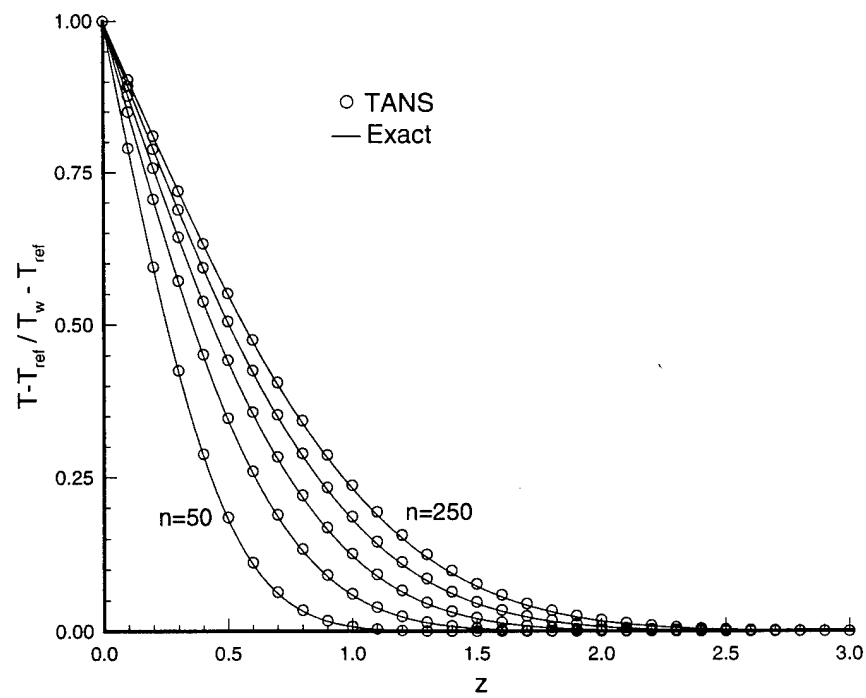


Figure 76. Unsteady heat conduction. Exact solution from Eq. 190.  $t = n\Delta t$ .

### *Appendix E. Simplified Euler Equations for Steady, Axisymmetric Flow*

One of the first studies to consider nonunique solutions of swirling flows is due to Leibovich and Kribus (1990). They categorized four distinct solution branches as static bifurcations of the Bragg-Hawthorne equation (BHE) (Bragg and Hawthorne (1950)). The Bragg-Hawthorne equation refers to a single, elliptic differential equation for the streamfunction, which results from simplifications of Euler's equations for steady, axisymmetric and incompressible flow.

The BHE is developed from Euler's equations in Section E.1. The analysis below follows that of Batchelor (1967). In Section E.2, the author extends this analysis to compressible flows. The result of this analysis yields two equations with two unknowns, the streamfunction,  $\psi$ , and the fluid density,  $\rho$ . One of the two equations can be viewed as a compressible version of the BHE. The second equation is obtained from the definition of the stagnation enthalpy, written in terms of the unknown variables. The two equations are referred to here as the compressible Bragg-Hawthorne equations (CBHE), and represent a simplified model for the study of compressible swirling flows previously unreported in the literature. The CBHE are valid for axisymmetric, inviscid, steady and subsonic flow.

#### *E.1 Development of the Bragg-Hawthorne Equation*

The goal of this analysis is to obtain a single differential equation in terms the streamfunction,  $\psi$ . To achieve this goal, it is first necessary to show that the total head,  $H$ , and the circulation,  $\Gamma$ , are functions of only the streamfunction. This implies that both  $H$  and  $\Gamma$  are constant along a streamline.

The radial, azimuthal and axial components of the velocity vector in cylindrical coordinates  $(r, \theta, z)$  are defined as  $\hat{u}$ ,  $\hat{v}$  and  $\hat{w}$  respectively. The components of the vorticity vector,  $\vec{w}$ , are obtained from the definition,  $\vec{w} = \nabla \times \vec{u}$ , resulting in  $\vec{w} = (-\hat{v}_z, \hat{u}_z - \hat{w}_r, \hat{v}/r + \hat{v}_r)^T$ . The circulation,  $\Gamma$ , (divided by  $2\pi$ ) is defined as

$$\Gamma \equiv r\hat{v} \tag{191}$$

For axisymmetric flow, the streamfunction,  $\psi$ , is defined in the cylindrical coordinate system such that

$$\hat{w} = \psi_r / r \quad \hat{u} = -\psi_z / r \quad (192)$$

Assuming a steady, inviscid and incompressible flow, the momentum equation is written as

$$\vec{u} \cdot \nabla \vec{u} + \nabla \left( \frac{p}{\rho} \right) = 0 \quad (193)$$

Eq. 193 can be rewritten by utilizing the vector identity

$$\vec{u} \cdot \nabla \vec{u} \equiv \frac{1}{2} \nabla (\vec{u} \cdot \vec{u}) - \vec{u} \times \vec{w} \quad (194)$$

Substituting Eq. 194 into Eq. 193 yields

$$\nabla \left( \frac{1}{2} [\vec{u} \cdot \vec{u}] + \frac{p}{\rho} \right) = \vec{u} \times \vec{w} \quad (195)$$

The momentum equation is now written in a form involving the total head,  $H$ , defined as  $H \equiv \frac{1}{2} |\vec{u}|^2 + p/\rho$ . Therefore, Eq. 195 can be written as

$$\nabla H = \vec{u} \times \vec{w} \quad (196)$$

Since  $\nabla H$  is normal to  $\vec{u}$ , from Eq. 196, and  $\vec{u}$  is locally tangent to the local streamline, then  $H$  must be constant along a streamline

$$H = H(\psi) \quad (197)$$

The following will show that  $\Gamma$  is constant along a streamline, which is a restatement of Kelvin's circulation theorem for incompressible, inviscid flows. For axisymmetric flow, the azimuthal component of  $\nabla H$  is identically zero. Therefore, the azimuthal component of Eq. 196 can be expanded to find

$$0 = \frac{\hat{u}\hat{v}}{r} + \hat{u}\hat{v}_r + \hat{w}\hat{v}_z \quad (198)$$

The right-hand side of Eq. 198 is now shown to be related to the substantial derivative of the circulation, which for steady flow is

$$\frac{D(r\hat{v})}{Dt} = \vec{u} \cdot \nabla(r\hat{v}) = \vec{u} \cdot \hat{v} \nabla r + \vec{u} \cdot r \nabla \hat{v} \quad (199)$$

Performing the dot products in Eq. 199, we obtain

$$\frac{D(r\hat{v})}{Dt} = \hat{u}\hat{v} + r\hat{u}\hat{v}_r + r\hat{w}\hat{v}_z \quad (200)$$

Comparing Eq. 198 with Eq. 200, we find that

$$\frac{D(r\hat{v})}{Dt} = \frac{D(\Gamma)}{Dt} = 0 \quad (201)$$

which implies that

$$\Gamma = \Gamma(\psi) \quad (202)$$

i.e., the circulation depends only on  $\psi$ .

The Bragg-Hawthorne equation can now be obtained by considering the axial component of Eq. 196, which is written as

$$H_z = \hat{u}(\hat{u}_z - \hat{w}_r) + \hat{v}\hat{v}_z \quad (203)$$

Eq. 203 can be rewritten in terms of the streamfunction by utilizing Eq. 192, Eq. 197 and Eq. 202 to obtain

$$H_z = \frac{-\psi_z}{r} \left[ \frac{-\psi_{zz}}{r} - \frac{\psi_{rr}}{r} + \frac{\psi_r}{r^2} \right] + \frac{\Gamma \Gamma_z}{r^2} \quad (204)$$

From the chain rule of differentiation, we find that  $H_z = \dot{H}\psi_z$  and  $\Gamma_z = \dot{\Gamma}\psi_z$ , where  $\dot{H} = dH/d\psi$  and  $\dot{\Gamma} = d\Gamma/d\psi$ . Substituting the expressions for  $H_z$  and  $\Gamma_z$  into Eq. 204 yields

$$\frac{-\psi_z}{r} \left[ \frac{-\psi_{zz}}{r} - \frac{\psi_{rr}}{r} + \frac{\psi_r}{r^2} \right] + \frac{\psi_z \Gamma \dot{\Gamma}}{r^2} = \psi_z \dot{H} \quad (205)$$

Multiplying Eq. 205 by  $r^2/\psi_z$  yields the final form of the Bragg-Hawthorne equation (Bragg-Hawthorne (1950))

$$\psi_{zz} + \psi_{rr} - \frac{\psi_r}{r} = r^2 \dot{H} - \Gamma \dot{\Gamma}. \quad (206)$$

The approach used by Leibovich and Kribus (1990) to solve Eq. 206 is to choose a “specifying” flow, which defines  $H(\psi)$  and  $\Gamma(\psi)$  to yield a particular form of the BHE that can be solved for  $\psi$ . Leibovich and Kribus chose a columnar specifying flow, finding nonunique solution paths (Figure 9 of Section 2.1.3) which bifurcate from the branch of columnar solutions.

## *E.2 Extension to Compressible Flows*

The following will show how the development of the Bragg-Hawthorne equation (BHE), given in Section E.1, can be extended to compressible flows. The result of this analysis yields a set of two equations: a modified BHE which includes density terms, and an auxiliary equation which represents the conservation of energy. These two equations, termed the compressible Bragg-Hawthorne equations (CBHE), can be solved for  $\psi$  and  $\rho$  once a specifying flow has been defined (Leibovich and Kribus (1990)). The CBHE are nondimensionalized in terms of a freestream Mach number,  $M_\infty$ , and are valid for steady, inviscid and axisymmetric flow. Subsonic flow is also assumed, allowing for the use of isentropic state relations.

The governing equations representing conservation of mass, momentum, and energy for steady, inviscid, adiabatic, and compressible flow can be written in dimensional form as

$$\nabla \cdot (\rho \vec{u}) = 0 \quad (207)$$

$$\vec{u} \cdot \nabla \vec{u} + \frac{\nabla p}{\rho} = 0 \quad (208)$$

$$\nabla \cdot (\rho \tilde{H} \vec{u}) = 0 \quad (209)$$

where  $\tilde{H}$  is the stagnation enthalpy, defined by

$$\tilde{H} \equiv h + \frac{1}{2}(\vec{u} \cdot \vec{u}) = e + \frac{p}{\rho} + \frac{1}{2}(\vec{u} \cdot \vec{u}) \quad (210)$$

and  $h$  is the specific enthalpy. The specific internal energy,  $e$ , can be written in terms of pressure and density for a perfect gas using Eq. 147 to obtain

$$\tilde{H} = \frac{1}{2}(\vec{u} \cdot \vec{u}) + \frac{\gamma}{\gamma - 1} \frac{p}{\rho} \quad (211)$$

By expanding Eq. 209 we see that

$$\nabla \cdot (\rho \tilde{H} \vec{u}) = \nabla(\rho \tilde{H}) \cdot \vec{u} + \rho \tilde{H}(\nabla \cdot \vec{u}) = 0 \quad (212)$$

which can be simplified from Eq. 207, since

$$\nabla \cdot \vec{u} = -\frac{\nabla \rho \cdot \vec{u}}{\rho} \quad (213)$$

Substituting Eq. 213 into Eq. 212 and simplifying yields

$$\vec{u} \cdot \nabla \tilde{H} = 0 \quad (214)$$

which implies that the stagnation enthalpy is constant along streamlines for steady, inviscid, and adiabatic flows (Batchelor (1967)). This statement is written as

$$\tilde{H} = \tilde{H}(\psi) \quad (215)$$

It is now desirable to obtain an expression similar to Eq. 196, written in terms of  $\tilde{H}$ . This can be accomplished by utilizing the fact that the flow is subsonic and isentropic, allowing for the use of the isentropic relation

$$p = K \rho^\gamma \quad (216)$$



where  $K$  is a constant. With Eq. 216 it follows that

$$\frac{\nabla p}{\rho} = \frac{\gamma}{\gamma - 1} \nabla \left( \frac{p}{\rho} \right) \quad (217)$$

Rewriting the momentum equation

$$\vec{u} \cdot \nabla \vec{u} + \frac{\nabla p}{\rho} = 0$$

and the vector identity

$$\vec{u} \cdot \nabla \vec{u} \equiv \frac{1}{2} \nabla (\vec{u} \cdot \vec{u}) - \vec{u} \times \vec{w}$$

we see that, by utilizing Eq. 217, the momentum equation simplifies to

$$\nabla \left( \frac{1}{2} \vec{u} \cdot \vec{u} + \frac{\gamma}{\gamma - 1} \frac{p}{\rho} \right) = \vec{u} \times \vec{w} \quad (218)$$

or

$$\nabla \tilde{H} = \vec{u} \times \vec{w} \quad (219)$$

Eq. 219 also indicates that  $\tilde{H}$  is constant along streamlines.

Now the axial component of Eq. 219 can be expanded as in the incompressible analysis to yield a compressible version of the BHE. This requires a new definition of the streamfunction which satisfies the compressible form of the continuity equation, Eq. 207.

$$\hat{w} = \frac{1}{\rho r} \psi_r \quad \hat{u} = -\frac{1}{\rho r} \psi_z \quad (220)$$

The azimuthal velocity component is defined as before in terms of the circulation from Eq. 191. The axial component of Eq. 219 is written as

$$\tilde{H}_z = \hat{u}(\hat{u}_z - \hat{w}_r) + \hat{v}\hat{v}_z \quad (221)$$

Substituting Eqs. 191 and 220 into Eq. 221 yields the first of two equations comprising the CBHE.

$$\frac{1}{\rho^2} \left[ \psi_{zz} + \psi_{rr} - \frac{\psi_r}{r} - \frac{1}{\rho} (\rho_z \psi_z + \rho_r \psi_r) \right] = r^2 \dot{\tilde{H}} - \Gamma \dot{\Gamma} \quad (222)$$

Eq. 222 contains two unknowns:  $\psi$  and  $\rho$  (cf. Eq. 206).

A second equation is required to solve for the streamfunction, since the flow density represents a second unknown. Equation 211 represents a suitable second equation, since it can be written in terms of only  $\psi$  and  $\rho$  by using Eqs. 220 and 216.

Before Eq. 211 is rewritten in terms of  $\psi$  and  $\rho$ , a nondimensionalization of the governing equations is performed. This is done to allow for the freestream Mach number to be introduced into the equations. Until now, all of the equations presented have been in dimensional form. For the analysis to follow, let the dimensional variables be denoted with an asterisk, while nondimensional variables have no asterisk. The nondimensional variables are defined as follows:

$$\hat{u} = \hat{u}^*/U_\infty \quad \hat{v} = \hat{v}^*/U_\infty \quad \hat{w} = \hat{w}^*/U_\infty$$

$$\rho = \rho^*/\rho_\infty$$

$$p = p^*/\rho_\infty U_\infty^2$$

$$T = \gamma R T^*/c_\infty^2$$

where  $T$  is the temperature and  $R$  is the gas constant.  $U_\infty$ ,  $\rho_\infty$ , and  $c_\infty$  represent dimensional reference conditions, where  $c$  is the speed of sound. Under this nondimensionalization, the two governing equations, Eq. 222 and Eq. 211 are unaltered in form. However, Eq. 211 contains a pressure term which must be rewritten in terms of the density. The equation of state,  $p^* = \rho^* R T^*$ , can be written in nondimensional form as

$$p = \frac{\rho T}{\gamma M_\infty^2} \quad (223)$$

where  $M_\infty$  is the reference Mach number. For isentropic flow

$$\frac{p^*}{T^{*\gamma/(\gamma-1)}} = K_1 \quad (224)$$

where  $K_1$  is a constant. The nondimensional form of Eq. 224 can be written in the form

$$\frac{pM_\infty^2}{T^{\gamma/(\gamma-1)}} = K_2 \quad (225)$$

where  $K_2$  is a constant. Now Eq. 223 can be substituted into Eq. 225 to eliminate temperature. This results in

$$\frac{p}{\rho^\gamma} = \frac{K_3}{M_\infty^2} \quad (226)$$

where  $K_3$  is a constant and is evaluated by writing Eq. 226 at the reference condition. Eq. 226 can now be written as

$$p = \frac{\rho^\gamma}{\gamma M_\infty^2} \quad (227)$$

Eq. 211 can now be written in nondimensional form by substituting in Eqs. 191, 220, and 227 to yield

$$\tilde{H} - \frac{\Gamma^2}{2r^2} = \frac{1}{2\rho^2 r^2} (\psi_r^2 + \psi_z^2) + \frac{\rho^{\gamma-1}}{(\gamma-1)M_\infty^2} \quad (228)$$

which is only a function of  $\psi$  and  $\rho$ .

Eqs. 222 and 228 represent the compressible Bragg-Hawthorne equations (CBHE), consisting of two equations with the two unknowns;  $\psi$  and  $\rho$ . The CBHE are repeated here in non-dimensional form as

$$\frac{1}{\rho^2} \left[ \psi_{zz} + \psi_{rr} - \frac{\psi_r}{r} - \frac{1}{\rho} (\rho_z \psi_z + \rho_r \psi_r) \right] = r^2 \dot{\tilde{H}} - \Gamma \dot{\Gamma}$$

$$\tilde{H} - \frac{\Gamma^2}{2r^2} = \frac{1}{2\rho^2 r^2} (\psi_r^2 + \psi_z^2) + \frac{\rho^{\gamma-1}}{(\gamma-1)M_\infty^2}$$

The CBHE can be solved once a specifying flow is defined and appropriate boundary conditions on  $\psi$  and  $\rho$  are formulated. The CBHE represent a simplified set of equations which will allow for the analysis of the effect of compressibility on steady, axisymmetric and inviscid swirling flows.

## Appendix F. Derivation and Application of the Beam-Warming Scheme.

Details of the TANS solution procedure are contained in this chapter. The solution procedure is a modified version of the Beam-Warming scheme, outlined by Anderson, et al. (1984). The major differences in the application of the scheme are (1) the use of fourth-order compact differencing for discretizing spatial derivatives, (2) the use of governing equations written in nonconservative form, and (3) the explicit treatment of viscous terms.

A derivation of the compact operator is given in Section F.1. Section F.2 provides a derivation of the time-marching scheme used by Beam and Warming (1978). This analysis results in an expression for the solution correction,  $\Delta^n U$ , written to first or second-order temporal accuracy. Section F.3 applies this general time-marching scheme to the non-conservative system of equations. Spatial discretization is performed using the compact scheme.

### F.1 The Fourth-Order Compact Scheme Approximation

The compact scheme approximation (Lele, 1992) is derived in this section. As a general example, approximate the first derivative of the scalar  $u$  with respect to  $x$  at a general node index,  $i$ . The compact scheme approximation considers not only the value,  $u$ , at adjacent points but also the derivative of  $u$ , denoted  $u_x$ . This results in a tridiagonal system of equations for  $u_x$  along a line of nodes. The approximation is in terms of  $u_{i+1}$ ,  $u_{i-1}$ ,  $u_{x,i+1}$ , and  $u_{x,i-1}$ . An approximation of these terms is found by expanding in a Taylor series about the node  $i$  assuming  $x_i - x_{i-1} = x_{i+1} - x_i = h$ .

$$u_{i-1} = u_i - hu_{x,i} + \frac{h^2}{2}u_{xx,i} - \frac{h^3}{6}u_{xxx,i} + \frac{h^4}{24}u_{xxxx,i} - \mathcal{O}(h^5) \quad (229)$$

$$u_{i+1} = u_i + hu_{x,i} + \frac{h^2}{2}u_{xx,i} + \frac{h^3}{6}u_{xxx,i} + \frac{h^4}{24}u_{xxxx,i} + \mathcal{O}(h^5) \quad (230)$$

$$hu_{x,i+1} = hu_{x,i} + h^2u_{xx,i} + \frac{h^3}{2}u_{xxx,i} + \frac{h^4}{6}u_{xxxx,i} + \mathcal{O}(h^5) \quad (231)$$

$$hu_{x,i-1} = hu_{x,i} - h^2u_{xx,i} + \frac{h^3}{2}u_{xxx,i} - \frac{h^4}{6}u_{xxxx,i} + \mathcal{O}(h^5) \quad (232)$$

A linear combination of Eqs. 229–232 is desired such that all of the  $h^2$ ,  $h^3$ , and  $h^4$  terms vanish. Then  $u_{x,i}$  is solved to the desired fourth-order accuracy since it is written

above with a coefficient of  $h$ . To form the linear combination of Eqs. 229–232, multiply Eq. 229 by a scalar  $a$ , Eq. 230 by  $b$ , Eq. 231 by  $c$ , and Eq. 232 by  $d$ . Then sum Eqs. 229–232 and group terms of similar powers of  $h$ . The coefficients  $a - d$  are solved to yield a single expression for  $u_{x,i}$ . If  $u_i$  is not to appear in the approximation then we must require that

$$a + b = 0 \quad (233)$$

The requirement that the  $h^2$  and  $h^4$  terms vanish result in the conditions

$$a + b + 2c - 2d = 0 \quad (234)$$

$$a + b + 4c - 4d = 0$$

These two equations are redundant if  $a + b = 0$ , therefore, only the first of these two will be retained. The  $h^3$  terms vanish if

$$-a + b + 3c + 3d = 0 \quad (235)$$

Finally, it is desired that  $u_{x,i}$  does not vanish, since this is the term requiring approximation. To insure that this term does not vanish, it will be required that

$$-a + b + c + d = -4 \quad (236)$$

The right-hand-side of Eq. 236 is selected to provide a nonsingular solution, and to reduce the number of manipulations to obtain the expression for  $u_{x,i}$ . Solving Eqs. 233–236 yields  $a = 3$ ,  $b = -3$ ,  $c = d = 1$ . The linear combination of Eqs. 229–232 becomes

$$3u_{i-1} - 3u_{i+1} + hu_{x,i+1} + hu_{x,i-1} = -4hu_{x,i} + \mathcal{O}(h^5)$$

which is rearranged as

$$h(6u_{x,i} + [u_{x,i+1} - 2u_{x,i} + u_{x,i-1}]) = 3(u_{i+1} - u_{i-1}) + \mathcal{O}(h^5) \quad (237)$$

Eq. 237 is further simplified in form by defining  $\delta_x = u_{i+1} - u_{i-1}$  and  $\delta_x^2 u_{x,i} = u_{x,i+1} - 2u_{x,i} + u_{x,i-1}$ , to yield

$$6h(1 + \delta_x^2/6)u_{x,i} = 3\delta_x u_i + \mathcal{O}(h^5) \quad (238)$$

which simplifies for  $S_x \equiv 1 + \delta_x^2/6$  to

$$S_x(u_{x,i}) = \frac{\delta_x u_i}{2h} + \mathcal{O}(h^4) \quad (239)$$

Eq. 239, written over a line of nodes, represents a tridiagonal system of equations for  $u_x$ . Boundary conditions are imposed at boundary nodes to complete the system of equations. The approximation for  $u_x$  also appears in the literature (Anderson et al. (1984)) in the form

$$u_{x,i} = \frac{1}{2h} \left( \frac{\delta_x u_i}{S_x} \right) + \mathcal{O}(h^4) \quad (240)$$

where the  $S$  operator appears in the denominator on the right-hand-side of Eq. 240.

## F.2 A General 3 Time-Level Marching Scheme.

The Beam-Warming scheme utilizes a general three time-level marching scheme. The temporal derivative of the solution vector,  $U_t$ , at a point in space, is written as a sum of implicit ( $n+1$ ) and explicit ( $n$ ) contributions which satisfy a three time-level discretization of the form

$$\theta_1 U_t^{n+1} + (1 - \theta_1) U_t^n = \frac{\theta_2 U^{n-1} + \theta_3 U^n + \theta_4 U^{n+1}}{\Delta t} \quad (241)$$

where  $\theta_1$  is defined between  $\theta_1 = 0$  (fully explicit) and  $\theta_1 = 1$  (fully implicit) and  $\theta_2 - \theta_4$  are parameters selected to achieve different schemes.

The time-marching scheme is written such that  $\Delta^n U$  is either first or second-order accurate, depending on the parameters  $\theta_1 - \theta_4$ . Since  $\Delta^n U$  is of  $\mathcal{O}(\Delta t)$ , first/second-order accuracy of  $\Delta^n U$  requires truncation errors of  $\mathcal{O}(\Delta t^2)/\mathcal{O}(\Delta t^3)$ , respectively. Similarly, since  $U_t^{n+1}$  is of  $\mathcal{O}(1)$ , it must be written to  $\mathcal{O}(\Delta t)/\mathcal{O}(\Delta t^2)$  to achieve first/second-order accuracy, respectively.

An approximate expression for  $U_i^{n+1}$  is found by writing Eq. 241 at level  $n + 1$ ; approximating terms at the other time levels with Taylor series to obtain

$$\begin{aligned} \theta_1 U_i^{n+1} + (1 - \theta_1) [U_i^{n+1} - \Delta t U_{it}^{n+1}] = \\ \frac{\theta_4}{\Delta t} [U^{n+1}] + \frac{\theta_3}{\Delta t} \left[ U^{n+1} - \Delta t U_t^{n+1} + \frac{\Delta t^2}{2} U_{tt}^{n+1} \right] + \\ \frac{\theta_2}{\Delta t} \left[ U^{n+1} - 2\Delta t U_t^{n+1} + \frac{2\Delta t^2}{2} U_{tt}^{n+1} \right] + \mathcal{O}(\Delta t)^2 \end{aligned} \quad (242)$$

Rearranging Eq. 242 results in

$$\frac{-U^{n+1}}{\Delta t} (\theta_2 + \theta_3 + \theta_4) + U_t^{n+1} (1 + 2\theta_2 + \theta_3) + U_{tt}^{n+1} \Delta t \left( \theta_1 - 2\theta_2 - \frac{1}{2}\theta_3 - 1 \right) + \mathcal{O}(\Delta t)^2 = 0 \quad (243)$$

For first-order accuracy, the  $\mathcal{O}(\Delta t)$  terms can remain in Eq. 243, only requiring that

$$\theta_2 + \theta_3 + \theta_4 = 0 \quad (244)$$

$$1 + 2\theta_2 + \theta_3 = 0 \quad (245)$$

Eqs. 244-245 represent two equations with three unknowns,  $(\theta_2, \theta_3, \theta_4)$ . Therefore, the solution must be in terms of one of the parameters. Choosing  $\theta_2$  as this parameter, the requirement for first-order accuracy is

$$\theta_3 = -(1 + 2\theta_2) \quad (246)$$

$$\theta_4 = 1 + \theta_2 \quad (247)$$

For second-order accuracy, Eqs. 244-245 must again be satisfied, along with the additional constraint that  $\mathcal{O}(\Delta t)$  terms in Eq. 243 vanish, requiring that

$$\theta_1 - 2\theta_2 - \frac{1}{2}\theta_3 - 1 = 0 \quad (248)$$

Eqs. 244-245 and Eq. 248 represent three equations with four unknowns. The solution in terms of  $\theta_2$  results in Eqs. 246-247, along with the following additional constraint for

second-order temporal accuracy

$$\theta_1 = \theta_2 + \frac{1}{2} \quad (249)$$

Substituting Eqs. 246-247 into Eq. 241 yields a two-parameter discretization of  $U_t$  of the form

$$\begin{aligned} \theta_1 U_t^{n+1} + (1 - \theta_1) U_t^n = & \frac{(1 + \theta_2) U^{n+1} - (1 + 2\theta_2) U^n + \theta_2 U^{n-1}}{\Delta t} + \\ & \mathcal{O} \left[ \left( \theta_1 - \frac{1}{2} - \theta_2 \right) (\Delta t) + (\Delta t)^2 \right] \end{aligned} \quad (250)$$

which is second-order accurate in time when Eq. 249 is satisfied.

Eq. 250 is now cast into the delta form. The delta form of an equation is in terms of the difference between unknown quantities at time level  $n + 1$  and known quantities at time level  $n$ . For a scalar,  $q$ , the term  $\Delta^n q$  is defined as

$$\Delta^n q = q^{n+1} - q^n$$

Casting Eq. 250 into the delta form results in

$$\begin{aligned} \left[ \theta_1 \frac{\partial}{\partial t} (U^n + \Delta^n U) + (1 - \theta_1) \frac{\partial}{\partial t} U^n \right] \Delta t = \\ (1 + \theta_2)(U^n + \Delta^n U) - (1 + 2\theta_2)U^n + \theta_2(U^n - \Delta^{n-1}U) + \\ \mathcal{O} \left[ \left( \theta_1 - \frac{1}{2} - \theta_2 \right) (\Delta t)^2 + (\Delta t)^3 \right] \end{aligned} \quad (251)$$

where upon cancelling terms and rearranging yields

$$\begin{aligned} \Delta^n U = \left[ \frac{\theta_1 \Delta t}{1 + \theta_2} \right] \frac{\partial}{\partial t} (\Delta^n U) + \left[ \frac{\Delta t}{1 + \theta_2} \right] \frac{\partial}{\partial t} (U^n) + \left[ \frac{\theta_2}{1 + \theta_2} \right] \Delta^{n-1} U + \\ \mathcal{O} \left[ \left( \theta_1 - \frac{1}{2} - \theta_2 \right) (\Delta t)^2 + (\Delta t)^3 \right] \end{aligned} \quad (252)$$

Eq. 252 is the general three-time-level scheme found in the literature. For example, refer to Anderson et al. (1984), Eq. 9-42.



Various time-integration schemes are employed by specifying  $\theta_1$  and  $\theta_2$ , as shown in Table 21.

Table 21. Time marching schemes.

Scheme	$\theta_1$	$\theta_2$	Time Accuracy
<i>Euler Explicit</i>	0	0	1st
<i>Euler Implicit</i>	1	0	1st
<i>Trapezoidal</i>	1/2	0	2nd
<i>3-point Backward</i>	1	1/2	2nd

### F.3 The Beam-Warming Scheme Applied to Equations in Nonconservative Form.

The governing equations in nonconservative form are incorporated into the time-marching scheme, Eq. 252, to ultimately arrive at the approximately factored equation given by Eq. 120 in Section 3.6. The governing equations in nonconservative form, Eq. 25, are rewritten here for convenience as

$$U_t + AU_\xi + BU_\eta + CU_\zeta = D \quad (253)$$

Using Eq. 253, expressions for the first two terms on the right-hand side of Eq. 252 are found, using

$$\begin{aligned} \frac{\partial}{\partial t}(\Delta^n U) = & D^{n+1} - D^n - A^{n+1}\Delta^n U_\xi - A^{n+1}U_\xi^n + A^n U_\xi^n \\ & - B^{n+1}\Delta^n U_\eta - B^{n+1}U_\eta^n + B^n U_\eta^n \\ & - C^{n+1}\Delta^n U_\zeta - C^{n+1}U_\zeta^n + C^n U_\zeta^n \end{aligned} \quad (254)$$

$$\frac{\partial}{\partial t}(U^n) = D^n - A^n U_\xi^n - B^n U_\eta^n - C^n U_\zeta^n \quad (255)$$

Eq. 254 is simplified by lagging the viscous terms with the approximation

$$D^{n+1} = D^n + \mathcal{O}(\Delta t) \quad (256)$$

This results in a significant simplification of the fully implemented Beam-Warming scheme given by Anderson, et al. (1984). The impact on the solution is a formal reduction of tem-

poral accuracy to first order. However, the convection terms, which greatly dominate the magnitude of the viscous terms in this study are still computed to second-order temporal accuracy.

Substituting Eqs. 254-255 into Eq. 252 yields

$$\Delta^n U = t1 + \left[ \frac{\theta_1 \Delta t}{1 + \theta_2} \right] (-\mathcal{A}^{n+1} \Delta^n U_\xi - \mathcal{A}^{n+1} U_\xi^n + \mathcal{A}^n U_\xi^n) \quad (257)$$

$$- \mathcal{B}^{n+1} \Delta^n U_\eta - \mathcal{B}^{n+1} U_\eta^n + \mathcal{B}^n U_\eta^n - \mathcal{C}^{n+1} \Delta^n U_\zeta - \mathcal{C}^{n+1} U_\zeta^n + \mathcal{C}^n U_\zeta^n) -$$

$$\left[ \frac{\Delta t}{1 + \theta_2} \right] (\mathcal{A}^n U_\xi^n + \mathcal{B}^n U_\eta^n + \mathcal{C}^n U_\zeta^n) + \mathcal{O} \left[ \left( \theta_1 - \frac{1}{2} - \theta_2 \right) (\Delta t)^2 + (\Delta t)^3; \Delta t^2 \right]$$

where  $t1$  is rewritten from Section 3.6 as

$$t1 = \frac{\Delta t D^n + \theta_2 \Delta^{n-1} U}{1 + \theta_2}$$

and the first and second elements of the truncation error term refer to the temporal error of the inviscid/viscous terms respectively.

The nonconservative form of the equations do not allow the matrices  $\mathcal{A}^{n+1}$ ,  $\mathcal{B}^{n+1}$ , and  $\mathcal{C}^{n+1}$  to be “absorbed” into the delta terms like they are in a conservative set of equations. Therefore, these matrices are approximated by extrapolation in Section 3.6 to yield

$$(\mathcal{A}, \mathcal{B}, \mathcal{C})^{n+1} = (\mathcal{A}, \mathcal{B}, \mathcal{C})^n + (\mathcal{A}_t, \mathcal{B}_t, \mathcal{C}_t)^n \Delta t + \mathcal{O}(\Delta t^2) \quad (258)$$

The second term on the right-hand side of Eq. 258 is required for second-order temporal accuracy in  $\Delta^n U$ . To see this, consider the term  $\mathcal{A}^{n+1} U_\xi^n$  in Eq. 257.

The delta terms appearing on the right-hand side of Eq. 257 are approximated to fourth-order spatial accuracy by writing

$$\Delta^n U_\xi = \frac{1}{2} \left( \frac{\delta_\xi \Delta^n U}{S_\xi} \right) + \mathcal{O}(\Delta x^4, \Delta y^4, \Delta z^4) \quad (259)$$

$$\Delta^n U_\eta = \frac{1}{2} \left( \frac{\delta_\eta \Delta^n U}{S_\eta} \right) + \mathcal{O}(\Delta x^4, \Delta y^4, \Delta z^4) \quad (260)$$

$$\Delta^n U_\zeta = \frac{1}{2} \left( \frac{\delta_\zeta \Delta^n U}{S_\zeta} \right) + \mathcal{O}(\Delta x^4, \Delta y^4, \Delta z^4) \quad (261)$$

where the operators  $\delta$  and  $S$  are defined in Sections 3.6 and F.1. Substituting Eqs. 259-261 into Eq. 257 and rearranging terms yields

$$\begin{aligned} & \left[ I + \frac{\theta_1 \Delta t}{1 + \theta_2} \left( \frac{\mathcal{A}^{n+1}}{2} \frac{\delta_\xi}{S_\xi} + \frac{\mathcal{B}^{n+1}}{2} \frac{\delta_\eta}{S_\eta} + \frac{\mathcal{C}^{n+1}}{2} \frac{\delta_\zeta}{S_\zeta} \right) \right] \Delta^n U = \\ & t1 + \left[ \frac{\theta_1 \Delta t}{1 + \theta_2} \right] (-\mathcal{A}^{n+1} U_\xi^n + \mathcal{A}^n U_\xi^n - \mathcal{B}^{n+1} U_\eta^n + \mathcal{B}^n U_\eta^n - \mathcal{C}^{n+1} U_\zeta^n + \mathcal{C}^n U_\zeta^n) - \\ & \left[ \frac{\Delta t}{1 + \theta_2} \right] (\mathcal{A}^n U_\xi^n + \mathcal{B}^n U_\eta^n + \mathcal{C}^n U_\zeta^n) + \\ & \mathcal{O} \left[ \left( \theta_1 - \frac{1}{2} - \theta_2 \right) (\Delta t)^2 + (\Delta t)^3; (\Delta t)^2; (\Delta x^4, \Delta y^4, \Delta z^4) \right] \end{aligned} \quad (262)$$

where the third element in the truncation error term is included to denote the spatial accuracy and  $I$  represents the identity matrix.

The left-hand side of Eq. 262 is now approximately factorized to  $\mathcal{O}(\Delta t)^3$  accuracy (Beam and Warming (1978)). Derivatives appearing on the right-hand side are discretized to fourth-order spatial accuracy and rearranged. The final result is

$$\begin{aligned} & \left[ I + \frac{\theta_1 \Delta t}{1 + \theta_2} \frac{\mathcal{A}^{n+1}}{2} \frac{\delta_\xi}{S_\xi} \right] \left[ I + \frac{\theta_1 \Delta t}{1 + \theta_2} \frac{\mathcal{B}^{n+1}}{2} \frac{\delta_\eta}{S_\eta} \right] \left[ I + \frac{\theta_1 \Delta t}{1 + \theta_2} \frac{\mathcal{C}^{n+1}}{2} \frac{\delta_\zeta}{S_\zeta} \right] \Delta^n U = t1 + t3 + \\ & \mathcal{O} \left[ \left( \theta_1 - \frac{1}{2} - \theta_2 \right) (\Delta t)^2 + (\Delta t)^3; (\Delta t)^2; (\Delta x^4, \Delta y^4, \Delta z^4) \right] \end{aligned} \quad (263)$$

where

$$\begin{aligned} t3 = & \frac{1}{2} \left[ (\theta_1 \mathcal{A}^{n+1} + (1 - \theta_1) \mathcal{A}^n) \frac{\delta_\xi}{S_\xi} U^n + (\theta_1 \mathcal{B}^{n+1} + (1 - \theta_1) \mathcal{B}^n) \frac{\delta_\eta}{S_\eta} U^n + \right. \\ & \left. (\theta_1 \mathcal{C}^{n+1} + (1 - \theta_1) \mathcal{C}^n) \frac{\delta_\zeta}{S_\zeta} U^n \right] \left[ -\frac{\Delta t}{1 + \theta_2} \right] \end{aligned}$$

Eq. 263 is the approximately factored expression given by Eq. 120 in Section 3.6 (minus the implicit and explicit damping terms). The truncation errors are valid at interior nodes. Errors associated with discretizing the boundary conditions are given in Section 3.5.

*Appendix G. TANS Run Matrix and Grid Specification.*

Table 22. TANS run matrix.

Run No.	$Re$	$\mathcal{V}$	$M$	$\Delta t$	$\alpha$	BC Type	Grid	Accuracy (Time/Space)
1	100	1.80	0.3	.030	0.00	1	G7	1st/2nd
2	100	1.80	0.3	.030	0.00	1	G8	1st/2nd
3	100	1.80	0.3	.030	0.00	1	G9	1st/2nd
4	100	1.80	0.3	.030	0.00	1	G10	1st/2nd
5	100	1.80	0.3	.030	0.00	1	G11	1st/2nd
6	100	1.80	0.3	.030	0.00	1	G12	1st/2nd
7	100	1.80	0.3	.030	0.00	1	G13	1st/2nd
8	100	1.80	0.3	.040	0.00	1	G1	2nd/4th
9	100	1.80	0.3	.025	0.00	1	G6	2nd/4th
10	100	1.00	0.3	.030	0.05	2	G6	1st/2nd
11	100	1.70	0.3	.030	0.05	2	G6	1st/2nd
12	100	1.00	0.3	.040	0.05	2	G1	2nd/4th
13	100	1.50	0.3	.040	0.05	2	G1	2nd/4th
14	100	1.70	0.3	.040	0.05	2	G1	2nd/4th
15	100	1.80	0.3	.040	0.05	2	G1	2nd/4th
16	250	1.00	0.3	.040	0.05	2	G1	2nd/4th
17	250	1.50	0.3	.040	0.05	2	G1	2nd/4th
18	250	1.53	0.3	.040	0.05	2	G1	2nd/4th
19	250	1.55	0.3	.040	0.05	2	G1	2nd/4th
20	250	1.60	0.3	.040	0.05	2	G1	2nd/4th
21	250	1.65	0.3	.040	0.05	2	G1	2nd/4th
22	250	1.70	0.3	.040	0.05	2	G1	2nd/4th
23	250	1.80	0.3	.040	0.05	2	G1	2nd/4th
24	250	1.90	0.3	.040	0.05	2	G1	2nd/4th
25	250	2.10	0.3	.040	0.05	2	G1	2nd/4th

Table 22. TANS run matrix (con't).

Run No.	$Re$	$\mathcal{V}$	$M$	$\Delta t$	$\alpha$	BC Type	Grid	Accuracy (Time/Space)
26	250	2.30	0.3	.040	0.05	2	G1	2nd/4th
27	250	1.50	0.3	.025	0.05	2	G2	2nd/4th
28	250	1.53	0.3	.025	0.05	2	G2	2nd/4th
29	250	1.53	0.3	.040	0.05	2	G5	2nd/4th
30	250	1.55	0.3	.025	0.05	2	G2	2nd/4th
31	250	1.55	0.3	.025	0.05	2	G1	2nd/4th
32	500	1.49 <sup>s+</sup>	0.3	.040	0.05	2	G1	2nd/4th
33	500	1.49 <sup>s-</sup>	0.3	.040	0.05	2	G1	2nd/4th
34	500	1.49 <sup>u</sup>	0.3	.040	0.05	2	G1	2nd/4th
35	500	1.50	0.3	.040	0.05	2	G1	2nd/4th
36	1000	1.475 <sup>s+</sup>	0.3	.040	0.05	2	G1	2nd/4th
37	1000	1.475 <sup>s-</sup>	0.3	.040	0.05	2	G1	2nd/4th
38	1000	1.475 <sup>u</sup>	0.3	.040	0.05	2	G1	2nd/4th
39	1000	1.475 <sup>s+</sup>	0.3	.025	0.05	2	G2	2nd/4th
40	1000	1.475 <sup>s-</sup>	0.3	.025	0.05	2	G2	2nd/4th
41	1000	1.475 <sup>u</sup>	0.3	.025	0.05	2	G2	2nd/4th
42	1000	1.47 <sup>s+</sup>	0.3	.025	0.05	2	G3	2nd/4th
43	1000	1.47 <sup>s-</sup>	0.3	.025	0.05	2	G3	2nd/4th
44	1000	1.47 <sup>u</sup>	0.3	.025	0.05	2	G3	2nd/4th
45	1000	1.50	0.3	.025	0.05	2	G3	2nd/4th
46	1000	1.60	0.3	.025	0.05	2	G3	2nd/4th
47	1000	1.70	0.3	.025	0.05	2	G3	2nd/4th
48	1000	1.90	0.3	.025	0.05	2	G3	2nd/4th
49	1000	1.90	0.3	.025	0.05	2	G4	2nd/4th
50	1000	2.10	0.3	.025	0.05	2	G3	2nd/4th

Table 23. 3-D grid parameters.

Grid	$nx$	$ny$	$nz$	$L$	$\Delta x_0$	$\beta$	$x_2$
G1	98	41	41	20	.206	0.0	-
G2	122	61	61	20	.200	.25	10
G3	172	61	61	30	.200	.25	10
G4	222	61	61	40	.200	.25	10
G5	146	41	41	30	.206	0.0	-
G6	98	61	61	20	.206	0.0	-
G7	51	61	61	20	.400	0.0	-
G8	101	61	61	20	.200	0.0	-
G9	201	61	61	20	.100	0.0	-
G10	51	61	61	10	.200	0.0	-
G11	201	61	61	40	.200	0.0	-
G12	101	41	41	20	.200	0.0	-
G13	101	81	81	20	.200	0.0	-

Table 24. 2-D grid parameters (grids g1-g4 used in conjunction with grids G1-G4).

Grid	$nx$	$nr$	$L$	$\Delta x_0$	$\beta$	$x_2$
g1	98	32	20	.206	0.0	-
g2	122	48	20	.200	.25	10
g3	172	48	30	.200	.25	10
g4	222	48	40	.200	.25	10

*G.1 Estimate of Computer Usage.*

The two primary computers used to run the TANS model for this study are the DEC 4620/Alpha AXP Workstation and the Cray C-90 (Naval Oceanographic Office, Bay St. Louis, MS.).

The DEC workstation ran the  $Re = 100, 250$  and  $500$  jobs. The estimated CPU time to perform these runs is 7000 DEC CPU hours.

The C-90 computer ran all of the  $Re = 1000$  jobs. The estimated CPU time to perform these runs is 800 C-90 CPU hours.



### Bibliography

1. Abarbanel, S., & Kumar, A. 1988. Compact High Order Schemes for the Euler Equations, NASA CR-181625.
2. Anderson, D.A., Tannehill, J.C., & Pletcher, R.H. 1984. *Computational Fluid Mechanics and Heat Transfer*, Hemisphere Publishing Corporation.
3. Batchelor, G.K. 1967. *An Introduction to Fluid Dynamics*. Cambridge University Press.
4. Beam, R.M. & Warming, R.F. 1976. An Implicit Finite-Difference Algorithm for Hyperbolic Systems in Conservation-Law Form, *J. Comp. Physics*, **22**, p. 87-110.
5. Benjamin, T.B. 1962. Theory of the Vortex Breakdown Phenomenon, *J. Fluid Mech.*, **14**, (4), p. 593-629.
6. Benjamin, T.B. 1967. Some Developments in the Theory of Vortex Breakdown, *J. Fluid Mech.*, **28**, p. 65-84.
7. Beran, P.S. 1987. Numerical Simulations of Trailing Vortex Bursting, *AIAA Paper* 87-1313. Presented at the 19th AIAA Fluid Dynamics, Plasma Dynamics and Lasers Conference, Jun 8-10, Honolulu, HI.
8. Beran, P.S. 1989. *An Investigation of the Bursting of Trailing Vortices Using Numerical Simulation*, Ph.D. Dissertation, California Inst. Of Technology.
9. Beran, P.S. & Culick, F.E.C. 1992. The Role of Non-Uniqueness in the Development of Vortex Breakdown in Tubes, *J. Fluid Mech.*, **242**, p. 491-527.
10. Beran, P.S. 1995. Private Communication.
11. Beran, P.S. 1994. The Time-Asymptotic Behavior of Vortex Breakdown in Tubes, *Computers Fluids*, **23**, No. 7, p. 913-937.
12. Berger, M.S. 1989. Vortex Cores and Vortex Breakdown, *AFOSR-TR-89-1587*.
13. Boyce, W.E. & DiPrima, R.C. 1969. *Elementary Differential Equations and Boundary Value Problems*. Second Edition; John Wiley & Sons, Inc.
14. Bragg, S.L. & Hawthorne, W.R. 1950. Some Exact Solutions of the Flow Through Annular Cascade Discs, *J. Aero. Sci.*, **17**, p. 243-249.
15. Brown G.L. & Lopez, J.M. 1990. Axisymmetric Vortex Breakdown: Part 2. Physical Mechanisms, *J. Fluid Mech.*, **221**, p. 553-576.
16. Brücker, C. 1993. Study of Vortex Breakdown by Particle Tracking Velocimetry (PTV). Part 2: Spiral-type Vortex Breakdown, *Experiments in Fluids*, **14**, p. 133-139.
17. Chorin, A.J. 1967. A Numerical Method for Solving Incompressible Viscous Flow Problems, *J. Comp. Phys.*, **2**, p. 12-26.
18. Darmofal, D.L. 1993. The Role of Vorticity Dynamics in Vortex Breakdown, *AIAA Paper* 93-3036. Presented at the 24th Fluid Dynamics Conference, July 6-9, Orlando, FL.

19. Darmofal, D.L. 1994. On the Trapped Wave Nature of Axisymmetric Vortex Breakdown, *AIAA Paper* 94-2318. Presented at the 25th Fluid Dynamics Conference, June 20-23, Colorado Springs, CO.
20. Désidéri, J., Steger, J.L., and Tannehill, J.C. 1978. On Improving the Iterative Convergence Properties of an Implicit Approximate-Factorization Finite Difference Algorithm, NASA TM 78495.
21. Ekaterinaris, J.A. 1993. Effects of Spatial Accuracy on the Computation of Vortical Flowfields, *AIAA Paper* 93-3371CP. Proc. of the 11th AIAA Computational Fluid Dynamics Conference, July 6-9, Orlando, FL., 1, p. 797-804.
22. Elle, B.J. 1960. On the Breakdown at High Incidences of the Leading E.V. on Delta Wings, *J. of the Royal Aero. Soc.*, **64**, p. 491-493.
23. Faler, J.H. & Leibovich, S. 1977. Disrupted States of Vortex Flow and Vortex Breakdown, *The Physics of Fluids*, **20**, (9), p. 1385-1400.
24. Faler, J.H. & Leibovich, S. 1978. An Experimental Map of the Internal Structure of a Vortex Breakdown. *J. Fluid Mech.*, **86**, p. 313-335.
25. Garg, A.K. & Leibovich, S. 1979. Spectral Characteristics of Vortex Breakdown Flowfields, *The Physics of Fluids*, **22**, (11), p. 2053-2064.
26. Grabowski, W.J. & Berger, S.A. 1976. Solutions of the Navier-Stokes Equations for Vortex Breakdown, *J. Fluid Mech.*, **75**, (3), p. 525-544.
27. Hafez, M., Kuruvila, G., & Salas, M.D. 1986. Numerical Study of Vortex Breakdown, *AIAA Paper* 86-0558. Presented at the 24th AIAA Aerospace Sciences Meeting, Jan. 6-9, Reno, NV.
28. Hafez, M., Ahmad, J., Kuruvila, G., & Salas, M.D. 1987. Vortex Breakdown Simulation, *AIAA Paper* 87-1343. Presented at the 19th AIAA Fluid Dynamics, Plasma Dynamics and Lasers Conference, Jun 8-10, Honolulu, HI.
29. Hall, M.G. 1967. A New Approach to Vortex Breakdown. (Vortex Breakdown Treated as Failure of Quasi-Cylindrical Approximation for Viscous Axisymmetric Flow), *Proc. of 1967 Heat Transfer and Fluid Mech. Inst.*, p. 319-340.
30. Hall, M.G. 1972. Vortex Breakdown, *Ann. Rev. of Fluid Mech.*, **4**, p. 195-218.
31. Harvey, J.K. 1962. Some Observations of the Vortex Breakdown Phenomenon, *J. Fluid Mech.*, **14**, p. 585-592.
32. Kandil, O.A. & Kandil, H.A. 1991. Computation of Compressible Quasi-Axisymmetric Slender Vortex Flow and Breakdown, *Computer Physics Comm.*, North-Holland Publishing, **65**, p. 164-172.
33. Kandil, O.A., Kandil, H.A. & Liu, C.H. 1991A. Supersonic Quasi-Axisymmetric Vortex Breakdown, *AIAA Paper* 91-3311CP. Proc. of the 9th AIAA Applied Aero. Conference, Baltimore, MD., 2, p. 851-863.
34. Kandil, O.A., Kandil, H.A., & Liu, C.H. 1991B. Computation of Steady and Unsteady Compressible Quasi-Axisymmetric Vortex Flow and Breakdown, *AIAA Paper* 91-0752. Presented at the 29th AIAA Aerospace Sciences Meeting, Jan. 7-10, Reno, NV.

35. Kandil, O.A. & Kandil, H.A. 1992. Critical Effects of Downstream Boundary Conditions on Vortex Breakdown, *AIAA Paper* 92-2601. Proc. of the 10th AIAA Applied Aerodynamics Conference, Palo Alto, CA., 1, p. 12-26.
36. Kirkpatrick, D.L.I. 1964. Experimental Investigation of the Breakdown of a Vortex in a Tube, Aero. Res. Council, CP-821.
37. Kopecky, R.M. & Torrance, K.E. 1973. Initiation and Structure of Axisymmetric Eddies in a Rotating Stream, *Computers and Fluids*, 1, p. 289-300.
38. Krause, E., Shi, X.G., & Hartwich, P.M. 1983. Computation of Leading Edge Vortices, *AIAA Paper* 83-1907CP, 1, p. 154-162.
39. Krause, E. 1986. Theoretical and Experimental Investigation of Vortex Breakdown, NASA-CR-176853.
40. Kuruvila, G. & Salas, M.D. 1990. Three-Dimensional Simulation of Vortex Breakdown, NASA-TM-102664.
41. Lambourne, N.C. & Bryer, D.W. 1961. The Bursting of Leading-edge Vortices— Some Observations and Discussions of the Phenomenon, Aero. Res. Council RM-3282.
42. Leibovich, S. 1978. The Structure of Vortex Breakdown, *Ann. Rev. of Fluid Mech.*, 10, p. 221-246.
43. Leibovich, S. 1984. Vortex Stability and Breakdown: Survey and Extension, *AIAA Journal*, 22, (9), p. 1192-1206.
44. Leibovich S. & Kribus, A. 1990. Large-Amplitude Wavetrains and Solitary Waves in Vortices, *J. Fluid Mech.*, 216, p. 459-504.
45. Leibovich, S. 1991. Vortex Dynamics, Final Report 1 June 1989 - 31 May 1991, AFOSR-TR-91-0633.
46. Lele, S.K. 1992. Compact Finite Difference Schemes with Spectral-like Resolution, *J. of Comp. Physics*, 103, p. 16-42.
47. Liu, C.H., Krause, E., & Menne, S. 1986. Admissible Upstream Conditions for Slender Compressible Vortices, *AIAA Paper* 86-1093. Presented at the 4th AIAA/ASME Fluid Mechanics, Plasma Dynamics and Lasers Conference, May 12-14, Atlanta, GA.
48. Liu, C.H. & Menne, S. 1989. Simulation of a Three-Dimensional Vortex Breakdown, *AIAA Paper* 89-1806. Presented at the 20th AIAA Fluid Dynamics, Plasma Dynamics and Lasers Conference, June 12-14, Buffalo, NY.
49. Lopez, J.M. 1994. On the Bifurcation Structure of Axisymmetric Vortex Breakdown in a Constricted Pipe, *Phys. Fluids*, 11, p. 3683-3693.
50. Lugt, H.J. & Abboud, M. 1987. Axisymmetric Vortex Breakdown With and Without Temperature Effects in a Container With a Rotating Lid, *J. Fluid Mech.*, 179, p. 179-200.
51. Lugt, H.J. 1989. Vortex Breakdown in Atmospheric Columnar Vortices, *Bull. Am. Met. Soc.*, 70, p. 1526-1537.
52. MathCAD 2.0 Users Manual. 1988. Mathsoft, Inc. Cambridge, MA 02139.

53. Menne, S. 1988. Vortex Breakdown in an Axisymmetric Flow, *AIAA Paper* 88-0506. Presented at the 26th AIAA Aerospace Sciences Meeting, Jan. 11-14, Reno, NV.
54. Morton, S.A. 1989. *Numerical Simulation of Compressible Vortices*, M.S. Thesis, Air Force Inst. of Tech., AFIT/GAE/ENY/89D-24.
55. Neitzel, G.P. 1988. Streak-line Motion During Steady and Unsteady Axisymmetric Vortex Breakdown, *Physics of Fluids*, **31**, (5), p. 958-960.
56. Pagan, D. & Benay, R. 1988. Numerical Analysis of Vortex Breakdowns Under Pressure Gradients, *La Recherche Aerospaciale* (English Edition), **1**, p. 15-27.
57. Peckham, D.H. & Atkinson, S.A. 1957. Preliminary Results of Low-Speed Wind Tunnel Tests on Gothic Wing of AR 1.0. Aero. Res. Council CP-508.
58. Press, W.H., Flannery, B.P., Teukolsky, S.A. & Vetterling, W.T. 1989. Numerical Recipes, The Art of Scientific Computing. Fortran Version. Cambridge University Press. p. 86-89.
59. Pulliam, T.H. 1984. Euler and Thin Layer Navier-Stokes Codes: ARC2D, ARC3D. Computational Fluid Dynamics User's Workshop, Univ. of Tennessee Space Institute.
60. Pulliam, T.H. 1985. Recent Improvements in Efficiency, Accuracy, and Convergence for Implicit Approximate Factorization Algorithms, *AIAA Paper* 85-0360. Presented at the 23rd AIAA Aerospace Sciences Meeting, Jan. 14-17, Reno, NV.
61. Roach, R.L. & Jenkins, J.E. 1995. Improvements to the Numerical Simulation of Pitching Delta Wings, *AIAA Paper* 95-0761. Presented at the 33rd AIAA Aerospace Sciences Meeting and Exhibit, Jan. 9-12, Reno, NV.
62. Salas, M.D. & Kuruvila, G. 1989. Vortex Breakdown Simulation - A Circumspect Study of the Steady, Laminar Axisymmetric Model, *Computers and Fluids*, **17**, (1), p. 247-262.
63. Sarpkaya, T. 1971A. On Stationary and Travelling Vortex Breakdowns, *J. Fluid Mech.*, **45**, (3), p. 545-559.
64. Sarpkaya, T. 1971B. Vortex Breakdown in Swirling Conical Flows, *AIAA Journal*, **9**, (9), p. 1792-1799.
65. Sarpkaya, T. 1974. Effect of the Adverse Pressure Gradient on Vortex Breakdown, *AIAA Journal*, **12**, p. 602-607.
66. Schlichting, H. 1955. *Boundary Layer Theory*, McGraw-Hill.
67. Seydel, R. 1988. *From Equilibrium to Chaos: Practical Bifurcation and Stability Analysis*, Elsevier Publishing.
68. Shah, G. H. 1990. Effect of Vortex Flow Characteristics on Tail Buffet and High-Angle-of-Attack Aerodynamics of a Twin-Tail Fighter Configuration. High Angle-of-Attack Technology Conference, NASA Langley Research Center.
69. Shi, X. 1985. Numerical Simulation of Vortex Breakdown, NASA-TM-77951.
70. Singh, P.I. & Uberoi, M.S. 1976. Experiments on Vortex Stability, *Phys. Fluids*, **19**, p. 1858-1863.

71. Smith, M.J. & Sankar, L.N. 1991. Evaluation of a Fourth-Order Compact Operator Scheme for Euler/Navier-Stokes Simulations of a Rotor in Hover. *AIAA Paper* 91-0766. Presented at the 29th AIAA Aerospace Sciences Meeting, Jan. 7-10, Reno, NV.
72. Soh, W. 1994. Unsteady Jet Flow Computation Towards Noise Prediction, *AIAA Paper* 94-0138. Presented at the 32nd AIAA Aerospace Sciences Meeting, Jan. 8-11, Reno, NV.
73. Spall, R.E. & Ash, R.L. 1987. Numerical Study of Three-Dimensional Vortex Breakdown, NASA-CR-181068.
74. Spall, R.E. & Gatski, T.B. 1990. A Computational Study on the Taxonomy of Vortex Breakdown, *AIAA Paper* 90-1624. Presented at the 21st AIAA Fluid Dynamics, Plasma Dynamics and Lasers Conference, June 18-20, Seattle, WA.
75. Spall, R.E., Gatski, T.B. & Ash, R.L. 1990. The Structure and Dynamics of Bubble-Type Vortex Breakdown, *Royal Society (London), Proceedings, Series A - Mathematical and Physical Sciences*, **429**, p. 613-637.
76. Spall, R.E. & Gatski, T.B. 1991. A Computational Study of the Topology of Vortex Breakdown, *Royal Society (London), Proceedings, Series A - Mathematical and Physical Sciences*, **435**, (1894), p. 321-337.
77. Squire, H.B. 1960. Analysis of the Vortex Breakdown Phenomenon, Part I. Aero. Dept., Imperial Coll., Rep. No. 102.
78. Steinbrenner, J.P., Chawner, J.R., and Fouts, C.L. 1990. The GRIDGEN 3D Multiple Block Grid Generation System, Vol. 1, Final Report, WRDC-TR-90-3022.
79. Suematsu, Y., Ito, T., & Hayase, T. 1986. Vortex Breakdown Phenomena in a Circular Pipe. V - Axisymmetric Breakdown in Rotating Conical Pipes, *JSME*, **29**, p. 4122-4129.
80. Suematsu, Y., Kato, N., & Ito, T. 1989. Growing Process and Structure of Axisymmetric Vortex Breakdown - Experiments on the Bubble Growing Process, *JSME Int. Journal*, Series II, **32**, p. 63-70.
81. Táasan, S. 1986. Multigrid Method for a Vortex Breakdown Simulation. *NASA CR-178106*.
82. Tsai, C. & Widnall, S.E. 1980. Examination of Group-Velocity Criterion for Breakdown of Vortex Flow in a Divergent Duct, *Phys. Fluids*, **23** (5) p. 864-870.
83. Uchida, S., Nakamura, Y., & Ohsawa, M. 1985. Experiments on the Axisymmetric Vortex Breakdown in a Swirling Air Flow, *Japan Society for Aeronautical and Space Sciences*, **27**, p. 206-216.
84. Visbal, M.R. 1993A. Computational Study of Vortex Breakdown on a Pitching Delta Wing, *AIAA Paper* 93-2974. Presented at the 24th AIAA Fluid Dynamics Conference, July 6-9, Orlando, FL.
85. Visbal, M.R. 1993B. Structure of Vortex Breakdown on a Pitching Delta Wing, *AIAA Paper* 93-0434. Presented at the 31st AIAA Aerospace Sciences Meeting and Exhibit, Jan. 11-14, Reno, NV.

86. White, F.M. 1974. *Viscous Fluid Flow*. McGraw-Hill.
87. Whitham, G.B. 1974. *Linear and Nonlinear Waves*. John Wiley and Sons.
88. Wu, J. & Hwang, S. 1991. Computational Study of Vortex Breakdown in Circular Tube, *AIAA Paper* 91-1820. Presented at the 22nd AIAA Fluid Dynamics, Plasma Dynamics and Lasers Conference, June 24-26, Honolulu, HI.

REPORT DOCUMENTATION PAGE			Form Approved OMB No. 0704-0188	
Public reporting burden for this collection of information is estimated to average 1 hour per response, including the time for reviewing instructions, searching existing data sources, gathering and maintaining the data needed, and completing and reviewing the collection of information. Send comments regarding this burden estimate or any other aspect of this collection of information, including suggestions for reducing this burden, to Washington Headquarters Services, Directorate for Information Operations and Reports, 1215 Jefferson Davis Highway, Suite 1204, Arlington, VA 22202-4302, and to the Office of Management and Budget, Paperwork Reduction Project (0704-0188), Washington, DC 20503.				
1. AGENCY USE ONLY (Leave blank)	2. REPORT DATE July 1995	3. REPORT TYPE AND DATES COVERED Dissertation Sep 1991-Jul 1995		
4. TITLE AND SUBTITLE  THE DEPENDENCE OF THE TIME-ASYMPTOTIC STRUCTURE OF 3-D VORTEX BREAKDOWN ON BOUNDARY AND INITIAL CONDITIONS		5. FUNDING NUMBERS		
6. AUTHOR(S)  Jeffrey C. Tromp				
7. PERFORMING ORGANIZATION NAME(S) AND ADDRESS(ES)  Air Force Institute of Technology, WPAFB OH 45433-6583		8. PERFORMING ORGANIZATION REPORT NUMBER  AFIT/DS/ENY/95-4		
9. SPONSORING / MONITORING AGENCY NAME(S) AND ADDRESS(ES)  Flight Dynamics Directorate Wright Laboratory (WL/F1) Wright-Patterson AFB OH 45433		10. SPONSORING / MONITORING AGENCY REPORT NUMBER		
11. SUPPLEMENTARY NOTES				
12a. DISTRIBUTION / AVAILABILITY STATEMENT  Distribution Unlimited		12b. DISTRIBUTION CODE		
13. ABSTRACT (Maximum 200 words)  The three-dimensional, compressible Navier-Stokes equations are solved numerically to simulate vortex breakdown in tubes. Time integration is performed with an implicit Beam-Warming algorithm, which uses fourth-order compact operators to discretize spatial derivatives. Initial conditions are obtained by solving the steady, compressible, and axisymmetric form of the Navier-Stokes equations using Newton's method. Stability of the axisymmetric initial conditions is assessed through 3-D time integration. Unique axisymmetric solutions at a Reynolds number of 250 lose stability to 3-D disturbances at a critical value of vortex strength, resulting in 3-D and time-periodic flow. Axisymmetric solutions at a Reynolds number of 1000 contain regions of nonuniqueness. Within this region, 3-D time integration reveals only unique solutions, with nonunique, axisymmetric initial conditions converging to a unique solution that is steady and axisymmetric. Past the primary limit point, which approximately identifies critical flow, the solutions bifurcate into 3-D periodic flows. Thus, the author postulates that the development of critical flow is approximately coincident with the loss of stability associated with a Hopf bifurcation. Visualization of the time-asymptotic flow structures, as vortex strength is increased, reveal the growth of flow asymmetries. These asymmetric flows ultimately result in the spiral mode of breakdown.				
14. SUBJECT TERMS  Computational Fluid Dynamics, Vortex Breakdown, Hopf Bifurcation, Navier-Stokes Equations, Compressible Flow, Compact Scheme			15. NUMBER OF PAGES 251	
			16. PRICE CODE	
17. SECURITY CLASSIFICATION OF REPORT UNCLASSIFIED	18. SECURITY CLASSIFICATION OF THIS PAGE UNCLASSIFIED	19. SECURITY CLASSIFICATION OF ABSTRACT UNCLASSIFIED	20. LIMITATION OF ABSTRACT UL	